



Technische Universität München

Fakultät für Mathematik

Lehrstuhl M2 – Fachgebiet Numerische Mathematik (Prof. B. Wohlmuth)

Multiscale methods for flow and transport in porous media

Dipl.-Math. Ettore Vidotto

Vollständiger Abdruck der von der Fakultät für Mathematik der Technischen Universität München zur Erlangung des akademischen Grades eines

Doktors der Naturwissenschaften (Dr. rer. nat.)

genehmigten Dissertation.

Vorsitzende: Prof. Dr. Christina Kuttler

Prüfer der Dissertation:

1. Prof. Dr. Barbara Wohlmuth
2. Prof. Paolo Zunino, Ph.D., Politecnico di Milano
3. Assoc. Prof. Kundan Kumar, Ph.D., Karlstad University

Die Dissertation wurde am 18.12.2018 bei der Technischen Universität München eingereicht und durch die Fakultät für Mathematik am 17.05.2019 angenommen.

Acknowledgements

First and foremost I would like to express my deep gratitude towards my advisor Prof. Dr. Barbara Wohlmuth for her support during the past years. I also thank her for the opportunities she gave me to develop various collaborations and to present my work at several conferences. I would also like to thank Prof. Dr. Rainer Helmig for all the time he dedicated me despite his busy schedule.

I am deeply thankful to the reviewers of the thesis, Prof. Paolo Zunino, Ph.D. and Prof. Kundan Kumar, Ph.D. for spending their valuable time writing the referee reports for this work. I had the opportunity to visit Prof. Paolo Zunino, Ph.D. twice in Milano and I am very thankful to him for inviting me and for the time he invested in our discussions. I am also really grateful to Prof. Kundan Kumar, Ph.D. for finding the time to discuss with me several times and for all the precious suggestions. Special thanks go to Prof. Dr. Christina Kuttler for taking the chair of the examination committee.

My sincere gratitude goes to Dr. Tobias Köppl for all the good work we have done together. Moreover, I would like to thank Martin Schneider and Timo Koch for all the time they invested in our common projects.

I also thank my present and former colleagues at the chair of numerical mathematics (M2) at the TUM. In particular, I would like to thank Dr. Thomas Horger and Dr. Linus Wunderlich not only for carefully proof-reading my thesis, but mostly for their support and for the time spent together. Their daily visits in my office are greatly missing. A special thank goes to Dr. Klaus-Dieter Reinsch for his kindness and support. Sincere thanks go to Dr. Markus Huber and Daniel Drzisga for carefully reading parts of this thesis. And thanks to Markus Muhr and Marvin Fritz for all the fruitful discussions about past, present and future of the MCU.

My deepest gratitude goes to Bettina. Your support and belief in me got me through all these years and I am grateful to have you in my life.

Un ringraziamento speciale va a mio fratello Cesare, che anche se distante, riesce comunque a farmi fare sport, altrimenti quando torno a casa mi batte sempre.

Infine, il mio pensiero più grato va ai miei genitori. Se sono quello che sono, se sono arrivato dove sono arrivato, è soprattutto per merito vostro, per i vostri sacrifici e per la costante fiducia che avete riposto in me.

Abstract

The first part of this thesis deals with multiscale methods for blood flow simulation in microvascular networks. Two different coupling strategies between the tissue and the network of vessels are discussed. A new hybrid approach based on homogenization techniques is proposed and an application to cerebral blood flow simulation is shown. In the second part, an improved streamline method to simulate transport of two-phase systems in heterogeneous porous media is presented and validated by means of numerical experiments.

Zusammenfassung

Im ersten Teil der Arbeit werden Multiskalenmethoden zur Simulation von Blutfluss in mikrovaskulären Netzwerken betrachtet. Zwei verschiedene Kopplungsstrategien zwischen dem Gewebe und dem Netzwerk der Adern werden präsentiert. Ein neues hybrides Verfahren basierend auf Homogenisierung wird entwickelt und zur Simulation von Blutversorgung des Gehirns verwendet. Im zweiten Teil wird ein verbessertes Stromlinienverfahren beschrieben, um den Transport eines zweiphasigen Systems in heterogenen porösen Medien zu simulieren. Numerische Beispiele werden zur Validierung durchgeführt.

Publications by the author

- Vidotto, E., Koch, T., Köppl, T., Helmig, R., Wohlmuth, B.,
Hybrid models for simulating blood flow in microvascular networks.
<https://arxiv.org/abs/1811.10373>, 2018, [219].
- Vidotto, E., Helmig, R., Schneider M., Wohlmuth, B.,
Streamline method for resolving sharp fronts for complex two-phase flow in porous media.
Computational Geosciences, Vol. 22(6), pp. 1487-1502, 2018, [218].
- Köppl, T., Vidotto, E., Wohlmuth, B., Zunino, P.,
Mathematical modeling, analysis and numerical approximation of second order elliptic problems with inclusions.
M3AS: Mathematical Models and Methods in Applied Sciences, Vol. 28, No. 05, pp. 953-978, 2018, [139].
- Köppl, T., Vidotto, E., Wohlmuth, B.,
A local error estimate for the Poisson equation with a line source term.
Numerical Mathematics and Advanced Applications - ENUMATH 2015 Proceedings, pp. 421-429, 2016, [138].

Contents

I. Introduction and mathematical background	11
1. Introduction	11
2. Mathematical background	15
2.1. Sobolev spaces	15
2.2. Discretization methods for elliptic problems	17
2.2.1. Finite element method	18
2.2.2. Discontinuous Galerkin method	21
2.2.3. Cell-centered finite volume method	22
II. Multiscale modeling of blood flow	25
3. Model equations	29
3.1. Considerations on the one-dimensional flow equation	29
3.2. 3D-1D coupled systems	32
4. Analysis of a three-dimensional elliptic problem with line source term	40
4.1. Local error estimate for FEM approximations	41
4.2. Numerical experiments	45
5. Analysis of a two-dimensional elliptic problem with line source terms	47
5.1. Two trace inequalities	49
5.2. Model derivation and analysis	51
5.3. Analysis of the modeling error	53
5.4. Numerical approximation	58
5.5. Numerical experiments	63
5.5.1. Investigation of the modeling error	63
5.5.2. Convergence tests	65
6. 3D-1D coupled system and FEM approximation	69
6.1. Algorithmic aspects of the FEM discretization	69
6.2. Convergence test	74
6.3. A problem with application to microcirculation	76
7. Hybrid models for simulating blood flow in microvascular networks .	80
7.1. An hybrid 3D-3D-1D model	82
7.2. Numerical discretization	90
7.3. Numerical tests	92
7.3.1. Subdivision in large and small vessels	93
7.3.2. Homogenization of the capillaries	94
7.3.3. Investigation of the mass fluxes	97
7.3.4. Investigation of averaged pressures	100
7.3.5. Comments on the hybrid 3D-3D-1D model	103

III. An improved streamline method for two-phase flow in porous media	105
8. Mathematical formulations for two-phase flow	106
8.1. Fully coupled formulation	107
8.2. Fractional flow formulation	109
8.3. Operator splitting methods	111
9. Streamline method for sharp fronts in complex two-phase flow	114
9.1. Solution of the pressure equation	115
9.2. $H(\text{div})$ -projection of the DG-velocity	116
9.3. Front tracking method	118
9.4. Improved streamline method for higher dimensions	122
9.5. Streamline method on decomposed domains	126
9.6. Numerical experiments	129
9.6.1. Two-dimensional heterogeneous problem	129
9.6.2. Anisotropic permeability	132
9.6.3. Segregation test	133
9.6.4. Application to the three-dimensional SPE10 Benchmark	134
Summary and outlook	137
Figures	141
Tables	145
Bibliography	147

Introduction and mathematical background

In this chapter we give an introduction to the work done in this thesis and we list some basic concepts of the functional and numerical settings.

1. Introduction

A wide range of applications like drug transport through biological tissue, biological processes in plant root systems, nuclear waste or CO₂ storage or oil recovery involve flow and transport of substances in porous media. With porous medium we intend a material that contains pores, such as rocks, soil and biological tissues. Looking at the relevant applications listed above, it is clear that the events considered occur on completely different space and time scales. In fact, the transport of a substance through the circulatory system deals with small structures and is considered on a scale of minutes or hours. On the other hand, nuclear waste or CO₂ storage requires simulations spanned over years, so that we can formulate a prediction of potential environmental risks of the procedure. Therefore, in this thesis we deal with two main topics: in the first part, we focus on mathematical methods for blood flow simulations in biological tissues, while in the second we present an efficient method to quickly simulate the transport of a substance such as water or oil in the subsurface.

Blood flow simulation

Being able to accurately simulate the blood flow in the circulatory system, possibly without the need for invasive or expensive procedures, may help studying physiological processes and provide a valuable aid in the understanding of certain diseases. For example, it is fundamental that the effects of a certain therapy are limited to the diseased portion of the tissue, leaving intact the healthy part. This is the case, for example, of the *hyperthermia therapy*, which consists of heating tumorous tissue to cause the death of carcinogenic cells [181]. Modern techniques based on nanotechnology have improved the efficacy of hyperthermia treatments since it provides localized and minimally invasive tumour therapy [24]. In fact, an important role in these treatments is played by the *specific absorption rate*, which evaluates the amount of heat generated when concentrating external energy sources onto the nanoparticles [146]. The techniques discussed in this thesis to simulate the blood flow can be used, combined with appropriate transport models, for example to estimate the heating efficiency of different strategies for delivering such nanoparticles to a

tumour as done in [165].

The blood flow is governed by fundamental equations, whose solutions are approximated by means of simulations on the computer. Of course, these results have to be trustworthy, in the sense that they should be physiological and retrace the real behaviour. Furthermore, it is crucial to obtain such results in a reasonable amount of time so that prompt changes in the therapy or in the dosage can be made.

In the first part of this work, we present some numerical schemes that allow us, under specific simplifications, to simulate certain behaviours of the blood flow. To this end, the motion of the blood in the vessels is usually described by three-dimensional models such as the Navier-Stokes equations [93], for which calculating the numerical solution on a computer is extremely expensive, in particular if one aims to model large portions of the circulatory system with millions of vessels. However, if we consider some specific features of the blood flow, we can simplify our initial problem. The strategy we follow in this thesis is based on a *model reduction technique* [65], which is based on shrinking the vessels to their centerlines, therefore yielding a one-dimensional structure. Under the additional assumption that we restrict to microcirculation, we can rewrite the original three-dimensional models in a one-dimensional flow problem governed by a Hagen-Poiseuille type of equations [106]. The numerical solution of the latter equations is by far easier to obtain, having to deal with a steady one-dimensional problem instead of a three-dimensional and time-dependent one. Despite such drastic dimension reduction, the results obtained by means of this approach still give us a good insight of the situation at a lower computational expense, making this technique an ideal tool in clinical practice [93, Chapter 11]. For example, such model reduction strategy constitutes the first step to study, e.g., the efficiency of cancer therapies delivered through microcirculation [52], or to observe the effects of hyperthermia as a cancer treatment [165].

Flow and transport in the subsurface

The second part of this work is concerned with the simulation of transport of substances in the underground. While the scale of the processes described in the first part is in the order of millimetres, the phenomena considered now occur at a scale of hundreds of meters. In these geological structures, we want to simulate the flow and transport of substances in order to predict, e.g., the propagation of pollutants in the soil, or the extraction of oil from the reservoir. In fact, an accurate prediction of the travel time of a pollutant may be important to prevent a determinate site from contamination. For example, it would allow us to predict the behaviour of an eventual oil leakage from a petrol station, and test whether or not the pollutant may reach a source of potable underground water situated not so far away from the petrol station. In order to prevent such dangerous event, it would be smart to construct the petrol station sufficiently far away from the water source, such that the contaminant may evaporate before reaching the water site [48]. Another example regards the nuclear waste disposal, where the aim consists of predicting radioactive contaminations in the geological site where they are stored [119]. For

practical reasons, the time needed to compute these simulations should not be too long and the results have to be reliable.

Mathematical models are available to describe the flow and transport in the subsurface and they consist of equations, as for the blood flow in biological tissues. To obtain these equations, one usually has to make some simplifications, because it is quite difficult to keep track of every single aspect of the phenomena under observation. Therefore, the question that arises is whether the simulations that we just obtained on our computers are actually approximations of the expected behaviour of the process under observation or something else entirely. From a practical point of view, a fast and accurate numerical solution of such problems is important to obtain the predictions within a reasonable time. To this end, we develop a fast method for simulating flow and transport in the soil that allows us to accurately predict the propagation fronts of, e.g., a pollutant.

Structure of the thesis

The thesis is organized as follows. In Section 2 of Chapter I, we present and discuss some basic definitions and well-known results from numerical analysis that will be referred to throughout this work. In particular, the functional setting is given and the main type of equation considered in the rest of the thesis is presented. The essential steps of three standard numerical methods for approximating the solution of such equations are described.

Chapter II deals with the numerical solution of models for blood flow in microvascular networks and consists of five sections. In Section 3, the governing equations for the blood flow in microcirculation considered in this thesis are provided and the main ideas of the model reduction strategy are presented. In particular, we discuss the coupling strategies between the one-dimensional network and the surrounding tissue, considered as a three-dimensional porous medium. In fact, this kind of interaction between equations defined on different dimensions is not standard. In [67], it is shown that one can combine the equations describing the flow in both the network and the tissue by their source terms. Moreover, it is revealed that the source terms in the three-dimensional equations are given by *Dirac δ -functions*, where the effects of the vessel in the tissue are concentrated on the one-dimensional network itself. In such setting, the reduced regularity of the solution causes standard numerical discretization methods to fail converging with optimal order. In Section 4, we show for a simplified problem derived from the coupled one that the Dirac δ -function actually deteriorates the numerical solution only in a neighbourhood of the singularity, meaning that the numerical method converges with optimal order in a local L^2 -norm. On the other hand, the exchanges between the vessels and the tissue actually occur across the surface of the vessel. Therefore, in Section 5 we present a new coupling approach, where the source term of the three-dimensional flow equation describing these interactions is now concentrated on the lateral wall of each vessel. Analysis of the error that we commit replacing the original equation with the reduced one is carried out for a simplified two-dimensional case. Furthermore, we show a better

order of convergence for the finite element method, if compared with the standard coupling strategy. In Section 6, to show the flexibility of our new coupling strategy, we apply the method to a problem related to microcirculation, where a relatively small set of capillaries is considered. Furthermore, some algorithmic aspects of the implementation are discussed, with the focus posed on the computation of the coupling terms. Finally, in Section 7 we present a new hybrid method to simulate blood flow in microcirculation based on homogenization of the vessels at the capillary scale. To show the flexibility of both methods, we employ them to simulate the flow in a portion of a rat's brain. In the example examined in this thesis, more than 15000 vessels are present, but the number would rapidly increase, if a larger portion of an organ is considered. In this situation the coupled model described above requires an exact resolution of the microvascular network, which cannot be obtained by means of non-invasive techniques. Therefore, we develop a new approach, where the smaller capillaries are homogenized and considered as a three-dimensional porous medium. Thus, in this approach, the physical properties have to be available only on a larger scale. The results obtained by means of both methods are compared and discussed in terms of averaged pressures and fluxes.

In Chapter III, an accurate and fast numerical method to simulate the transport of two different substances in the underground is thoroughly described. The approach presented in this thesis allows us, under appropriate assumptions, to split the model problem in an elliptic pressure equation and an advective equation, as we report in Section 8. In Section 9, we describe the numerical method we employ to solve the resulting system of equations. In particular, we discuss a streamline method for the solution of the advective step, where the original two- or three-dimensional advection equation is reformulated into a set of one-dimensional equations defined along streamlines. The combination of the streamline method with the front tracking method for solving the one-dimensional advective step allows us to reduce the computational costs, if compared with more standard methods [213]. The reason of this complexity reduction consists in the fact that solving the advective step along one-dimensional streamlines is cheaper than solving it for the original two- or three-dimensional problem. For this reason, streamline methods are widely employed in groundwater simulations, if one needs fast informations about the reservoir to, e.g., determine the travelling time of a substance. However, streamlines are efficient, if combined with an accurate and fast solver of the pressure equation, which can be expensive and slow for large and realistic three-dimensional simulations. For this reason, the implementation of our streamline method is developed to work on parallel architectures, so that domain decomposition strategies may be employed to reduce the computational complexity. Our method is validated in terms of travelling time of a substance with respect to the solution obtained with a more standard method.

2. Mathematical background

In this section, we introduce the necessary backgrounds and notations to the results presented in this thesis. In particular, some general results to the numerical solutions of partial differential equations (PDEs) are provided. We point out that the definitions and the results presented in the this section are well-known in the literature, see, e.g., [38, 149, 191].

2.1. Sobolev spaces

The theoretical and the numerical results presented in this work are based on the notion of weak solutions and the corresponding Sobolev function spaces. We consider the relevant standard results on Sobolev spaces and introduce the definitions needed. For more details, we refer, e.g., to [6, 36, 38, 82].

Throughout this thesis, let $\Omega \subset \mathbb{R}^d$ for $d \in \{2, 3\}$ denote a bounded convex polyhedral domain. For a function $u: \Omega \rightarrow \mathbb{R}$ and for a number $1 \leq p < \infty$, we define

$$\|u\|_{L^p(\Omega)} := \left(\int_{\Omega} |u(\mathbf{x})|^p d\mathbf{x} \right)^{1/p}$$

and for $p = \infty$ we set

$$\|u\|_{L^\infty(\Omega)} := \operatorname{ess\,sup}_{\mathbf{x} \in \Omega} \{|u(\mathbf{x})|\}.$$

In either case, we define the Lebesgue spaces

$$L^p(\Omega) := \left\{ u: \Omega \rightarrow \mathbb{R} : \|u\|_{L^p(\Omega)} < \infty \right\}.$$

Integrability can also be defined locally and the set of locally integrable functions is given by

$$L^1_{\text{loc}}(\Omega) := \left\{ u: \Omega \rightarrow \mathbb{R} : u \in L^1(K), \quad \forall K \subset \Omega \text{ compact} \right\}.$$

The multiindex α of order $|\alpha| = \alpha_1 + \dots + \alpha_d$ denotes a vector of the form $\alpha = (\alpha_1, \dots, \alpha_d)$, where each component α_i is a non-negative integer. In the standard multiindex notation, if α is a multiindex and $u, v \in L^1_{\text{loc}}(\Omega)$, we say that u has the α -th weak derivative v , i.e., $D^\alpha u = v$, if

$$\int_{\Omega} u D^\alpha \varphi d\mathbf{x} = (-1)^{|\alpha|} \int_{\Omega} v \varphi d\mathbf{x}$$

for all infinitely differentiable test functions $\varphi \in C_c^\infty(\Omega)$ with compact support.

Let $k \geq 0$ be an integer and let $u \in L^1_{\text{loc}}(\Omega)$. Suppose that the weak derivatives $D^\alpha u$ exist for all $|\alpha| \leq k$. We define the Sobolev norm

$$\|u\|_{W^{k,p}(\Omega)} := \left(\sum_{|\alpha| \leq k} \int_{\Omega} |D^\alpha u|^p d\mathbf{x} \right)^{1/p}$$

in the case $1 \leq p < \infty$, and in the case $p = \infty$

$$\|u\|_{W^{k,\infty}(\Omega)} := \sum_{|\alpha| \leq k} \operatorname{ess\,sup}_{\Omega} \{|D^\alpha u|\}.$$

In either case, we define the Sobolev space

$$W^{k,p}(\Omega) := \left\{ u \in L^1_{\text{loc}}(\Omega) : \|u\|_{W^{k,p}(\Omega)} < \infty \right\}.$$

All Sobolev spaces are Banach spaces. The case $p = 2$ is a special case, since a natural inner product on the Sobolev space $W^{k,2}$ is induced by the norm. Therefore, these spaces are Hilbert spaces and are denoted by $H^k(\Omega) := W^{k,2}(\Omega)$ in the following. The notion of fractional Sobolev space needs to be introduced as well. We define the corresponding interpolation spaces $H^s(\Omega)$ for fractional values $s = k + r$, where k is an integer and $r \in (0, 1)$. In order to do that, we introduce interpolation spaces using the so-called real- or K-method as defined in [6, 29, 212]. Let X, Y be two separable Hilbert spaces with $X \subset Y$ dense in Y . Then we can define the interpolation spaces as

$$(X, Y)_{r,q} := \left\{ u \in Y : \|u\|_{(X,Y)_{r,q}} < \infty \right\}$$

with the norms

$$\|u\|_{(X,Y)_{r,q}} := \begin{cases} \left(\int_0^\infty \left[t^{-r} K(u, t) \right]^q \frac{1}{t} dt \right)^{1/q}, & \text{for } 1 \leq q < \infty, \\ \sup_{0 < t < \infty} \left\{ t^{-r} K(u, t) \right\}, & \text{for } q = \infty, \end{cases}$$

where

$$K(u, t) := \inf_{\substack{v \in X, w \in Y, \\ v+w=u}} \|v\|_X + t\|w\|_Y.$$

All in all, for $s = k + r$ and $r \in (0, 1)$, we can define $H^s(\Omega)$ as

$$H^s(\Omega) := \left(H^k(\Omega), H^{k+1}(\Omega) \right)_{r,2}.$$

An important special case is the space

$$H^{1/2}(\partial\Omega) := \left(L^2(\partial\Omega), H^1(\partial\Omega) \right)_{\frac{1}{2},2},$$

which is the trace space of $H^1(\Omega)$. Furthermore, the space $H_0^1(\Omega)$ is defined as the subspace of $H^1(\Omega)$ in which the traces vanish on $\partial\Omega$, see, e.g., [82].

In the following sections, the notion of dual space arises several times. If X is a real vector space, we denote its dual space by X' , which is given by

$$X' := \{ f : X \rightarrow \mathbb{R} : f \text{ bounded and linear} \}.$$

If the space X is normed, the dual norm on X' is given by

$$\|f\|_{X'} := \sup_{x \in X} \frac{f(x)}{\|x\|_X}.$$

The dual space of $H^s(\Omega)$ is denoted by $H^{-s}(\Omega)$.

Furthermore, in order to work with discontinuous Galerkin methods, we need to introduce another category of Sobolev spaces, the so-called broken Sobolev spaces. Let $T \subset \mathbb{R}^d$ be a bounded polygonal domain with diameter h_T defined by

$$h_T := \sup_{\mathbf{x}, \mathbf{y} \in T} |\mathbf{x} - \mathbf{y}|. \quad (2.1)$$

Let us denote by \mathcal{T}_h a conforming subdivision of Ω [191], where h is the maximum element diameter. We further assume, that \mathcal{T}_h is quasi-uniform [61], which means that if h_T denotes the diameter of the element $T \in \mathcal{T}_h$ and ρ_T denotes the maximum diameter of a ball inscribed in T , then there is a constant $\rho > 0$ such that

$$\frac{h_T}{\rho_T} \leq \rho \quad \forall T \in \mathcal{T}_h.$$

The broken Sobolev spaces depend strongly on the subdivision \mathcal{T}_h of the domain Ω and are defined for any real number s as

$$H^s(\mathcal{T}_h) := \left\{ v \in L^2(\Omega) : v|_T \in H^s(T) \quad \forall T \in \mathcal{T}_h \right\},$$

equipped with the broken Sobolev norm

$$\|v\|_{H^s(\mathcal{T}_h)} := \left(\sum_{T \in \mathcal{T}_h} \|v\|_{H^s(T)}^2 \right)^{1/2}.$$

For more informations, we refer the reader to, e.g., [191, Chapter 2.3].

2.2. Discretization methods for elliptic problems

Having the functional setting at hand, we now briefly describe the three discretization techniques that are employed in this work for approximating solutions of boundary value problems. We begin stating the Lax-Milgram lemma, which represents an important tool in this thesis to prove existence and uniqueness of a weak solution.

Let $\Omega \subset \mathbb{R}^d$ be defined as in Section 2.1. We subdivide the boundary $\partial\Omega$ into two disjoint subsets, Γ_D and Γ_N , where Dirichlet and Neumann conditions are posed, respectively. Let \mathbf{n} be the outward unit normal vector to the boundary and let $f \in L^2(\Omega)$, $g_D \in H^{1/2}(\Gamma_D)$ and $g_N \in L^2(\Gamma_N)$ be given functions. We consider the following general elliptic boundary value problem

$$\begin{cases} -\nabla \cdot (\mathbf{K} \nabla u) = f, & \text{in } \Omega, \\ u = g_D, & \text{on } \Gamma_D, \\ -\mathbf{K} \nabla u \cdot \mathbf{n} = g_N, & \text{on } \Gamma_N, \end{cases} \quad (2.2)$$

where $\mathbf{K} : \Omega \rightarrow \mathbb{R}^{d \times d}$ is a tensor and plays the role of a permeability field. \mathbf{K} is assumed to be sufficiently smooth, symmetric, uniformly positive definite and such

that $\mathbf{K}(\mathbf{x}) \geq \alpha_0 \mathbf{I}$, where \mathbf{I} is the identity matrix, for some $\alpha_0 > 0$ and all $\mathbf{x} \in \Omega$. The boundary problem (2.2) can be reformulated in a weak form, which reads as

$$\text{Find } u \in V \text{ such that: } a(u, v) = \ell(v), \quad \forall v \in V, \quad (2.3)$$

where $a: V \times V \rightarrow \mathbb{R}$, $\ell \in V'$ and the space V depend on the discretization method employed and are defined in the next sections.

To prove the existence and uniqueness of a weak solution to problem (2.3), a standard tool is provided by the Lax-Milgram lemma as stated in [36, 38]. In order to be able to apply this lemma, it is requested that a is a continuous and coercive bilinear form on the Hilbert space H , i.e., for each $u, v \in H$ there exist two positive constants $c_1, c_2 \in \mathbb{R}$ such that

$$|a(u, v)| \leq c_1 \|u\|_H \|v\|_H \quad \text{and} \quad |a(u, u)| \geq c_2 \|u\|_H^2.$$

With these definitions at hand, we can formulate the lemma.

Lemma 2.1 (Lax-Milgram). *Given a Hilbert space H , a continuous, coercive bilinear form $a: H \times H \rightarrow \mathbb{R}$ and a continuous linear functional $\ell \in H'$, there exists a unique solution $u \in H$ such that $a(u, v) = \ell(v)$ for every $v \in H$.*

The common strategy of the discretization methods presented in the following consists of taking a finite dimensional version of (2.3), where the continuous problem is approximated by a discrete weak formulation. To do so, a finite dimensional subspace $V_h \subset V$ has to be defined. There are multiple choices for the space V_h and, for each method, the definition is provided in the corresponding section.

Once we have a finite dimensional space V_h , the discrete weak formulation of (2.3) reads now:

$$\text{Find } u_h \in V_h \text{ such that: } a(u_h, v_h) = \ell(v_h), \quad \forall v_h \in V_h. \quad (2.4)$$

The solution of such problem consists now in solving a linear system, whose dimension and structure depend on the discretization method employed.

2.2.1. Finite element method

The first numerical discretization method we present is the standard finite element method (FEM). For its great flexibility, the great amount of numerical results available, and its relative ease of implementation, the FEM is one of the most used strategies for solving boundary value problems.

To formulate the weak problem, we first define the space V as

$$V := \left\{ v \in H^1(\Omega) : v|_{\Gamma_D} = 0 \right\} \subset H^1(\Omega), \quad (2.5)$$

the bilinear form a and the linear form ℓ as

$$a(u, v) := \int_{\Omega} \mathbf{K} \nabla u \cdot \nabla v \, d\mathbf{x}, \quad \text{and} \quad \ell(v) := \int_{\Omega} f v \, d\mathbf{x} + \int_{\Gamma_N} g_N v \, dS.$$

Regarding the boundary conditions g_D , from the inverse trace theorem there exists an extension $\widetilde{g}_D \in H^1(\Omega)$ of $g_D \in H^{1/2}(\Gamma_D)$ on the entire domain Ω such that $\widetilde{g}_D = g_D$ on Γ_D . With these definitions at hand, the variational formulation of problem (2.2) reads:

$$\text{Find } u \text{ such that: } u - \widetilde{g}_D \in V \text{ and } a(u, v) = \ell(v), \quad \forall v \in V. \quad (2.6)$$

Given a conforming quasi-uniform subdivision \mathcal{T}_h of size h of the polyhedral domain Ω , the discrete weak formulation (2.4) is defined on the standard FEM space provided by continuous piecewise polynomials of degree k , namely

$$V_h^k := \{v \in V : v|_T \in \mathbb{P}^k(T), T \in \mathcal{T}_h\}, \quad (2.7)$$

where $\mathbb{P}^k(T) := \{p : p = \sum_{|\alpha| \leq k} c_\alpha x^\alpha\}$ in the standard multiindex notation denotes the space of polynomials of degree k on T . The FEM approximation of the continuous problem (2.6) involves, typically, the use of an interpolant $\widetilde{g}_{D,h}$ of the Dirichlet data. Finally, we pick the subspace $V_h^k \subset V$ and define the discrete weak problem:

$$\text{Find } u_h \text{ such that: } u_h - \widetilde{g}_{D,h} \in V_h^k \text{ and } a(u_h, v_h) = \ell(v_h), \quad \forall v_h \in V_h^k. \quad (2.8)$$

In case of second order elliptic equations on a convex domain with an H^1 -coercive bilinear form and an L^2 -right hand side, the FEM possesses optimal order of convergence in the H^1 - and L^2 -norms, as stated in the next theorem. For the proof, we refer the reader to, e.g., [38, Section 5.4].

Theorem 2.1. *Let V_h^k be the FEM space (2.7), $u \in H^{k+1}(\Omega)$ the weak solution of (2.6) and u_h the FEM solution of (2.8). Then, the error of the FEM approximation can be bounded by*

$$\|u - u_h\|_{H^1(\Omega)} \leq Ch^k \|u\|_{H^{k+1}(\Omega)}.$$

Furthermore, under assumption of H^2 -regularity in the L^2 -norm, we have the estimate

$$\|u - u_h\|_{L^2(\Omega)} \leq Ch^{k+1} \|u\|_{H^{k+1}(\Omega)}.$$

In Theorem 2.1, the optimal convergence of the FEM is guaranteed by the assumptions that $u \in H^{k+1}(\Omega)$ and $f \in L^2(\Omega)$. However, in most of our applications we deal with Dirac δ -function [73], which means, in particular, that the source term $f \notin L^2(\Omega)$. In such cases, the Dirac δ -function pollutes the numerical solution and no optimal convergence for the FEM can be expected, if some adjustments are not used, such as locally refined meshes [10].

For example, let us denote the Dirac δ -function concentrated at the point $\mathbf{y} \in \Omega$ by $\delta_{\mathbf{y}}$. By this, we interpret $\delta_{\mathbf{y}}$ as the Dirac measure on \mathbb{R}^d giving unit mass to the point \mathbf{y} and can be defined by means of Sobolev's inequality [38, Theorem (1.4.6)]. Therefore, the Dirac δ -function is a continuous linear functional on $W^{k,p}(\Omega)$, provided $k \geq 1$ integer and $1 \leq p < \infty$ are such that

$$\begin{aligned} k &\geq d, & \text{if } p = 1, \\ k &> d/p, & \text{if } p > 1. \end{aligned}$$

Therefore, the Dirac δ -function is the linear functional

$$W^{k,p}(\Omega) \ni v \mapsto v(\mathbf{y}) =: \delta_{\mathbf{y}}(v).$$

When a singular right-hand side is considered, the weak solution of the corresponding version of (2.3) possesses a reduced regularity, which causes the FEM approximation to converge with a suboptimal order with respect to Theorem 2.1, as discussed in the next example.

Example 2.1. *Let us consider $\Omega = (0, 1)^2$ and let $\mathbf{y} := (0.5, 0.5)$. The model problem reads*

$$\begin{cases} -\Delta u = \delta_{\mathbf{y}}, & \text{in } \Omega, \\ u = g_{\text{D}}, & \text{on } \partial\Omega, \end{cases} \quad (2.9)$$

where the boundary function g_{D} is such that the exact solution is given by

$$u(x) = -\frac{1}{2\pi} \ln |\mathbf{x} - \mathbf{y}|.$$

The weak solution is not in $H^1(\Omega)$, but in $W^{1,p}(\Omega)$ for $p \in [1, 2)$. Therefore, the Lax-Milgram lemma 2.1 cannot be applied. However, existence and uniqueness of a weak solution can be proven [51]. Furthermore, in [198], the author proves the convergence order of $2 - d/2$ in the $L^2(\Omega)$ -norm for the error of a FEM approximation of problem (2.9) on quasi-uniform meshes. Further analysis and considerations on such a singular problem are postponed to the next sections. With this example, we show numerically the reduced convergence order for the FEM scheme on a uniform grid when solving (2.9). The meshsize is given by $h = 2^{-\ell}$ for $\ell = 2, \dots, 7$ and the results are collected in Table 2.1. As expected, the order of convergence is suboptimal, independently of the polynomial degree of the FEM approximation.

Table 2.1.: Numerical L^2 -convergence rates for the FEM solution of problem (2.9) with singular right hand side and trial functions of order one and two.

	$k = 1$		$k = 2$	
ℓ	$\ u - u_h\ _{L^2(\Omega)}$	Rate	$\ u - u_h\ _{L^2(\Omega)}$	Rate
2	$1.5775e - 02$	/	$5.5845e - 03$	/
3	$7.9500e - 03$	0.99	$2.7960e - 03$	1.00
4	$3.9884e - 03$	1.00	$1.3981e - 03$	1.00
5	$1.9960e - 03$	1.00	$6.9904e - 04$	1.00
6	$9.9821e - 04$	1.00	$3.4952e - 04$	1.00
7	$4.9913e - 04$	1.00	$1.7476e - 04$	1.00
	expected:	1.00	expected:	1.00

2.2.2. Discontinuous Galerkin method

The second discretization method we present is the discontinuous Galerkin (DG) method, which can be seen as a finite element method that allows for discontinuities in the discrete trial and test spaces. For simplicity, let \mathcal{T}_h be a conforming quasi-uniform subdivision of Ω given by rectangles for $d = 2$ or rectangular hexahedra for $d = 3$. A discretization of the domain by simplices is done analogously, but it is beyond the scope of this work. Before considering a variational formulation as in (2.3), we have to introduce the concepts of mesh faces, averages and jumps. These play a central role in the design and analysis of DG methods, since the approximated solution depends on the way neighbouring mesh elements come into contact.

We subdivide the faces of each element in the following way: the interior faces are collected in the set Γ_h and the boundary faces in the sets Γ_D and Γ_N . For each interior edge/face e , we fix a unit normal vector \mathbf{n}_e and denote by T_e^+ and T_e^- the elements in \mathcal{T}_h such that $e = \partial T_e^+ \cap \partial T_e^-$. We set \mathbf{n}_e to point from T_e^- to T_e^+ . For a function v , we also define its values on both sides of e by $v_e^\pm := v|_{T_e^\pm}$. The weighted average and jump of a function v on the face e are given respectively by

$$\{v\}_{e,w} := w_e^- v_e^- + w_e^+ v_e^+, \quad \text{and} \quad [v]_e := v_e^- - v_e^+, \quad (2.10)$$

with non-negative weights satisfying $w_e^- + w_e^+ = 1$.

If e is a boundary face, then the average and jump are defined as

$$\{v\}_{e,w} = v_e^-, \quad \text{and} \quad [v]_e = v_e^-.$$

The usual (arithmetic) average at interfaces corresponds to the particular choice $w_e^+ = w_e^- = 1/2$. In Section 9.1, a specific \mathbf{K} -dependent choice for the weights is introduced. For the rest of this section, the standard arithmetic average is considered.

With this notation at hand, we can introduce the DG version of the weak formulation (2.3). In this work, we consider only one DG method, namely the so-called *symmetric interior penalty Galerkin* (SIPG) method [72, 226]. For other more general formulations, we refer to [191] and the references therein. We choose as trial and test spaces the broken Sobolev space $V := H^s(\mathcal{T}_h)$ for $s > 3/2$. This choice guarantees us that the trace of the gradient of a function $v \in H^s(\mathcal{T}_h)$ is well-defined. The bilinear form in (2.3) is given for $u, v \in V$ by

$$\begin{aligned} a(u, v) &:= \sum_{T \in \mathcal{T}_h} \int_T \mathbf{K} \nabla u \cdot \nabla v \, d\mathbf{x} - \sum_{e \in \Gamma_h \cup \Gamma_D} \int_e \{\mathbf{K} \nabla u \cdot \mathbf{n}_e\}_e [v]_e \, dS \\ &\quad - \sum_{e \in \Gamma_h \cup \Gamma_D} \int_e \{\mathbf{K} \nabla v \cdot \mathbf{n}_e\}_e [u]_e \, dS \\ &\quad + \sum_{e \in \Gamma_h \cup \Gamma_D} \frac{\sigma_e}{|e|^\beta} \int_e [u]_e [v]_e \, dS, \end{aligned}$$

and the linear form by

$$\ell(v) := \int_\Omega f v \, d\mathbf{x} + \sum_{e \in \Gamma_D} \int_e \left(\frac{\sigma_e}{|e|^\beta} v - \mathbf{K} \nabla v \cdot \mathbf{n}_e \right) g_D \, dS - \sum_{e \in \Gamma_N} \int_e v g_N \, dS,$$

where the number $\sigma_e > 0$ is called *penalty parameter* and the power β is usually given as a function of the dimension of the problem, for example $\beta = (d-1)^{-1}$ [191]. The parameter σ_e is usually defined as functions of other quantities of the problem, such as \mathbf{K} , and a more detailed description is postponed to Section 9.1.

The variational formulation of (2.2) now reads

$$\text{Find } u \in H^s(\mathcal{T}_h) \text{ such that: } a(u, v) = \ell(v), \quad \forall v \in H^s(\mathcal{T}_h). \quad (2.11)$$

As for the FEM, we consider a finite-dimensional subspace of the broken Sobolev space $H^s(\mathcal{T}_h)$ for $s > 3/2$. The natural choice for the DG subspace is the following

$$W_h^k := \left\{ v \in L^2(\Omega) : v|_T \in \mathbb{Q}^k(T), T \in \mathcal{T}_h \right\}, \quad (2.12)$$

where $\mathbb{Q}^k(T) := \{p : p = \sum_{\|\alpha\|_\infty \leq k} c_\alpha x^\alpha\}$ in the standard multiindex notation. The discrete weak formulation of (2.2) now reads

$$\text{Find } u_h \in W_h^k \text{ such that: } a(u_h, v_h) = \ell(v_h), \quad \forall v_h \in W_h^k. \quad (2.13)$$

For $\sigma_e > 0$ large enough, the bilinear form is coercive and bounded with respect to the energy norm on W_h^k defined by

$$\|v\|_\mathcal{E} := \left(\int_\Omega \mathbf{K}(\nabla v)^2 d\mathbf{x} + \sum_{e \in \Gamma_h \cup \Gamma_D} \int_e [v]^2 dS \right)^{1/2}.$$

A similar result to Theorem 2.1 can also be obtained for the SIPG method. To this end, proceeding as in [191, Theorem 2.13-2.14], one can show the optimal convergence properties of the SIPG method, which are collected in the following result.

Theorem 2.2. *Let $u \in H^s(\mathcal{T}_h)$ for $s > 3/2$ be the weak solution of (2.11). Assume moreover that the penalty parameter σ_e is large enough and the power $\beta = 1/(d-1)$. Let u_h be the solution of (2.13). Then there exists a constant C independent of h such that the following optimal a priori error estimates hold*

$$\begin{aligned} \|u - u_h\|_\mathcal{E} &\leq Ch^{\min(k+1, s)-1} \|u\|_{H^s(\mathcal{T}_h)}, \\ \|u - u_h\|_{L^2(\Omega)} &\leq Ch^{\min(k+1, s)} \|u\|_{H^s(\mathcal{T}_h)}. \end{aligned}$$

From a practical point of view, the SIPG method guarantees, in particular, optimal order of convergence, depending on the regularity of the solution, also in the case where the tensor \mathbf{K} is discontinuous, which is the main feature of the problems considered in Chapter III.

2.2.3. Cell-centered finite volume method

The cell-centered finite volume method based on two-point flux approximation (TPFA) is often employed as numerical discretization method because of its ease of

implementation and intrinsic mass-conservation properties. Here, we briefly present the key ingredients of the TPFA method, while a more extensive description of the finite volume method in general can be found, e.g., in [149].

The TPFA method is similar to the finite difference method, in the sense that values of the numerical solution are calculated at discrete places on a meshed geometry. Following [45], we take the integral of (2.2) over any control volume $C \subset \bar{\Omega}$ with a Lipschitz boundary and apply the Gauss divergence theorem on the left-hand side. On the space

$$V := \left\{ v \in H^1(\Omega) : v|_{\Gamma_D} = 0 \right\} \cap H^2(\Omega),$$

the weak formulation of (2.3) reads

$$\text{Find } u \in V \text{ such that: } - \int_{\partial C} \mathbf{K} \nabla u \cdot \mathbf{n} \, dS = \int_C f \, d\mathbf{x} \quad (2.14)$$

for any volume $C \subset \bar{\Omega}$ with Lipschitz boundary, where \mathbf{n} is the unit normal vector on ∂C . The TPFA method is consistent, if the so-called \mathbf{K} -orthogonality is fulfilled [2], which is guaranteed if the tensor \mathbf{K} is diagonal and the discretization of the polyhedral domain Ω is given by a structured mesh \mathcal{T}_h of size h , i.e., the domain has to be subdivided into rectangles (if $d = 2$) or to rectangular hexahedra (if $d = 3$). This property is satisfied in both Section 7 and Chapter III, where the method is used. For a more general setting, one has to employ, e.g., a finite volume method based on multi-point flux approximation [136]. The reason for requiring this property consists in the fact that the accuracy and convergence of the TPFA scheme is assured for this setting, whereas the reliability of the TPFA scheme is, in general, lost for non- \mathbf{K} -orthogonal grids.

As a finite dimensional subspace V_h of V , we consider

$$V_h := \left\{ v \in L^2(\Omega) : v|_T \in \mathbb{P}^0(T), T \in \mathcal{T}_h \right\},$$

where $\mathbb{P}^0(T)$ indicates polynomials of degree 0 on T . We then define the numerical flux of u_h through the edge (or face) e of an element T (using the notation depicted in Figure 2.1) as follows

$$\bar{F}_{T,e} := \int_e -\mathbf{K} \nabla_h u_h \cdot \mathbf{n}_e \, dS,$$

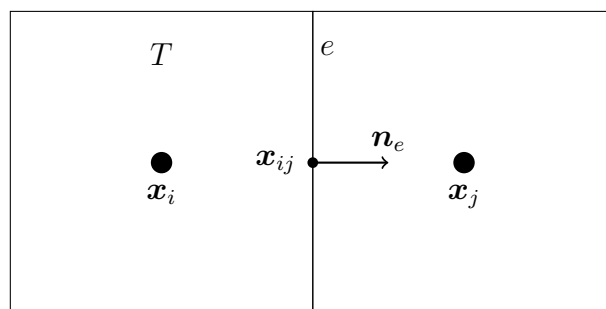


Figure 2.1.: Scheme of the two-point flux approximation $\bar{F}_{T,e}$ for the TPFA method.

where the discrete gradient $\nabla_h u_h$ is computed using standard first-order finite difference in the outer normal direction. Thus, the discrete version of (2.14) reads now as follows:

$$\text{Find } u_h \in V_h \text{ such that: } \sum_{e \in \partial T} \bar{F}_{T,e} = \int_T f \, d\mathbf{x} \quad \forall T \in \mathcal{T}_h.$$

Therefore, the TPFA method employs the elements of the grid as control volumes and for each one, all discrete values are determined at the cell center. For the TPFA method, the treatment of Neumann boundary conditions is straightforward. In fact, it is sufficient to specify the flux $\mathbf{K} \nabla_h u_h \cdot \mathbf{n}$ whenever the edge (or face) E coincides with a Neumann boundary. On the other hand, Dirichlet boundary conditions are imposed at the boundary control volumes. Standard a priori error estimates for the TPFA approximation of the solution to (2.2) can be found, e.g., in [131, 136].

Multiscale modeling of flow processes in microcirculation

In this chapter, we deal with the simulation of blood flow in the context of microcirculation. An accurate reproduction of the pressure and velocity fields in such systems is essential, if one wants to simulate the transport of substances such as oxygen or drugs [52]. Developing a reliable numerical method for such simulations can help designing and optimizing new drugs and surgery methods, as we discussed in the introduction to this thesis. For example, simulations of flow and transport in complex vascular networks are becoming a popular approach to study the physiology of tumors and to design new treatments [96, 200, 206]. Furthermore, such models may also be employed for studying the impact of diseases like Alzheimer's [125], the waste removal from the interstitial space [116] or to improve drugs and therapies for cancer treatment [52, 155, 165]. Regarding this last point, well known therapies consist of heating the carcinogenic tissue by a process called *hyperthermia* [181, 222]. In such therapies, cancer cells die because of the high temperature. Another therapy for treating carcinogenic tissue is provided by the injection of drugs that prevent the vascularization of cancer tissue [207]. In order to increase the efficiency of these cancer therapies, it is crucial to focus the heat or the drug injection on the carcinogenic part while maintaining the rest of the tissue healthy. However, even for vascular systems contained in small volumes covering just a few cubic millimeters, it is a challenging task to simulate flow in the microvascular networks and the interstitial space, since the flow occurs in a complex structure consisting of thousands of vessels. An example is provided in Figure II.1, where a small portion of approximately $1.137 \times 1.137 \times 2.164$ millimetres of a rat's brain is fully resolved. This microvascular system has been generated in a work by the group of B. Weber [190]. In this example, more than 15000 vessels are present. This is due to the fact that their diameters have the size of few micrometers and thus it is obvious that on the scale of an organ, covering usually several cubic centimeters, billions of vessels have to be modelled. Furthermore, simulating the flow in such networks coupled with the surrounding tissue may become unfeasible on standard computers, if an appropriate approach is not employed to reduce the computational costs.

To develop a suitable numerical method, we first need to give a rough description of the microvascular structure appearing in II.1. For a throughout description not restricted to microcirculation, we refer, e.g., to [93]. The types of vessels involved in system II.1 consist of larger structures, called *arterioles* and *venules*, which have a radius of approximately 10 $[\mu\text{m}]$. The smaller vessels are called *capillaries* and their radius is around the micrometer. While the arterioles are responsible for a

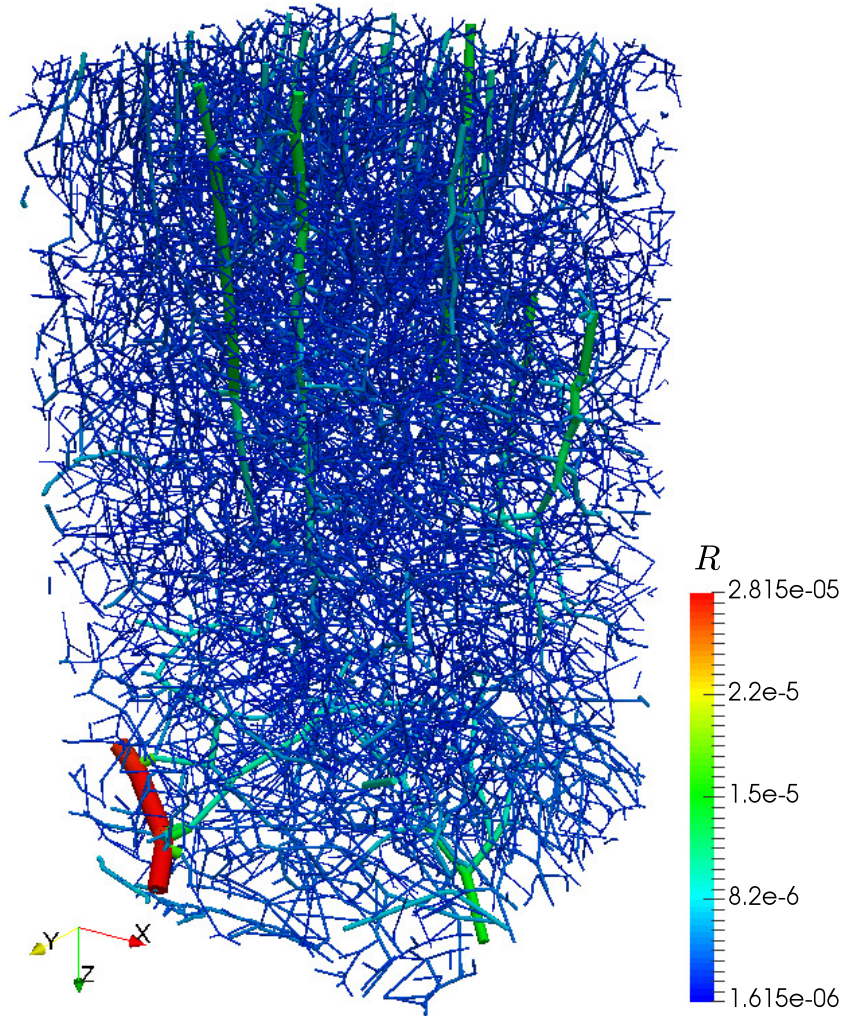


Figure II.1.: The image depicts synchrotron radiation based X-ray tomographic microscopy data of rat somatosensory cortex. Details of the data acquisition methodology can be found in [183]. The representation of the microscopy data in the vascular graph model is shown. The tortuous vessel parts between bifurcation or end points are replaced by straight connections, i.e., cylinders with a radius corresponding to the mean radius R of the vessel [190].

faster transport of substances like nutrients and oxygen to the tissue and organs, the capillaries reduce the blood velocity and pressure in order to allow biochemical processes and exchanges with the organ tissue. Next, the venules belong to a low-pressure region and are responsible for transporting the deoxygenised blood from the capillaries back to the larger vessels. Moreover, the vessel walls of the arterioles and venules are thicker and not as permeable as those of the capillaries.

The first step towards the simulation of such a complex system consists in exploiting the different features of the vessels involved in the process. As explained above, the arterioles and venules are mainly responsible for transporting material through the circulatory system, while capillaries enable exchanges with the tissue through diffusion processes. While the flow in large and medium sized vessels is governed by the Navier-Stokes equations, where the assumption of Newtonian fluid is acceptable, the blood flow in microvascular networks requires non-Newtonian models, which modify the expression for the viscosity by making it dependent on the shear rate [93, Chapter 6]. However, employing these non-Newtonian models would further increase the computational costs required for solving the Navier-Stokes equations, in particular because of the aggravated non-linearity of the problem [179].

To decrease the computational costs, we employ a well-established approach based on dimensionally reduced models [46, 92, 173, 188]. Such models allow us to replace, under appropriate assumptions, the three-dimensional flow problem in the vessels with a one-dimensional system of Poiseuille type on segments representing the main axis of each vessel. The extraction procedure of the centerlines is schematically reported in Figure II.2. This strategy clearly reduces the computational costs, while

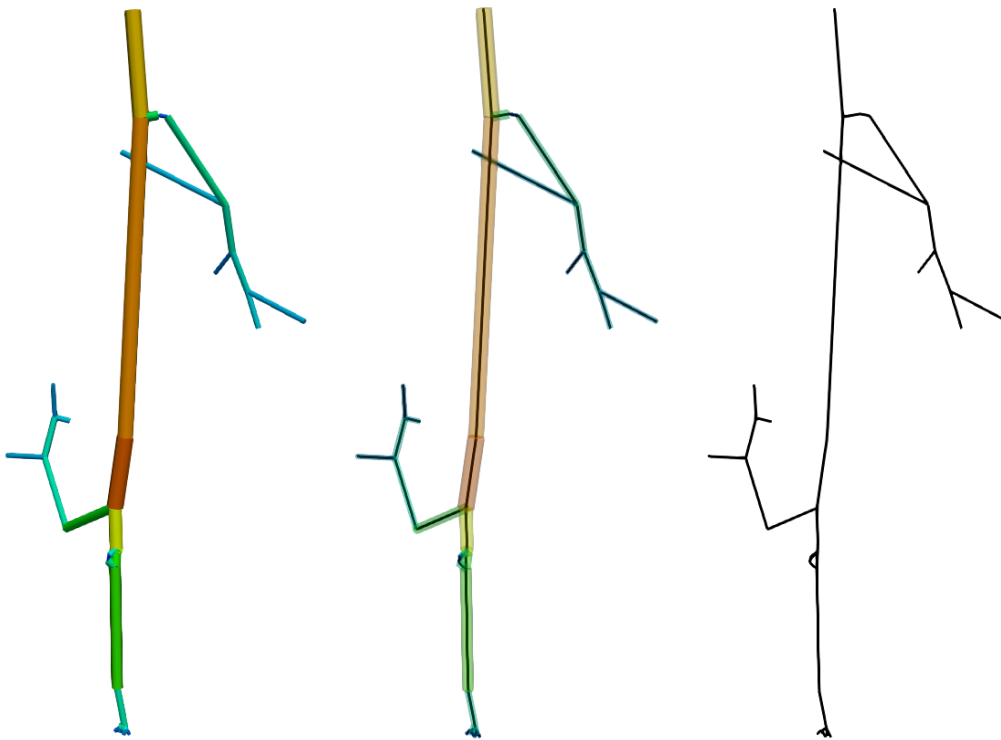


Figure II.2.: The figure shows the generation of a vascular graph model for an arteriole. On the left, the arteriole is fully resolved and approximated by cylinders. In the middle, the centerlines are depicted and on the right, the vascular graph model for the arteriole is extracted. The arteriole is taken from Figure II.1.

preserving the geometry of the network, and the equations obtained are briefly discussed in Section 3.1.

The second step consists in modeling the flow in the interstitial space that surrounds the vessels. To this aim, the standard procedure consists in treating this space as a three-dimensional porous medium [78, 178, 192, 204], where the flow is governed by a diffusion-reaction equation and Darcy's law [110, 133]. More complex models can be used, such as the Brinkman model, but are beyond the scope of this work. We refer the reader to the review [133] for an extensive description of flow models in biological tissues.

Once the equations modeling the flow have been posed for both the tissue and the vascular system, the next step consists in providing an appropriate relationship that describes the exchanges between the three-dimensional porous medium and the reduced one-dimensional network. The approach we follow is not standard, in the sense that we do not treat these systems as two separate entities, which interact with each other only through the vessel wall by means of appropriate boundary conditions. Instead, the interstitial space fills the entire domain and the interactions between both continua are described by appropriate source terms. For coupling the flow in the network with the flow in the tissue, we first follow the approach used in [65], where the source term of the three-dimensional problem is given by a weighted Dirac δ -function concentrated on the one-dimensional network. The second possibility to couple the vascular network and the tissue has been first presented and analysed in a two-dimensional setting in [139]. Here, the Dirac δ -function is concentrated on the lateral surface of the vessel, not on the network itself. Both strategies give rise to a system of coupled elliptic second order PDEs, as we describe in Section 3.2. In the following, we refer to such systems as *3D-1D coupled systems*. These are employed nowadays to study, for example, the physiology of tumors and to design new treatments [52, 165, 185].

Let us briefly comment on both coupling strategies. Employing the first coupling, the reduced one-dimensional circulatory system acts as a one-dimensional source term for the three-dimensional problem posed on the tissue. This strategy has already been investigated by several authors, see, e.g., [65, 141] and the references therein for a comprehensive review of the method. The presence of a Dirac source term makes the analysis of such PDE systems more complicated and causes the deterioration of the convergence rate of classical numerical scheme, as the FEM or the DG method. In this context, in Section 4, we present a way to regain optimal convergence for the FEM, without the need to resort adaptive meshes or weighted Sobolev norms as in [66]. To simplify the analysis, a standard Poisson problem with a Dirac source term is considered, which can be derived under some simplifying assumptions from the 3D-1D coupled system. Following the idea developed in [138], a quasi-optimal convergence behaviour for the standard FEM is shown, if the error is computed in a domain that excludes a neighbourhood surrounding the singularity.

In Section 5, the second coupling strategy is considered in a two-dimensional setting, where the one-dimensional network reduces to points. Thus, the interactions between the two systems occur through the boundaries of the inclusions. We show

that this approach allows us to perform a more standard analysis and to obtain a higher order of convergence for the FEM.

To show the flexibility of our new coupling strategy, an academic application is presented in Section 6 on a three-dimensional microvascular network extracted from the superficial cortex of a rat.

Finally, in Section 7, we employ our new coupling strategy to simulate blood flow in the portion of a rat's brain depicted in Figure II.1. However, if one plans to simulate blood flow in a larger portion of an organ, e.g., the entire brain, this approach proves to be too expensive. In fact, every single vessel has to be resolved and coupled with the surrounding tissue, where the number of these vessels can become extremely large, if several cubic centimeters of tissue are examined. Motivated by this, we develop a new hybrid approach, based on the consideration that the capillaries constitute a quite dense network in the tissue. Thus, the idea consists of modeling the larger vessels such as the arterioles and the venules by the one-dimensional model described above, therefore maintaining the main geometry of the vascular system. On the other hand, the capillaries are homogenized and considered as a three-dimensional porous medium. Our new hybrid approach is applied on the network II.1 and the numerical solution is compared with the solution obtained solving the 3D-1D coupled model.

3. Model equations

In Section 3.1, we discuss the basic modeling assumptions we make for the one-dimensional flow. Then, in Section 3.2, we introduce the notation used throughout this chapter and we propose the two 3D-1D coupled systems.

3.1. Considerations on the one-dimensional flow equation

In general, blood flow is modeled by three-dimensional models such as the Navier-Stokes equations, which are extremely expensive to compute numerically [179]. A standard strategy to reduce the complexity of the problem in a vessel consists in replacing the three-dimensional model with a one-dimensional model defined on the centerlines of the vessels [106]. In particular, for a straight, cylindrical pipe of length L and radius R , the one-dimensional model can be reduced to the Hagen-Poiseuille equation, which reads

$$Q = \frac{\rho_{\text{bl}} \pi R^4}{8 \mu_{\text{bl}} L} \cdot \delta p \quad [\text{kg/s}], \quad (3.1)$$

where the mass flow rate Q is calculated as a function of the pressure difference δp between the two ends of the cylinder, given the density ρ_{bl} of the blood and the dynamic viscosity μ_{bl} [Pa · s] of the blood.

As in [223, Equation (C.12)], we can relate (3.1) to an intrinsic phase average form of Darcy's law by

$$\mathbf{v} := -\frac{\mathbf{K}_v}{\mu_{\text{bl}}} \cdot \frac{dp}{dz} \quad [\text{m/s}], \quad \mathbf{K}_v := \frac{R^2}{8} \quad [\text{m}^2],$$

where dp/dz is the pressure gradient along the centerline z of the cylinder and \mathbf{K}_v is a permeability.

Before presenting the 3D-1D coupled problems, we discuss some further modeling assumptions that hold for the rest of this chapter:

- (A1) The non-Newtonian flow behaviour of the blood can suitably be modeled by an algebraic relation;
- (A2) The influence of gravity is neglected;
- (A3) Inertial effects are neglected;
- (A4) The density ρ_{bl} [kg/s] of the blood and the density ρ_{int} [kg/s] of the interstitial fluid that is exchanged between the capillaries and the tissue are constant;
- (A5) The pulsatility can be neglected;
- (A6) The vessel walls of arterioles and venules are impermeable.

To motivate these assumptions, we need a deeper insight in the physiology of the problem. It is well known that blood consists of blood cells suspended in blood plasma. Blood plasma constitutes approximately 55% of the blood fluid and is a mixture of water, ions, proteins, glucose and carbon dioxide. The blood cells are mainly red blood cells, white blood cells and blood platelets [93, Chapter 1.1.4]. In particular the red blood cells determine the flow behaviour of blood significantly in what is called the *Fahraeus-Lindquist effect* [88]. In fact, moving through the microvessels, the red blood cells have to deform as the vessel diameters become smaller, see [93, Chapter 1.2.3] for a detailed description. This results in a varying apparent viscosity for the individual blood vessels depending on their radius. This behaviour is taken into account by Assumption (A1). Theoretical approaches can be used to derive expressions for the apparent viscosity [134], but we restrict here to the *in vivo* viscosity law given in [187]. For a vessel of diameter D , we set

$$\mu_{bl}(D) := \mu_p \left(1 + (\mu_{0.45} - 1) \frac{(1-H)^C - 1}{(1-0.45)^C - 1} \cdot \left(\frac{D}{D-1.1} \right)^2 \right) \cdot \left(\frac{D}{D-1.1} \right)^2. \quad (3.2)$$

Please note that in (3.2) the diameter D is dimensionless, i.e., the physical diameter has to be divided by 1.0 [μm] to obtain D . The viscosity of the blood plasma μ_p is considered constant and H stands for the discharge hematocrit, which is defined by the ratio between the volume of the red blood cells and the total blood volume. The apparent viscosity $\mu_{0.45}$ for a discharge hematocrit of 0.45 is calculated by

$$\mu_{0.45} := 6e^{-0.085 \cdot D} + 3.2 - 2.44e^{-0.06 \cdot D^{0.645}}.$$

The coefficient C determines the influence of H on μ_{bl} and is given by

$$C := \left(0.8 + e^{-0.075 \cdot D} \right) \left(-1 + \frac{1}{1 + 10^{-11} \cdot D^{12}} \right) + \frac{1}{1 + 10^{-11} \cdot D^{12}}.$$

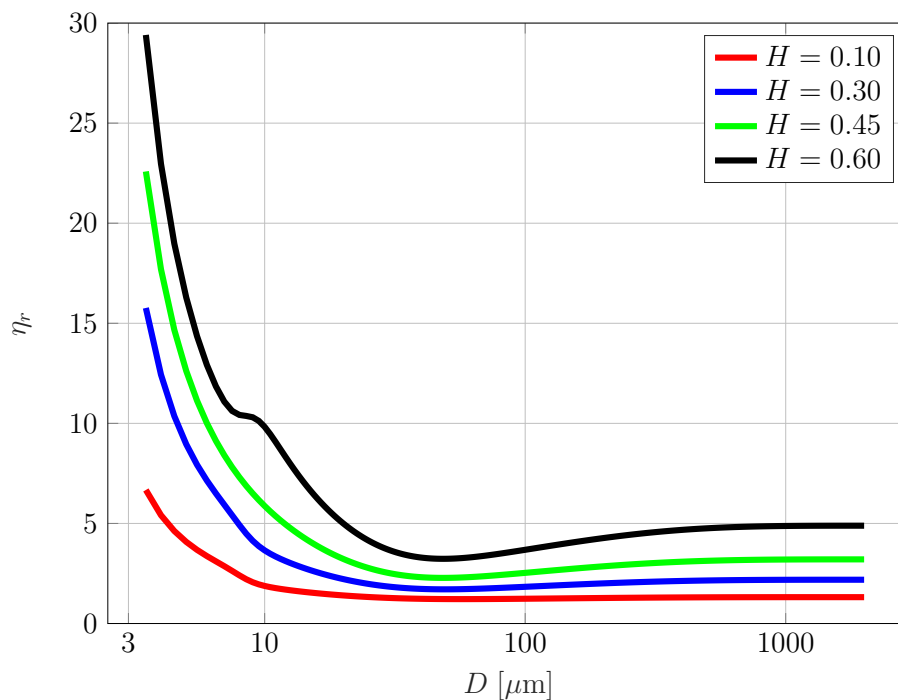


Figure 3.1.: Ratio $\eta_r = \mu_{bl}/\mu_p$ after the *in vivo* viscosity (3.2) with respect to the diameter D of the vessel. The values for ν_r are plotted for different hematocrit levels.

A plot of the *in vivo* viscosity function μ_{bl} for different values of the discharge hematocrit is depicted in Figure 3.1. Please note that the function (3.2) for the *in vivo* viscosity has been derived for the human blood. However we are not aware of such a function for rat blood, and therefore we assume that this function can be used in the flow problem II.1 as well.

Regarding Assumption (A2), the quantity of fluids contained in the volume under consideration is relatively small, and therefore we neglect the effect of gravity.

Since the blood velocity is about 0.1 [mm/s] in the arterioles and venules and about 0.01 [mm/s] in the capillaries [93, Tab. 1.7], it can be concluded that the Reynolds number Re , defined by

$$Re := \frac{|\mathbf{v}|L\rho_{bl}}{\mu_{bl}}, \quad (3.3)$$

in the whole microvascular system is significantly lower than 1. Therefore, viscous effects completely dominate any inertial force and Assumption (A3) is reasonable [93, Chapter 1.2.3].

For simplicity, blood is assumed to be incompressible, from which Assumption (A4) follows. Furthermore, to simplify the notation, we assume for this section that $\rho_{bl} = \rho_{int}$ as well, so that we can neglect the density in the conservation equations. However, this last assumption can be easily avoided, as we do in Section 7, where

the fluids are still assumed to be incompressible, but $\rho_{\text{bl}} \neq \rho_{\text{int}}$.

Regarding Assumption (A5), we emphasize that it is reasonable only in the microcirculation. In fact, only in arterioles, venules and capillaries the Reynolds numbers and the Womersley numbers are lower than 1. In particular, the Womersley number is a dimensionless number relating the frequency of a pulse and the viscosity of a fluid to each other and is, in the case of microcirculation, much smaller than 0.1 [93, Tab. 1.7].

The last Assumption (A6) is motivated by the fact that the vessel wall consists of a thin layer of endothelial cells with gaps between them such that oxygen and other substances can migrate into the interstitial space and then to the tissue cells or vice versa. Contrary to that, the vessel walls of arterioles and venules are thicker and not as permeable, since they exhibit a continuous endothelial cell layer that is surrounded by one or two concentric layers of smooth muscle cells [93, Chapter 1.2.3].

3.2. 3D-1D coupled systems

Let us denote by $\Omega \subset \mathbb{R}^3$ the domain where the problem is defined. As in [190], we assume that the one-dimensional vascular network Λ under consideration is completely contained in $\overline{\Omega}$ and that it has been already segmented and approximated by extracting the mid-lines Λ_i of each blood vessels, i.e.,

$$\Lambda = \bigcup_{i=1}^N \Lambda_i.$$

Each segment Λ_i is equipped with a constant radius value R_i . Therefore, the entire vascular system can be approximated by the union of N cylinders Ω_i for $i = 1, \dots, N$. We point out that this union corresponds only approximately to the original vascular network, since the cylinders Ω_i may not perfectly match to each other. Then, we split the three-dimensional domain in two parts:

$$\Omega_v := \bigcup_{i=1}^N \Omega_i, \quad \Omega_t := \Omega \setminus \overline{\Omega_v}, \quad (3.4)$$

where Ω_v represents the vascular system, while Ω_t the interstitial tissue. Each segment Λ_i is assumed to be parametrized by the arc length s_i and the two endpoints are denoted by $\mathbf{x}_{i,1}$ and $\mathbf{x}_{i,2}$. Then, we define the tangent unit vector by

$$\boldsymbol{\lambda}_i := \frac{\mathbf{x}_{i,2} - \mathbf{x}_{i,1}}{|\Lambda_i|}, \quad (3.5)$$

which gives an orientation of Λ_i . Then, the cylinder Ω_i is given by

$$\Omega_i := \left\{ \mathbf{x} \in \mathbb{R}^3 : \mathbf{x} = \mathbf{x}_i + \mathbf{r}_i \right\},$$

where \mathbf{x}_i denotes the points along the centerline and \mathbf{r}_i the points in the cross-section of the cylinder. The centerline of the cylinder consists of the points

$$\mathbf{x}_i := \mathbf{x}_{i,1} + s_i \boldsymbol{\lambda}_i \in \Lambda_i, \quad s_i \in (0, |\Lambda_i|), \quad (3.6)$$

and the cross-section is given by the points

$$\mathbf{r}_i \in \mathcal{D}(\Lambda_i) := \left\{ r \mathbf{n}_{\Lambda_i}(s_i, \theta) : r \in (0, R_i), s_i \in (0, |\Lambda_i|), \theta \in [0, 2\pi) \right\},$$

where \mathbf{n}_{Λ_i} denotes a unit normal vector with respect to Λ_i . Finally, we denote by Γ_i the lateral surface of the branch Ω_i and with Γ their union, i.e.,

$$\Gamma := \bigcup_{i=1}^N \Gamma_i.$$

Because of Assumption (A6), we have to subdivide the network in two subsets. For the problem depicted in Figure II.1, we do not precisely know how to distinguish capillaries from arterioles or venules. Thus, for simplicity, in this work we separate the capillaries from the larger vessel using their radius as indicator. A further discussion is postponed to Section 7.3.1. So, given a fixed threshold $R_T > 0$, we assume that the set Λ_L contains the arterioles and venules, while Λ_C collects all capillaries, i.e.,

$$\Lambda_L := \{\Lambda_i \in \Lambda : R_i \geq R_T\} \quad \text{and} \quad \Lambda_C := \{\Lambda_i \in \Lambda : R_i < R_T\}. \quad (3.7)$$

Similar definitions are provided for Γ_L and Γ_C . Associated to this separation, we define the corresponding index sets

$$I_L := \{i \in \{1, \dots, N\} : \Lambda_i \in \Lambda_L\} \quad \text{and} \quad I_C := \{i \in \{1, \dots, N\} : \Lambda_i \in \Lambda_C\}. \quad (3.8)$$

In particular, the lateral surface of the capillaries is given by

$$\Gamma_C := \bigcup_{i \in I_C} \Gamma_i.$$

With this notation at hand, we can now present the model used in this work to describe the blood flow in microvascular networks. The idea consists in reformulating (3.1) to ensure mass conservation in the entire network. First, we define differentiation over each branch Λ_i using the tangent unit vector as $dw/ds_i = \nabla w \cdot \boldsymbol{\lambda}_i$, i.e., d/ds_i represents the projection of ∇ along $\boldsymbol{\lambda}_i$. Then, the blood flow along each branch Λ_i is described by Poiseuille's law for conservation of momentum and mass

$$-\frac{d}{ds_i} \left(\pi R^2 \frac{\mathbf{K}_v}{\mu_{bl}} \cdot \frac{du^v}{ds_i} \right) = f_i^v, \quad (3.9)$$

where f_i^v is the transmural flux across the vessel. Finally, the governing flow equations for the entire network Λ are obtained by summing the governing equation (3.9) over the index i and the global variable s is used [171].

As already mentioned in the introduction to this chapter, a standard diffusion model combined with Darcy's law is used to describe the flow in the interstitial tissue [110]. All in all, the system of equations for the reference model, yet to be coupled, in the unknowns u_{ref}^t for the tissue and u^v for the network reads

$$\left\{ \begin{array}{ll} -\nabla \cdot \left(\frac{\mathbf{K}_t}{\mu_{\text{int}}} \nabla u_{\text{ref}}^t \right) = f^t, & \text{in } \Omega_t, \\ -\frac{d}{ds} \left(\pi R^2 \frac{\mathbf{K}_v}{\mu_{\text{bl}}} \cdot \frac{du^v}{ds} \right) = f^v, & \text{in } \Lambda, \\ \mathbf{K}_t \nabla u_{\text{ref}}^t \cdot \mathbf{n} = q, & \text{on } \Gamma_C, \end{array} \right. \quad (3.10)$$

where $\mathbf{K}_t = k_t \cdot \mathbf{I}$ [m^2] for $0 < k_t \in \mathbb{R}$ denotes an isotropic scalar permeability of the tissue, μ_{int} [$\text{Pa} \cdot \text{s}$] represents the viscosity of the interstitial fluid, and f^t and f^v are source terms. The outer normal vector of Γ_C is denoted by \mathbf{n} . The radius R and the permeability \mathbf{K}_v are defined as piecewise constants on each segment Λ_i , i.e.,

$$R|_{\Lambda_i} := R_i, \quad \text{and} \quad \mathbf{K}_v|_{\Lambda_i} := \frac{R_i^2}{8}. \quad (3.11)$$

The term q , defined on the interface Γ_C , describes the volumetric transfer from the vessel to the tissue and is discussed in the following. The system is provided with appropriate boundary conditions on Ω and Λ . In particular, for the microvascular system depicted in Figure II.1, Dirichlet boundary conditions are set at each boundary node according to the data set provided by [190]. For the tissue, boundary data are usually not available and therefore we will resort in the following, for simplicity, to homogeneous Neumann boundary conditions. These conditions are meaningful, if $\partial\Omega$ represents, for example, the surface of an organ, where no fluxes occur. However, if measurements or appropriate data became available, other boundary conditions can easily be used. Please note that a further reaction term of the form $r^t \cdot u_{\text{ref}}^t$ may also be easily considered in the three-dimensional equation as in [141, Chapter 3], but it is avoided here to simplify the notation.

It is clear that for applications with many small inclusions, as the microvascular system from Figure II.1, model (3.10) is computationally not feasible. In fact, it would be extremely difficult to generate a mesh of the interstitial tissue that conforms to every single vessel. For this reason, we present in the following a strategy that allows us to consider the entire domain Ω as a porous medium and to avoid constructing such a complex mesh of Ω_t .

As first step, we need to define appropriately the exchange term q that describes the flux occurring between the tissue and the capillaries. That means, for each segment $\Lambda_i \in \Lambda_C$, the term q is defined on Γ_i and stands for the mass transfer from the three-dimensional porous medium into the capillary, or vice versa. To enforce the conservation of the global flux across each interface Γ_i , the source term f^v has to fulfil the balance equation

$$\int_{\Lambda_i} f^v(s_i) ds_i = \int_{\Gamma_i} q dS_i.$$

In [141, Section 3.1], the author showed by means of an asymptotic analysis that the source term f^v can be written as

$$f^v(s_i) = 2\pi R_i \bar{q}(\mathbf{x}_i),$$

where the term $\bar{q}(\mathbf{x}_i)$ is defined as the average of q along the circle with center in $\mathbf{x}_i = \Lambda_i(s_i)$, radius R_i and perpendicular to Λ_i , that is

$$\bar{q}(\mathbf{x}_i) := \frac{1}{2\pi R_i} \int_0^{2\pi} q(\mathbf{x}_i + R_i \mathbf{n}_{\Lambda_i}(\mathbf{x}_i, \theta)) R_i d\theta. \quad (3.12)$$

We present now two possibilities to insert this source term in the three-dimensional problem. The reduced models we present are written for a new unknown u_{red}^t , which is defined on the entire domain Ω . Furthermore, the source term f^t needs to be extended on the cylinders Ω_i as well. As we do in [139], we assume that the function $F: \Omega \rightarrow \mathbb{R}$ coincides with f^t on Ω_t , i.e.,

$$F(\mathbf{x}) := \begin{cases} f^t(\mathbf{x}), & \text{for } \mathbf{x} \in \Omega_t, \\ f_i^t(\mathbf{x}), & \text{for } \mathbf{x} \in \Omega_i. \end{cases} \quad (3.13)$$

In addition to that, we assume that F exhibits no jumps at the interfaces Γ_i and that for a constant $C_F > 0$ it holds

$$\|f_i^t\|_{L^2(\Omega_i)} \leq C_F \|f^t\|_{L^2(\Omega_t)}, \quad \forall i \in \{1, \dots, N\}. \quad (3.14)$$

We can now present the two different strategies considered in this work to replace problem (3.10) with computationally less expensive models.

- (S1) The first possibility is justified by an asymptotic analysis for the limit $R_i \rightarrow 0$, see [65, Section 3.2]. Here, the network appears as a one-dimensional source term for the three-dimensional problem. That means, we have the following (still decoupled) system of PDEs

$$\begin{cases} -\nabla \cdot \left(\frac{\mathbf{K}_t}{\mu_{\text{int}}} \nabla u_{\text{red}}^t \right) = F + \sum_{i \in I_C} f^v(s_i) \delta_{\Lambda_i}, & \text{in } \Omega, \\ -\frac{d}{ds} \left(\pi R^2 \frac{\mathbf{K}_v}{\mu_{\text{bl}}} \frac{du^v}{ds} \right) + \sum_{i \in I_C} f^v(s_i) = 0, & \text{in } \Lambda, \end{cases} \quad (3.15)$$

being δ_{Λ_i} the Dirac measure concentrated on Λ_i defined as follows: For each edge $\Lambda_i \in \Lambda_C$ and $g \in L^2(\Lambda_i)$, we indicate with $g\delta_{\Lambda_i}$ the linear operator in $\mathcal{C}(\Omega)$ defined by

$$\langle g\delta_{\Lambda_i}, \phi \rangle = \int_{\Lambda_i} g\phi ds_i \quad \forall \phi \in \mathcal{C}_0^\infty(\Omega). \quad (3.16)$$

The boundary conditions for the three-dimensional equation have to be posed now only on $\partial\Omega$.

(S2) The second possibility has been first presented in a two-dimensional setting in [139] and consists in projecting the source term directly on the surface Γ . This idea is naturally justified by the physics of the problem itself, where the actual exchanges between vessels and surrounding tissue occur across the interface of the vessel itself. A possible way to describe this interaction consists in using a Dirac δ -function on the lateral surface Γ_i of the inclusion, i.e., the decoupled system (3.10) now reads

$$\begin{cases} -\nabla \cdot \left(\frac{\mathbf{K}_t}{\mu_{\text{int}}} \nabla u_{\text{red}}^t \right) = F + \sum_{i \in I_C} \frac{1}{2\pi R_i} f^v(s_i) \delta_{\Gamma_i}, & \text{in } \Omega, \\ -\frac{d}{ds} \left(\pi R^2 \frac{\mathbf{K}_v}{\mu_{\text{bl}}} \cdot \frac{du^v}{ds} \right) + \sum_{i \in I_C} f^v(s_i) = 0, & \text{in } \Lambda, \end{cases} \quad (3.17)$$

where δ_{Γ_i} stands for a Dirac measure concentrated on the surface of the branch defined as follows: For each edge $\Lambda_i \in \Lambda_C$, its lateral surface Γ_i and $g \in L^2(\Gamma_i)$, we indicate with $g\delta_{\Gamma_i}$ the linear operator in $\mathcal{C}(\Omega)$ defined by

$$\langle g\delta_{\Gamma_i}, \phi \rangle = \int_{\Lambda_i} \int_{\partial B(\mathbf{x}_i, R_i, \boldsymbol{\lambda}_i)} g\phi \, dS \, ds_i \quad \forall \phi \in \mathcal{C}_0^\infty(\Omega). \quad (3.18)$$

The symbol $\partial B(\mathbf{x}_i, R_i, \boldsymbol{\lambda}_i)$ denotes the circle with center in \mathbf{x}_i and radius R_i perpendicular to $\boldsymbol{\lambda}_i$. As in the previous case, boundary conditions for u_{red}^t have to be posed only on $\partial\Omega$.

To complete the mathematical model, we establish the coupling between the two subproblems. In applications, the terms g and f^v are not known a priori. Usually a constitutive law has to be chosen, making the derivation of the asymptotic problem more complicated [65, Chapter 3]. Even if more complex non-linear models such as, e.g., the Kedem-Katchalsky equations [100] could be adopted, we employ here a simplified version of the linear Starling's filtration law [150, 208], where oncotic pressures are neglected for ease of presentation. Proceeding as in [65, Section 3.2.2], we find that

$$f^v(s_i) = 2\pi R_i \cdot L_{p,i} \left(u^v(s_i) - \overline{u_{\text{red}}^t}(\mathbf{x}_i) \right), \quad (3.19)$$

where $L_{p,i} > 0$ [m/(Pa · s)] denotes the hydraulic conductivity of the membrane and is assumed for this section to be constant along the branch Λ_i with $i \in I_C$. The average $\overline{u_{\text{red}}^t}$ denotes the mean value of u_{red}^t as defined by (3.12). We point out that a further term representing the oncotic gradient across the capillary wall can easily be considered, as we describe in Section 7.

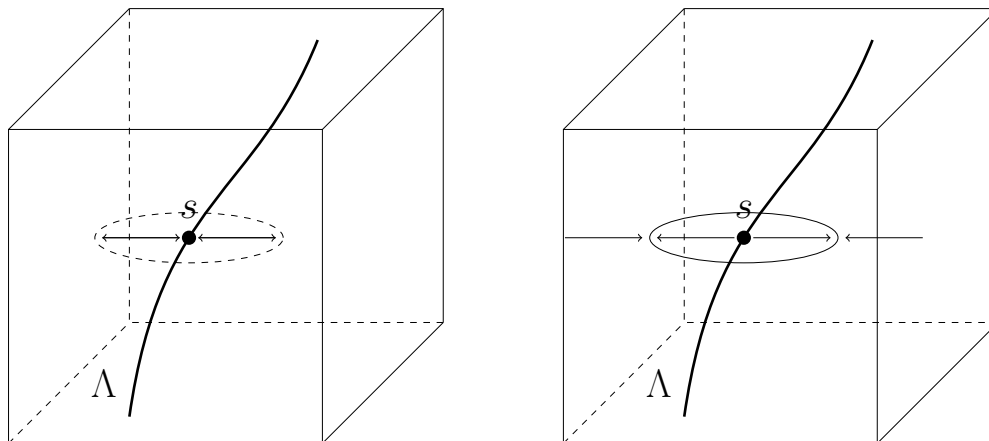


Figure 3.2.: Schematic representation of the different coupling concepts: in the left figure, the exchange between the one-dimensional network and the porous medium is concentrated on the point s . On the right picture, the exchange between the two systems occurs at the surface of the circle centered in s .

Problems (3.15) and (3.17) combined with (3.19) give rise to coupled systems of PDEs defined on embedded domains with heterogeneous dimensionality [65, 67, 101, 158]. The fundamental difference between the two coupling strategies consists in the dimension of the manifolds, where the source term is concentrated. In the type of systems as (3.15), the Dirac δ -function is concentrated on manifolds of codimension two. On the other hand, in (3.17) the Dirac δ -function is concentrated on the physical boundary of the inclusions and therefore a dimensional gap of only one is present in the coupling term. Thus, the corresponding solution is more regular. In fact, the new formulation (S2) allows for a more natural mathematical analysis of the model, numerical discretization and error analysis of a FEM approximation, as we will show in a two-dimensional setting.

As mentioned before, these coupling strategies allow us to reduce the computational costs, if compared with solving the full-dimensional problem (3.10). On the other hand, we have to deal with singular right-hand sides in the three-dimensional problems. The numerical analysis and discretization of these types of problems have been investigated in several publications [66, 67, 126, 145]. For the numerical treatment of interface problems with codimension one, XFEM methods have proved to be very effective [91, 196]. When the lower dimensional problems are represented by a distribution of Dirac source terms embedded into the higher dimensional space, the reduced regularity deteriorates the convergence of numerical methods and optimal convergence rates can only be recovered using graded meshes or local error norms [10, 66, 138, 140].

In order to investigate the mathematical nature of the three-dimensional solution for both coupling strategies, we make some simplifications to the general problems (3.15) and (3.17). First of all, we assume that the one-dimensional problem has a constant

solution $u^v(s_i) \equiv U_i > 0$ on each branch Λ_i of the network and that $\mathbf{K}_t/\mu_{\text{int}} = \mathbf{I}$. These assumptions yield the following three-dimensional elliptic problem with singular right-hand side

$$\begin{cases} -\Delta u_{\text{red}}^t = F + \sum_{i \in I_C} a_i L_{p,i} (U_i - \overline{u_{\text{red}}^t}) \delta_{M_i}, & \text{in } \Omega, \\ u_{\text{red}}^t = g_D^t, & \text{on } \partial\Omega, \end{cases} \quad (3.20)$$

where the manifold M_i is either Λ_i or Γ_i , such that $\cup_i M_i = \Lambda_C$ or $\cup_i M_i = \Gamma_C$, the function g_D^t denotes a Dirichlet boundary condition and the coefficients a_i are defined as

$$a_i := \begin{cases} 2\pi R_i, & \text{if strategy (S1) is used,} \\ 1, & \text{if strategy (S2) is used.} \end{cases}$$

In Section 4, we consider the coupling strategy (S1), where the source terms are concentrated on manifolds of codimension two. In particular, we investigate the pollution effects on the FEM solution induced by the singularities. In fact, standard FEM solutions converge suboptimal in classical norms, as we have already seen in Example 2.1. To simplify the analysis, we make some further assumptions for problem (3.20). In particular, we assume that the network consists of a single \mathcal{C}^2 -curve $M_1 = \Lambda_1$ and that

$$2\pi R_1 L_{p,1} (U_1 - \overline{u_{\text{red}}^t}) \equiv 1 \quad \text{and} \quad F \equiv 0.$$

This leads to a simple Poisson problem with singular right-hand side

$$\begin{cases} -\Delta u_{\text{red}}^t = \delta_\Lambda & \text{in } \Omega, \\ u_{\text{red}}^t = g_D^t & \text{on } \partial\Omega, \end{cases} \quad (3.21)$$

The singularity of the solution to problem (3.21) is investigated in Section 4, where we show that the linear FEM converges optimal up to a log-factor in a local norm. The theoretical considerations are confirmed by numerical tests.

In Section 5, we consider a two-dimensional version of problem (3.20), where the coupling is given by the strategy (S2). To derive the two-dimensional problem from (3.20), we consider a special case where the network consists of N separated segments, each one of them being a single line parallel to the z -axis crossing the whole domain, as depicted in Figure 3.3, on the left. For this special case, we can reduce problem (3.20) to a two-dimensional version, where the source terms are concentrated on points or on circles, depending on the coupling strategy, see Figure 3.3, on the right. If we assume that each inclusion B_i is permeable, i.e., $\Lambda_C = \Lambda$, then the model problem reads

$$\begin{cases} -\Delta u_{\text{red}}^{2D} = F + \sum_{i=1}^N a_i L_{p,i} (U_i - \overline{u_{\text{red}}^{2D}}) \delta_{M_i}, & \text{in } \Omega^{2D}, \\ u_{\text{red}}^{2D} = g_D^{2D}, & \text{on } \partial\Omega^{2D}, \end{cases} \quad (3.22)$$

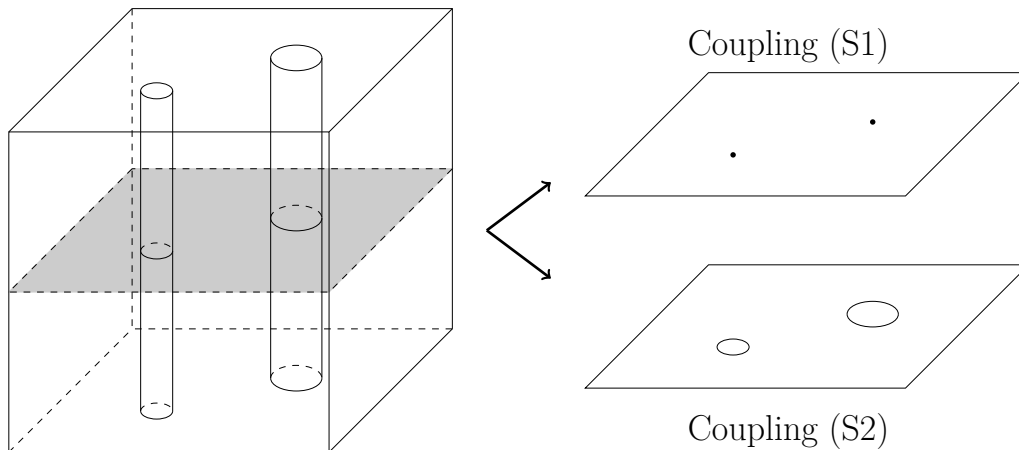


Figure 3.3.: Simplified two-dimensional situation obtained from a particular three-dimensional setting. On the top right figure, the coupling strategy (S1) is employed and therefore the source terms are concentrated on zero-dimensional manifolds. On the bottom right figure, the new coupling strategy (S2) is used and the exchanges occur across circular inclusions.

where now each M_i is either the point \mathbf{x}_i or the circle $\partial B(\mathbf{x}_i, R_i)$.

Following [57], one can estimate the modelling error occurring when considering (3.22) with $M_i = \mathbf{x}_i$, as depicted in Figure 3.3, on the upper right, in the special case where $2\pi R_i L_{p,i} \left(U_i - \overline{u_{\text{red}}^{2D}}(\mathbf{x}_i) \right) \equiv b_i$, with b_i given. In their work, the authors have shown that the modelling error can be estimated as

$$\max_{x \in \Omega_t^{2D}} \left| u_{\text{ref}}^{2D} - u_{\text{red}}^{2D} \right| \leq C \sum_{i \in C} |b_i \ln R_i| R_i,$$

where u_{ref}^{2D} is the corresponding two-dimensional version of u_{ref}^t for the sliced domain. In Section 5, we derive an estimate for the modelling error occurring if we consider (3.22) with $M_i = \partial B(\mathbf{x}_i, R_i)$. This situation is depicted in Figure 3.3, on the bottom right. In this setting, N separated small circular inclusions B_i are present. Employing the new coupling strategy (S2), the source terms for the two-dimensional equation are now given by Dirac δ -functions concentrated on N circles and the model problem reads

$$\begin{cases} -\Delta u_{\text{red}}^{2D} = F^{2D} + \sum_{i=1}^N L_{p,i} \left(U_i - \overline{u_{\text{red}}^{2D}} \right) \delta_{\partial B(\mathbf{x}_i, R_i)}, & \text{in } \Omega, \\ u_{\text{red}}^{2D} = g_D^{2D}, & \text{on } \partial\Omega, \end{cases} \quad (3.23)$$

where F^{2D} denotes a source term. We demonstrate that this new strategy allows us to prove a higher regularity of the solution of (3.23) and to derive an estimate of the modeling error. Furthermore, the well-posedness of the variational formulation

is proven together with a discussion of the convergence behaviour of the FEM with respect to this model. Our theoretical results are confirmed by numerical tests. We point out that for the 3D-1D coupled problem (3.20), the analysis can be worked out in a similar way for special cases such as one isolated inclusion on a straight line. However since the embedding results presented in Section 5 are dimension dependent and since the choice of the boundary condition influences the regularity of the solution, we do not work out the three-dimensional case in detail.

In Section 6, the weak formulation of the 3D-1D coupled problem (3.17) is presented and discretized using FEM. Some algorithmic aspects of the method are also discussed and the new coupling concept is used to address a relevant application such as the perfusion of vascularized biological tissues.

Finally, in Section 7, the new coupling strategy (S2) is employed to simulate the blood flow in the system depicted in Figure II.1 and used as reference solution for a new hybrid method.

4. Analysis of a three-dimensional elliptic problem with line source term

In this section, we consider problem (3.21) and show a local a priori error estimate for its FEM approximation. We recall that the source term in (3.21) is given by a Dirac measure concentrated on a manifold of codimension two, while the problem is posed on a three-dimensional domain. We show that the singularities arising from such Dirac measures do not deteriorate the convergence behaviour at a distance from the curve. Please note that the considerations presented in this section are partially taken from a publication by the author [138]:

T. Köppl, E. Vidotto and B. Wohlmuth

A local error estimate for the Poisson equation with a line source term
ENUMATH 2015 Proceedings, pp. 421-429.

We briefly recall the setting under consideration. Our model problem is defined on an open, convex and polyhedral domain $\Omega \subset \mathbb{R}^3$. Within Ω , we consider a \mathcal{C}^2 -curve Λ , having the following properties:

$$\Lambda \subset \Omega, \quad |\Lambda| \leq C < \infty \quad \text{and} \quad \text{dist}(\Lambda, \partial\Omega) \geq c > 0, \quad (4.1)$$

where $C, c > 0$ are fixed constants and dist denotes the Euclidean distance. Using these definitions, the model problem reads

$$\begin{cases} -\Delta u = \delta_\Lambda & \text{in } \Omega, \\ u = 0 & \text{on } \partial\Omega, \end{cases} \quad (4.2)$$

where δ_Λ is the Dirac measure concentrated on the curve Λ as defined in (3.16). For notational convenience, we drop the notation u_{red}^\dagger to denote the solution as introduced

in Section 3 and, to simplify the analysis, homogeneous Dirichlet boundary conditions are considered.

Existence and uniqueness of a weak solution for problem (4.2) have been shown in [51, Theorem 1], where the source term is actually given by a general, real and regular Borel measure. There, the author proved that the weak solution belongs to the space $W_0^{1,p}(\Omega)$ for $p \in [1, 3/2)$ and that linear FEM has a suboptimal order of convergence, namely $1/2$, with respect to the standard L^2 -norm.

For the case of a Dirac measure concentrated on a \mathcal{C}^2 -curve fulfilling the conditions (4.1), in [103, Theorem 2.1, Case (ii)] the authors showed a higher regularity of the weak solution of (4.2), namely they have proven that $u \in W_0^{1,p}(\Omega)$ for $p \in [1, 2)$. Furthermore, they were able to predict first order of convergence for linear FEM in the standard L^2 -norm.

Regarding the solution of the 3D-1D coupled problem (3.15), in [53] the authors have performed numerical tests to investigate the convergence behaviour of the FEM solution of the problem. Motivated by the numerical results, we consider in this section problem (4.2) and prove a quasi-optimal convergence of the linear FEM with respect to a local L^2 -norm. To this end, the L^2 -error of the problem is not calculated on the entire domain Ω , but instead on a subdomain $\Omega \setminus Z_R$, where Z_R is a domain covering a certain neighborhood of the curve Λ , specifically

$$Z_R := \{\mathbf{x} \in \Omega : \text{dist}(\mathbf{x}, \Lambda) < R\},$$

where $0 < R < \text{dist}(\Lambda, \partial\Omega)$ is a fixed constant.

The rest of the section is organized as follows. In Section 4.1, the main result is proven, which states a quasi-optimal convergence of the linear FEM in a local norm. In section 4.2, our theoretical result is supported by two numerical tests.

4.1. Local error estimate for FEM approximations

The weak formulation of problem (4.2) reads as follows: Find $u \in W_0^{1,p}(\Omega)$ for $p \in [1, 2)$ such that

$$(\nabla u, \nabla \varphi)_\Omega = \int_\Lambda \varphi \, ds \quad \forall \varphi \in W_0^{1,q}(\Omega), \quad (4.3)$$

where $(\cdot, \cdot)_\Omega$ denotes the duality pairing of $L^p(\Omega)$ and $L^q(\Omega)$, and $q > 2$ satisfies $1/p + 1/q = 1$. Proceeding as in [103, Theorem 2.1, Case (ii)], one can show that the weak formulation admits a unique solution for $p \in [1, 2)$.

In order to solve (4.3), let us consider a conforming quasi-uniform subdivision \mathcal{T}_h of Ω , where $h := \max_{T \in \mathcal{T}_h} h_T$ is the meshsize and h_T the diameter of the element T defined as in (2.1). Our FEM space is then defined by the standard conforming linear finite elements V_h^1 from (2.7). Due to $V_h^1 \subset W_0^{1,q}(\Omega) \subset W_0^{1,p}(\Omega)$, the following discrete weak formulation of (4.3) is well-defined: Find $u_h \in V_h^1$ such that

$$(\nabla u_h, \nabla \varphi_h)_\Omega = \int_\Lambda \varphi_h \, ds \quad \forall \varphi_h \in V_h^1.$$

To derive an upper bound for the FEM error, we use a standard duality argument, where we define the following dual problem

$$\begin{cases} -\Delta w = e\chi_{\Omega \setminus Z_R} & \text{in } \Omega, \\ w = 0 & \text{on } \partial\Omega, \end{cases} \quad (4.4)$$

where $\chi_{\Omega \setminus Z_R}$ is the characteristic function of $\Omega \setminus Z_R$ and $e := u - u_h$. Since Ω is convex and $e\chi_{\Omega \setminus Z_R} \in L^2(\Omega)$, it holds that $w \in H^2(\Omega) \cap H_0^1(\Omega)$ [99, Chapter 8].

For the rest of this section, we fix $p = 7/5$. The choice is somehow arbitrary, but guarantees that $H^2(\Omega) \subset W^{1,q}(\Omega)$ for $q = 7/2$. Therefore, we have $w \in W^{1, \frac{7}{2}}(\Omega)$. A weak formulation of (4.4) is given by: Find $w \in W^{1, \frac{7}{2}}(\Omega)$ such that

$$(\nabla w, \nabla \varphi)_\Omega = (e\chi_{\Omega \setminus Z_R}, \varphi)_\Omega, \quad \forall \varphi \in W^{1, \frac{7}{2}}(\Omega) \quad (4.5)$$

and it is well defined. The corresponding FEM approximation $w_h \in V_h^1$ satisfies

$$(\nabla w_h, \nabla \varphi_h)_\Omega = (e\chi_{\Omega \setminus Z_R}, \varphi_h)_\Omega, \quad \forall \varphi_h \in V_h^1. \quad (4.6)$$

The main result is reported in Theorem 4.1 at the end of this section. First, for the proof a pointwise error estimate for the FEM error $w - w_h$ is required and is obtained in the following.

Let $\mathbf{x}_0 \in \Lambda$ be fixed and let us denote by C , C_1 and C_2 positive constants independent of the meshsize h . As we report in the original paper [138], an exact derivation of the dependency of the constants in the following on the radius R is beyond the scope of the work. Therefore, let us denote a ball of radius r around \mathbf{x}_0 by B_r and assume $h < r/4$. Moreover, we demand $B_{r+2h} \subset B_{2r} \subset Z_R$. In order to study the FEM error of the dual problem within B_r , a smooth cut-off function η is introduced. Besides $\eta \in \mathcal{C}^\infty(\Omega)$, this function is supposed to satisfy

$$\begin{cases} \eta(\mathbf{x}) = 1, & \text{if } \mathbf{x} \in B_r, \\ \eta(\mathbf{x}) = 0, & \text{if } \mathbf{x} \in \Omega \setminus B_{2r}, \\ 0 \leq \eta(\mathbf{x}) \leq 1, & \text{if } \mathbf{x} \in B_{2r} \setminus B_r. \end{cases}$$

By the help of this cut-off function, an auxiliary Dirac problem is introduced, where the Dirac measure is concentrated at $\mathbf{x}_0 \in \Lambda$, that is

$$\begin{cases} -\Delta z = \alpha(\delta_{\mathbf{x}_0} + f_0) & \text{in } \Omega, \\ z = 0 & \text{on } \partial\Omega, \end{cases} \quad (4.7)$$

with $\alpha := \text{sgn}((w - w_h)(\mathbf{x}_0))$. The function f_0 is defined as

$$f_0(\mathbf{x}) := \begin{cases} -2\nabla\eta \cdot \nabla G_{\mathbf{x}_0} - G_{\mathbf{x}_0}\Delta\eta, & \text{if } \mathbf{x} \in B_{2r} \setminus B_r, \\ 0, & \text{if } \mathbf{x} \notin B_{2r} \setminus B_r, \end{cases}$$

where $G_{\mathbf{x}_0}$ denotes the three-dimensional Green's function with respect to \mathbf{x}_0 , i.e.,

$$G_{\mathbf{x}_0}(\mathbf{x}) := \frac{1}{4\pi} \cdot \frac{1}{|\mathbf{x} - \mathbf{x}_0|}, \quad \text{for } \mathbf{x} \neq \mathbf{x}_0.$$

This choice of f_0 leads to the following solution of the Dirac problem (4.7)

$$z = \alpha \cdot \eta \cdot G_{\mathbf{x}_0}.$$

A straightforward computation shows that $z \notin H^1(\Omega)$, but $z \in W_0^{1,p}(\Omega)$ for $p \in [1, 3/2)$. The weak formulation of (4.7) reads now: Find $z \in W_0^{1, \frac{7}{5}}(\Omega)$ such that

$$(\nabla z, \nabla \varphi)_\Omega = \alpha \left(\int_\Omega f_0 \varphi d\Omega + \varphi(\mathbf{x}_0) \right), \quad \forall \varphi \in W_0^{1, \frac{7}{5}}(\Omega). \quad (4.8)$$

The discrete version of (4.8) is given by

$$(\nabla z_h, \nabla \varphi_h)_\Omega = \alpha \left(\int_\Omega f_0 \varphi_h d\Omega + \varphi_h(\mathbf{x}_0) \right), \quad \forall \varphi_h \in V_h^1. \quad (4.9)$$

Due to the continuous embedding $H^2(\Omega) \subset W^{1, \frac{7}{2}}(\Omega)$, it holds that $w - w_h \in W^{1, \frac{7}{2}}(\Omega)$. Setting $\varphi = w - w_h$ in (4.8), we obtain

$$(\nabla z, \nabla(w - w_h))_\Omega = (f_0, \alpha(w - w_h))_\Omega + |(w - w_h)(\mathbf{x}_0)|.$$

This yields

$$|(w - w_h)(\mathbf{x}_0)| = (\nabla z, \nabla(w - w_h))_\Omega - (f_0, \alpha(w - w_h))_\Omega. \quad (4.10)$$

Using Hölder's inequality, the facts that $f_0 \in L^2(\Omega)$ and $w \in H^2(\Omega)$, and standard FEM estimates, one obtains obviously

$$\int_\Omega \alpha(w - w_h) f_0 d\Omega \leq \|f_0\|_{L^2(\Omega)} \cdot \|w - w_h\|_{L^2(\Omega)} \leq Ch^2.$$

Inserting this bound in (4.10) and using the Galerkin orthogonality, it follows

$$|(w - w_h)(\mathbf{x}_0)| \leq C \left[h^2 + (\nabla(z - z_h), \nabla(w - w_h))_\Omega \right].$$

It remains to estimate the second term on the right-hand side. For this purpose, we consider an interpolation operator $S_h : W^{n,p}(\Omega) \rightarrow V_h^1$ of Scott-Zhang type [197], due to its stability properties. By means of Galerkin orthogonality, we have

$$|(w - w_h)(\mathbf{x}_0)| \leq C \left[h^2 + (\nabla(z - z_h), \nabla(w - S_h w))_\Omega \right].$$

Splitting the domain Ω into B_r and $\Omega \setminus B_r$ and applying the Hölder inequality yields

$$\begin{aligned} |(w - w_h)(\mathbf{x}_0)| &\leq C \left[h^2 + \|\nabla(z - z_h)\|_{L^2(\Omega \setminus B_r)} \|\nabla(w - S_h w)\|_{L^2(\Omega \setminus B_r)} \right. \\ &\quad \left. + \|\nabla(z - z_h)\|_{L^1(B_r)} \|\nabla(w - S_h w)\|_{L^\infty(B_r)} \right]. \end{aligned} \quad (4.11)$$

Next, we have to bound the four error terms occurring on the right-hand side of (4.11). The estimates for these error terms are provided in the following.

For the second term $\|\nabla(w - S_h w)\|_{L^2(\Omega \setminus B_r)}$, a standard estimate (see, e.g. [197, Theorem 4.1]) and the H^2 -regularity of w yield

$$\|\nabla(w - S_h w)\|_{L^2(\Omega \setminus B_r)} \leq Ch \|w\|_{H^2(\Omega)},$$

Next we estimate the interpolation error $\|\nabla(w - S_h w)\|_{L^\infty(B_r)}$ exploiting the interior regularity of w .

Lemma 4.1. *Let w be the solution of (4.5) and let us assume that $B_{r+2h} \subset B_{2r} \subset Z_R$ and $4h < r$ holds. Then we have on B_r the estimate*

$$\|\nabla(w - S_h w)\|_{L^\infty(B_r)} \leq Ch \|w\|_{H^2(\Omega)}.$$

Proof. Using the approximation properties of S_h (see, e.g., [140, Lemma 3.3]) and the Sobolev embedding $W^{4,2}(B_{r+2h}) \hookrightarrow W^{2,\infty}(B_{r+2h})$ (see [6, Theorem 4.12]), we obtain

$$\|\nabla(w - S_h w)\|_{L^\infty(B_r)} \leq Ch \|w\|_{W^{2,\infty}(B_{r+2h})} \leq Ch \|w\|_{W^{4,2}(B_{r+2h})}.$$

Interior regularity [99, Theorem 8.10], H^2 -regularity of w and the fact that w is harmonic in Z_R (and in particular in B_{2r}) yield

$$\|w\|_{W^{4,2}(B_{r+2h})} \leq C \|w\|_{W^{1,2}(B_{2r})} \leq C \|w\|_{H^2(\Omega)},$$

which completes the proof. \square

Finally, we have to derive suitable bounds for terms involving the FEM error $z - z_h$. Since z is the weak solution of a homogeneous Poisson problem whose source term consists of a L^2 -function and a pointwise Dirac measure, we can use the results derived in [140].

Lemma 4.2. *Let $z \in H^2(\Omega \setminus B_r) \cap W_0^{1,p}(\Omega)$ for $p \in [1, 3/2)$ be defined by (4.8) and let $z_h \in V_h^1$ be its FEM approximation defined by (4.9). Then the following two bounds are valid:*

$$\|\nabla(z - z_h)\|_{L^2(\Omega \setminus B_r)} \leq C_1 h + C_2 \|z - z_h\|_{L^2(\Omega \setminus B_{r-2h})}.$$

and

$$\|\nabla(z - z_h)\|_{L^1(B_r)} \leq Ch |\ln h|. \quad (4.12)$$

Proof. The proof of this lemma is a direct consequence of [140, Lemma 3.6] and [140, Lemma 3.10]. \square

Having these four bounds for all the terms appearing in (4.11), we can finally show the pointwise error estimate for $w - w_h$.

Lemma 4.3. *Let $w \in H_0^1(\Omega) \cap H^2(\Omega)$ be the solution of problem (4.4) and let $w_h \in V_h^1$ be its FEM approximation given by (4.6). Then for a $\mathbf{x}_0 \in \Lambda$, the following pointwise error estimate holds*

$$|(w - w_h)(\mathbf{x}_0)| \leq Ch^2 |\ln h| \|w\|_{H^2(\Omega)}. \quad (4.13)$$

Proof. Combining equation (4.11)- (4.12), we find

$$|(w - w_h)(\mathbf{x}_0)| \leq C_1 h^2 |\ln h| \|w\|_{H^2(\Omega)} + C_2 h \|z - z_h\|_{L^2(\Omega \setminus B_{r-2h})} \|w\|_{H^2(\Omega)}.$$

Proceeding as in [140, Theorem 2.1] for the term $\|z - z_h\|_{L^2(\Omega \setminus B_{r-2h})}$ and exploiting the H^2 -regularity of w yield the thesis. \square

Comparing this result with the standard L^∞ -estimate [60, Theorem 22.7], we have on the right-hand side of (4.13) the norm $\|w\|_{H^2(\Omega)}$ and not the stronger norm $\|w\|_{W^{2,\infty}(\Omega)}$. This is a consequence of the H^2 -regularity of w and the fact that w is harmonic in Z_R . By means of this lemma, we can prove the main result for this section.

Theorem 4.1. *Let $u \in W^{1,p}(\Omega)$ for $p \in [1, 2)$ be the weak solution of (4.2) and let $u_h \in V_h^1$ be its FEM approximation. Then it holds the following quasi-optimal estimate for the local error*

$$\|u - u_h\|_{L^2(\Omega \setminus Z_R)} \leq Ch^2 |\ln h|. \quad (4.14)$$

Proof. Using the Galerkin orthogonality, properties (4.1) of Λ , Lemma 4.3 and H^2 -regularity of w , we obtain

$$\begin{aligned} \|e\|_{L^2(\Omega \setminus Z_R)}^2 &= (e\chi_{\Omega \setminus Z_R}, u - u_h)_\Omega = (\nabla w, \nabla(u - u_h))_\Omega \\ &= (\nabla(w - w_h), \nabla(u - u_h))_\Omega = (\nabla u, \nabla(w - w_h))_\Omega \\ &= \int_\Lambda (w - w_h) ds \leq \int_\Lambda |w - w_h| d\Lambda \leq |\Lambda| \max_{\mathbf{x} \in \Lambda} |(w - w_h)(\mathbf{x})| \\ &\leq Ch^2 |\ln h| \|w\|_{H^2(\Omega)} \leq Ch^2 |\ln h| \|e\|_{L^2(\Omega \setminus Z_R)}. \end{aligned}$$

Dividing by $\|e\|_{L^2(\Omega \setminus Z_R)}$ yields the thesis. \square

4.2. Numerical experiments

In this section, we validate the theoretical estimate (4.14) by means of two numerical examples. For this purpose, we choose the unit cube $\Omega := (0, 1)^3$ as computational domain. By the help of the curves

$$\begin{aligned} \Lambda_1: [0, 1] &\rightarrow \bar{\Omega}, \quad \Lambda_1(s) := (0.5, 0.5, s), \\ \Lambda_2: [0, 1] &\rightarrow \Omega, \quad \Lambda_2(s) := 0.5(1 + 0.06 \cos(2\pi s), 1 + 0.06 \sin(2\pi s), s + 0.5), \end{aligned}$$

we define two different Poisson problems, setting in the original one (4.2) the line Λ equal to Λ_1 or Λ_2 . We denote the corresponding solutions by u_1 and u_2 , respectively.

In the first case, we modify the homogeneous boundary condition in (4.2), such that the exact solution of the Poisson problem under consideration is given by

$$u_1(\mathbf{x}) := -\frac{1}{2\pi} \log |\mathbf{x} - \Lambda_1(z)|.$$

In the second case, homogeneous boundary conditions are posed. However, for this problem no analytical solution is available. Therefore, we precompute a numerical reference solution $u_{2,\text{fine}}$ on a fine mesh and determine the FEM errors by comparing the numerical solutions obtained on coarser meshes to the reference solution $u_{2,\text{fine}}$. A plot of the numerical solution $u_{2,\text{fine}}$ of the second problem is given in Figure 4.1. The numerical solutions to both problems are obtained by means of a linear FEM solver implemented in DUNE [18].

According to Theorem 4.1, we report the global L^2 -error and the local L^2 -error on $\Omega \setminus Z_R$ for $R = 0.25$. For more tests, we refer the reader to the original paper [138]. The approximation errors and convergence rates for the different refinement levels ℓ , such that $h = 2^{-\ell}$, are listed in Table 4.1 and 4.2. It can be seen that for $R = 0$ the FEM converges only with first order, as predicted in [103, Lemma 3.3]. In the remaining cases second order convergence can be observed, which is in agreement with our estimate (4.14) in Theorem 4.1. As we report in the original work [138], the second order of convergence can be observed if $h < R$ holds.

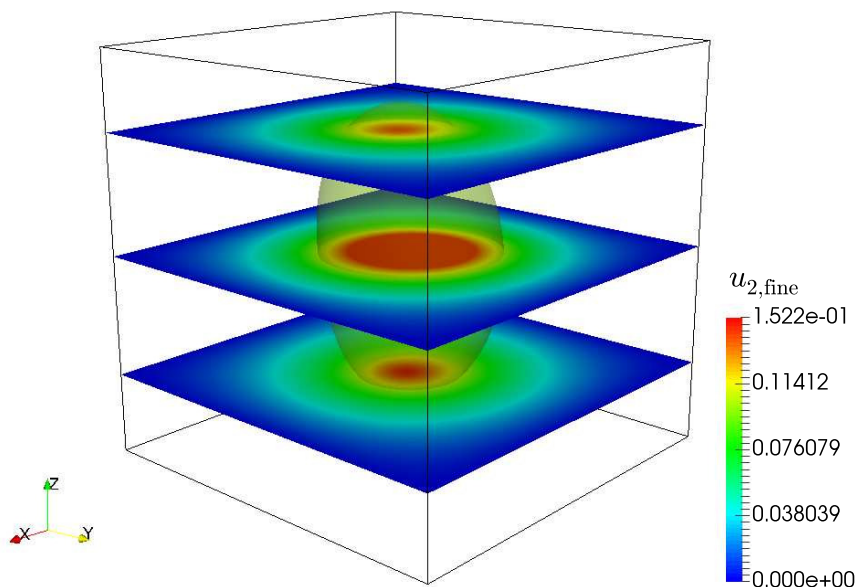


Figure 4.1.: The figure shows a contour plot for $u_{2,\text{fine}} = 0.1$ together with three different slices at $z = 0.2, 0.5, 0.8$.

Table 4.1.: L^2 -error on $\Omega \setminus Z_R$ for $\Lambda = \Lambda_1$.

	$R = 0$		$R = 0.25$	
ℓ	$\ u_1 - u_{1,h}\ _{L^2(\Omega)}$	Rate	$\ u_1 - u_{1,h}\ _{L^2(\Omega \setminus Z_R)}$	Rate
2	$1.0461e - 02$	/	$4.3424e - 03$	/
3	$5.4648e - 03$	0.94	$1.4692e - 03$	1.56
4	$2.7741e - 03$	0.98	$2.3815e - 04$	2.63
5	$1.3968e - 03$	0.99	$5.7466e - 5$	2.05
6	$7.0077e - 04$	1.00	$1.4533e - 05$	1.98
7	$3.5097e - 04$	1.00	$3.6356e - 06$	2.00
	expected:	1.00	expected:	2.00

Table 4.2.: Discrete L^2 -error on $\Omega \setminus Z_R$ for $\Lambda = \Lambda_2$.

	$R = 0$		$R = 0.25$	
ℓ	$\ u_{2,\text{fine}} - u_{2,h}\ _{L^2(\Omega)}$	Rate	$\ u_{2,\text{fine}} - u_{2,h}\ _{L^2(\Omega \setminus Z_R)}$	Rate
2	$9.9816e - 03$	/	$2.8019e - 03$	/
3	$6.5546e - 03$	0.61	$6.3984e - 04$	2.13
4	$4.6708e - 03$	0.49	$1.5896e - 04$	2.01
5	$1.8626e - 03$	1.33	$3.9731e - 05$	2.00
6	$7.7970e - 04$	1.26	$8.2663e - 06$	2.26
	expected:	1.00	expected:	2.00

5. Analysis of a two-dimensional elliptic problem with line source terms

In this section, we consider problem (3.23). Please note that the considerations presented here are partially taken from a publication by the author [139]:

T. Köppl, E. Vidotto, B. Wohlmuth and P. Zunino

Mathematical modeling, analysis and numerical approximation of second-order elliptic problems with inclusions

Mathematical Models and Methods in Applied Sciences 2018 28:05, pp. 953-978.

Let us first first briefly recall the setting and the notation introduced in Section 3. We consider an open, bounded, convex and polygonal domain $\Omega \subset \mathbb{R}^2$. Within Ω

there are $N \in \mathbb{N}$ open balls $B_i \subset \Omega$ with center $\mathbf{x}_i \in \Omega$ and radius R_i . For a given constant $C > 0$ it holds

$$\text{dist}(\partial\Omega, B_j) > C, \text{dist}(B_i, B_j) > C, i \neq j, i, j \in \{1, \dots, N\}, \quad (5.1)$$

where

$$\text{dist}(M, B_j) := \min_{\mathbf{x} \in M, \mathbf{y} \in \overline{B_j}} |\mathbf{x} - \mathbf{y}|, \quad M \in \{\partial\Omega, B_i\}.$$

For simplicity, we drop the notation ‘‘2D’’ from problem (3.23). The domain Ω is subdivided in two parts, according to (3.4), where Ω_v represents the union of the balls B_i and $\Omega_t = \Omega \setminus \Omega_v$. Similarly to (3.10), the reference model problem reads

$$\begin{cases} -\Delta u_{\text{ref}} = f, & \text{in } \Omega_t, \\ -\nabla u_{\text{ref}} \cdot \mathbf{n}_i = L_{p,i}(U_i - u_{\text{ref}}), & \text{on } \partial B_i, \\ u_{\text{ref}} = 0, & \text{on } \partial\Omega, \end{cases} \quad (5.2)$$

with $f \in L^2(\Omega_t)$. The term $L_{p,i}(U_i - u_{\text{ref}})$ denotes a filtration term as in (3.19) and describes the flux through the interface ∂B_i from the inclusions into the porous medium or vice versa. The permeability coefficients $L_{p,i}$ are assumed to be constant along the entire boundary ∂B_i . The terms U_i are given intensities of the corresponding inclusion B_i , and \mathbf{n}_i denotes the outward unit normal vector to ∂B_i .

The reduced model we propose consists of the following system

$$\begin{cases} -\Delta u_{\text{red}} = F + \sum_{i=1}^N L_{p,i}(U_i - \bar{u}_{\text{red}}^{(i)}) \delta_{\partial B_i}, & \text{in } \Omega, \\ u_{\text{red}} = 0, & \text{on } \partial\Omega, \end{cases} \quad (5.3)$$

where $\delta_{\partial B_i}$ stands for a Dirac measure concentrated on ∂B_i and the expression $\bar{u}_{\text{red}}^{(i)}$ abbreviates the mean value of u_{red} on ∂B_i defined as

$$\bar{u}_{\text{red}}^{(i)} = \frac{1}{2\pi R_i} \int_{\partial B_i} u_{\text{red}} dS. \quad (5.4)$$

The source term $F \in L^2(\Omega)$ denotes an extension of f as in (3.13) such that conditions (3.14) are satisfied. The introduction of the average term $\bar{u}_{\text{red}}^{(i)}$ in (5.3) instead of $u_{\text{red}}|_{\partial B_i}$ induces an error, which is given by the fluctuations $\tilde{u}_{\text{red}}^{(i)}$ of u_{red} along the corresponding interface ∂B_i . These fluctuations are defined by

$$\tilde{u}_{\text{red}}^{(i)} := u_{\text{red}}|_{\partial B_i} - \bar{u}_{\text{red}}^{(i)}, \quad (5.5)$$

and they will be discussed in the following. The rest of the section is organized as follows: in Section 5.1, we derive three trace inequalities that represent fundamental tools for the mathematical analysis in the other sections. In Section 5.2, we derive the weak formulation of the model problem (5.3) and show existence and uniqueness of the weak solution. In Section 5.3, we investigate the modeling error that we commit replacing the original problem (5.2) with the reduced one (5.3). In Section 5.4, we consider the numerical discretization by FEM and study its convergence. Our theoretical results are confirmed by numerical tests, which are presented in Section 5.5.

5.1. Two trace inequalities

Before going into the analysis of problem (5.3), we discuss some trace inequalities that are key ingredients for our results. The first trace inequality allows us to bound the mean value $\bar{v}^{(i)}$ of a function $v \in H_0^1(\Omega)$. The second trace inequality is an inequality of Steklov-type that provides an upper bound for traces of functions w , whose averages vanish on ∂B_i , that is

$$\int_{\partial B_i} w \, dS = 0.$$

To prove the well-posedness of our model problem (5.3) in the next section and to derive suitable upper bounds for the modeling error in Section 5.3, it is crucial to know how the arising constants depend on the radii R_i of the circular inclusions B_i . Therefore, we investigate these constants in more detail.

Lemma 5.1. *Let $B_i \subset \Omega$ be a ball with a sufficiently small radius R_i . Then it holds for the mean value $\bar{v}^{(i)}$ of $v \in H_0^1(\Omega)$*

$$\bar{v}^{(i)} \leq C |\ln R_i|^{\frac{1}{2}} \|\nabla v\|_{L^2(\Omega)},$$

where the constant $C > 0$ is independent of R_i .

Proof. According to [9, Remark 1], it holds on B_i the estimate

$$\bar{v}^{(i)} \leq \frac{1}{2\pi R_i} \left(\frac{2}{R_i} \int_{B_i} |v| \, dx + \int_{B_i} |\nabla v| \, dx \right).$$

Applying Hölder's inequality to both summands, we have

$$\begin{aligned} \bar{v}^{(i)} &\leq \frac{1}{\pi R_i^2} \left(\pi R_i^2 \right)^{\frac{1}{q}} \|v\|_{L^p(B_i)} + \frac{\sqrt{\pi R_i^2}}{2\pi R_i} \|\nabla v\|_{L^2(B_i)}, \\ &\leq \left(\pi R_i^2 \right)^{-\frac{1}{p}} \|v\|_{L^p(B_i)} + \frac{1}{2\sqrt{\pi}} \|\nabla v\|_{L^2(B_i)}. \end{aligned}$$

for the parameters p and q such that $1/p + 1/q = 1$, while the L^1 -norm in the second summand is estimated by a product of L^2 -norms. The choice $p = |\ln R_i| \geq 2$ and $q = |\ln R_i| / (|\ln R_i| - 1)$ yields

$$\begin{aligned} \bar{v}^{(i)} &\leq \pi^{-\frac{1}{|\ln R_i|}} R_i^{-\frac{2}{|\ln R_i|}} \|v\|_{L^p(B_i)} + \frac{1}{2\sqrt{\pi}} \|\nabla v\|_{L^2(B_i)} \\ &\leq e^2 \|v\|_{L^p(\Omega)} + \frac{1}{2\sqrt{\pi}} \|\nabla v\|_{L^2(\Omega)}. \end{aligned} \tag{5.6}$$

According to a Sobolev inequality [215, Equation (6.20)], there exists a constant $C > 0$ independent of R_i such that for $v \in H_0^1(\Omega)$ it holds

$$\|v\|_{L^p(\Omega)} \leq Cp^{\frac{1}{2}} \|\nabla v\|_{L^2(\Omega)}. \tag{5.7}$$

Therefore, we have

$$\bar{v}^{(i)} \leq C \left(|\ln R_i|^{\frac{1}{2}} \|\nabla v\|_{L^2(\Omega)} + \|\nabla v\|_{L^2(\Omega)} \right),$$

with a constant $C > 0$ independent of R_i . \square

Next, we derive by means of the Steklov inequality a trace inequality for the fluctuation $\tilde{v}^{(i)}$ with respect to a ball B_i .

Lemma 5.2. *Let $B_i \subset \mathbb{R}^2$ be a ball with a sufficiently small radius R_i and $v \in H_0^1(\Omega)$. Then we have*

$$\|\tilde{v}^{(i)}\|_{L^2(\partial B_i)} \leq \sqrt{R_i} \|\nabla v\|_{L^2(B_i)}. \quad (5.8)$$

Proof. Using the definitions (5.5) of fluctuation and (5.4) of mean value, we obtain

$$\begin{aligned} \int_{\partial B_i} v - \bar{v}^{(i)} dS &= \int_{\partial B_i} \left(v - \frac{1}{2\pi R_i} \int_{\partial B_i} v d\tilde{S} \right) dS \\ &= \int_{\partial B_i} v dS - \int_{\partial B_i} v d\tilde{S} \cdot \frac{1}{2\pi R_i} \int_{\partial B_i} 1 dS = 0. \end{aligned}$$

Then, it follows from the Steklov inequality [117, Section 3] that

$$\int_{\partial B_i} (v - \bar{v}^{(i)})^2 dS \leq \frac{1}{C_T(B_i)} \int_{B_i} |\nabla v|^2 dx.$$

For the constant $C_T(B_i)$ one can show by means of a Steklov eigenvalue problem [147, Section 5] that $C_T(B_i) = R_i^{-1}$. From this, (5.8) follows. \square

Combining the two Lemmas 5.1 and 5.2, we can prove the following trace inequality for a function $v \in H_0^1(\Omega)$.

Lemma 5.3. *Let $B_i \subset \mathbb{R}^2$ be a ball with a sufficiently small radius R_i and $v \in H_0^1(\Omega)$. Then we have*

$$\|v\|_{L^2(\partial B_i)} \leq C \sqrt{R_i |\ln R_i|} \|\nabla v\|_{L^2(\Omega)}, \quad (5.9)$$

where $C > 0$ is a constant independent of R_i .

Proof. Using the decomposition (5.5), we obtain

$$\begin{aligned} \|v\|_{L^2(\partial B_i)}^2 &= \|\bar{v}^{(i)} + \tilde{v}^{(i)}\|_{L^2(\partial B_i)}^2 \\ &= \|\bar{v}^{(i)}\|_{L^2(\partial B_i)}^2 + \|\tilde{v}^{(i)}\|_{L^2(\partial B_i)}^2 + 2 \int_{\partial B_i} |\bar{v}^{(i)} \cdot \tilde{v}^{(i)}| dS \\ &\leq 2\pi R_i (\bar{v}^{(i)})^2 + \|\tilde{v}^{(i)}\|_{L^2(\partial B_i)}^2 + 2\|\bar{v}^{(i)}\|_{L^2(\partial B_i)} \cdot \|\tilde{v}^{(i)}\|_{L^2(\partial B_i)}. \end{aligned}$$

Applying Young's inequality, we obtain

$$\begin{aligned} \|v\|_{L^2(\partial B_i)}^2 &\leq 2\pi R_i (\bar{v}^{(i)})^2 + \|\tilde{v}^{(i)}\|_{L^2(\partial B_i)}^2 + \|\bar{v}^{(i)}\|_{L^2(\partial B_i)}^2 + \|\tilde{v}^{(i)}\|_{L^2(\partial B_i)}^2 \\ &\leq 4\pi R_i (\bar{v}^{(i)})^2 + 2\|\tilde{v}^{(i)}\|_{L^2(\partial B_i)}^2. \end{aligned}$$

Using Lemmas 5.1 and 5.2, we can prove (5.9) after taking the square root on both sides. \square

5.2. Model derivation and analysis

Let us start with the variational formulation of the reference problem (5.2), where we consider the following function space

$$V(\Omega_t) := \left\{ v \in H^1(\Omega_t) : v|_{\partial\Omega} = 0 \right\}.$$

The weak formulation of problem (5.2) now reads: Find $u_{\text{ref}} \in V(\Omega_t)$ such that for all $v \in V(\Omega_t)$ it holds

$$(\nabla u_{\text{ref}}, \nabla v)_{\Omega_t} + \sum_{i=1}^N L_{p,i}(u_{\text{ref}}, v)_{\partial B_i} = (f, v)_{\Omega_t} + \sum_{i=1}^N L_{p,i} U_i \int_{\partial B_i} v \, dS, \quad (5.10)$$

where we have adopted the standard notation for the L^2 -inner product. Having the definitions (5.4) of the mean value and (5.5) of the fluctuation at hand, the interface terms can be written as

$$\begin{aligned} (u, v)_{\partial B_i} &= \int_{\partial B_i} (\bar{u}^{(i)} + \tilde{u}^{(i)})(\bar{v}^{(i)} + \tilde{v}^{(i)}) \, dS \\ &= 2\pi R_i \bar{u}^{(i)} \cdot \bar{v}^{(i)} + \int_{\partial B_i} \tilde{u} \cdot \tilde{v} \, dS + \underbrace{\bar{u}^{(i)} \int_{\partial B_i} \tilde{v}^{(i)} \, dS}_{=0} + \bar{v}^{(i)} \underbrace{\int_{\partial B_i} \tilde{u}^{(i)} \, dS}_{=0}, \end{aligned}$$

where we used the same argument as in the proof of Lemma 5.2. Therefore, we obtain

$$(u, v)_{\partial B_i} = 2\pi R_i \bar{u}^{(i)} \bar{v}^{(i)} + \int_{\partial B_i} \tilde{u}^{(i)} \tilde{v}^{(i)} \, dS. \quad (5.11)$$

To derive a weak formulation of the reduced model (5.3), we make the following modeling assumptions, which rely on the fact that the inclusions are small:

(MA1) We identify the domain Ω_t with the entire Ω ;

(MA2) The residual term in (5.11) is small, namely

$$\int_{\partial B_i} \tilde{u}^{(i)} \tilde{v}^{(i)} \, dS \simeq 0.$$

In Section 5.3, we define the error components associated with both modeling assumptions (MA1) and (MA2), and we analyse their magnitude in terms of the parameters of the problem.

We now replace (5.10) with a surrogate problem: Find $u_{\text{red}} \in H_0^1(\Omega)$ such that for all $v \in H_0^1(\Omega)$ it holds

$$(\nabla u_{\text{red}}, \nabla v)_{\Omega} + 2\pi \sum_{i=1}^N R_i L_{p,i} \bar{u}_{\text{red}}^{(i)} \bar{v}^{(i)} = (F, v)_{\Omega} + 2\pi \sum_{i=1}^N R_i L_{p,i} U_i \bar{v}^{(i)}. \quad (5.12)$$

Problem (5.12) is equivalent to finding $u_{\text{red}} \in H_0^1(\Omega)$ such that

$$a(u_{\text{red}}, v) = \ell(v), \quad \forall v \in H_0^1(\Omega), \quad (5.13)$$

where the bilinear form $a(\cdot, \cdot) : H_0^1(\Omega) \times H_0^1(\Omega) \rightarrow \mathbb{R}$ is given by

$$a(u, v) := (\nabla u, \nabla v)_\Omega + 2\pi \sum_{i=1}^N R_i L_{p,i} \bar{u}^{(i)} \bar{v}^{(i)}. \quad (5.14)$$

The linear form ℓ is defined as follows

$$\ell : H_0^1(\Omega) \rightarrow \mathbb{R}, \quad \ell(v) := (F, v)_\Omega + 2\pi \sum_{i=1}^N R_i L_{p,i} U_i \bar{v}^{(i)}. \quad (5.15)$$

Obviously, (5.13) is the weak formulation of the reduced problem (5.3). The variational problem (5.13) is well-posed in the sense of Lax-Milgram's Lemma 2.1, as we prove with the following result.

Proposition 5.1. *Let the radii R_i of the inclusions be sufficiently small as required by Lemma 5.1. Then problem (5.13) has a unique solution*

$$u_{\text{red}} \in H_0^1(\Omega) \cap H^{\frac{3}{2}-\varepsilon}(\Omega), \quad \forall \varepsilon > 0.$$

Furthermore it holds the following stability estimate

$$\|u_{\text{red}}\|_{H_0^1(\Omega)} \leq C \left(\|F\|_{L^2(\Omega)} + \sum_{i=1}^N L_{p,i} R_i |\ln R_i|^{\frac{1}{2}} U_i \right). \quad (5.16)$$

Proof. We begin by proving that the symmetric bilinear form (5.14) is continuous and coercive. The coercivity is a direct consequence of the Poincaré inequality. More precisely, for any $v \in H_0^1(\Omega)$ there exists a positive constant C_P independent of R_i and $L_{p,i}$, such that:

$$a(v, v) \geq (\nabla v, \nabla v)_\Omega \geq (1 + C_P^2)^{-1} \|v\|_{H_0^1(\Omega)}^2. \quad (5.17)$$

To prove the boundedness of the bilinear form, we have by means of Lemma 5.1

$$2\pi R_i \bar{u}^{(i)} \bar{v}^{(i)} \leq 2\pi R_i C |\ln R_i| \|u\|_{H_0^1(\Omega)} \|v\|_{H_0^1(\Omega)}.$$

Thus, the bilinear form can be bounded by

$$a(u, v) \leq \left(1 + 2\pi C \sum_{i=1}^N L_{p,i} R_i |\ln R_i| \right) \|u\|_{H_0^1(\Omega)} \|v\|_{H_0^1(\Omega)}. \quad (5.18)$$

The boundedness of the linear form (5.15) remains to be proven. According to Lemma 5.1, we have

$$2\pi R_i \bar{v}^{(i)} \leq 2\pi R_i C |\ln R_i|^{\frac{1}{2}} \|\nabla v\|_{L^2(\Omega)} \leq 2\pi R_i C |\ln R_i|^{\frac{1}{2}} \|v\|_{H_0^1(\Omega)}.$$

All in all, it follows the existence and uniqueness of a solution $u_{\text{red}} \in H_0^1(\Omega)$ of (5.13). We now show that the solution is in the space $H^{\frac{3}{2}-\varepsilon}(\Omega)$ as well. Due to the presence of Dirac source terms in (5.3) no H^2 -regularity can be recovered and the question arises as to which interspace \tilde{V} with $H^2(\Omega) \subset \tilde{V} \subset H_0^1(\Omega)$ the solution u_{red} belongs. Having the unique solution u of (5.13) at hand, the crucial step consists of showing

$$\sum_{i=1}^N L_{p,i} (U_i - \bar{u}^{(i)}) \delta_{\partial B_i} \in H^{-(\frac{1}{2}+\varepsilon)}(\mathbb{R}^2), \quad \forall \varepsilon > 0.$$

Since $u \in H_0^1(\Omega)$, it follows that $u|_{\partial B_i} \in H^{1/2}(\partial B_i)$ (see, e.g., [153, Theorem 9.4]) and therefore $\bar{u}^{(i)} < \infty$. By a trace theorem [153, Section 9.2], it holds that

$$\|v\|_{L^2(\partial B_i)} \leq C \|v\|_{H^{\frac{1}{2}+\varepsilon}(\mathbb{R}^2)}, \quad \forall v \in H^{\frac{1}{2}+\varepsilon}(\mathbb{R}^2).$$

From this and $\bar{u}^{(i)} < \infty$, we can conclude that

$$\tilde{\ell} : H^{\frac{1}{2}+\varepsilon}(\mathbb{R}^2) \rightarrow \mathbb{R}, \quad v \mapsto \sum_{i=1}^N \int_{\partial B_i} L_{p,i} (U_i - \bar{u}^{(i)}) v \, dS$$

is a linear and bounded functional for all positive ε . Now, the rest of the proof can be adapted from [103, Theorem 2.1, Case (iii)].

To show the stability estimate, we test (5.13) with $v = u_{\text{red}}$. Using the coercivity of the bilinear form a , the continuity result of the linear form ℓ and the Cauchy-Schwarz inequality, the stability estimate (5.16) can be derived. \square

5.3. Analysis of the modeling error

We aim to analyse the error arising from both modeling assumptions (MA1) and (MA2) at the basis of the reduced model (5.12). Proceeding as in [209, Theorem 4.12], one can prove that problem (5.10) admits a unique weak solution $u_{\text{ref}} \in V(\Omega_t)$. Having the reference solution at hand, we can define the modeling error due to assumptions (MA1) and (MA2) as $e := u_{\text{ref}} - u_{\text{red}}|_{\Omega_t}$. Then, the following theorem can be shown.

Theorem 5.1. *Let the radii R_i of the inclusions be sufficiently small as required by Lemma 5.1 and let $u_{\text{ref}} \in V(\Omega_t)$, and $u_{\text{red}} \in H_0^1(\Omega)$ be the solutions to the variational problems (5.10) and (5.12), respectively. Then the modeling error can be estimated by*

$$\begin{aligned} \|e\|_{H^1(\Omega_t)} \leq & C_1 \left[\|F\|_{L^2(\Omega)} \sum_{i=1}^N (1 + L_{p,i}) R_i |\ln R_i|^{\frac{1}{2}} + \sum_{i=1}^N U_i L_{p,i} R_i |\ln R_i|^{\frac{1}{2}} \right] \\ & + C_2 \left[\|F\|_{L^2(\Omega)} \sum_{i=1}^N L_{p,i} R_i + \sum_{i,j=1}^N U_j L_{p,i} L_{p,j} R_i R_j |\ln R_j|^{\frac{1}{2}} \right], \end{aligned} \quad (5.19)$$

where the constants C_1 and C_2 are independent of R_i , $L_{p,i}$ and U_i for every $i \in \{1, \dots, N\}$.

Remark 5.1. Estimate (5.19) informs us of the structure of the modeling error. In particular, the first two terms on the right hand side relate to modeling assumption (MA1), which concerns with the extension of the physical domain Ω_t to the whole domain Ω . This component of the error scales quasi-linearly with the size of the inclusions. The third and fourth components on the right-hand side quantify the error caused by modeling assumption (MA2). Since the modeling error for one interface B_i affects all the other interfaces B_j , not surprisingly the fourth term is proportional to the sum of each product $R_i R_j$.

Proof. We first need to introduce an intermediate problem. Let us denote by u_{int} the solution of the problem obtained after assuming (MA1), that is $u_{\text{int}} \in H_0^1(\Omega)$ satisfies the variational problem

$$(\nabla u_{\text{int}}, \nabla v)_{\Omega} + \sum_{i=1}^N L_{p,i}(u_{\text{int}}, v)_{\partial B_i} = (F, v)_{\Omega} + \sum_{i=1}^N L_{p,i} U_i \int_{\partial B_i} v \, dS \quad (5.20)$$

for every $v \in H_0^1(\Omega)$. Proceeding as in Proposition (5.1), one can prove that problem (5.20) admits a unique solution $u_{\text{int}} \in H_0^1(\Omega)$.

We can now naturally decompose the modeling error as the error related to assumption (MA1), that is $e_1 := u_{\text{ref}} - u_{\text{int}|_{\Omega_t}}$ and the one associated to (MA2), namely $e_2 := u_{\text{int}} - u_{\text{red}}$. Using the triangle inequality, we can split the modeling error as

$$\|e\|_{H^1(\Omega_t)} \leq \|e_1\|_{H^1(\Omega_t)} + \|e_2\|_{H^1(\Omega)}.$$

We proceed estimating both errors separately, starting with deriving an upper bound for e_1 . As first step, we define another elliptic auxiliary problem

$$\begin{cases} -\Delta u_f = F, & \text{in } \Omega, \\ u_f = 0, & \text{on } \partial\Omega. \end{cases}$$

The weak solution u_f of this problem clearly satisfies

$$(\nabla u_f, \nabla v)_{\Omega} = (F, v)_{\Omega} \quad (5.21)$$

for every $v \in H_0^1(\Omega)$. By means of the solution u_f , we decompose the solutions of (5.10) and (5.20) as follows

$$u_{\text{ref}} = w_{\text{ref}} + u_f|_{\Omega_t} \quad \text{and} \quad u_{\text{int}} = w_{\text{int}} + u_f. \quad (5.22)$$

Therefore, we want now to estimate the error

$$\|e_1\|_{H^1(\Omega_t)} = \|w_{\text{ref}} - w_{\text{int}}\|_{H^1(\Omega_t)} \leq \|w_{\text{ref}}\|_{H^1(\Omega_t)} + \|w_{\text{int}}\|_{H_0^1(\Omega)}. \quad (5.23)$$

To this end, we need the two extension operators

$$E_{\text{sa}} : V(\Omega_t) \rightarrow H_0^1(\Omega) \quad \text{and} \quad E_{\text{st}} : H^2(\Omega) \rightarrow H_0^2(\hat{\Omega})$$

introduced in [194, Section 2.1] and [99, Theorem 7.25], respectively. Here, $\hat{\Omega}$ is an open and bounded set with $\Omega \Subset \hat{\Omega} \subset \mathbb{R}^2$. In order to derive a stability estimate for w_{ref} , we exploit the following properties of E_{sa} and E_{st} :

(P1) Let $v \in V(\Omega_t)$ then it holds: $E_{\text{sa}}v|_{\Omega_t} = v$ and $\overline{E_{\text{sa}}v}^{(i)} = \bar{v}^{(i)}$.

(P2) According to [194, Lemma 2.2, Theorem 2.2, Example 2.1], there is a constant $C_{\text{sa}} > 0$ independent of R_i , such that

$$\|\nabla E_{\text{sa}}v\|_{L^2(\Omega)} \leq C_{\text{sa}}\|\nabla v\|_{L^2(\Omega_t)} \text{ for } v \in V(\Omega_t).$$

(P3) For $v \in H^2(\Omega)$, there is a constant $C_{\text{st}} > 0$, such that

$$\|E_{\text{st}}v\|_{H^2(\hat{\Omega})} \leq C_{\text{st}}\|v\|_{H^2(\Omega)} \text{ and } E_{\text{st}}v|_{\Omega} = v.$$

We begin bounding the term $\|w_{\text{ref}}\|_{H^1(\Omega_t)}$. For $v = w_{\text{ref}} \in V(\Omega_t)$ in (5.10), using the decomposition in (5.22) we obtain

$$\begin{aligned} \|\nabla w_{\text{ref}}\|_{L^2(\Omega_t)}^2 &\leq (F, E_{\text{sa}}w_{\text{ref}})_{\Omega} - (\nabla u_{\text{f}}, \nabla E_{\text{sa}}w_{\text{ref}})_{\Omega} - \sum_{i=1}^N (f_i, E_{\text{sa}}w_{\text{ref}})_{B_i} \\ &\quad + \sum_{i=1}^N (\nabla u_{\text{f}}, \nabla E_{\text{sa}}w_{\text{ref}})_{B_i} - \sum_{i=1}^N L_{\text{p},i} (u_{\text{f}}, w_{\text{ref}})_{\partial B_i} + \sum_{i=1}^N U_i L_{\text{p},i} \int_{\partial B_i} w_{\text{ref}} dS. \end{aligned}$$

Testing (5.21) with $v = E_{\text{sa}}w_{\text{ref}} \in H_0^1(\Omega)$, we have

$$(F, E_{\text{sa}}w_{\text{ref}})_{\Omega} - (\nabla u_{\text{f}}, \nabla E_{\text{sa}}w_{\text{ref}})_{\Omega} = 0$$

and by (P1) and the Hölder inequality, it follows

$$\|\nabla w_{\text{ref}}\|_{L^2(\Omega_t)}^2 \leq \sum_{i=1}^N \|f_i\|_{L^2(B_i)} \|E_{\text{sa}}w_{\text{ref}}\|_{L^2(B_i)} \quad (\text{i})$$

$$+ \sum_{i=1}^N \|\nabla u_{\text{f}}\|_{L^2(B_i)} \|\nabla E_{\text{sa}}w_{\text{ref}}\|_{L^2(B_i)} \quad (\text{ii})$$

$$+ \sum_{i=1}^N L_{\text{p},i} \|u_{\text{f}}\|_{L^2(\partial B_i)} \|w_{\text{ref}}\|_{L^2(\partial B_i)} \quad (\text{iii})$$

$$+ 2\pi \sum_{i=1}^N U_i L_{\text{p},i} R_i \cdot \bar{w}_{\text{ref}}^{(i)} \quad (\text{iv}).$$

In order to bound (i), we consider once again the Hölder inequality with the parameters r and s fulfilling the condition $1/r + 1/s = 1$. By means of this, one can show that

$$\|E_{\text{sa}}w_{\text{ref}}\|_{L^2(B_i)} \leq CR_i^{\frac{1}{r}} \|E_{\text{sa}}w_{\text{ref}}\|_{L^{2s}(B_i)} \quad (5.24)$$

Setting $s = p/2$ and using (5.7), we obtain for $1/r = 1 - 2/p$

$$\|E_{\text{sa}}w_{\text{ref}}\|_{L^2(B_i)} \leq CR_i^{1-\frac{2}{p}} p^{\frac{1}{2}} \|\nabla E_{\text{sa}}w_{\text{ref}}\|_{L^2(\Omega)}.$$

Setting $p = |\ln R_i|$ and using the same argument as in (5.6) together with (3.14) and (P2), it follows

$$\begin{aligned} \text{(i)} &= \sum_{i=1}^N \|f_i\|_{L^2(B_i)} \|E_{\text{sa}} w_{\text{ref}}\|_{L^2(B_i)} \\ &\leq C \|F\|_{L^2(\Omega)} \|\nabla w_{\text{ref}}\|_{L^2(\Omega_t)} \sum_{i=1}^N R_i |\ln R_i|^{\frac{1}{2}}. \end{aligned} \quad (5.25)$$

To bound (ii), we proceed analogously as for (5.24) and we obtain

$$\|\nabla u_f\|_{L^2(B_i)} \leq C R_i^{1-\frac{2}{p}} \|\nabla u_f\|_{L^p(B_i)}.$$

To bound the term $\|\nabla u_f\|_{L^p(B_i)}$, the Sobolev estimate (5.7) cannot be applied directly to the function $\nabla u_f \notin H_0^1(\Omega)$. Instead, exploiting the H^2 -regularity of u_f , we consider its extension $E_{\text{st}} u_f$ on $\hat{\Omega}$. Therefore, combining the estimate (5.7) with property (P3) and using the H^2 -regularity of u_f , we obtain

$$\begin{aligned} \|\nabla u_f\|_{L^p(B_i)} &\leq \|\nabla u_f\|_{L^p(\Omega)} = \left(\sum_{i=1}^2 \|\partial_{x_i} u_f\|_{L^p(\Omega)}^p \right)^{1/p} \\ &\leq \left(\sum_{i=1}^2 \|\partial_{x_i} E_{\text{st}} u_f\|_{L^p(\hat{\Omega})}^p \right)^{1/p} \\ &\leq C p^{\frac{1}{2}} \left(\sum_{i=1}^2 \|\nabla (\partial_{x_i} E_{\text{st}} u_f)\|_{L^2(\hat{\Omega})}^p \right)^{1/p} \\ &\leq C p^{\frac{1}{2}} \left(\sum_{i=1}^2 \|E_{\text{st}} u_f\|_{H^2(\hat{\Omega})}^p \right)^{1/p} \\ &\leq C \cdot 2^{\frac{1}{p}} p^{\frac{1}{2}} \|E_{\text{st}} u_f\|_{H^2(\hat{\Omega})} \leq C \cdot 2^{\frac{1}{p}} p^{\frac{1}{2}} \|u_f\|_{H^2(\Omega)} \\ &\leq C \cdot 2^{\frac{1}{p}} p^{\frac{1}{2}} \|F\|_{L^2(\Omega)}. \end{aligned}$$

Regarding the second factor in (ii), one easily obtain using (P2)

$$\|\nabla E_{\text{sa}} w_{\text{ref}}\|_{L^2(B_i)} \leq C \|\nabla E_{\text{sa}} w_{\text{ref}}\|_{L^2(\Omega)} \leq C \cdot C_{\text{sa}} \|\nabla w_{\text{ref}}\|_{L^2(\Omega_t)}.$$

Choosing $p = |\ln R_i|$ the estimate for (ii) results in

$$\begin{aligned} \text{(ii)} &= \sum_{i=1}^N \|\nabla u_f\|_{L^2(B_i)} \|\nabla E_{\text{sa}} w_{\text{ref}}\|_{L^2(B_i)} \\ &\leq C \|F\|_{L^2(\Omega)} \|\nabla w_{\text{ref}}\|_{L^2(\Omega_t)} \sum_{i=1}^N R_i |\ln R_i|^{\frac{1}{2}}. \end{aligned} \quad (5.26)$$

Now we want to bound the third summand (iii). Considering a standard Sobolev embedding (see, e.g., [38, Theorem (1.4.6)]) together with the H^2 -regularity of u_f , we have for each inclusion B_i

$$\|u_f\|_{L^2(\partial B_i)} \leq C \sqrt{R_i} \|u_f\|_{L^\infty(\Omega)} \leq C \sqrt{R_i} \|u_f\|_{H^2(\Omega)} \leq C \sqrt{R_i} \|f\|_{L^2(\Omega_t)}$$

For the second term in (iii), using (P1), Lemma 5.3 and (P2), we obtain for each inclusion the estimate

$$\|w_{\text{ref}}\|_{L^2(\partial B_i)} \leq C \sqrt{R_i |\ln R_i|} \|\nabla w_{\text{ref}}\|_{L^2(\Omega_t)}.$$

All together, we obtain:

$$\begin{aligned} \text{(iii)} &= \sum_{i=1}^N L_{p,i} \|u_f\|_{L^2(\partial B_i)} \|w_{\text{ref}}\|_{L^2(\partial B_i)} \\ &\leq C \|F\|_{L^2(\Omega)} \|\nabla w_{\text{ref}}\|_{L^2(\Omega_t)} \sum_{i=1}^N L_{p,i} R_i |\ln R_i|^{\frac{1}{2}}. \end{aligned} \quad (5.27)$$

The bound for the last summand (iv) follows directly from (P1) and Lemma 5.1

$$\text{(iv)} = 2\pi \sum_{i=1}^N U_i L_{p,i} R_i \cdot \bar{w}_{\text{ref}}^{(i)} \leq C \|\nabla w_{\text{ref}}\|_{L^2(\Omega_t)} \sum_{i=1}^N U_i L_{p,i} R_i |\ln R_i|^{\frac{1}{2}}. \quad (5.28)$$

Summarizing (5.25), (5.26), (5.27) and (5.28), we finally have

$$\begin{aligned} \|\nabla w_{\text{ref}}\|_{L^2(\Omega_t)} &\leq C \left[\|F\|_{L^2(\Omega)} \sum_{i=1}^N (1 + L_{p,i}) R_i |\ln R_i|^{\frac{1}{2}} \right. \\ &\quad \left. + \sum_{i=1}^N U_i L_{p,i} R_i |\ln R_i|^{\frac{1}{2}} \right]. \end{aligned} \quad (5.29)$$

In the next step, we derive a bound for the second term in (5.23), for which we first need a stability estimate for the function w_{int} . To this end, (5.20) is tested with $v = w_{\text{int}} \in H_0^1(\Omega)$. Inserting the decomposition (5.22) of u_{int} into (5.20), it follows that

$$\begin{aligned} \|\nabla w_{\text{int}}\|_{L^2(\Omega)}^2 &\leq (F, w_{\text{int}})_{\Omega} - (\nabla u_f, \nabla w_{\text{int}})_{\Omega} - \sum_{i=1}^N L_{p,i} (u_f, w_{\text{int}})_{L^2(\partial B_i)} \\ &\quad + 2\pi \sum_{i=1}^N U_i L_{p,i} R_i \cdot \bar{w}_{\text{int}}^{(i)}. \end{aligned}$$

By means of the techniques that have been used to derive the stability estimate (5.29) for w_{ref} , one can obtain

$$\|\nabla w_{\text{int}}\|_{L^2(\Omega)} \leq C \left[\|F\|_{L^2(\Omega)} \sum_{i=1}^N L_{p,i} R_i |\ln R_i|^{\frac{1}{2}} + \sum_{i=1}^N U_i L_{p,i} R_i |\ln R_i|^{\frac{1}{2}} \right]. \quad (5.30)$$

Based on (5.23), (5.29) and (5.30), the following upper bound for the error component e_1 can be derived

$$\begin{aligned} \|e_1\|_{H^1(\Omega_t)} &\leq \|w_{\text{ref}}\|_{H^1(\Omega_t)} + \|w_{\text{int}}\|_{H_0^1(\Omega)} \leq \|E_{\text{sa}} w_{\text{ref}}\|_{H_0^1(\Omega)} + \|w_{\text{int}}\|_{H_0^1(\Omega)} \\ &\leq C \left(\|\nabla w_{\text{ref}}\|_{L^2(\Omega_t)} + \|\nabla w_{\text{int}}\|_{L^2(\Omega)} \right) \\ &\leq C_1 \left[\|F\|_{L^2(\Omega)} \sum_{i=1}^N R_i |\ln R_i|^{\frac{1}{2}} (1 + L_{p,i}) + \sum_{i=1}^N U_i L_{p,i} R_i |\ln R_i|^{\frac{1}{2}} \right]. \end{aligned}$$

Now, we aim to derive an upper bound for e_2 in terms of the data and the geometrical configuration of the inclusions. By subtracting problem (5.12) from (5.20) and rearranging the terms, we obtain the following equation

$$(\nabla(u_{\text{int}} - u_{\text{red}}), \nabla v)_{\Omega} + \sum_{i=1}^N L_{p,i} (u_{\text{int}} - \bar{u}_{\text{red}}^{(i)}, v)_{\partial B_i} = 0, \quad \forall v \in H_0^1(\Omega).$$

Adding the solution u_{red} in the second term, we can split the sum into two parts, the first involving the error $e_2 = u_{\text{int}} - u_{\text{red}}$ and the second involving the fluctuation $\tilde{u}_{\text{red}}^{(i)} = u_{\text{red}} - \bar{u}_{\text{red}}^{(i)}$

$$(\nabla(u_{\text{int}} - u_{\text{red}}), \nabla v)_{\Omega} + \sum_{i=1}^N L_{p,i} (u_{\text{int}} - u_{\text{red}}, v)_{\partial B_i} + \sum_{i=1}^N L_{p,i} (u_{\text{red}} - \bar{u}_{\text{red}}^{(i)}, v)_{\partial B_i} = 0$$

for every $v \in H_0^1(\Omega)$. Choosing $v = e_2 \in H_0^1(\Omega)$, it follows

$$\begin{aligned} \|\nabla e_2\|_{L^2(\Omega)}^2 &\leq \sum_{i=1}^N L_{p,i} (\tilde{u}_{\text{red}}^{(i)}, e_2)_{\partial B_i} \\ &= \sum_{i=1}^N L_{p,i} (\tilde{u}_{\text{red}}^{(i)}, e_2 - \bar{e}_2^{(i)})_{\partial B_i} + \underbrace{L_{p,i} (\tilde{u}_{\text{red}}^{(i)}, \bar{e}_2^{(i)})_{\partial B_i}}_{=0} \\ &\leq \sum_{i=1}^N L_{p,i} \|\tilde{u}_{\text{red}}^{(i)}\|_{L^2(\partial B_i)} \|e_2 - \bar{e}_2^{(i)}\|_{L^2(\partial B_i)}, \end{aligned}$$

where we used again the same techniques as in the proof of Lemma 5.2. This intermediate result is coherent with assumption (MA2), because it shows that if the fluctuations on the interfaces ∂B_i are small, then the modeling error is small as well. Now by estimate (5.8) and the stability estimate (5.16), we have

$$\begin{aligned} \|\nabla e_2\|_{L^2(\Omega)}^2 &\leq \sum_{i=1}^N L_{p,i} R_i \|\nabla u_{\text{red}}\|_{L^2(\Omega)} \|\nabla e_2\|_{L^2(\Omega)} \\ &\leq C_2 \left[\|F\|_{L^2(\Omega)} \sum_{i=1}^N L_{p,i} R_i + \sum_{i,j=1}^N L_{p,i} L_{p,j} R_i R_j |\ln R_j|^{\frac{1}{2}} U_j \right] \|\nabla e_2\|_{L^2(\Omega)}. \end{aligned}$$

By means of Poincaré's inequality, the result reported in inequality (5.19) is proved. \square

5.4. Numerical approximation

In this section, we study the convergence behaviour of a standard FEM discretization applied to the variational problem (5.13). Let \mathcal{T}_h be a conforming quasi-uniform triangulation of the computational domain Ω . By h , we denote the characteristic mesh size of the grid.

As discretization space, we consider the standard linear FEM space V_h^1 as defined in (2.7). Then, we denote by $u_{\text{red},h} \in V_h^1$ the solution of the problem

$$a(u_{\text{red},h}, v_h) = \ell(v_h), \quad \forall v_h \in V_h^1. \quad (5.31)$$

A first convergence result for this discretization is provided in the next theorem.

Theorem 5.2. *Let $u_{\text{red}} \in H_0^1(\Omega) \cap H^{\frac{3}{2}-\varepsilon}(\Omega)$ be the solution of (5.13) and let $u_{\text{red},h}$ be defined by (5.31). Then, the error of the FEM approximation can be bounded by*

$$\|u_{\text{red}} - u_{\text{red},h}\|_{H^1(\Omega)} \leq C_1 h^{\frac{1}{2}-\varepsilon} \|u_{\text{red}}\|_{H^{\frac{3}{2}-\varepsilon}(\Omega)} \quad (5.32)$$

and

$$\|u_{\text{red}} - u_{\text{red},h}\|_{L^2(\Omega)} \leq C_2 h^{1-\varepsilon} \|u_{\text{red}}\|_{H^{\frac{3}{2}-\varepsilon}(\Omega)} \quad (5.33)$$

for $0 < \varepsilon \leq 1/2$ and some constants C_1, C_2 independent of h .

Proof. From the proof of Proposition 5.1, it is obvious that the bilinear form a in (5.14) and the linear form ℓ in (5.15) fulfil all the conditions for C ea's Lemma [38, Theorem (2.8.1)]. Therefore, the H^1 -error can be bounded by an interpolation error

$$\|u_{\text{red}} - u_{\text{red},h}\|_{H^1(\Omega)} \leq \sqrt{\frac{C_a}{\alpha}} \|u_{\text{red}} - S_h u_{\text{red}}\|_{H^1(\Omega)}, \quad (5.34)$$

where $S_h : H^1(\Omega) \rightarrow V_h^1$ is a suitable interpolation operator. α and C_a denote the coercivity and continuity constants of the bilinear form a as they appear in (5.17) and (5.18). Choosing for S_h the Scott-Zhang operator [197, Theorem 4.1] and considering the regularity result in Proposition 5.1, the first estimate follows. We also note that from the proof of Proposition 5.1 it can be concluded that the constant in (5.34) is bounded, even if R_i tends to zero. Based on the first estimate, the second estimate can be shown by means of an Aubin-Nitsche argument. Thus, we consider the following dual problem

$$\begin{cases} -\Delta w + \sum_{i=1}^N L_{p,i} \bar{w}^{(i)} \delta_{\partial B_i} = u_{\text{red}} - u_{\text{red},h}, & \text{in } \Omega, \\ w = 0, & \text{on } \partial\Omega. \end{cases}$$

Proceeding as in Proposition 5.1, we can prove that $w \in H_0^1(\Omega) \cap H^{\frac{3}{2}-\varepsilon}(\Omega)$. The weak formulation of the dual problem reads as follows: Find $w \in H_0^1(\Omega)$ such that

$$(\nabla w, \nabla v)_\Omega + 2\pi \sum_{i=1}^N R_i L_{p,i} \bar{w}^{(i)} \bar{v}^{(i)} = (u_{\text{red}} - u_{\text{red},h}, v)_\Omega, \quad \forall v \in H_0^1(\Omega). \quad (5.35)$$

The discrete version of (5.35) is given by: Find $w_h \in V_h^1(\Omega)$ such that

$$(\nabla w_h, \nabla v_h)_\Omega + 2\pi \sum_{i=1}^N R_i L_{p,i} \bar{w}_h^{(i)} \bar{v}_h^{(i)} = (u_{\text{red}} - u_{\text{red},h}, v_h)_\Omega, \quad \forall v_h \in V_h^1.$$

Choosing $v = u_{\text{red}} - u_{\text{red},h}$ in (5.35), using the Galerkin orthogonality, Cauchy-Schwarz inequality, Lemma (5.1), the error bound (5.32) and the exploiting the regularity of w , we obtain:

$$\begin{aligned} \|u_{\text{red}} - u_{\text{red},h}\|_{L^2(\Omega)}^2 &= a(\nabla w, \nabla(u_{\text{red}} - u_{\text{red},h})) \\ &= a(\nabla(w - w_h), \nabla(u_{\text{red}} - u_{\text{red},h})) \\ &\leq C \|\nabla(u_{\text{red}} - u_{\text{red},h})\|_{L^2(\Omega)} \cdot \|\nabla(w - w_h)\|_{L^2(\Omega)} \\ &\leq C_1 h^{\frac{1}{2}-\varepsilon} \|u_{\text{red}}\|_{H^{\frac{3}{2}-\varepsilon}(\Omega)} \cdot C_3 h^{\frac{1}{2}-\varepsilon} \|w\|_{H^{\frac{3}{2}-\varepsilon}(\Omega)} \\ &\leq C_2 h^{1-2\varepsilon} \|u_{\text{red}}\|_{H^{\frac{3}{2}-\varepsilon}(\Omega)} \cdot \|u_{\text{red}} - u_{\text{red},h}\|_{L^2(\Omega)}, \end{aligned}$$

where the last step follows from [14], Lemma 5.1 and the stability estimate (5.16). This proves (5.33). \square

We note that although the solution is globally not in H^2 , and thus we cannot expect $\mathcal{O}(h)$ convergence in the H^1 -norm, its restrictions to Ω_t and Ω_v can be expected to be in H^2 . Therefore we show how to improve the accuracy of the numerical approximation by means of particular techniques. More specifically, we discuss two possibilities to bypass the reduced regularity of the solution by modifying the computational grid. The modification of the grid consists in adapting the grid to the interfaces ∂B_i , $i \in \{1, \dots, N\}$ such that optimal error estimates can be derived. In the literature they are referred to as δ -resolving [151, Definition 3.1] and *graded meshes* [66, Section 3.1]. Other ways to handle the lower regularity require, e.g., appropriate error norms [140], or appropriate FEM spaces [95].

We say that a grid \mathcal{T}_h is δ -resolving with respect to an interface ∂B_i , if the boundaries of the subgrids corresponding to B_i and $\Omega \setminus B_i$ have a maximal distance of δ to the interface ∂B_i . Here, we consider a special type of a δ -resolving grid, in which the element edges adjacent to ∂B_i form an interpolating linear spline for this interface, see Figure 5.1, top. From standard interpolation theory, it is well known that in this case $\delta = \mathcal{O}(h^2)$ holds. Note that, in order to fulfil this property, \mathcal{T}_h does not have to be refined locally.

Contrary to that, a grid that is graded with respect to ∂B_i exhibits local refinements along ∂B_i , see Figure 5.1, on the bottom. In fact, a graded mesh has the feature that the diameters of the elements are scaled by the distance to the interface, such that the element diameters become smaller the nearer they are located to the interface [10, Section 2]. Let us denote the minimum distance of an element T to the interfaces ∂B_i by r_T and the diameter of T by h_T as defined in (2.1). For the purpose of this work, it is sufficient to consider a particular case of the graded meshes, as presented in [66, Section 3.1]. For a characteristic mesh size h , we assume that the local element size h_T scales as $\sqrt{r_T}$ and that $h_T \approx h^2$ if T is close to ∂B_i . In other words, let $\gamma > 0$ be a fixed coefficient, e.g., $\gamma := 1/2$. Then we assume

$$h_T \approx \begin{cases} h\sqrt{r_T}, & \text{if } r_T > \gamma h, \\ h^2, & \text{otherwise.} \end{cases} \quad (5.36)$$

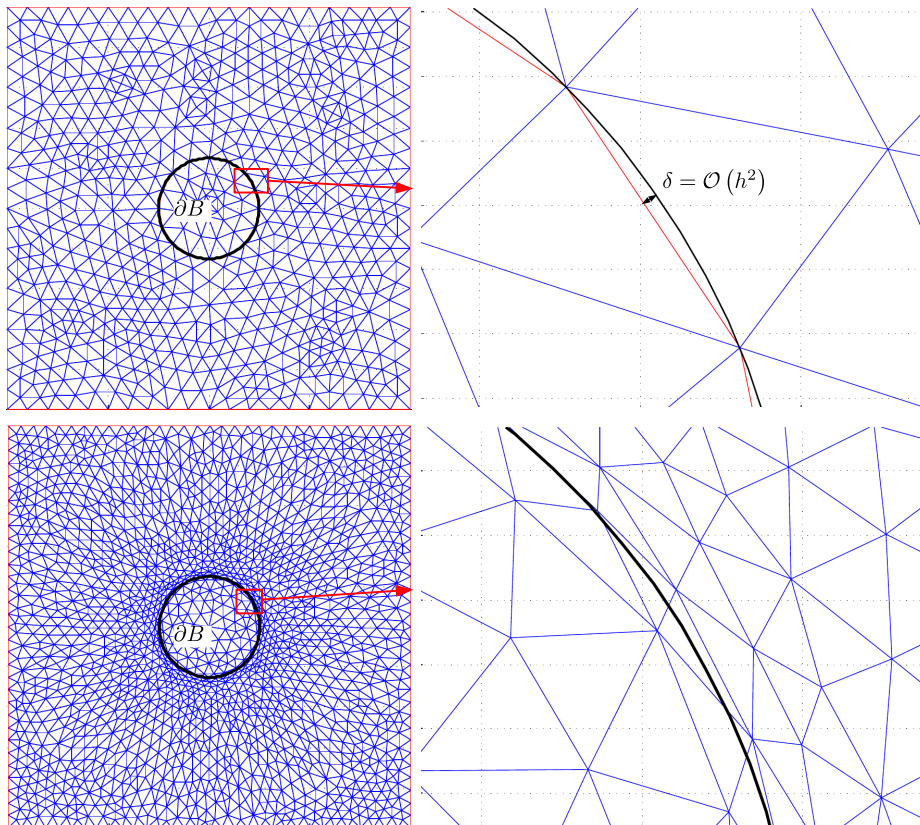


Figure 5.1.: Adapted meshes for a circular interface ∂B : δ -resolving mesh with $\delta = \mathcal{O}(h^2)$ (top), graded mesh (bottom).

In the next theorem, we show that using a δ -resolving or a graded mesh allows us to recover optimal convergence rates for the FEM approximations, provided that the corresponding solution exhibits appropriate local smoothness.

Theorem 5.3. *Let u_{red} be the weak solution of (5.13) such that $u_{\text{red}} \in H^2(\Omega_t \cup \Omega_v)$. By \mathcal{T}_h^δ we denote a family of δ -resolving meshes with $\delta = \mathcal{O}(h^2)$ and by \mathcal{T}_h^g we denote a family of graded meshes. Both meshes are adapted to the interfaces ∂B_i , for $i = 1, \dots, N$. The FEM solutions of (5.31) are denoted by $u_{\text{red},h}^\delta$ and $u_{\text{red},h}^g$, respectively. Under these conditions, the following optimal $H^1(\Omega)$ - and $L^2(\Omega)$ -error estimates hold true*

$$(E1) \quad \|u_{\text{red}} - u_{\text{red},h}^\delta\|_{H^1(\Omega)} + \frac{1}{h} \|u_{\text{red}} - u_{\text{red},h}^\delta\|_{L^2(\Omega)} \leq Ch \|u_{\text{red}}\|_{H^2(\Omega_t \cup \Omega_v)},$$

$$(E2) \quad \|u_{\text{red}} - u_{\text{red},h}^g\|_{H^1(\Omega)} + \frac{1}{h} \|u_{\text{red}} - u_{\text{red},h}^g\|_{L^2(\Omega)} \leq Ch^{1-\varepsilon} \|u_{\text{red}}\|_{H^{\frac{3}{2}-\varepsilon}(\Omega)} \\ + h \|u_{\text{red}}\|_{H^2(\Omega_t \cup \Omega_v)},$$

where $0 < \varepsilon \leq 1/2$.

Proof. As in the proof of the previous theorem, the H^1 -errors for both discretizations can be bounded by an interpolation error. In the case of the δ -resolving mesh, we use a modified Clément operator S_h^c presented in [151, Def. 3.3]. For this operator one can prove the following approximation result [151, Theorem 3.5]

$$\|u_{\text{red}} - S_h^c u_{\text{red}}\|_{H^1(\Omega)}^2 \leq C \left[h^2 \|u_{\text{red}}\|_{H^2(\Omega_t \cup \Omega_v)}^2 + \delta \|u_{\text{red}}\|_{H^2(\Omega_t \cup \Omega_v)}^2 \right].$$

Then estimate (E1) follows from the assumption $\delta = \mathcal{O}(h^2)$.

For a graded mesh \mathcal{T}_h^g , we choose the Scott-Zhang operator S_h^{SZ} from [197, Theorem 4.1] and compute

$$\begin{aligned} \|u_{\text{red}} - S_h^{\text{SZ}} u_{\text{red}}\|_{H^1(\Omega)}^2 &= \sum_{T \in \mathcal{T}_h^g} \|u_{\text{red}} - S_h^{\text{SZ}} u_{\text{red}}\|_{H^1(T)}^2 \\ &= \sum_{\substack{T \in \mathcal{T}_h^g \\ r_T \leq \delta h}} \|u_{\text{red}} - S_h^{\text{SZ}} u_{\text{red}}\|_{H^1(T)}^2 + \sum_{\substack{T \in \mathcal{T}_h^g \\ r_T > \delta h}} \|u_{\text{red}} - S_h^{\text{SZ}} u_{\text{red}}\|_{H^1(T)}^2. \end{aligned}$$

Using the error estimate (5.32), for the elements of the first summand we have

$$\|u_{\text{red}} - S_h^{\text{SZ}} u_{\text{red}}\|_{H^1(T)}^2 \leq Ch_T^{1-2\varepsilon} \|u_{\text{red}}\|_{H^{\frac{3}{2}-\varepsilon}(\omega_T)}^2,$$

where ω_T is a patch of elements around T . For $0 < \varepsilon \leq 1/2$ and using (5.36), we obtain

$$\sum_{\substack{T \in \mathcal{T}_h^g \\ r_T \leq \delta h}} \|u_{\text{red}} - S_h^{\text{SZ}} u_{\text{red}}\|_{H^1(T)}^2 \leq Ch^{2-4\varepsilon} \|u_{\text{red}}\|_{H^{\frac{3}{2}-\varepsilon}(\Omega)}^2. \quad (5.37)$$

Using $u_{\text{red}} \in H^2(\Omega_t \cup \Omega_v)$ and the approximation properties of S_{zh} , for the second summand we have

$$\sum_{\substack{T \in \mathcal{T}_h^g \\ r_T > \delta h}} \|u_{\text{red}} - S_h^{\text{SZ}} u_{\text{red}}\|_{H^1(T)}^2 \leq Ch^2 \|u_{\text{red}}\|_{H^2(\Omega_t \cup \Omega_v)}^2. \quad (5.38)$$

Combing (5.37) and (5.38), we obtain the H^1 -estimate (E2). The L^2 -estimates follow again from an Aubin-Nitsche argument as in the proof of Theorem 5.2. \square

In the next section, we validate numerically the results from Theorem 5.3, which means, we have to construct meshes that fit the inclusions. While for two-dimensional problems, the use of interface fitting or graded meshes is computationally still feasible, these strategies can drastically increase the numerical costs, if one wants to simulate realistic complex 1D structures embedded in a three-dimensional domain as, e.g., the network from Figure II.1. In this case, the 3D-1D approach still features significant advantages with respect to the full three-dimensional discretization of the inclusions. Moreover, as we see in more detail in Section 6, the scheme proposed in this section does not require any point by point coherence of the computational meshes of the two-dimensional domain Ω and the inclusions B_i , ensuring greater flexibility in the construction of the mesh for Ω .

5.5. Numerical experiments

The objective of this section is to support by means of numerical evidence the theoretical results of Section 5.3 and 5.4. In the first part, we show to what extent the solutions of problem (5.10) and of the simplified model (5.12) differ. The second part contains several tests addressing the convergence results in Theorem 5.2 and 5.3. For the algorithmic aspects of the averaging strategy, a detailed description is postponed to Section 6, where a 3D-1D coupled problem is considered.

5.5.1. Investigation of the modeling error

In this subsection, we validate numerically the estimate (5.19) for the modeling error. To this end, let us consider a single source term, that is, we set $N = 1$ in (5.3). We denote with u_{ref} and u_{red} the analytical solutions to problem (5.10) and (5.12), respectively. In the general case, these solutions are not known a priori. Therefore, we verify (5.19) using their linear FEM approximations $u_{\text{ref},h}$ and $u_{\text{red},h}$, respectively, since the numerical solutions converge to the corresponding analytical solutions as the mesh size goes to zero. We define the reduced problem (5.12) on the domain $\Omega := (-1, 1)^2$, while the full dimensional problem (5.10) is posed on $\Omega_t = \Omega \setminus B_1$, where the only circular inclusion B_1 is a ball of radius R with center in $(0.3, 0.4)$. In many applications, the radius of the inclusion is the most relevant parameter and with estimate (5.19) we have proved that the error introduced adopting the reduced model tends to zero as the radius of the inclusion becomes smaller. Therefore, in this test, we analyse the influence of the size of the inclusion, that is, we vary its radius R , while keeping the other parameters constant. In order to verify the dependency of the modeling error on the radius R of the inclusion, we take $R \in \{0.1, 0.05, 0.025, 0.0125, 0.00625, 0.003125\}$, while we set $L_{p,1} = U_1 = 1$ constant for all simulations. As source term, we choose the function

$$F(\mathbf{x}) := \sin(9x) + \sin(13y) + x + y, \quad \text{for } (x, y) \in \Omega.$$

According to Theorem 5.2 and standard convergence results, we can bound the modeling error by

$$\begin{aligned} \|u_{\text{ref}} - u_{\text{red}}\|_{H^1(\Omega_t)} &\leq \|u_{\text{ref}} - u_{\text{ref},h}\|_{H^1(\Omega_t)} + \|u_{\text{red}} - u_{\text{red},h}\|_{H^1(\Omega_t)} \\ &\quad + \|u_{\text{ref},h} - u_{\text{red},h}\|_{H^1(\Omega_t)} \\ &\leq \mathcal{O}\left(h^{\frac{1}{2}}\right) + C\|u_{\text{ref},h} - u_{\text{red},h}\|_{H^1(\Omega_t)}. \end{aligned}$$

As the mesh size h tends to zero, we may assume that the modeling error between numerical solutions converges to the actual modeling error, as Figure 5.2 suggests. As an error measure, we employ the numerical modeling error defined by

$$\text{err} := \|u_{\text{ref},h} - u_{\text{red},h}\|_{H^1(\Omega_t)}.$$

Furthermore, we define an error functional to show the experimental order of convergence by

$$\text{Rate} := \frac{\log(\text{err}(R_1)/\text{err}(R_2))}{\log(R_1/R_2)},$$

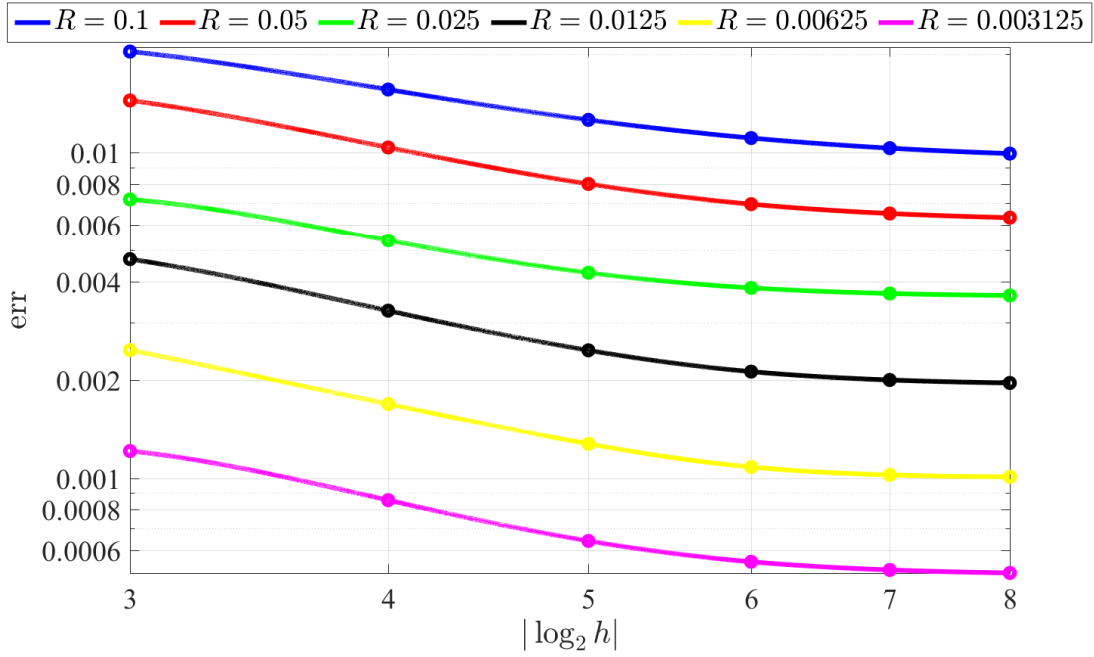


Figure 5.2.: The numerical modeling error is calculated for different values of the mesh characteristic size ($h = 2^{-i}$ for $i = 3, \dots, 8$) and for different radii of the ball B_1 (each line shown with different colors). For each radius the modeling error values are interpolated using splines. We observe that as the mesh size h tends to zero, the error converges to a fixed value, which is the actual modeling error.

where $\text{err}(R)$ is the numerical modeling error for the radius R . In Table 5.1, the modeling error, computed at the finest level of the δ -resolving mesh, is provided for different radii together with the rate of convergence with respect to the radius R of the inclusion. We observe that the modeling error decays quasi-linearly as R , which is in good agreement with our estimate (5.19).

Table 5.1.: The numerical modelling error is shown for different radii and $L_{p,1} = U = 1$. The numerical convergence rate is reported in the last column.

R	err	Rate
0.1	$9.9277e - 03$	/
0.05	$6.3175e - 03$	0.65
0.025	$3.6245e - 03$	0.80
0.0125	$1.9559e - 03$	0.89
0.00625	$1.0088e - 03$	0.96
0.003125	$5.1217e - 04$	0.98

5.5.2. Convergence tests

The objective of this section is to illustrate the convergence results of Theorems 5.2 and 5.3 by means of numerical experiments based on test cases where the analytical solution is explicitly available. We provide experiments in the case where only one inclusion is present and one case with multiple inclusions. To simplify the notation, we drop for this section the index “red” when referring to the solution of problem (5.12) and its numerical approximation.

Single inclusion

For our first convergence test, we consider a single source term, i.e., we set in (5.3) $N = 1$. The ball B_1 has the radius $R_1 = 0.25$ and the center $\mathbf{x}_1 := (0, 0)$. As a computational domain, we choose the square $\Omega := (-1, 1)^2 \subset \mathbb{R}^2$. The remaining parameters of the problem are given by $L_{p,1} = 2$ and $U_1 = 1$. Setting $F \equiv 0$ and appropriate Dirichlet boundary conditions, the exact solution is given by

$$u_{e,1}(\mathbf{x}) = \begin{cases} U_1 \frac{L_{p,1}}{1 + L_{p,1}} \left(1 - R_1 \ln \left(\frac{r(\mathbf{x})}{R_1} \right) \right), & r(\mathbf{x}) > R_1, \\ U_1 \frac{L_{p,1}}{1 + L_{p,1}}, & r(\mathbf{x}) \leq R_1, \end{cases}$$

where $r(\mathbf{x}) := |\mathbf{x} - \mathbf{x}_1|$ denotes the Euclidean distance from an arbitrary point $\mathbf{x} \in \Omega$ to the center of the inclusion. The numerical solution $u_{h,1}$ is defined by (5.31), and the numerical discretization error $e_{h,1}$ is given by $e_{h,1} := u_{e,1} - u_{h,1}$. For the triangulation of Ω , we employ three different types of meshes. The second refinement level of each grid is depicted in Figure 5.3, where we use a uniform mesh, a δ -resolving mesh and a graded mesh, as defined by (5.36). Tables 5.2 and 5.3 show the discretization errors $e_{h,1}$ with respect to the L^2 - and the H^1 -norm and the refinement level ℓ . Considering

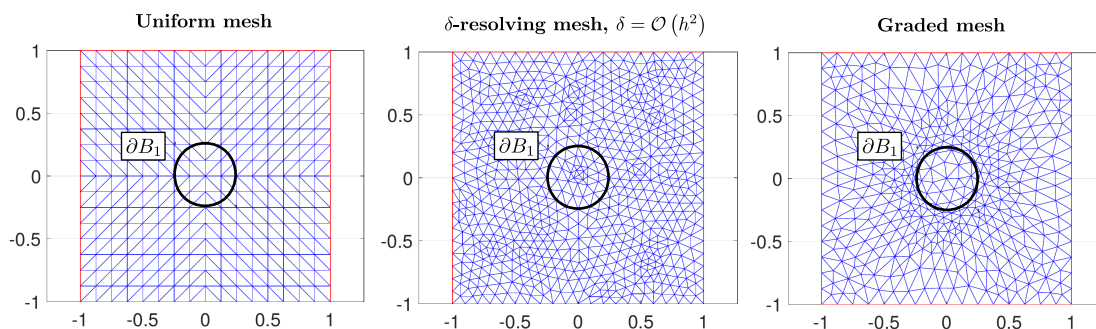


Figure 5.3.: Three different types of meshes are used for the first convergence test (single point source term). left: Uniform mesh (521 elements), middle: δ -resolving mesh, $\delta = \mathcal{O}(h^2)$ (1368 elements), right: Graded mesh (870 elements).

the convergence rates in both tables it can be seen that the theoretical convergence results in Theorem 5.2 and 5.3 are confirmed, since it holds $u_{e,1} \in H^2(\Omega_t \cup \Omega_v)$.

Table 5.2.: L^2 -norms of $e_{h,1}$ and convergence rates for three different meshes (uniform, δ -resolving, graded). In the last line of the table the theoretical convergence rates are listed.

	Uniform mesh		δ -resolving mesh		Graded mesh	
ℓ	$\ e_{h,1}\ _{L^2(\Omega)}$	Rate	$\ e_{h,1}\ _{L^2(\Omega)}$	Rate	$\ e_{h,1}\ _{L^2(\Omega)}$	Rate
1	$2.5869e - 02$	/	$3.6451e - 03$	/	$4.8976e - 03$	/
2	$1.0432e - 02$	1.31	$1.1183e - 03$	1.70	$1.1861e - 03$	2.05
3	$4.7747e - 03$	1.13	$2.7824e - 04$	2.01	$4.5986e - 04$	1.37
4	$2.3942e - 03$	1.00	$8.1655e - 05$	1.77	$1.3194e - 04$	1.80
5	$1.1392e - 03$	1.07	$2.0988e - 05$	1.96	$2.6130e - 05$	2.34
	expected:	1.00	expected:	2.00	expected:	2.00

Table 5.3.: H^1 -norms of $e_{h,1}$ and convergence rates for three different meshes (uniform, δ -resolving, graded). In the last line of the table the theoretical convergence rates are listed.

	Uniform mesh		δ -resolving mesh		Graded mesh	
ℓ	$\ e_{h,1}\ _{H^1(\Omega)}$	Rate	$\ e_{h,1}\ _{H^1(\Omega)}$	Rate	$\ e_{h,1}\ _{H^1(\Omega)}$	Rate
1	$2.6469e - 01$	/	$1.0490e - 01$	/	$1.1263e - 01$	/
2	$1.5866e - 01$	0.74	$4.4191e - 02$	1.25	$5.8234e - 02$	0.95
3	$1.1722e - 01$	0.44	$2.1785e - 02$	1.02	$3.5154e - 02$	0.73
4	$8.2193e - 02$	0.51	$1.0808e - 02$	1.01	$1.9686e - 02$	0.84
5	$5.9665e - 02$	0.46	$5.3807e - 03$	1.01	$8.4113e - 03$	1.23
	expected:	0.50	expected:	1.00	expected:	1.00

Multiple inclusions

In this paragraph, we study problem (5.3) with several circular inclusions B_i for $i = 1, \dots, N$ with $N > 1$. For this purpose, we need to determine the analytical solution $u_{e,2}$ for an arbitrary number N of inclusions. We define the solution $u_{e,2}$ as a linear combination of fundamental solutions

$$u_{e,2}(\mathbf{x}) = \begin{cases} \sum_{i=1}^N y_i \left(1 - R_i \log \frac{r_i(\mathbf{x})}{R_i} \right), & \mathbf{x} \notin \bigcup_{i=1}^N B_i, \\ G_i(\mathbf{x}), & \mathbf{x} \in B_i, \end{cases}$$

where $y_i \in \mathbb{R}$ and $G_i(\mathbf{x})$ is an harmonic function in B_i and $r_i(\mathbf{x}) := |\mathbf{x} - \mathbf{x}_i|$ denotes the distance between the center \mathbf{x}_i of the ball and an arbitrary point $\mathbf{x} \in \Omega$. Then we have

$$-\Delta u_{e,2} = \sum_{i=1}^N y_i \delta_{\partial B_i}. \quad (5.39)$$

A comparison of the right hand sides in (5.39) and (5.3) yields the following equations for the coefficients

$$y_i = L_{p,i} \left(U_i - \bar{u}_{e,2}^{(i)} \right), \quad i \in \{1, \dots, N\}.$$

To compute the average $\bar{u}_{e,2}^{(i)}$, we use the fact that the functions

$$u_j(\mathbf{x}) = 1 - R_j \log \frac{r_j(\mathbf{x})}{R_j}, \quad j \in \{1, \dots, N\} \setminus \{i\}$$

are harmonic in B_i . By the mean-value formula for harmonic functions [82, Chapter 2.2, Theorem 2], we obtain

$$\bar{u}_j^{(i)} = 1 - R_j \log \frac{|\mathbf{x}_j - \mathbf{x}_i|}{R_j}, \quad i \neq j.$$

With this equality, we obtain

$$\bar{u}_{e,2}^{(i)} = y_i + \sum_{j \neq i} y_j \bar{u}_j^{(i)}.$$

Now, the coefficient vector $\mathbf{y} = (y_1, \dots, y_N)^T$ can be determined solving the following system of equations

$$\mathbf{A} \cdot \mathbf{y} = \mathbf{b},$$

where the entries of the matrix $\mathbf{A} \in \mathbb{R}^{N \times N}$ and of the right hand side $\mathbf{b} \in \mathbb{R}^N$ are given for each $i, j = 1, \dots, N$ by

$$\mathbf{A}(i, j) := (1 + L_{p,i}) \delta_{ij} + L_{p,i} \bar{u}_j^{(i)} (1 - \delta_{ij}), \quad \text{and} \quad \mathbf{b}(i) := L_{p,i} U_i,$$

Table 5.4.: Parameter set used for problem (5.3) with $N = 5$ source terms.

	\mathbf{x}_i	R_i	U_i	$L_{p,i}$
B_1	$(-0.50, -0.50)$	0.15	2.30	1.20
B_2	$(0.75, -0.25)$	0.20	2.00	1.30
B_3	$(-0.50, 0.50)$	0.30	1.80	0.90
B_4	$(0.25, 0.25)$	0.10	1.50	1.10
B_5	$(0.25, -0.75)$	0.05	0.50	1.50

where δ_{ij} denotes the standard Kronecker δ -function.

It remains to determine the functions G_i on B_i . An appropriate expression for these functions is given by the following linear combination

$$G_i(\mathbf{x}) = y_i + \sum_{j \neq i} y_j \left(1 - R_j \log \frac{r_j(\mathbf{x})}{R_j} \right),$$

since these functions are harmonic. Furthermore, the function $u_{e,2}$ is now continuous on the entire domain Ω by definition.

For the numerical simulations, we again consider $\Omega = (-1, 1)^2$, but now we include $N = 5$ source terms. In Table 5.4, all the parameters used to define the problem are collected. The domain Ω is discretized using a uniform triangulation, as the one depicted in Figure 5.3, on the left. As for the previous example, the boundary conditions are adjusted such that $u_{e,2}$ is the exact solution of problem (5.3) with parameters from Table 5.4. The numerical solution $u_{h,2}$ is depicted in Figure 5.4 and in Table 5.5, we summarize the discretization error $e_{h,2} := u_{e,2} - u_{h,2}$ in both the L^2 - and H^1 -norms. We observe that the discretization scheme converges as predicted by Theorem 5.2.

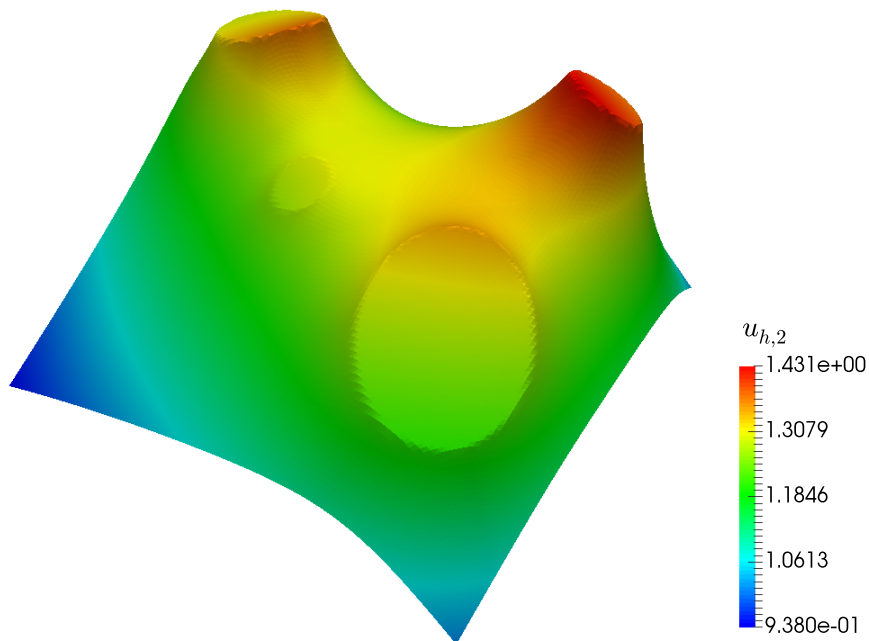


Figure 5.4.: Three-dimensional graph of the numerical solution $u_{h,2}$ based on the parameters in Table 5.4.

Table 5.5.: L^2 - and H^1 -norms and of $e_{h,2}$. The theoretical convergence rates are listed in the last line of the table .

ℓ	$\ e_{h,2}\ _{L^2(\Omega)}$	Rate	$\ e_{h,2}\ _{H^1(\Omega)}$	Rate
1	$6.3850e - 02$	/	$4.2235e - 01$	/
2	$2.2381e - 02$	1.51	$3.5915e - 01$	0.23
3	$1.0876e - 02$	1.04	$2.5007e - 01$	0.52
4	$3.3240e - 03$	1.71	$1.7622e - 01$	0.50
5	$1.5808e - 03$	1.07	$1.2713e - 01$	0.47
6	$7.3069e - 04$	1.11	$8.9042e - 02$	0.51
	expected:	1.00	expected:	0.50

6. 3D-1D coupled system and FEM approximation

The scope of this section consists of showing the flexibility of our new coupling strategy (S2) for solving a general 3D-1D coupled problem. In Section 6.1, we first focus on the algorithmic aspects of the coupling, where we describe the strategy employed to obtain a fast computation of the average value of a function on the surface of the network. More theoretical investigations regarding, e.g., the existence and uniqueness of a weak solution of the 3D-1D coupled problem are not considered here. In fact, the extension of the theory presented in the previous sections to a 3D-1D coupled problem is not trivial, in particular if the structure of the network is complex and contains multiple branches and bifurcations. To this end, we refer to [102], where the authors investigate a three-dimensional elliptic problem with line source terms, but without the coupling terms. To validate the numerical discretization, a convergence test is conducted in Section 6.2 in the case where an analytical solution is available. Finally, in Section 6.3, our coupling strategy (S2) is used to address a relevant application, such as the perfusion of vascularized biological tissues.

6.1. Algorithmic aspects of the FEM discretization

The general 3D-1D coupled problem on which we focus in this section reads as follows

$$\left\{ \begin{array}{ll} -\nabla \cdot \left(\frac{\mathbf{K}_t}{\mu_{\text{int}}} \nabla u^t \right) = L_p \sum_{i=1}^N (u^v - \bar{u}^t) \delta_{\Gamma_i}, & \text{in } \Omega, \\ u^t = 0, & \text{on } \partial\Omega, \\ -\frac{d}{ds} \left(\pi R^2 \frac{\mathbf{K}_v}{\mu_{\text{bl}}} \cdot \frac{du^v}{ds} \right) = L_p \sum_{i=1}^N 2\pi R_i (\bar{u}^t - u^v), & \text{in } \Lambda, \\ u^v = g_D^v, & \text{on } \partial\Lambda. \end{array} \right. \quad (6.1)$$

The variable u^t stands for u_{red}^t from (S2), where we drop the index “red” for better readability. The function $g_{\text{D}}^v \in H^{1/2}(\partial\Lambda)$ represents a Dirichlet boundary condition for the network for which an extension to the entire network is denoted by $\widetilde{g}_{\text{D}}^v \in H^1(\Lambda)$. For simplicity, we assume homogeneous boundary conditions for the three-dimensional equation and the permeability L_{p} of the vessel wall is assumed to be constant for all branches of the network.

Consistently with the numerical discretization method from Section 5, the solution of (6.1) is computed using a primal FEM approximation instead of, e.g., a mixed formulation as in our previous work [139, Section 7]. The usage of a mixed type model is motivated by the need of having a locally conservative velocity field, which is not guaranteed by the primal FEM approximation. In this section, the focus is posed on the algorithmic aspects that one has to consider when solving numerically the 3D-1D coupled problem (6.1), and it is clear that the discussions conducted in this section can be adapted for other numerical methods.

The coupling strategy (S2) requires, among others, the computation of the average (3.12) along a circle perpendicular to the branch Λ_i . In order to have the entire manifold Γ contained in the three-dimensional domain, we assume analogously to (5.1) that the distance between Λ and the boundary $\partial\Omega$ is sufficiently large for computing the average, i.e., $\text{dist}(\Lambda_i, \partial\Omega) > \max_i R_i$ for each branch Λ_i .

Let us define the space $V := H_0^1(\Omega) \times H_0^1(\Lambda)$. The weak formulation of problem (6.1) reads now: Find $\mathbf{u} = (u^t, u^v)$ such that $(u^t, u^v - \widetilde{g}_{\text{D}}^v) \in V$ and

$$a(\mathbf{u}, \mathbf{v}) = 0, \quad \forall \mathbf{v} = (v^t, v^v) \in V, \quad (6.2)$$

where

$$\begin{aligned} a(\mathbf{u}, \mathbf{v}) := & \int_{\Omega} \frac{\mathbf{K}_t}{\mu_{\text{int}}} \nabla u^t \cdot \nabla v^t + \int_{\Lambda} \pi R^2 \frac{\mathbf{K}_v}{\mu_{\text{bl}}} \cdot \frac{du^v}{ds} \cdot \frac{dv^v}{ds} \\ & + L_{\text{p}} \sum_{i=1}^N 2\pi R_i \int_{\Lambda_i} \overline{u^t}(\mathbf{x}_i) \cdot \overline{v^t}(\mathbf{x}_i) ds_i \\ & - L_{\text{p}} \sum_{i=1}^N 2\pi R_i \int_{\Lambda_i} u^v(s_i) \cdot \overline{v^t}(\mathbf{x}_i) ds_i \\ & + L_{\text{p}} \sum_{i=1}^N 2\pi R_i \int_{\Lambda_i} (u^v(s_i) - \overline{u^t}(\mathbf{x}_i)) \cdot v^v(s_i) ds_i. \end{aligned} \quad (6.3)$$

We recall that \mathbf{x}_i is such that $\mathbf{x}_i = \Lambda_i(s_i)$ for a $i = 1, \dots, N$ according to definition (3.6). Employing a standard FEM discretization for problem (6.2), we can notice that the first two integrals in (6.3) are calculated as usual, while all remaining terms require some extra care, as we describe in the following.

First, let us consider a conforming quasi-uniform subdivisions $\mathcal{T}_H(\Omega)$ of Ω and $\mathcal{T}_h(\Lambda)$ of Λ . We point out that the meshsizes h and H can be chosen independently from each other. In other works, e.g., [65], it is assumed that the segments of the one-dimensional network coincide with the edges of three-dimensional elements, which lead to clear advantages in the implementation. To keep the setting as general as possible, we require no particular connections between the triangulation $\mathcal{T}_H(\Omega)$ and

the subdivision $\mathcal{T}_h(\Lambda)$. To approximate the solution, we use piecewise linear FEM for both subproblems, i.e., we search the solution in the space $V_{H,h} \subset V$, defined as

$$V_{H,h} := \left\{ (v, w) \in V : v|_T \in \mathbb{P}^1(T) \text{ and } w|_I \in \mathbb{P}^1(I), \forall T \in \mathcal{T}_H(\Omega) \text{ and } I \in \mathcal{T}_h(\Lambda) \right\}.$$

Let us denote by $\widetilde{g_{D,h}^v}$ an interpolant of the function $\widetilde{g_D^v}$. Then, the FEM solution $\mathbf{u}_{H,h} = (u_{H,h}^t, u_{h,h}^v)$ satisfies the following discrete weak problem: Find $\mathbf{u}_{H,h}$ such that $(u_{H,h}^t, u_{h,h}^v - \widetilde{g_{D,h}^v}) \in V_{H,h}$ and

$$a(\mathbf{u}_{H,h}, \mathbf{v}_{H,h}) = 0, \quad \forall \mathbf{v}_{H,h} = (v_H^t, v_h^v) \in V_{H,h}. \quad (6.4)$$

Let us denote by

$$\mathbf{u}^t := (u_1^t, \dots, u_{N_H}^t) \quad \text{and} \quad \mathbf{u}^v := (u_1^v, \dots, u_{N_h}^v)$$

the components of the approximated solutions with respect to the standard Lagrangian finite element basis functions $\{\varphi_k^t\}_k$ and $\{\varphi_k^v\}_k$. Then, equation (6.4) yields a linear system that reads

$$\begin{pmatrix} \mathbf{A} & \mathbf{B} \\ \mathbf{C} & \mathbf{D} \end{pmatrix} \begin{pmatrix} \mathbf{u}^t \\ \mathbf{u}^v \end{pmatrix} = \begin{pmatrix} 0 \\ \mathbf{b}^v \end{pmatrix},$$

where each block is defined as follows

$$\begin{aligned} \mathbf{A}(k, j) &:= \int_{\Omega} \frac{\mathbf{K}_t}{\mu_{\text{int}}} \nabla \varphi_j^t \cdot \nabla \varphi_k^t \, d\mathbf{x} \\ &\quad + L_p \sum_{i=1}^N 2\pi R_i \int_{\Lambda_i} \overline{\varphi_j^t}(\mathbf{x}_i) \cdot \overline{\varphi_k^t}(\mathbf{x}_i) \, ds_i, \quad k, j = 1, \dots, N_H, \\ \mathbf{B}(k, j) &:= -L_p \sum_{i=1}^N 2\pi R_i \int_{\Lambda_i} \varphi_j^v(s_i) \cdot \overline{\varphi_k^t}(\mathbf{x}_i) \, ds_i, \quad k = 1, \dots, N_H, \\ &\quad j = 1, \dots, N_h, \\ \mathbf{C}(k, j) &:= -L_p \sum_{i=1}^N 2\pi R_i \int_{\Lambda_i} \overline{\varphi_j^t}(\mathbf{x}_i) \cdot \varphi_k^v(s_i) \, ds_i, \quad k = 1, \dots, N_h, \\ &\quad j = 1, \dots, N_H, \\ \mathbf{D}(k, j) &:= \int_{\Lambda} \pi R^2 \frac{\mathbf{K}_v}{\mu_{\text{bl}}} \cdot \frac{d\varphi_j^v}{ds} \cdot \frac{d\varphi_k^v}{ds} + L_p \sum_{i=1}^N 2\pi R_i \int_{\Lambda_i} \varphi_j^v \cdot \varphi_k^v \, ds_i, \quad k, j = 1, \dots, N_h. \end{aligned}$$

The load vector \mathbf{b}^v implements the boundary conditions for the network.

We now briefly describe the procedure we that is used to approximate the line integrals. First, along the centerline Λ_i , we employ an appropriate quadrature formula on the reference interval $[0, 1]$ with nodes ξ_m and weights ω_m for $m = 1, \dots, N_q$. With s_m we denote the curvilinear abscissa corresponding to the image of ξ_m by the

geometrical transformation that maps $[0, 1]$ on the element Λ_i . Then, considering, e.g., the entry (k, j) of the block \mathbf{C} , we can write

$$\int_{\Lambda_i} \overline{\varphi_j^t}(\mathbf{x}_i) \cdot \varphi_k^v(s_i) ds_i \approx \sum_{m=1}^{N_q} \varphi_k^v(s_m) \cdot \overline{\varphi_j^t}(\mathbf{x}_m) |J_m| \omega_m, \quad (6.5)$$

where $|J_m|$ is the absolute value of the determinant of the Jacobian of the transformation at ξ_m .

For the computation of $\overline{\varphi_j^t}(\mathbf{x}_m)$, we use a simple midpoint rule on the interval $[0, 1]$ with N_p -equidistant nodes ζ_t for $t = 1, \dots, N_p$, see Figure 6.1. Thus, the integral (6.5) becomes

$$\begin{aligned} \int_{\Lambda_i} \overline{\varphi_j^t}(\mathbf{x}_i) \cdot \varphi_k^v(s_i) ds_i &\approx \sum_{m=1}^{N_q} \varphi_k^v(s_m) |J_m| \omega_m \cdot \left(\frac{1}{2\pi} \int_0^{2\pi} \varphi_j^t(P(\mathbf{x}_m, R_i, \theta)) d\theta \right) \\ &\approx \sum_{m=1}^{N_q} \varphi_k^v(s_m) |J_m| \omega_m \cdot \left(\frac{1}{N_p} \sum_{t=1}^{N_p} \varphi_j^t(P(\mathbf{x}_m, R_i, 2\pi\zeta_t)) \right). \end{aligned}$$

The coordinates of the point $\mathbf{p}_t = P(\mathbf{x}_m, R_i, 2\pi\zeta_t)$ along the circle $\partial B(\mathbf{x}_i, R_i, \boldsymbol{\lambda}_i)$ in the three-dimensional domain are easy to compute, having the angle $2\pi\zeta_t$, the

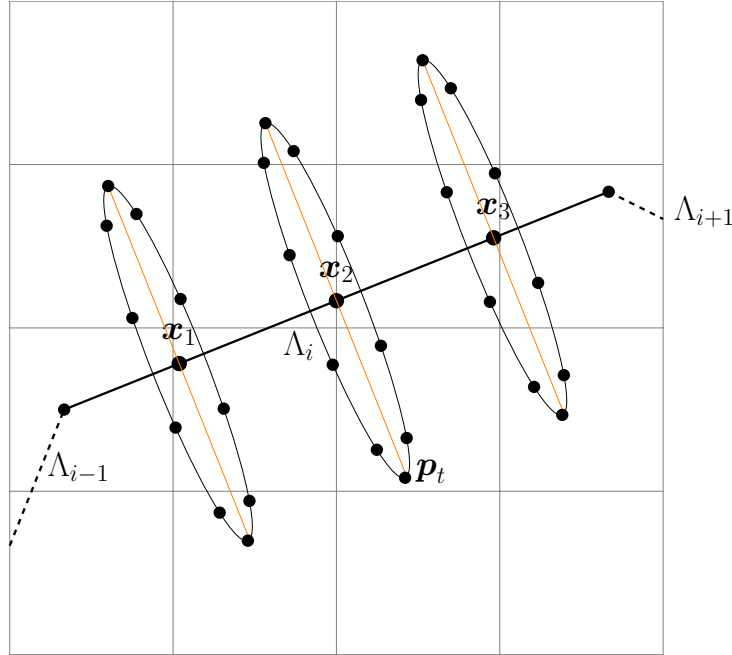


Figure 6.1.: Schematic representation of the average computation for the segment Λ_i . Around the quadrature points \mathbf{x}_1 , \mathbf{x}_2 and \mathbf{x}_3 , the corresponding circles with radius R_i are drawn, together with the quadrature points \mathbf{p}_t along them. No alignment of the segments with the three-dimensional mesh is required.

tangent unit vector $\boldsymbol{\lambda}_i = (\lambda_{i,x}, \lambda_{i,y}, \lambda_{i,z})$ as in (3.5), the radius R_i and the center \boldsymbol{x}_m of the circle. In fact, denoting by $c := \cos(2\pi\zeta_t)$ and by $s := \sin(2\pi\zeta_t)$, we have

$$\boldsymbol{p}_t = P(\boldsymbol{x}_m, R_i, 2\pi\zeta_t) := \boldsymbol{x}_m + R_i \cdot \boldsymbol{R} \cdot \boldsymbol{r},$$

where $\boldsymbol{r} := (\lambda_{i,z}, 0, -\lambda_{i,x})$ and

$$\boldsymbol{R} := \begin{pmatrix} \lambda_{i,x}^2(1-c) + c & \lambda_{i,x}\lambda_{i,y}(1-c) - \lambda_{i,z}s & \lambda_{i,x}\lambda_{i,z}(1-c) + \lambda_{i,y}s \\ \lambda_{i,x}\lambda_{i,y}(1-c) + \lambda_{i,z}s & \lambda_{i,y}^2(1-c) + c & \lambda_{i,y}\lambda_{i,z}(1-c) - \lambda_{i,x}s \\ \lambda_{i,x}\lambda_{i,z}(1-c) - \lambda_{i,y}s & \lambda_{i,y}\lambda_{i,z}(1-c) + \lambda_{i,x}s & \lambda_{i,z}^2(1-c) + c \end{pmatrix}.$$

More effort has to be invested in finding, possibly in a fast way, the three-dimensional element T in the mesh $\mathcal{T}_H(\Omega)$ that contains \boldsymbol{p}_t . As mentioned in [65, Section 5], it is crucial for the overall speed of the method to have a fast algorithm that allows for a quick finding of an element, in particular if a complex network as the one depicted in Figure 6.3 is considered. In order to simplify the computations, the author in [65] projected each segment Λ_i of the network on an edge of a three-dimensional element. Furthermore, a lumped strategy for the average was employed, where the radius of the inclusion was assumed to be much smaller than the meshsize, so that it was immediate to evaluate the basis function for the element T at the quadrature point. In this work, we do not make any of these assumptions, instead we allow the network to be general, not aligned with the edges of the three-dimensional mesh and with arbitrary radius. To quickly find the element T containing \boldsymbol{p}_t , we use an axis-aligned bounding box volume hierarchy for the module dune-grid [18, 19], originally developed for the Dumux-Framework [90], and based on an AABB tree implementation from [154].

Considering the block matrix \boldsymbol{A} , the computation of the integral

$$\int_{\Lambda_i} \overline{\varphi_j^t}(\boldsymbol{x}_i) \cdot \overline{\varphi_k^t}(\boldsymbol{x}_i) ds_i \quad (6.6)$$

requires some further care, because one has to accurately multiply the average of each non-vanishing basis function φ_k^t on the circle $\partial B(\boldsymbol{x}_i, R_i, \boldsymbol{\lambda}_i)$ with the average of all the other basis functions which do not vanish along the same circle. A possible way to implement this integral consists in creating first a list $\{k_1, \dots, k_n\}$ of indices of all the basis functions φ_k^t that do not vanish on the circle, that is, for which $\varphi_k^t(\boldsymbol{p}_t) \neq 0$ for at least one $t \in \{1, \dots, N_p\}$. Then, the integral (6.6) can be approximated by

$$\int_{\Lambda_i} \overline{\varphi_k^t}(\boldsymbol{x}_i) \cdot \overline{\varphi_j^t}(\boldsymbol{x}_i) ds_i \approx \sum_{m=1}^{N_q} |J_m| \omega_m \cdot \left(\frac{1}{N_p} \sum_{t=1}^{N_p} \varphi_k^t(P(\boldsymbol{x}_m, R_i, 2\pi\zeta_t)) \right) \left(\frac{1}{N_p} \sum_{t=1}^{N_p} \varphi_j^t(P(\boldsymbol{x}_m, R_i, 2\pi\zeta_t)) \right)$$

for all $k, j \in \{k_1, \dots, k_n\}$.

6.2. Convergence test

To validate the numerical discretization, we conduct in this section an experiment in the case where an analytical solution for the 3D-1D coupled problem (6.1) is available. To this end, we consider a simple geometry, where the computational domain is given by $\Omega := (0, 1)^3 \subset \mathbb{R}^3$. A single branch Λ of radius $R = 0.15$ and parallel to the third axis crosses the entire domain, i.e., the curvilinear abscissa s of Λ coincides with the coordinate z of the point. Thus, the parametric equation for the line is given by

$$\Lambda: [0, 1] \rightarrow \bar{\Omega}, \quad \Lambda(s) := \left(\frac{1}{2}, \frac{1}{2}, s \right).$$

We denote by u^t the pressure in Ω and by u^v the pressure in Λ . Then, the model problem reads

$$\left\{ \begin{array}{ll} -\Delta u^t + \beta (\bar{u}^t - u^v) \delta_\Gamma = 0, & \text{in } \Omega, \\ -\frac{d}{ds} \left(\mathbf{K}_v \frac{du^v}{ds} \right) + \beta (u^v - \bar{u}^t) = 0, & \text{in } \Lambda, \\ u^t = g_D^t, & \text{on } \partial\Omega, \\ u^v = g_D^v, & \text{on } \partial\Lambda, \end{array} \right. \quad (6.7)$$

with $\beta = 0.1$. The permeability of the one-dimensional medium is given by

$$\mathbf{K}_v(s) := \frac{\beta}{1 + \beta} \left(1 + s + \frac{1}{2}s^2 \right).$$

For the one-dimensional equation, the Dirichlet boundary conditions $g_D^v(0) = 1$ and $g_D^v(1) = 2$ are set. For the three-dimensional problem, the boundary condition $g_D^t \in H^{1/2}(\partial\Omega)$ is defined such that the exact solution u_e^t is given by

$$u_e^t(\mathbf{x}) := \begin{cases} (1+z) \frac{\beta}{1+\beta} \left(1 - R \ln \left(\frac{\tilde{r}(\mathbf{x})}{R} \right) \right), & \tilde{r}(\mathbf{x}) > R, \\ (1+z) \frac{\beta}{1+\beta}, & \tilde{r}(\mathbf{x}) \leq R, \end{cases}$$

where $\tilde{r}(\mathbf{x}) = |\mathbf{x} - \Lambda(z)|$. Thus, the analytical one-dimensional solution is given by

$$u_e^v(s) := 1 + s.$$

It is easy to check that the pair (u_e^t, u_e^v) is the exact solution of problem (6.7). In fact, given the definition (3.12) of the mean value, we have $\bar{u}_e^t(\mathbf{x}) = \frac{\beta}{1+\beta} (1+z)$, so that $\beta u^v(s) - \beta \bar{u}_e^t(\mathbf{x}) = \frac{\beta}{1+\beta} (1+s) = f(s)$, where f is such that $-\Delta u^t + f \delta_\Gamma = 0$ in the sense of distributions and

$$\frac{d}{ds} \left(-\mathbf{K}_v \frac{du^v}{ds} \right) - f = 0.$$

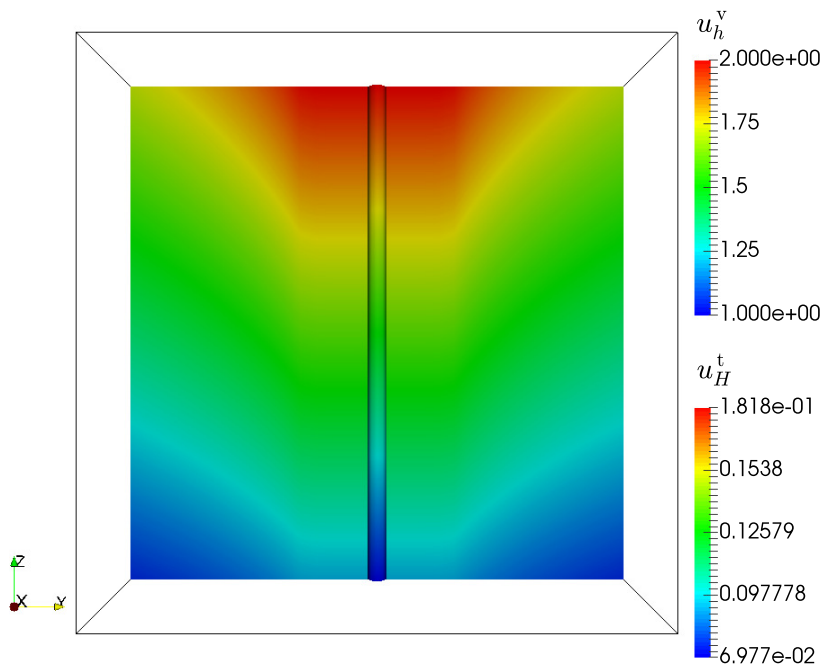


Figure 6.2.: Slice in the x -direction of the numerical solution of problem (6.7) on the finest mesh. The tube corresponding to the line Λ is depicted with a smaller radius that 0.15 for graphical reasons, so that the plateau of the solution u_H^t corresponding to each height z can easily be recognized.

The linear FEM discretization described in Section 6.1 is employed to compute the numerical solution. In this simple case, the meshsizes of the subdivisions $\mathcal{T}_H(\Omega)$ and $\mathcal{T}_h(\Lambda)$ coincide and have been defined as $H = h = 2^{-\ell}$ for $\ell = 3, \dots, 6$. The numerical solution on the finest mesh is depicted in Figure 6.2, where the plateau can be easily recognized for each z -value, which is consistent with the results reported in Section 5.5. For the error, we compute both the three-dimensional and one-dimensional components as follows

$$e_h^v := u_e^v - u_h^v. \quad \text{and} \quad e_H^t := u_e^t - u_H^t$$

The numerical convergence rates with respect to the meshsizes are reported in Table 6.1. We can observe that the numerical solution on the line converges with first order, while the three-dimensional solution appears to converge with an order slightly larger than 1. Moreover, we can observe that the numerical order of convergence of the three-dimensional solution is comparable with the theoretical results obtained in Section 5.4, where a two-dimensional, yet uncoupled, problem with source term concentrated on lines is studied and a convergence rate of 1 is proven. A theoretical investigation of these results will be subject of future work.

Table 6.1.: L^2 -norm of the errors e_h^v and e_H^t for the 3D-1D coupled problem (6.7).

ℓ	$\ e_h^v\ _{L^2(\Lambda)}$	Rate	$\ e_H^t\ _{L^2(\Omega)}$	Rate
3	$1.1168e - 04$	/	$3.9174e - 04$	/
4	$7.4630e - 05$	0.58	$1.8146e - 04$	1.11
5	$4.0659e - 05$	0.88	$6.9803e - 05$	1.38
6	$1.9848e - 05$	1.03	$2.7140e - 05$	1.36

6.3. A problem with application to microcirculation

In this section, we present a prototype model for stationary flow in biological tissue supplied by a network of capillaries. The experiment is set to show the flexibility of the coupling strategy (S2) and represents an idealized application. To this end, the coupling strategy is used to solve a 3D-1D coupled problem, where the network is obtained from [199], see Figure 6.3. In particular, it represents a portion of a rat cerebral cortex and consists of a relatively small set of microvessels¹. Employing this network instead of the larger one depicted in Figure II.1 has the only scope to reduce the computational complexity of the 3D-1D coupled problem, while still considering most of the features, as we describe in the following.

The discrete version Λ of the structure consists of $N = 50$ segments, see Figure 6.3, where multiple bifurcations are present and different radii are assigned to each branch, varying in a range from $2.5 \mu\text{m}$ to $4.5 \mu\text{m}$. We assume that each vessel is permeable, i.e., $I_C = \{1, \dots, N\}$. For the three-dimensional problem, the domain Ω surrounding Λ is taken as the cuboid

$$\Omega := \left\{ \mathbf{x} \in \mathbb{R}^3 : \begin{aligned} & -4.5 < x < 154.5 \text{ } [\mu\text{m}] \wedge -4.5 < y < 164.5 \text{ } [\mu\text{m}] \\ & \wedge 6.1 < z < 144.5 \text{ } [\mu\text{m}] \end{aligned} \right\}.$$

The 3D-1D coupled problem considered for this test now reads

$$\left\{ \begin{array}{ll} -\nabla \cdot \left(\frac{\mathbf{K}_t}{\mu_{\text{int}}} \nabla u^t \right) = L_p \sum_{i=1}^N (u^v - \bar{u}^t) \delta_{\Gamma_i}, & \text{in } \Omega, \\ \nabla u^t \cdot \mathbf{n} = 0, & \text{on } \partial\Omega, \\ -\frac{d}{ds} \left(\pi R^2 \frac{\mathbf{K}_v}{\mu_{\text{bl}}} \cdot \frac{du^v}{ds} \right) = L_p \sum_{i=1}^N 2\pi R_i (\bar{u}^t - u^v), & \text{in } \Lambda, \\ u^v = g_D^v, & \text{on } \partial\Lambda. \end{array} \right. \quad (6.8)$$

On the boundary $\partial\Omega$, no-flow conditions are posed for simplicity. However, other type of boundary conditions can easily be considered. On the boundary points of

¹The network is available at <https://physiology.arizona.edu/people/secomb/network/brain99>. Website retrieved on November 26, 2018

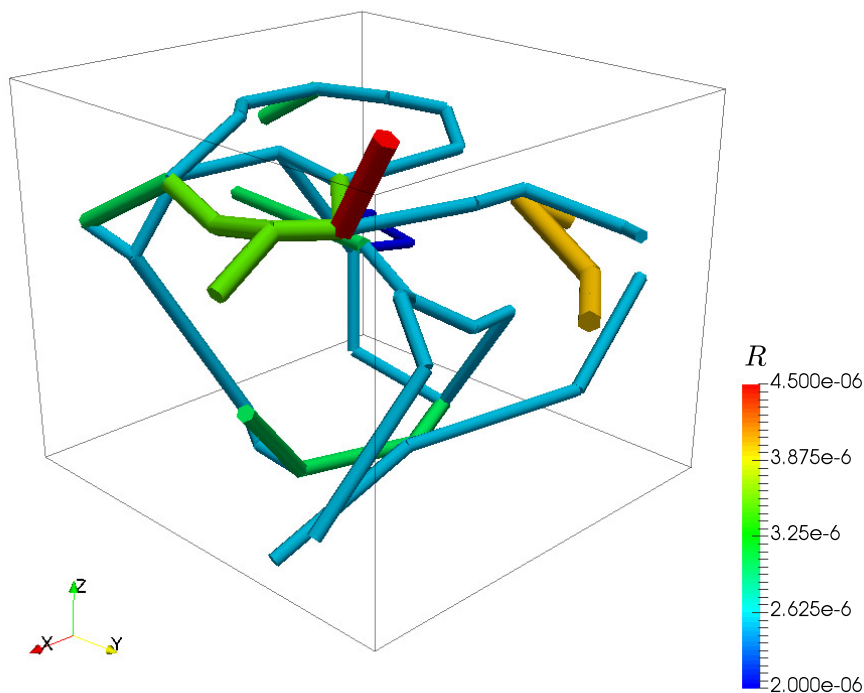


Figure 6.3.: Discrete network structure Γ from [199] used for the simulations in this section.

the network, fixed pressure values are provided and reported in Table 6.2, where the high and low pressure values have been taken in a suitable range accordingly to [124, Table 2]. The permeability \mathbf{K}_v is given as in (3.11), while the parameter $L_p = 10^{-10}$ [m/(Pa · s)] of the walls is chosen constant for each branch and is typical of tumoral tissues [66]. The permeability of the tissue is set to $\mathbf{K}_t = 10^{-18} \cdot \mathbf{I}$ [m²] and the viscosity of the interstitial fluid to $\mu_{\text{int}} = 1.3 \cdot 10^{-3}$ [Pa · s], while the viscosity of the blood has been chosen accordingly to the *in vivo* formula (3.2) for $\mu_p = 10^{-3}$ [Pa · s] and a discharge hematocrit of $H = 0.45$. Experimental values for these parameters are not provided in the original work [199] and if more realistic data become available they can easily be updated.

An analytical solution is not available, thus to validate numerically our solution we proceed as in Section 4.2 and calculate a reference solution $(u_{\text{fine}}^t, u_{\text{fine}}^v)$ on a fine mesh. To this end, we subdivide the domain Ω in $32 \times 32 \times 32$ hexahedral elements, while the original network depicted in Figure 6.3 is refined five times uniformly for a total of 1600 segments. The numerical solutions u_{fine}^t and u_{fine}^v are depicted in Figure 6.4, where we can observe the ability of our method to handle the quite complex configuration under consideration. As a consequence of the boundary

Table 6.2.: Positions and corresponding pressure values for the boundary nodes in the network from [199].

x [mm]	y [mm]	z [mm]	g_D^v [mmHg]
0.105	0.119	0.14	25
0	0.108	0.087	20
0.055	0.16	0.079	25
0.15	0.092	0.095	20
0.15	0.104	0.06	20
0.0655	0	0.0865	20
0.052	0	0.113	20
0.15	0.134	0.029	25
0.03	0.16	0.1014	20
0	0.14	0.074	20
0.15	0.115	0.013	25
0	0.006	0.064	20

conditions on the network, the solution u_{fine}^v is expected to vary along Λ , as shown in Figure 6.4, on the left, while the solution u_{fine}^t in Ω behaves correspondingly as the solution of a Poisson equation with a constant concentrated source distributed on Γ . Furthermore, the solution in the tissue is bounded by the maximal and minimal values of pressure in the network, as expected.

We now proceed with the determination of the FEM discrete errors. The numerical solutions (u_H^t, u_h^v) obtained on coarser meshes are compared to the reference solution

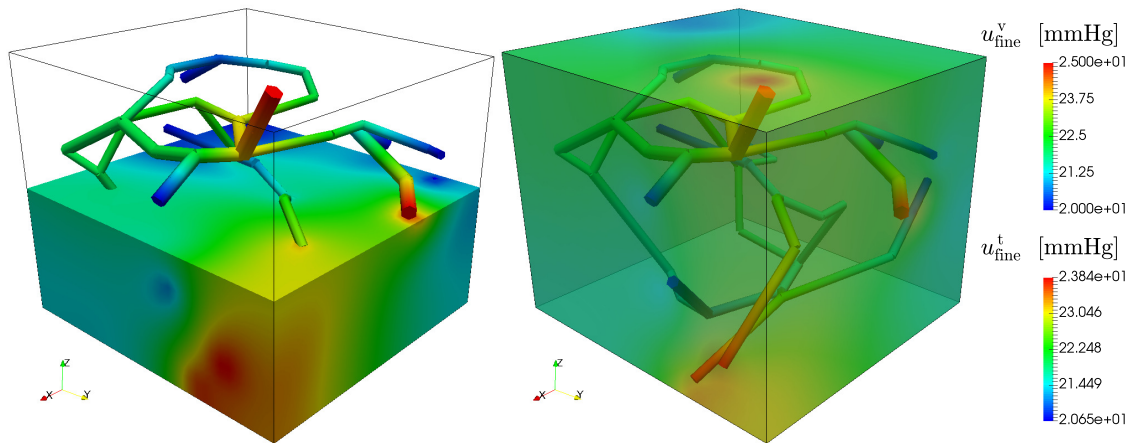


Figure 6.4.: Numerical solution of problem (6.8). On the left, a slice in the z -axis of the numerical solution is depicted. The solution in the tissue appears to behave in accordance to the solution in the network.

Table 6.3.: Discrete L^2 -norm of the errors in the network and in the tissue for the 3D-1D coupled problem (6.8).

ℓ	$\ u_{\text{fine}}^v - u_h^v\ _{L^2(\Lambda)}$	Rate	$\ u_{\text{fine}}^t - u_H^t\ _{L^2(\Omega)}$	Rate
0	$3.3297e - 03$	/	$6.4291e - 05$	/
1	$3.2708e - 03$	0.03	$4.6778e - 05$	0.46
2	$2.5721e - 03$	0.35	$3.3001e - 05$	0.50
3	$1.2026e - 03$	1.10	$1.7539e - 05$	0.91
4	$5.8610e - 04$	1.04	$6.8170e - 06$	1.36

$(u_{\text{fine}}^t, u_{\text{fine}}^v)$. Using the same refinement strategy described above, we denote by ℓ the refinement level of the domain Ω and of the network Λ for $\ell = 0, \dots, 4$, such that the tissue is subdivided by 2^ℓ -elements in each direction, while the original network is uniformly refined ℓ -times. In Table 6.3, the discrete L^2 -errors are reported, together with the numerical convergence rates with respect to the mesh refinement ℓ . If confronted with the previous test from Section 6.2, a similar behaviour of the numerical rates of convergence can be observed for both approximated solutions.

Finally, we report in Figure 6.5 the plasma fluid paths starting, for visualization purposes, from the diagonal passing through the points $(-4.5, -4.5, 6.1) - (154.5, 164.5, 144.5)$, where each coordinate is expressed in μm . In particular, the filtration through the tissue from capillaries with higher pressure towards capillary in low-pressure regions can be clearly seen. A validation of the numerical results by means of experimental data will be subject of a future work.

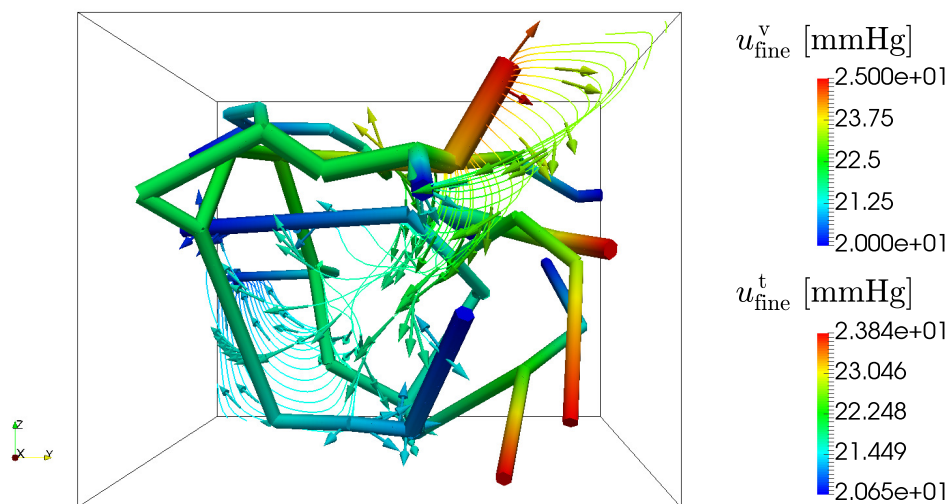


Figure 6.5.: Plasma fluid paths from high-pressure capillaries to low-pressure capillaries through the interstitial space for the 3D-1D coupled problem (6.8).

7. Hybrid models for simulating blood flow in microvascular networks

Please note that the considerations presented in this section are partially taken from a publication by the author [219]:

E. Vidotto , T. Koch, T. Köppl, R. Helmig and B. Wohlmuth
Hybrid models for simulating blood flow in microvascular networks
<https://arxiv.org/abs/1811.10373>, 2018.

In this section we simulate the microcirculation flow in the network depicted in Figure II.1 by means of the 3D-1D coupled model (3.17). However, when considering a larger portion of tissue than the one depicted in Figure II.1, this approach reveals to be too invasive, since no *in vivo* techniques are available to obtain a detailed description of microvascular networks, and also computationally too expensive, because every single capillary needs to be coupled with the surrounding tissue. The total number of capillaries is extremely large on the organ scale and therefore the coupling strategy may become unfeasible. Thus, we present an *hybrid model* based on homogenization that allows us to reduce the computational costs at the expense of some accuracy. The approach we follow yields a so-called *3D-3D-1D coupled model*, where the larger arterioles and venules are still considered as one-dimensional entities and the surrounding tissue as a three-dimensional porous medium, as in the 3D-1D coupled model. However, the capillaries are homogenized and treated as a three-dimensional porous medium as well. As we can observe in Figure 7.1, the set of capillaries constitutes a quite dense network in the portion of tissue under consideration, and therefore we consider it as a porous medium, where capillaries represent an interconnected network of pores embedded in the surrounding tissue. By leaving the larger vessels as one-dimensional networks, we maintain the main geometry and orientation of the system, and, using an homogenized 3D-3D model for the capillaries and the tissue, a less complex model has to be solved, since no singular terms occur and the properties of the microvascular network have to be available only in an averaged sense. Compared to other works investigating upscaling strategies for microvascular systems [77, 182], we include in our model the interactions of the homogenized capillaries with the surrounding tissue [81] and we discuss alternative coupling conditions between the one-dimensional vessels and the three-dimensional continuum for the capillaries.

The notation used for this section is the same as in Section 3 and is briefly summarized in the following. The cuboid containing the microvascular network depicted in Figure 7.1 is denoted by Ω and is given by

$$\Omega := \left\{ \mathbf{x} \in \mathbb{R}^3 : 0 < x, y < 1.13662 \text{ [mm]} \wedge 8.75 \cdot 10^{-7} < z < 2.16388 \text{ [mm]} \right\}.$$

To obtain a more realistic setting, we include in Starling's filtration law (3.19) the oncotic pressures π_p and π_{int} of the plasma and of the interstitial fluid, respectively.

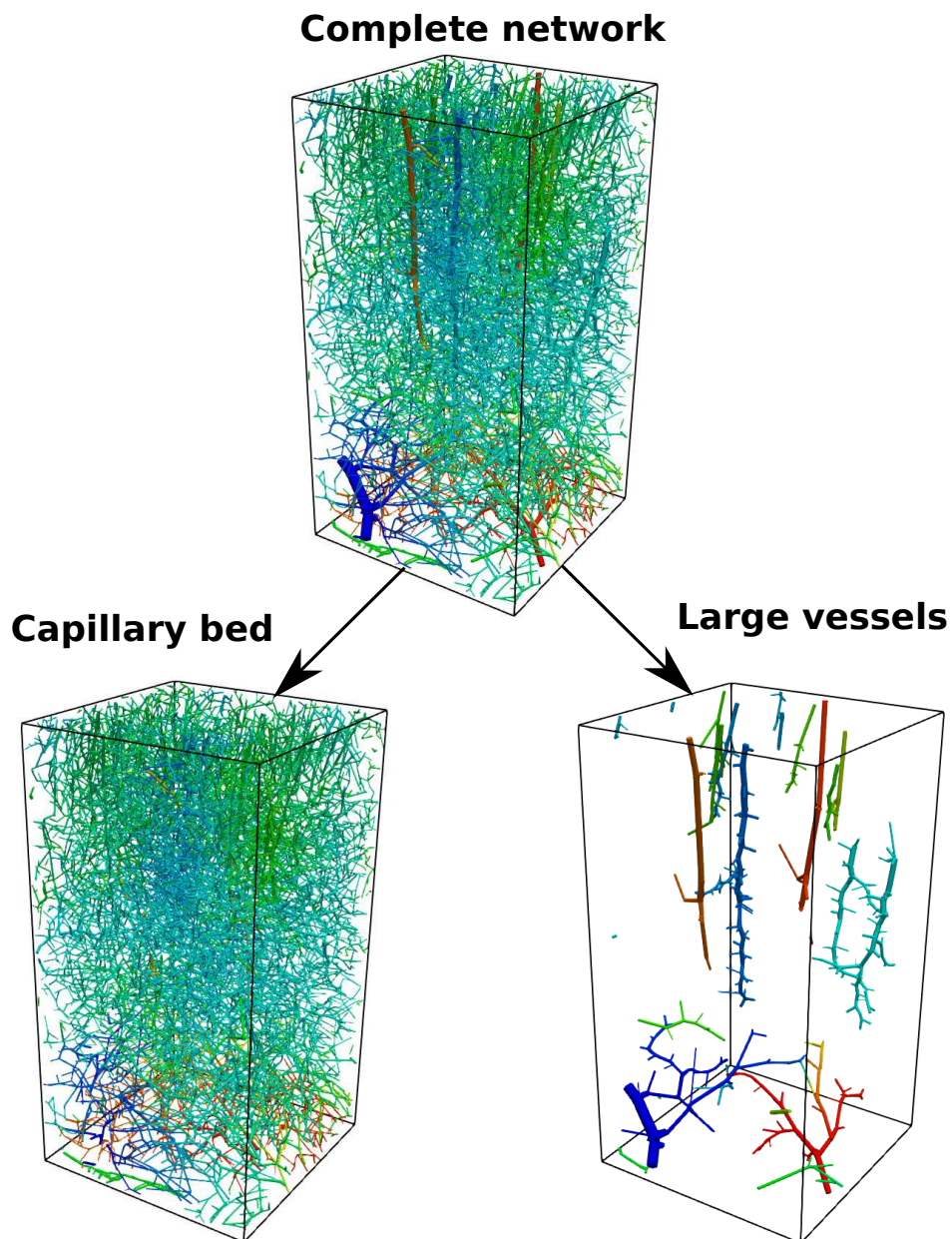


Figure 7.1.: On the top, the microvascular network from Figure II.1 is reported. A subdivision based on the vessel radius can be seen at the bottom of the figure. The network at the bottom left consists of the network Λ_C of capillaries contained in the microvascular network, whose radius is smaller than a given threshold R_T , here $7 [\mu\text{m}]$. The motivation for such threshold is postponed to Section 7.3.1. At the bottom right, the set Λ_L of arterioles and venules is reported.

Moreover, the density ρ_{bl} of the blood and ρ_{int} of the interstitial fluid are considered as well. All in all, the model problem for this section reads

$$\left\{ \begin{array}{ll} -\nabla \cdot \left(\rho_{\text{int}} \frac{\mathbf{K}_t}{\mu_{\text{int}}} \nabla u^t \right) = \rho_{\text{int}} L_p \sum_{i \in I_C} (u^v - \bar{u}^t + \pi_p - \pi_{\text{int}}) \delta_{\Gamma_i}, & \text{in } \Omega, \\ -\frac{d}{ds} \left(\rho_{\text{bl}} \pi R^2 \frac{\mathbf{K}_v}{\mu_{\text{bl}}} \cdot \frac{du^v}{ds} \right) = \rho_{\text{int}} L_p \sum_{i \in I_C} 2\pi R_i (\bar{u}^t - u^v - \pi_p + \pi_{\text{int}}), & \text{in } \Lambda, \\ \rho_{\text{int}} \frac{\mathbf{K}_t}{\mu_{\text{int}}} \nabla u^t \cdot \mathbf{n} = 0, & \text{on } \partial\Omega, \\ u^v = g_D^v, & \text{on } \partial\Lambda. \end{array} \right. \quad (7.1)$$

The numerical solution of the 3D-1D coupled problem (7.1) will be used as reference to validate our hybrid model. The set I_C denotes the set of capillaries defined as in (3.8), and δ_{Γ_i} stands for the Dirac measure concentrated on the lateral surface of the vessel Λ_i as defined in (3.18). The variable u^v denotes the pressure in the network, while u^t the pressure in the tissue, for which we dropped the index ‘‘red’’ from Section 3.2. The average term \bar{u}^t is defined as in (3.12) and L_p denotes the hydraulic conductivity of the membrane of the capillaries and, for simplicity, is assumed to be constant for all segments. The viscosity of the interstitial fluid μ_{int} is assumed to be constant as well, while the viscosity μ_{bl} of the blood is given by the *in vivo* formula (3.2). The permeability \mathbf{K}_v of the vessel is defined as in (3.11), while \mathbf{K}_t denotes the permeability of the tissue and is assumed to be homogeneous and isotropic, that is $\mathbf{K}_t = k_t \cdot \mathbf{I}$ for $k_t > 0$. The boundary condition g_D^v for the network is obtained directly from the data set of the network depicted in Figure II.1, while on the boundary of the tissue continuum homogeneous Neumann boundary conditions are set for lack of experimental data. If measurements should become available, other boundary conditions can easily be considered.

The rest of the section is structured as follows. In Section 7.1, we thoroughly describe our hybrid approach and pose particular attention on the homogenization strategy of the capillaries. The numerical discretizations of both the hybrid and 3D-1D coupled models are outlined in Section 7.2, while in Section 7.3, the flow is simulated in the given portion of the rat’s brain using both methods. Several discussions of the results in terms of fluxes and averaged pressures are reported.

7.1. An hybrid 3D-3D-1D model

As mentioned above, the network of capillaries is considered in this model as an homogenized porous medium. Thus, similarly as for the tissue, the flow in this new system can be described by Darcy’s law, that is

$$\left\{ \begin{array}{ll} -\nabla \cdot \left(\frac{\mathbf{K}_{\text{up}}}{\mu_{\text{bl}}} \nabla u^{\text{cap}} \right) = f^{\text{cap}}, & \text{in } \Omega, \\ u^{\text{cap}} = g_D^{\text{cap}}, & \text{on } \partial\Omega, \end{array} \right. \quad (7.2)$$

where u^{cap} denotes the pressure in the homogenized system, \mathbf{K}_{up} is a permeability tensor, $\mu_{\text{bl}}^{\text{up}}$ an averaged viscosity, f^{cap} a source term, and $g_{\text{D}}^{\text{cap}}$ a Dirichlet boundary condition. These terms are systematically described in the following.

The consequence of having an homogenized system is that the quantities under consideration, such as the hydraulic conductivity \mathbf{K}_{up} , have to be interpreted in an averaged sense. To this end, we need to assume that the domain Ω can be decomposed into *representative elementary volumes* (REVs) [110], that is

$$\bar{\Omega} = \bigcup_{j=1}^{N_{\text{REV}}} \overline{\text{REV}_j}, \quad (7.3)$$

where N_{REV} is the total number of rectangular cuboid REVs, as depicted in Figure 7.2. According to the theory of porous media [25, 110], the parameter \mathbf{K}_{up} in (7.2) is assumed to be constant on the REV scale. An open issue in this context consists in the determination of the REV-size such that the values of \mathbf{K}_{up} are actually representative of the homogenized system. We address this problematic in Section 7.3.2, where a suitable size of the REV is investigated numerically for the network under consideration. For the rest of the section, it is sufficient to assume that at least one REV exists.

Having the subdivision into REVs at hand, we denote by $I_{C,j}$ the set of indices of capillaries contained in the REV_j , that is, for each $j = 1, \dots, N_{\text{REV}}$ we define

$$I_{C,j} := \{i \in I_C \mid \Lambda_i \cap \text{REV}_j \neq \emptyset\}.$$

To this index set, we denote the corresponding collection of capillaries contained in the REV_j by

$$\Lambda_{C,j} := \bigcup_{i \in I_{C,j}} \Lambda_i.$$

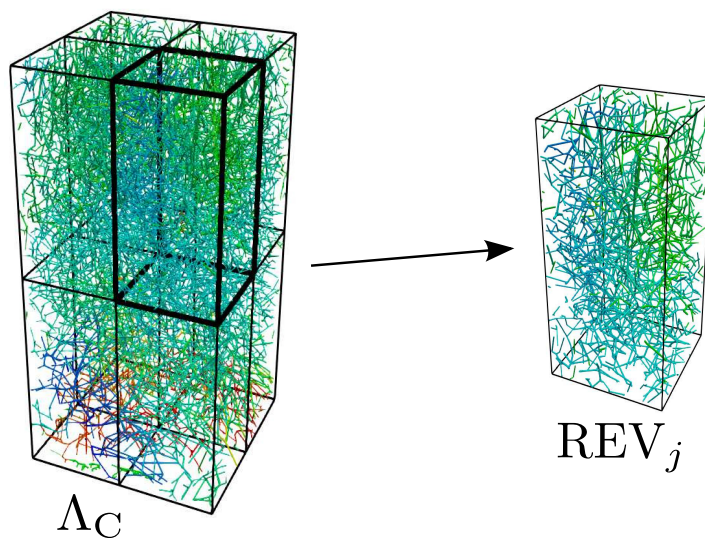


Figure 7.2.: Subdivision of the capillary bed Λ_C into eight REVs.

Viscosity

We define the viscosity $\mu_{\text{bl}}^{\text{up}}$ as a constant on each REV, that is we set

$$\mu_{\text{bl}}^{\text{up}}(\mathbf{x}) := \mu_{\text{bl},j}^{\text{up}}, \quad \text{if } \mathbf{x} \in \text{REV}_j.$$

More specifically, the viscosity in each REV is calculated as an average viscosity of all capillaries contained in the REV, that is

$$\mu_{\text{bl},j}^{\text{up}} := \frac{1}{|I_{C,j}|} \sum_{i \in I_{C,j}} \mu_{\text{bl}}(2R_i \cdot 10^6),$$

where μ_{bl} is given by (3.2).

Permeability tensor

The tensor \mathbf{K}_{up} represents the permeability of the homogenized capillaries, for which we assume the following properties:

- (i) The permeability tensor \mathbf{K}_{up} is constant on each REV_j , i.e.,

$$\mathbf{K}_{\text{up}}(\mathbf{x}) := \mathbf{K}_{\text{up}}^{(j)}, \quad \text{if } \mathbf{x} \in \text{REV}_j.$$

- (ii) The permeability tensor $\mathbf{K}_{\text{up}}^{(j)}$ is diagonal, that means we have

$$\mathbf{K}_{\text{up}}^{(j)} := \begin{pmatrix} k_x^{(j)} & 0 & 0 \\ 0 & k_y^{(j)} & 0 \\ 0 & 0 & k_z^{(j)} \end{pmatrix},$$

with $k_x^{(j)}, k_y^{(j)}, k_z^{(j)} > 0$.

Following the strategy presented in [78], one could neglect assumption (ii) and consider a full-tensor instead. However, in that paper the authors obtained non-symmetric tensors whose off-diagonal entries were found to be, on average, two orders of magnitude smaller than the diagonal terms. For these reasons, we neglect in this work the off-diagonal entries and consider only diagonal tensors. The advantages of having diagonal tensor are manifold. First, the tensor is symmetric and positive definite. Secondly, the \mathbf{K} -orthogonality property, described in Section 2.2.3, is fulfilled. Thus, the TPFA method can later be used for the numerical discretization.

To determine the components of the permeability tensor $\mathbf{K}_{\text{up}}^{(j)}$, we apply the upscaling strategy presented in [190], which we briefly describe in the following. For simplicity, we restrict the description to the computation of the permeability component $k_x^{(j)}$. The other components $k_y^{(j)}$ and $k_z^{(j)}$ can be computed analogously. Then the strategy reads:

1. On the network $\Lambda_{C,j}$, we apply no-flow boundary conditions to the boundary nodes $\partial\Lambda_{C,j}$ adjacent to the four facets of the REV_j whose normals are not aligned with the x -axis, as depicted in Figure 7.3.

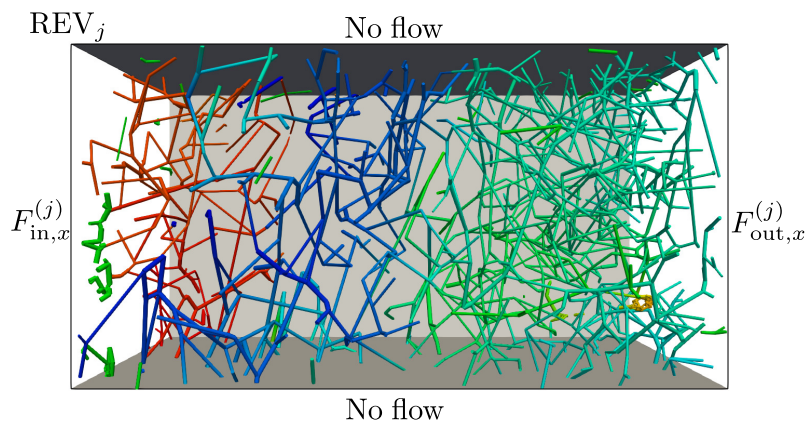


Figure 7.3.: Homogenization of a capillary network contained in a REV_j . On the facets $F_{in,x}^{(j)}$ and $F_{out,x}^{(j)}$ whose normals are aligned with the x -axis, we apply pressures $u_{in,x}$ and $u_{out,x}$, while on the other facets a no-flow condition is imposed. Having the value of the numerical flux between $F_{in,x}^{(j)}$ and $F_{out,x}^{(j)}$ at hand, the permeability component $k_x^{(j)}$ can be estimated.

2. The remaining two facets are denoted by $F_{in,x}^{(j)}$ and $F_{out,x}^{(j)}$, and represent an inflow and an outflow boundary, respectively. In particular we set the boundary pressure $u_{in,x}$ on the inflow boundary and $u_{out,x}$ on the outflow boundary, where $u_{in,x} > u_{out,x}$.
3. Having this setting at hand, we can use the numerical method described in Section 7.2 to determine the pressure field u^v in the reduced network $\Lambda_{C,j}$.
4. The volumetric flux $q_x^{(j)}$ through $F_{out,x}^{(j)}$ can now be computed as

$$q_x^{(j)} := \sum_{\mathbf{x}_i \in \Lambda_{C,j} \cap F_{out,x}^{(j)}} \frac{\pi R_i^4}{8\mu_{bl}} \cdot \frac{du^v}{ds}(s_i) \left[\text{m}^3/\text{s} \right],$$

where the point \mathbf{x}_i is such that $\mathbf{x}_i = \Lambda_i(s_i)$ for a $i \in I_{C,j}$, according to definition (3.6).

5. Based on the volumetric flux $q_x^{(j)}$, we set the permeability component $k_x^{(j)}$ to

$$k_x^{(j)} = \frac{q_x^{(j)} \cdot \mu_{bl,j}^{\text{up}} \cdot L_x^{(j)}}{|F_{out,x}^{(j)}| \cdot (u_{in,x} - u_{out,x})} \left[\text{m}^2 \right], \quad (7.4)$$

where $L_x^{(j)}$ is the edge length of REV_j in the x -direction.

Boundary conditions

For the computation of the boundary data g_D^{cap} , we consider an REV_j that is adjacent to the boundary $\partial\Omega$, i.e., $\overline{REV_j} \cap \partial\Omega \neq \emptyset$. The six faces of the REV_j are

denoted by F_{j1}, \dots, F_{jk} . For each face F_{jk} that is also on the boundary $\partial\Omega$, we compute an averaged boundary value $g_D^{(jk)}$. This is done by averaging all the pressure values $u^v(s_i)$ that are assigned to the boundary nodes $\mathbf{x}_i = \Lambda_i(s_i) \in \partial\Lambda_C$ and whose distance to the face F_{jk} is smaller than a parameter $\varepsilon_d > 0$, that is, $\text{dist}(F_{jk}, \mathbf{x}_i) < \varepsilon_d$, see Figure 7.4. For the rest of the section, we set $\varepsilon_d = 10^{-8}$ [m]. Assuming that N_{jk} nodes are fulfilling this condition, we compute the averaged pressure $g_D^{(jk)}$ by the arithmetic mean

$$g_D^{(jk)} := \frac{1}{N_{jk}} \sum_{i=1}^{N_{jk}} u^v(s_i).$$

In order to obtain a smooth function for the boundary values g_D^{cap} , we assign the pressure values $g_D^{(jk)}$ to the center of the faces F_{jk} and construct a linear interpolant on $\partial\Omega$ based on the described setup by means of the function `interpolate` from the package PDELab of Dune [35].

Source term

The source term f^{cap} in (7.2) consists of two components, one that accounts for the interaction of the homogenized capillaries with the larger vessels and one that incorporates the influence of the surrounding tissue. So, we define

$$f^{\text{cap}} := f_v^{\text{cap}} + f_t^{\text{cap}}.$$

Let us begin with the description of the component f_v^{cap} responsible for the mass transfer between the larger vessels Λ_L and the homogenized capillaries. Let \mathbf{x}_i be a node at the boundary of the subset Λ_L that is in the interior of the domain Ω , i.e., $\mathbf{x}_i \in \partial\Lambda_L \cap \Omega$. Therefore, we have that $\mathbf{x}_i = \Lambda_i(s_i) \in \Lambda_i \cap \text{REV}_j$ for an index $i \in I_L$ and an index $j \in \{1, \dots, N_{\text{REV}}\}$, where the set I_L is defined by (3.8). Then the mass flux occurring between the edge Λ_i and the capillary continuum is given by

$$\rho_{\text{bl}} \cdot \frac{\pi R_i^4}{8\mu_{\text{bl}}} \cdot \frac{du^v}{ds}(s_i) = \alpha_v^{\text{cap}}(\Lambda_i, \text{REV}_j) \left(u_{(j)}^{\text{cap}} - u^v(s_i) \right), \quad (7.5)$$

where the exchange factor α_v^{cap} is defined by

$$\alpha_v^{\text{cap}}(\Lambda_i, \text{REV}_j) := \rho_{\text{bl}} \cdot \frac{\pi R_i^2 K_v^{(j)}}{\mu_{\text{bl}}^{\text{up}} \ell_c^{(ij)}},$$

and the averaged pressure $u_{(j)}^{\text{cap}}$ of the REV_j is given by

$$u_{(j)}^{\text{cap}} := \frac{1}{|\text{REV}_j|} \int_{\text{REV}_j} u^{\text{cap}}(\mathbf{x}) \, d\mathbf{x}. \quad (7.6)$$

The coefficient $K_v^{(j)}$ represents the permeability of the capillaries connected to the coupling point \mathbf{x}_i , while the parameter $\ell_c^{(ij)}$ [m] indicates the average length of the

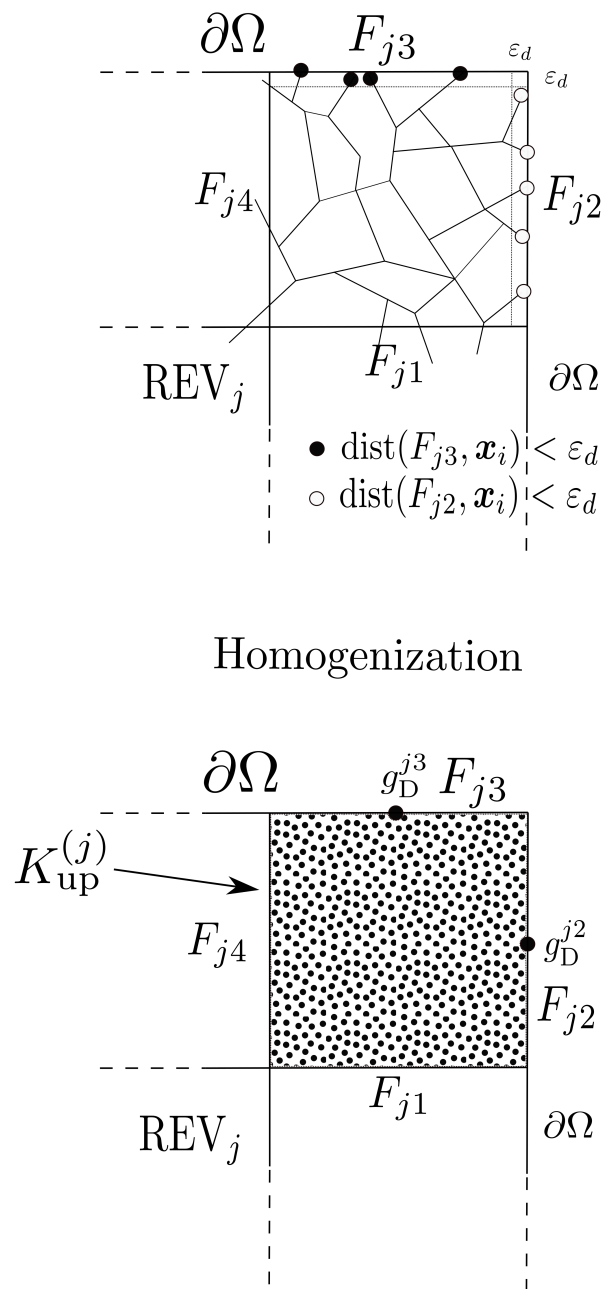


Figure 7.4.: The figure shows a two-dimensional layout parallel to the xy -plane of an REV_j that is located at an edge of the domain Ω . At the top of the figure, the discrete capillary network contained in the REV_j is shown, while in the bottom part of the figure, the homogenized system with the tensor $\mathbf{K}_{\text{up}}^{(j)}$ and the averaged boundary pressures $g_{\text{D}}^{(j2)}$ and $g_{\text{D}}^{(j3)}$ can be seen.

blood flow paths that begin at \mathbf{x}_i and are contained in the REV_j . Both these values are not known a priori and therefore we set

$$\frac{\mathbf{K}_v^{(j)}}{\ell_c^{(ij)}} = \alpha \frac{\overline{\mathbf{K}_v^{(j)}}}{L_{\min}^{(j)}}, \quad (7.7)$$

where

$$L_{\min}^{(j)} := \min \{L_x^{(j)}, L_y^{(j)}, L_z^{(j)}\}$$

and $\overline{\mathbf{K}_v^{(j)}}$ denotes the arithmetic average of the permeabilities (3.11) of the capillaries contained in the REV_j , i.e.,

$$\overline{\mathbf{K}_v^{(j)}} := \frac{1}{|I_{C,j}|} \sum_{i \in I_{C,j}} \frac{R_i^2}{8}.$$

A numerical study to determine the optimal value of the parameter $\alpha \in (0, 1)$ with respect to the fluxes within the system under consideration is postponed to Section 7.3.

Remark 7.1. *Considering the right hand side of (7.5) one has to note that the term*

$$\frac{u_{(j)}^{\text{cap}} - u^v(s_i)}{\ell_c^{(ij)}}$$

represents a finite difference approximation of a pressure gradient at the outlet \mathbf{x}_i of the larger vessel Λ_i . According to the REV-concept in porous media theory [25, 110], one can assign to each REV an averaged pressure $u_{(j)}^{\text{cap}}$, which is defined here by (7.6). Combined with the definition of $\ell_c^{(ij)}$, it becomes obvious that the finite difference above can be considered as an approximation of the pressure gradient between an outlet of Λ_L in the REV_j and the homogenized capillaries.

Using (7.5), the source term f_v^{cap} is computed for all $\mathbf{x} \in \text{REV}_j$ as

$$f_v^{\text{cap}}(\mathbf{x}) := \sum_{\mathbf{x}_i \in \partial\Lambda_L \cap \text{REV}_j} \frac{\alpha_v^{\text{cap}}(\Lambda_i, \text{REV}_j)}{|\text{REV}_j|} (u^v(s_i) - u_{(j)}^{\text{cap}}). \quad (7.8)$$

Combining (7.5) and (7.8), it is obvious that the model is mass conservative.

Now, it remains to specify the source term f_t^{cap} that models the mass transfer between the homogenized capillaries and the interstitial space of the tissue, which is considered as a porous structure as in the case of the 3D-1D coupled model (7.1). By means of the Darcy law, the pressure u^t in the hybrid model is the solution of the problem

$$\begin{cases} -\nabla \cdot \left(\rho_{\text{int}} \frac{\mathbf{K}_t}{\mu_{\text{int}}} \nabla u^t \right) = -f_t^{\text{cap}}, & \text{in } \Omega, \\ \rho_{\text{int}} \frac{\mathbf{K}_t}{\mu_{\text{int}}} \nabla u^t \cdot \mathbf{n} = 0, & \text{on } \partial\Omega. \end{cases}$$

For this purpose, we use as in (7.1) Starling's filtration law with respect to the vessel surface area S_j that is contained in an REV_j , that is we have

$$S_j := \sum_{i \in I_{C,j}} 2\pi R_i |\tilde{\Lambda}_i|,$$

where $\tilde{\Lambda}_i \subseteq \Lambda_i$ is such that $\Lambda_i \cap \text{REV}_j = \tilde{\Lambda}_i$. Using this value, f_t^{cap} is given by

$$f_t^{\text{cap}}(\mathbf{x}) := \rho_{\text{int}} \cdot \frac{S_j L_p}{|\text{REV}_j|} \left(u^t(\mathbf{x}) - u_{(j)}^{\text{cap}}(\mathbf{x}) - (\pi_p - \pi_{\text{int}}) \right), \quad \forall \mathbf{x} \in \text{REV}_j. \quad (7.9)$$

Summary of the equations governing the hybrid model

Summarizing all previous considerations, the hybrid 3D-3D-1D model is governed by the following equations:

- Large Vessels (one-dimensional discrete network):

$$\left\{ \begin{array}{ll} -\frac{d}{ds} \left(\rho_{\text{bl}} \pi R^2 \frac{\mathbf{K}_v}{\mu_{\text{bl}}} \cdot \frac{du^v}{ds} \right) = 0, & \text{in } \Lambda_L, \\ u^v = g_D^v, & \text{on } \partial\Lambda_L \cap \partial\Omega, \\ \frac{\mathbf{K}_v}{\mu_{\text{bl}}} \cdot \frac{du^v}{ds} = \frac{\overline{\mathbf{K}_v}}{\mu_{\text{bl}}^{\text{up}}} \cdot \frac{u^{\text{cap}} - u^v}{\ell_c}, & \text{on } \partial\Lambda_L \cap \Omega. \end{array} \right. \quad (7.10)$$

- Homogenized capillaries (three-dimensional porous medium):

$$\left\{ \begin{array}{ll} -\nabla \cdot \left(\rho_{\text{bl}} \frac{\mathbf{K}_{\text{up}}}{\mu_{\text{bl}}} \nabla u^{\text{cap}} \right) = f_v^{\text{cap}} + f_t^{\text{cap}}, & \text{in } \Omega, \\ u^{\text{cap}} = g_D^{\text{cap}}, & \text{on } \partial\Omega. \end{array} \right. \quad (7.11)$$

- Tissue (three-dimensional porous medium):

$$\left\{ \begin{array}{ll} -\nabla \cdot \left(\rho_{\text{int}} \frac{\mathbf{K}_t}{\mu_{\text{int}}} \nabla u^t \right) = -f_t^{\text{cap}}, & \text{in } \Omega, \\ \rho_{\text{int}} \frac{\mathbf{K}_t}{\mu_{\text{int}}} \nabla u^t \cdot \mathbf{n} = 0, & \text{on } \partial\Omega. \end{array} \right. \quad (7.12)$$

In particular, the coupling term f_v^{cap} is given by (7.8), and describes the mass flux between the extracted network Λ_L and the homogenized capillaries. The other coupling term f_t^{cap} is defined by (7.9), and stands for the mass exchange between tissue and homogenized capillaries.

7.2. Numerical discretization

In this section, we briefly describe the numerical scheme we use to solve the model equations (7.1) and (7.10)-(7.12). In particular, the solution of the 3D equations posed on the tissue and the homogenized capillaries are solved numerically by means of the standard TPFA method from Section 2.2.3. We choose this method over the FEM presented in Section 6 because of the intrinsic local mass conservation of the finite volume scheme and its reduced complexity with respect to linear FEM.

The numerical solution of the flow equations in the network Λ for the 3D-1D coupled model and in Λ_L for the hybrid model is obtained using the method described in [81, 182, 190]. Thereby, we approximate the pressure values at the grid nodes of the corresponding network. In both cases, the mass flow $Q(\mathbf{x}_{i_1}, \mathbf{x}_{i_2})$ in a vessel Λ_i connecting the vertices $\mathbf{x}_{i_1} = \Lambda_i(s_{i_1})$ and $\mathbf{x}_{i_2} = \Lambda_i(s_{i_2})$ is given by

$$Q(\mathbf{x}_{i_1}, \mathbf{x}_{i_2}) := \rho_{\text{bl}} \cdot \frac{\pi R_i^4}{8\mu_{\text{bl}}} \cdot \frac{u^v(s_{i_1}) - u^v(s_{i_2})}{|\Lambda_i|}. \quad (7.13)$$

Imposing mass-balance at each node \mathbf{x}_i , we get the following equation

$$\sum_{j \in \mathcal{N}(\mathbf{x}_i)} Q(\mathbf{x}_i, \mathbf{x}_j) = 0, \quad (7.14)$$

where $\mathcal{N}(\mathbf{x}_j)$ denotes the set of indices that share an edge with the point \mathbf{x}_j .

For the 3D-1D coupled model (7.1), the exchange with the tissue has to be considered together with the balance equation (7.14), which can be rewritten as follows. Around each grid node \mathbf{x}_i of the network Λ , a control volume CV_i is placed such that the grid node is in the center of the control volume, as depicted in Figure 7.5. Then, the mass fluxes $Q(\mathbf{x}_i, \mathbf{x}_j)$ and $Q^t(\mathbf{x}_i)$ across the surfaces of the control volume are computed and summed up such that the sum of the fluxes is equal to zero, that means

$$Q^t(\mathbf{x}_i) - \sum_{j \in \mathcal{N}(\mathbf{x}_i)} Q(\mathbf{x}_i, \mathbf{x}_j) = 0,$$

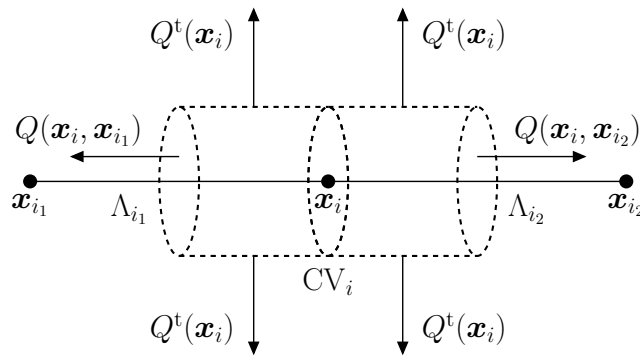


Figure 7.5.: Representation of the numerical fluxes through the surface of the control volume CV_i with center in \mathbf{x}_i .

where $Q(\mathbf{x}_i, \mathbf{x}_j)$ is given in (7.13) and $Q^t(\mathbf{x}_i)$ denotes the flux between the tissue and the capillaries. This flux is computed using an averaged pressure \bar{u}^t in the tissue with respect to the part of the vessel wall touching the control volume. Then this pressure value is compared to the network pressure associated with the grid node \mathbf{x}_i to determine the flux across the vessel wall, i.e.,

$$Q^t(\mathbf{x}_i) := \rho_{\text{int}} \cdot 2\pi L_p \left[\sum_{j \in \mathcal{M}(\mathbf{x}_i)} R_j \int_{\text{CV}_i \cap \Lambda_j} (\mathcal{I}(u^v) - \bar{u}^t + (\pi_p - \pi_{\text{int}})) ds \right], \quad (7.15)$$

where $\mathcal{M}(\mathbf{x}_i)$ is the index set for the edges Λ_j containing the grid node \mathbf{x}_i and $\mathcal{I}(u^v)$ is a linear interpolant for the pressure field u^v , whose shape on each edge is determined by the two pressure values of the edge. By means of this interpolant, an appropriate quadrature formula can be applied on each segment $\text{CV}_i \cap \Lambda_j$ to approximate (7.15).

The numerical method (7.14) is considered for the network instead of the TPFA as for the three-dimensional problems because it allows us for an easier treatment of bifurcations in the network. In fact, a degree of freedom is placed directly at a bifurcation and the mass balance equation (7.14) can easily be established. Applying the TPFA method, one can not place a degree of freedom directly at a bifurcation and therefore fluxes have to be computed through the bifurcation point, and their computation can be difficult, since the radii of the branches meeting at the bifurcation may differ. Furthermore, the continuity of the pressure at a bifurcation is guaranteed using (7.14).

Finally, with the inclusion of the boundary conditions, the source terms and the coupling conditions, we obtain a sparse linear system of equations, where each block of the system matrix is the discrete representative of an elliptic differential operator or a coupling term. The contributions of the oncotic pressures and the boundary conditions are incorporated into the right hand side of the system of equations. An example of the sparsity pattern related to the hybrid model is depicted in Figure 7.6, where the diagonal blocks \mathbf{A}^v , \mathbf{A}^{cap} and \mathbf{A}^t represent the discrete operators for the elliptic operators on the left hand sides of equations (7.10)-(7.12), respectively. The blocks $\mathbf{A}_v^{\text{cap}}$ and $\mathbf{A}_{\text{cap}}^v$ stand for the coupling terms (7.5) and (7.8) between the network of large vessels and the homogenized capillaries. The remaining blocks $\mathbf{A}_{\text{cap}}^t$ and $\mathbf{A}_t^{\text{cap}}$ are associated with the coupling term q_t^{cap} as in (7.11) and (7.12).

The linear system is then preconditioned by means of a block AMG-preconditioner and then solved with a stabilized bi-conjugate gradient method. This solver was realized using the generic interface of the ISTL-library of DUNE and its AMG implementation [33, 34].

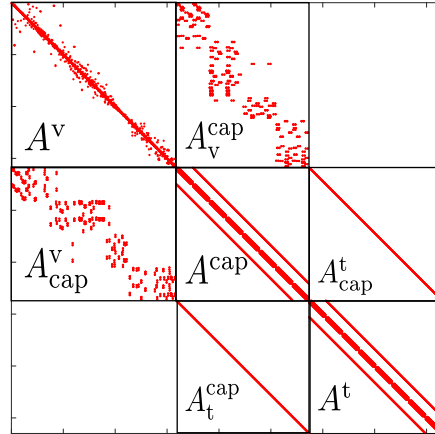


Figure 7.6.: Sparsity pattern of the discretization matrix of the hybrid model.

7.3. Numerical tests

In this section, we test the numerical models presented previously for solving the blood flow in the data set given by Figure II.1. Thereby, by means of the 3D-1D coupled model (7.1) a reference solution is computed for the hybrid model (7.10)-(7.12). In Table 7.1, the model parameters for the numerical simulations are summarized. In particular, the motivation for $R_T = 7$ [μm] is given in Section 7.3.1, while the number N_{REV} in (7.3) for the hybrid model is discussed in Section 7.3.2. The results obtained by both approaches are compared with respect to mass fluxes in Section 7.3.3 and averaged REV-pressures in Section 7.3.4. Finally, in Section 7.3.5 a general discussion of the hybrid method and of the results obtained is made.

Table 7.1.: Values of the parameters used for the numerical experiments.

Parameter	Symbol	Value
Hematocrit	H	0.45
Interstitial tissue hydraulic conductivity	k_t	10^{-18} [m^2]
Interstitial fluid viscosity	μ_{int}	$1.3 \cdot 10^{-3}$ [$\text{Pa} \cdot \text{s}$]
Plasma viscosity	μ_p	$1.0 \cdot 10^{-3}$ [$\text{Pa} \cdot \text{s}$]
Blood density	ρ_{bl}	1030 [kg/m^3]
Interstitial fluid density	ρ_{int}	1000 [kg/m^3]
Plasma oncotic pressure	π_p	3300 [Pa]
Interstitial oncotic pressure	π_{int}	666 [Pa]
Capillary wall hydraulic conductivity	L_p	10^{-12} [$\text{m}/(\text{Pa} \cdot \text{s})$]
Threshold large vessels/capillaries	R_T	7 [μm]

7.3.1. Subdivision in large and small vessels

In this section, we motivate the choice of the threshold $R_T = 7$ [μm] that we employ to separate the larger vessels from the capillaries. Let us consider the whole vessel system Λ as depicted in Figure 7.1, on the top. For each segment Λ_i , we calculate the blood velocity v_i , where we set a constant pressure gradient of δp at the vertices, that means

$$v_i = \frac{R_i^2}{8\mu_{\text{bl},i}} \cdot \frac{\delta p}{|\Lambda_i|} \text{ [m/s]},$$

where $\mu_{\text{bl},i}$ is the viscosity of the blood according to (3.2). The distribution of the velocities is reported in Figure 7.7 on the left, for the case where $\delta p = 1$ [Pa]. Having the definitions (3.7) at hand, if we fix the threshold R_T to 7 [μm], we obtain that the average velocity in the set Λ_C is approximately 60 times smaller than the average velocity in the set Λ_L . Furthermore, the set Λ_C consists of 14918 vessels, while only 337 vessels are contained in the set Λ_L . Despite the low number of larger vessel, the chosen threshold still allows us to capture the main geometry of the vessel system, as depicted in Figure 7.7, on the right. In fact, choosing a larger threshold, such as $R_T = 18$ [μm], would reduce drastically the number of larger vessels, yielding a network that provides restricted informations about the geometry of the original system. Moreover, considering the morphological values listed in [77, Table 1], we can observe that our choice for the threshold is close to the lower bound of the diameter range for the arterioles. Therefore, we fix the threshold to 7 [μm]. For different systems, another value for the threshold might be more suitable.

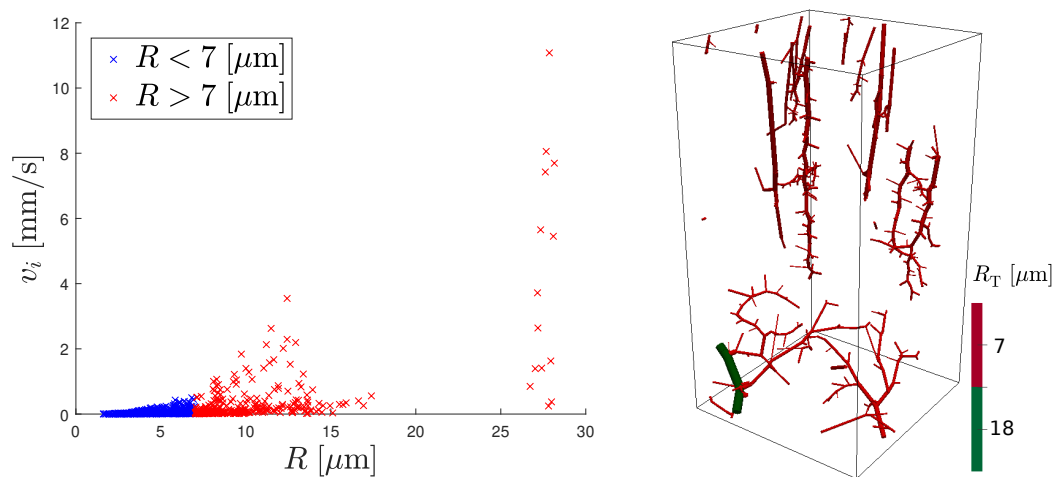


Figure 7.7.: On the left, the blood velocity for each vessel in the system Λ , where each segment is subject to a 1 [Pa] pressure difference. Setting the threshold to $R_T = 7$ [μm] yields 14918 vessels in the set Λ_C with average velocity of 0.00714 [mm/s], and 337 vessels in the set Λ_L with average velocity of 0.41533 [mm/s]. On the right, the system Λ_L is depicted in red for the threshold $R_T = 7$ [μm] and in green for the threshold $R_T = 18$ [μm].

7.3.2. Homogenization of the capillaries

In order to determine the admissible REV sizes for the approximation of the permeability tensor, we perform the following test. A single control volume, initially of size $12 \times 12 \times 24$ $[\mu\text{m}]$, is positioned in the center $(0.00056831, 0.00056831, 0.00113662)$ of the domain Ω and then enlarged in each space direction approximately by 4 $[\mu\text{m}]$ in the x - and y -directions and by 8 $[\mu\text{m}]$ in the z -direction. For each one of these control volumes, the values of the intrinsic permeability are determined using (7.4) and suitable adaptations for the y - and z -directions. In addition to that, we compute the *blood volume fraction*, which is defined as the ratio between the volume of the capillary network contained in the control volume under consideration and the volume of the control volume itself. The test is performed starting from the center of Ω , because this position allows for the larger margin of growth of the control volume. The numerical results confirm the expected oscillating behaviour of the intrinsic permeability that typically occurs when the size of the control volume is too small, as we can observe in Figure 7.8, on the left. The permeabilities appear to reach stable values, if the edges of the control volume are greater than approximately 500 μm in the x - and y -direction. Therefore, we can assert that the control volume with half the dimensions of the domain, i.e., $568.31 \times 568.31 \times 1081.503$ $[\mu\text{m}]$, and collocated in the center of Ω can be assumed to be an REV. A further argument to support this statement can be derived considering the blood volume fraction of the capillary continuum. As depicted in Figure 7.8, on the right, the blood volume fraction seems

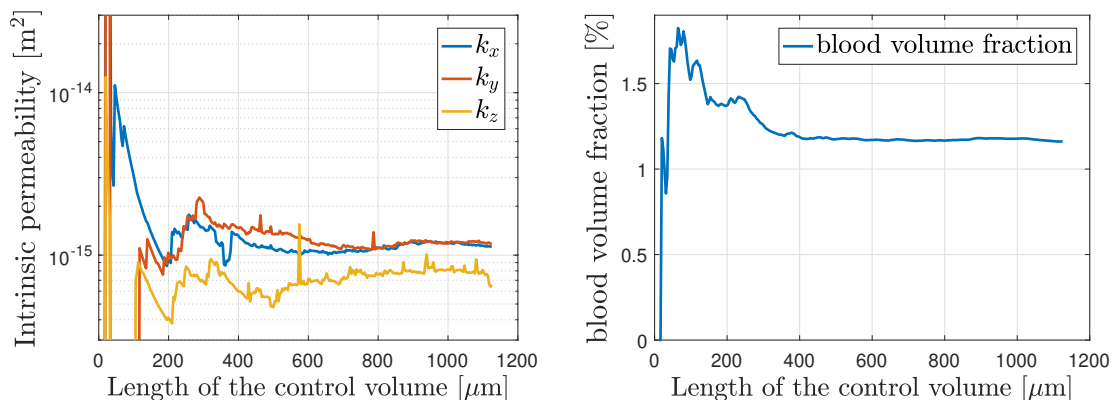


Figure 7.8.: On the left, the upscaled permeability is computed in the case where a single control volume is positioned in the center of the domain Ω . The dimensions of the control volume are enlarged by approximately $4 \times 4 \times 8$ $[\mu\text{m}]$ in each step until the control volume fills the entire domain Ω . The length of the control volume in the plot has to be doubled to obtain the actual size of the control volume in the z -direction. After an oscillating transition zone, each permeability stabilizes around a fixed value. On the right, the blood volume fraction of the corresponding control volume is reported.

to stabilize around the value 1.16%, if the length of the control volume is larger than approximately 400 [μm].

However, collocating a single REV in the center of the domain with half the sizes of Ω is not enough, since the entire capillary network has to be homogenized. On the other hand, having a single REV covering the entire domain would mean that the heterogeneity of the capillary system is lost. In fact, if we observe Figure 7.10 on the top left, we can notice that in the upper part of the system, the capillaries are mainly aligned with the z -direction, while in the bottom part, the main directions are the x - and y -directions. These orientations are consistent with the structure of the larger vessels, as reported in Figure 7.1, on the bottom right. To this end, we subdivide the domain into $2 \times 2 \times 2$ control volumes, each having half the sizes of the domain, as the central REV from the previous test. The centers of these control volumes and their corresponding numeration are reported in Table 7.3. To assert that this 8 control volumes are REVs as well, we observe in Figure 7.9 that the radii distribution of the capillaries contained in each control volume is similar to that of the central REV from the previous test. Furthermore, mean radii and standard deviations are similar as well. Supported by these observations, we can assume that the 8 control volumes considered are REVs and that the permeabilities reported in Figure 7.10 are representative.

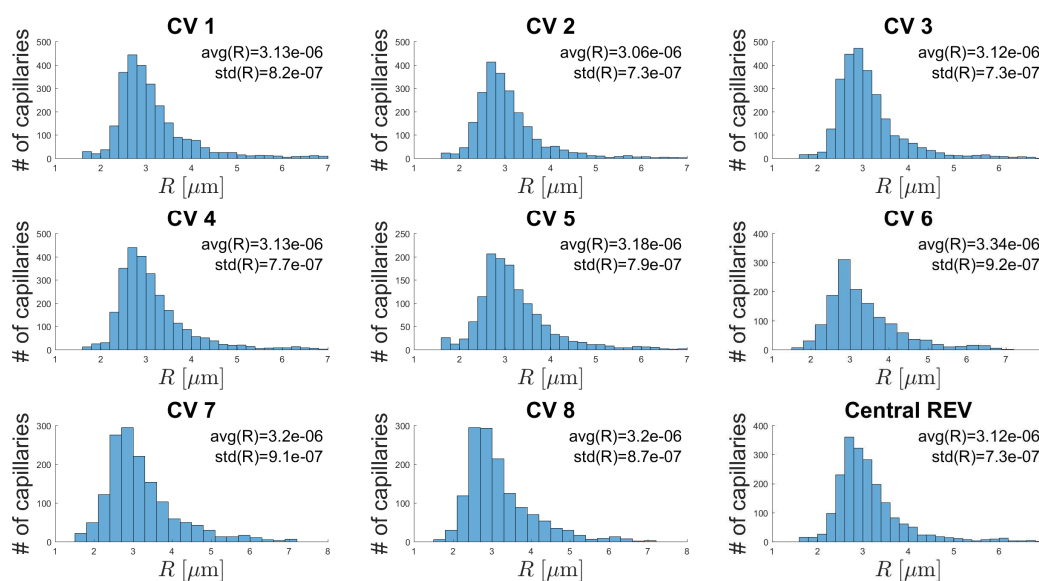


Figure 7.9.: Histograms of the radii distributions of the capillaries contained in each control volume (CV), which are given as in Figure 7.10. The numeration is given according to Table 7.3. For each CV, the mean value $\text{avg}(R)$ of the radii and the standard deviation $\text{std}(R)$ are provided. In the last histogram, the radii distribution of the capillaries contained in the REV with the same center as the domain Ω and same dimensions as the other control volumes is reported.

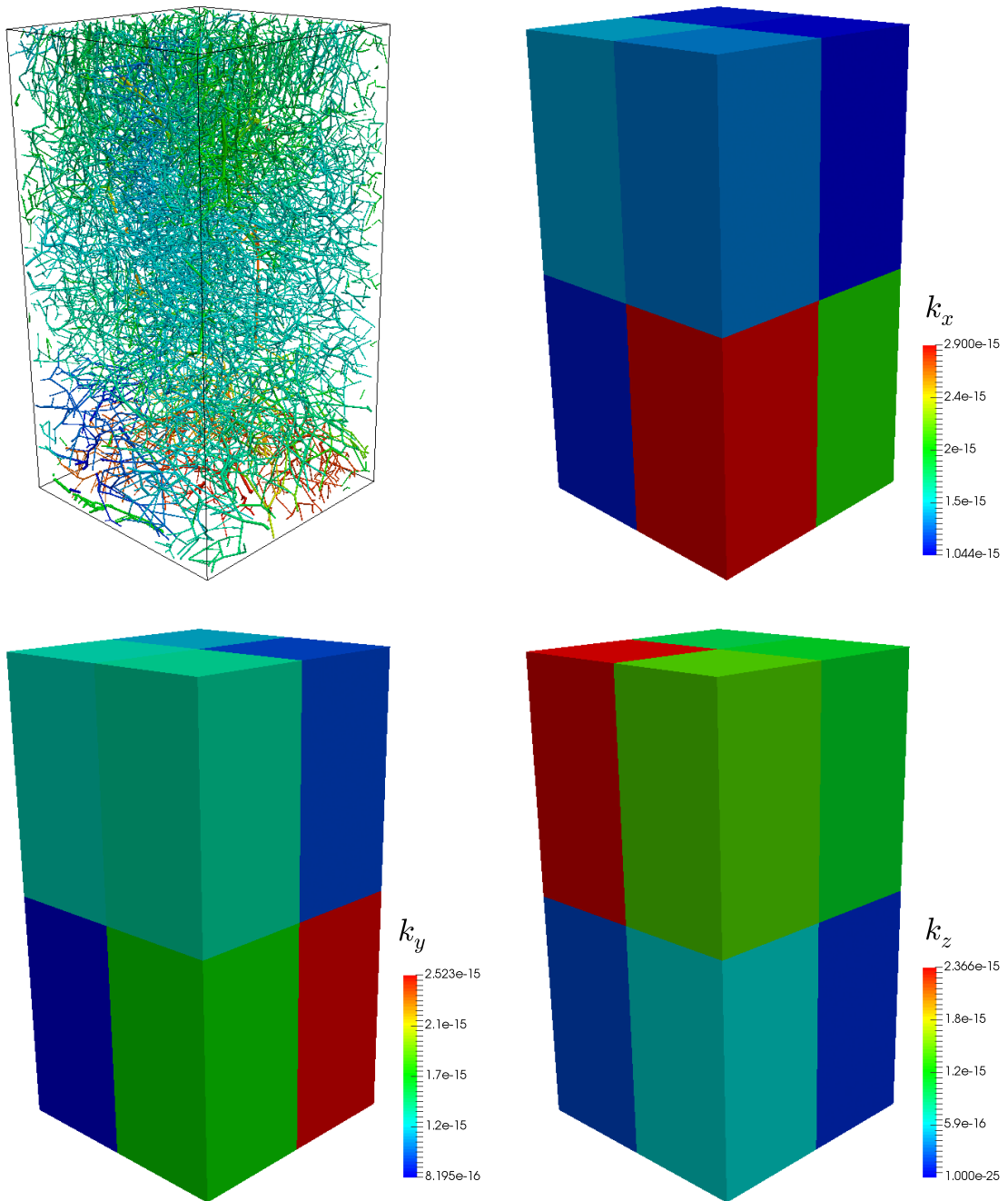


Figure 7.10.: Permeability tensors \mathbf{K}_{up} in the case of $2 \times 2 \times 2$ REVs. The heterogeneous distribution of the capillaries from Figure 7.1 is therefore incorporated, in the sense that in the lower part of the domain, the flow occurs mainly in the xy -plane, while on the top in the z -direction.

7.3.3. Investigation of the mass fluxes

In this section, a comparison between the two numerical models is provided in terms of mass fluxes across the boundaries of the domain and across the capillary walls into the interstitial space. To distinguish the results between models, we employ for the rest of the section the abbreviation “HY” when referring to the hybrid 3D-3D-1D model and the abbreviation “FC” (fully-coupled) for the 3D-1D coupled model.

For the one-dimensional systems in both models, the mass flux Q through a boundary node $\mathbf{x}_i = \Lambda_i(s_i) \in \partial\Lambda \cap \partial\Omega$ for a segment Λ_i is computed as in the left hand-side of equation (7.5), i.e.,

$$Q(\mathbf{x}_i) := \rho_{\text{bl}} \cdot \frac{\pi R_i^4}{8\mu_{\text{bl}}} \cdot \frac{du^v}{ds}(s_i).$$

The inflow Q_{in} through the boundary point \mathbf{x}_i is defined as

$$Q_{\text{in}}(\mathbf{x}_i) := \begin{cases} Q(\mathbf{x}_i), & \text{if } Q(\mathbf{x}_i) > 0, \\ 0, & \text{otherwise.} \end{cases}$$

In a similar way, we can define the outflow as

$$Q_{\text{out}}(\mathbf{x}_i) := \begin{cases} |Q(\mathbf{x}_i)|, & \text{if } Q(\mathbf{x}_i) < 0, \\ 0, & \text{otherwise.} \end{cases}$$

Having this notation at hand, we define the total inflow $Q_{\text{LV,in}}^{\text{HY}}$ and outflow $Q_{\text{LV,out}}^{\text{HY}}$ through the large vessels in the hybrid model as

$$Q_{\text{LV,in}}^{\text{HY}} := \sum_{\mathbf{x}_i \in \partial\Lambda_L \cap \partial\Omega} Q_{\text{in}}(\mathbf{x}_i) \quad \text{and} \quad Q_{\text{LV,out}}^{\text{HY}} := \sum_{\mathbf{x}_i \in \partial\Lambda_L \cap \partial\Omega} Q_{\text{out}}(\mathbf{x}_i).$$

The same procedure is used to define the fluxes $Q_{\text{LV,in}}^{\text{FC}}$ and $Q_{\text{LV,out}}^{\text{FC}}$ through the large vessels in the 3D-1D coupled model.

For the hybrid approach, the mass fluxes through the boundary $\partial\Omega$ of the capillary continuum have to be interpreted as single quantity for each boundary REV. To clarify this concept, let us assume that the REV_j shares at least one side with the boundary of the domain, that is $\partial\text{REV}_j \cap \partial\Omega \neq \emptyset$. Then we define the *net flux* $\tilde{Q}_{\text{cap}}^{\text{HY}}$ for the REV_j as

$$\tilde{Q}_{\text{cap}}^{\text{HY}}(\text{REV}_j) := \rho_{\text{bl}} \int_{\partial\text{REV}_j \cap \partial\Omega} \frac{\mathbf{K}_{\text{up}}^{(j)}}{\mu_{\text{bl},j}^{\text{up}}} \cdot \nabla u_{(j)}^{\text{cap}} \cdot \mathbf{n} \, dS,$$

where \mathbf{n} denotes the outward unit normal vector to the boundary. Numerically, the gradient $\nabla u_{(j)}^{\text{cap}}$ is calculated by the standard two-point flux approximation from Section 2.2.3. Analogously as for the one-dimensional fluxes, we define the inflow $\tilde{Q}_{\text{in}}^{\text{HY}}$ through the REV_j as

$$\tilde{Q}_{\text{in}}^{\text{HY}}(\text{REV}_j) := \begin{cases} \tilde{Q}_{\text{cap}}^{\text{HY}}(\text{REV}_j), & \text{if } \tilde{Q}_{\text{cap}}^{\text{HY}}(\text{REV}_j) > 0, \\ 0, & \text{otherwise,} \end{cases} \quad (7.16)$$

and the outflow as

$$\tilde{Q}_{\text{out}}^{\text{HY}}(\text{REV}_j) := \begin{cases} |\tilde{Q}_{\text{cap}}^{\text{HY}}(\text{REV}_j)|, & \text{if } \tilde{Q}_{\text{cap}}^{\text{HY}}(\text{REV}_j) < 0, \\ 0, & \text{otherwise.} \end{cases} \quad (7.17)$$

Therefore, the total net fluxes for the capillary continuum in the hybrid model are given by

$$Q_{\text{cap,in}}^{\text{HY}} := \sum_{j=1}^{N_{\text{REV}}} \tilde{Q}_{\text{in}}^{\text{HY}}(\text{REV}_j) \quad \text{and} \quad Q_{\text{cap,out}}^{\text{HY}} := \sum_{j=1}^{N_{\text{REV}}} \tilde{Q}_{\text{out}}^{\text{HY}}(\text{REV}_j). \quad (7.18)$$

In order to carry out a fair comparison, the fluxes through the capillaries in the 3D-1D coupled model have to be averaged in the same sense as for the hybrid approach. Therefore, we can similarly define the net flux $\tilde{Q}_{\text{cap}}^{\text{FC}}$ for the REV_j as the sum of the fluxes through the boundary capillaries, namely

$$\tilde{Q}_{\text{cap}}^{\text{FC}}(\text{REV}_j) := \sum_{\mathbf{x}_i \in \partial\Lambda_C \cap \partial\text{REV}_j \cap \partial\Omega} Q(\mathbf{x}_i).$$

Then, the inflow $\tilde{Q}_{\text{in}}^{\text{FC}}$ and outflow $\tilde{Q}_{\text{out}}^{\text{FC}}$ through the REV_j can be defined analogously to (7.16) and (7.17). Moreover, similarly to (7.18), we define the total inflow $Q_{\text{cap,in}}^{\text{FC}}$ and outflow $Q_{\text{cap,out}}^{\text{FC}}$ through the capillaries for the 3D-1D coupled model.

It remains to calculate the mass fluxes between capillaries and tissue in both models. For the hybrid model, we define the net flux $\tilde{Q}_{\text{cap,t}}^{\text{HY}}$ between the homogenized capillaries and the tissue in the REV_j as

$$\tilde{Q}_{\text{cap,t}}^{\text{HY}}(\text{REV}_j) := \rho_{\text{int}} \cdot \frac{L_p S_j}{|\text{REV}_j|} \int_{\text{REV}_j} \left(u^t(\mathbf{x}) - u^{\text{cap}}(\mathbf{x}) - (\pi_p - \pi_{\text{int}}) \right) d\mathbf{x}.$$

Defining the net inflow $\tilde{Q}_{\text{cap,t,in}}^{\text{HY}}$ and outflow $\tilde{Q}_{\text{cap,t,out}}^{\text{HY}}$ as in (7.16) and (7.17), the total inflow is given by

$$Q_{\text{cap,t,in}}^{\text{HY}} := \sum_{j=1}^{N_{\text{REV}}} \tilde{Q}_{\text{cap,t,in}}^{\text{HY}}(\text{REV}_j), \quad (7.19)$$

and the total outflow is calculated as the sum of the net outflows $\tilde{Q}_{\text{cap,t,out}}^{\text{HY}}$.

For the 3D-1D coupled model, the net flow $\tilde{Q}_{\text{cap,t}}^{\text{FC}}$ in the REV_j is defined as

$$\tilde{Q}_{\text{cap,t}}^{\text{FC}}(\text{REV}_j) := \rho_{\text{int}} \cdot 2\pi L_p \sum_{i \in \Lambda_{C,j}} R_i \int_{\Lambda_i} \left(\bar{u}^t - u^v - (\pi_p - \pi_{\text{int}}) \right) dS.$$

As for the hybrid model, the total inflow $Q_{\text{cap,t,in}}^{\text{FC}}$ can be defined analogously to (7.19).

Having these definitions at hand, we first compute the mass fluxes for the 3D-1D coupled model. Using these values, we determine the values of the parameter α in (7.7) such that both the following objective functions are minimized

$$f_1(\alpha) = \sqrt{\sum_{\beta} \sum_{\gamma} \frac{1}{2} \left(Q_{\beta,\gamma}^{\text{HY}} - Q_{\beta,\gamma}^{\text{FD}} \right)^2},$$

for $\beta \in \{\text{LV}, \text{cap}\}$ and $\gamma \in \{\text{in}, \text{out}\}$, and

$$f_2(\alpha) = \sqrt{\frac{1}{2} \left(Q_{\text{LV},\text{in}}^{\text{HY}} - Q_{\text{LV},\text{in}}^{\text{FD}} \right)^2}.$$

The results obtained with the hybrid model strongly depend on the value of α in (7.7), as we can deduce from Figure 7.11, where both objective functions f_1 and f_2 are plotted with respect to the parameter α . For the objective function f_2 , it is easy to identify the minimum at $\alpha = 0.4$, while for f_1 the minimum is attained at $\alpha = 0.46$. The choice between these two values of α is made comparing the fluxes listed in Table 7.2, where we report the fluxes obtained on the finest level for both the hybrid and the 3D-1D coupled models (details to the mesh refinements are postponed to Section 7.3.4). The results for the hybrid model are provided for $\alpha \in \{0.2, 0.4, 0.46, 0.9\}$. We can observe a good agreement between the solutions of both models, in particular with respect to the inflow due to the larger vessels, if $\alpha = 0.4$ is chosen. The major differences in the fluxes consist in the contributions of the homogenized capillaries. In fact, using the hybrid model, the mass fluxes into the capillary continuum and out of the capillary continuum are significantly overestimated than those of the 3D-1D coupled model. On the other hand, choosing $\alpha = 0.46$ yields an overall better agreement with the 3D-1D coupled model, because all four fluxes are optimized at the same time, but not a single quantity is as good approximated as for $\alpha = 0.4$. Moreover, due to the fact that in a small neighbourhood of the the minimum, the function f_1 is relatively flat, the difference $|f_1(0.4) - f_1(0.46)|$ is about $0.141 \mu\text{g/s}$. For completeness, we report the fluxes for $\alpha = 0.2$ and $\alpha = 0.9$ as well to shown by how much these results differ from the solution of the 3D-1D

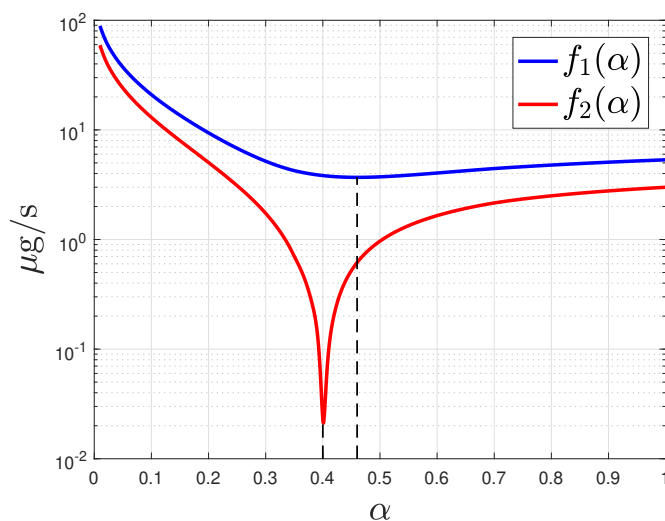


Figure 7.11.: Graphs of the objective functions f_1 and f_2 . For f_1 , the minimum is reached at $\alpha = 0.46$, while, for f_2 it can be seen at a first glance that the minimum is attained at $\alpha = 0.4$.

Table 7.2.: Mass fluxes at the boundaries and interfaces of the vascular system. All the fluxes that are presented in this table are reported in $\mu\text{g}/\text{s}$. For the hybrid method, the fluxes are obtained for two different α according to the minima of the objective functions f_1 and f_2 .

	Large vessels		Capillary bed		Tissue
Method	$Q_{LV,in}$	$Q_{LV,out}$	$Q_{cap,in}$	$Q_{cap,out}$	$Q_{cap,t,in}$
FD	9.80161	10.4964	1.30573	0.61093	$2.54991 \cdot 10^{-3}$
HY $_{\alpha=0.4}$	9.79829	7.80573	2.04311	4.03567	$1.10565 \cdot 10^{-3}$
HY $_{\alpha=0.46}$	8.89951	7.14353	1.87204	3.62801	$1.04549 \cdot 10^{-3}$
HY $_{\alpha=0.2}$	16.9280	13.2730	2.86975	6.52477	$1.48711 \cdot 10^{-3}$
HY $_{\alpha=0.9}$	5.87650	4.95714	1.17063	2.08998	$0.78677 \cdot 10^{-3}$

coupled model. Therefore, for the rest of the section, we proceed comparing the 3D-1D coupled model with the hybrid model, where we fixed $\alpha = 0.4$ in (7.7).

Lastly, to validate the numerical discretization of the hybrid model, we report in Figure 7.12 the numerical mass fluxes, where each plot of the flux is calculated with respect to the mesh refinement. It can be seen that for all the quantities reported, the curves plotted are approaching asymptotic values, as the mesh is refined. This behaviour demonstrates that the mass fluxes obtained at the finest level and reported in Table 7.2 are representative for the hybrid model.

7.3.4. Investigation of averaged pressures

After comparing the mass fluxes obtained with both models, we proceed with the comparison of the REV-pressures within the tissue and the capillaries. For the hybrid model, the averaged pressure $u_{(j),HY}^{cap}$ in the capillaries for the REV $_j$ is given by the definition (7.6), while the average pressure in the tissue is defined similarly as

$$u_{(j),HY}^t := \frac{1}{|\text{REV}_j|} \int_{\text{REV}_j} u^t(\mathbf{x}) \, d\mathbf{x}. \quad (7.20)$$

In case of the 3D-1D coupled model, we use again (7.20) to determine the REV-pressure within the tissue and label this value by $u_{(j),FC}^t$. On the other hand, the REV-pressure for the capillaries with respect to an REV $_j$ is approximated by

$$u_{(j),FC}^{cap} := \frac{1}{|\Lambda_{C,j}|} \int_{\Lambda_{C,j}} u^v(s) \, ds.$$

Furthermore, for the REV $_j$ we define the relative pressure error E_r^{cap} in the capillaries and E_r^t in the tissue as

$$E_r^\beta(j) := \frac{|u_{(j),HY}^\beta - u_{(j),FC}^\beta|}{u_{(j),HY}^\beta}, \quad \beta \in \{\text{cap}, \text{t}\}.$$

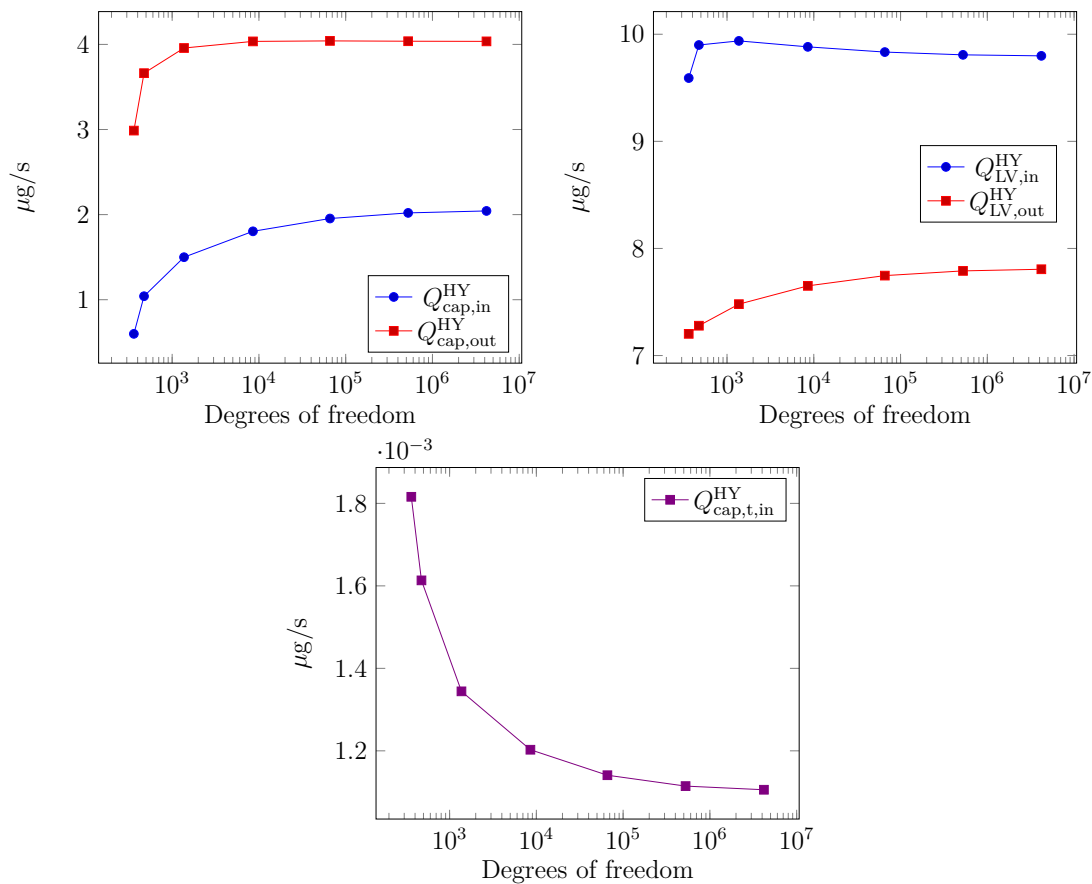


Figure 7.12.: Behaviour of the mass fluxes for the hybrid approach with respect to the number of degrees of freedom. At the top, the fluxes at the boundaries of the capillaries and of the large vessels are reported. At the bottom, the total net flux from the capillary bed into the tissue for the hybrid approach is presented.

The results obtained by means of the hybrid and 3D-1D coupled models are reported for each REV in Table 7.3, together with the numeration in the mesh and the center of each REV. The average difference between the pressures obtained with the hybrid and the 3D-1D coupled model is given by approximately 537.08 [Pa] \approx 4.03 [mmHg] for the capillaries, while the average difference within the tissue is given by approximately 316.27 [Pa] \approx 2.37 [mmHg]. These values yield an average relative error of the pressures between the hybrid model and the 3D-1D coupled of approximately $\overline{E}_r^{\text{cap}} = 11.37\%$ in the capillaries and of $\overline{E}_r^{\text{t}} = 13.97\%$ in the tissue.

Finally, in Table 7.4 we report the average relative errors $\overline{E}_r^{\text{cap}}$ and $\overline{E}_r^{\text{t}}$ of the pressures in the hybrid model with respect to the mesh refinement. These errors are calculated with respect to the REV-pressures obtained by the 3D-1D coupled model on the finest mesh, i.e., the values reported in Table 7.3 in the corresponding

Table 7.3.: Averaged REV-pressures in the capillaries and in the tissue.

REV		$u_{(j)}^{\text{cap}}$ [Pa]			$u_{(j)}^{\text{t}}$ [Pa]		
j	Center [mm]	HY	FC	E_r^{cap}	HY	FC	E_r^{t}
1	(0.284, 0.284, 0.542)	5107.77	4535.61	11.20%	2400.12	1972.80	17.80%
2	(0.852, 0.284, 0.542)	5217.07	4704.37	9.83%	2465.14	2027.71	17.74%
3	(0.284, 0.852, 0.542)	5002.77	4658.86	6.87%	2325.75	1961.99	15.64%
4	(0.852, 0.852, 0.542)	5041.25	4447.64	11.77%	2392.00	1939.18	18.93%
5	(0.284, 0.284, 1.623)	4843.99	5465.34	12.83%	2156.06	2469.00	14.51%
6	(0.852, 0.284, 1.623)	5041.86	5425.96	7.62%	2295.94	2440.22	6.28%
7	(0.284, 0.852, 1.623)	3789.44	4637.19	22.37%	1847.50	2192.57	18.68%
8	(0.852, 0.852, 1.623)	4960.14	4539.09	8.49%	2178.97	2132.44	2.14%

columns. Then, Table 7.4 suggests that the errors $\overline{E_r^\beta}$ converge to a fixed value and that the remaining error can be considered as the modeling error due to the homogenization. If we calculate the solution of the hybrid model on the mesh with $16 \times 16 \times 16$ elements in both the capillaries and tissue for a total of 8538 degrees of freedom, we obtain that the average relative errors differ by less than 1% from the average relative errors on the finest mesh. In this situation, we can assert that the modeling error dominates the discretization error and thus the obtained pressures can be considered as representative for the hybrid model. On the other hand, the relative error for the pressure in the 3D-1D coupled model is already less than 1% on the coarsest mesh, where the elements coincide with the REVs. However, in this case the linear system has still 12995 degrees of freedom in the network and 8 in the tissue. Therefore, compared with the 3D-1D coupled model, a smaller linear system can be solved to obtain representative values for the fluxes and pressures in the hybrid model. This reduction in the number of degrees of freedom is expected to become more sensible, if a larger system is considered.

Table 7.4.: Averaged relative errors of the REV-pressures in the capillaries and in the tissue with respect to the degrees of freedom (dofs).

dofs	$\overline{E_r^{\text{cap}}}$	$\overline{E_r^{\text{t}}}$
362	16.20%	22.30%
474	14.15%	17.70%
1370	12.71%	15.51%
8538	11.95%	14.56%
65882	11.58%	14.17%
524634	11.42%	14.02%
4194650	11.37%	13.97%

7.3.5. Comments on the hybrid 3D-3D-1D model

Let us briefly summarize the main features of our hybrid 3D-3D-1D method. In this work, the results obtained with our hybrid model are compared with the results of the 3D-1D coupled model (S2) in terms of mass fluxes at the boundaries of the microvascular system and averaged pressures in each REV. The hybrid model shows good agreement in terms of fluxes at the inlet and outlets of the larger vessels, if the parameter α in (7.7) is chosen appropriately. On the other hand, the net mass flux between the tissue and the capillaries is approximately 2.3 times higher for the 3D-1D coupled model than for the hybrid model. Regarding the averaged pressures for each REV, the simulations show that the pressures obtained with the hybrid model differ, in average, by approximately 4 [mmHg] in the capillaries and by approximately 2.37 [mmHg] in the tissue from the solution of the 3D-1D coupled model. Having these aspects in mind, we point out that our hybrid 3D-3D-1D method has the clear advantage that only meso-scale data are required to parametrize the model, whereas micro-scale data are necessary for 3D-1D coupled models. The results obtained suggest that it may be necessary to calibrate α for every experimental setting to obtain accurate approximations of the mass fluxes provided by the 3D-1D coupled model. Similarly, in [205] a parameter has to be optimized as well to model the flux between the different vessel types. These observations suggest that in context of hybrid models for microvasculature different unknown parameters occur, whose value is not known a priori. As a consequence, further investigations are required to improve the hybrid modeling approach. In particular, it would be of great interest to determine, if a combination of such parameters exists that can be applied to different settings and provides accurate results.

We believe that these results are not only influenced by the choice of the parameter α , but that the interpolated boundary condition g_D^{cap} plays an important role as well. In fact, for the data set considered in this work, we have to perform a linear interpolation of the boundary values in order to obtain a continuous boundary condition for our hybrid model. However, when considering an entire organ, we would expect that the error introduced by the interpolation of the boundary conditions may be reduced.

An improved streamline method for two-phase flow in porous media

In Chapter II, we dealt with microcirculation, while in the following we consider geological systems whose dimensions may be of hundreds of meters. The numerical simulation of flow and transport of substances in geological reservoir is widely used, e.g., to test locations for nuclear waste storage over the time [119], to verify the accumulation of CO₂ over the years [68], or to improve oil recovery [225]. Simulations of such complex processes are extremely difficult, because several factors have to be considered, such as, to cite some, the nature of the transported materials, the geological structure of the subsurface, the uncertainty that characterizes the field properties like the permeability and the porosity, the effects of gravity and the different temperatures depending on the depth of the reservoir. Complex models can be used to try to keep track of most features in such applications, see, e.g., [108], but in this work we restrict only on a particular aspect of these simulations. Namely, we choose here to focus our attention on questions related to the front displacement of flows in porous media, for which an accurate simulation is important in many applications such as, e.g., predicting the propagation of pollutants in porous media [48, 180] or estimating enhanced oil recovery [89, 105, 118, 174]. In particular, the correct simulation of a contaminant leakage into the subsurface may prevent water sources from being polluted [79, 201]. For example, in [211], the quantity of interest is the time at which the oxygen in the influent reaches the recovery well and the prediction of this time is important to trigger clogging processes.

Thus, we consider in this chapter only advection-dominated phenomena, where the main challenge consists in resolving correctly sharp fronts. The numerical solution of these problems is even more difficult, if the porous medium is highly heterogeneous, as we assume in the setting considered in this chapter. There exists a vast literature describing numerical methods for solving the advection-dominated equations considered in this chapter, see, e.g., [56, 107] for extensive reviews. However, the perfect strategy that solves all problems does not exist and therefore one has to choose the most appropriate method for the applications that is considering. In particular, the spatial dimensions of the simulation domain, the large times involved and the arbitrary structure of the medium pose difficult and different challenges to each solution strategy. We briefly discuss a couple of them. The most employed numerical methods for multiphase flow are based on finite volume schemes, because of their local mass-conservation properties and capability to handle general geometries. However, they might require extra care when dealing with arbitrary permeability fields or geometry [195]. Moreover, such numerical methods are usually combined

with an implicit scheme for the time discretization. In fact, an explicit scheme might become unfeasible, if simulations have to be performed over large time intervals. These methods based on an implicit time scheme and on a finite volume space discretization are stable and have many advantages, as we listed above, but their solution may be very time consuming, mainly because of the non-linear system of equations that has to be solved at each time step [175].

Other methods based, e.g., on discontinuous Galerkin schemes can handle arbitrary geometries and properties of the field and guarantee higher order of convergence, if combined with appropriate stabilization techniques. However, they may become extremely expensive to solve [17].

Methods based on mimetic finite differences [42] or mixed finite elements [11] combined with implicit time strategies are also employed for multiphase flow, but the major drawback of these schemes is that they are not unconditionally monotone, which means that maximum and minimum principles are not satisfied for arbitrary grids and permeability tensors [195].

In this chapter, the focus is posed on developing an efficient method that can quickly describe the main features of advection dominated two-phase subsurface flow problems. To this end, we present an efficient streamline-based method to simulate advection-dominated flow of a two-phase system of incompressible fluids in highly heterogeneous and anisotropic media, where capillary effects are neglected.

The chapter is structured as follows: in Section 8 we briefly present the equations that describe the two-phase flow in porous media and the strategies employed in this work to calculate the numerical solution. In Section 9, we thoroughly describe a streamline method for solving the transport equation, where particular attention is posed on the solution of the pressure equation and on our improved streamline method. At the end, two and three dimensional examples are provided, where our method is validated by comparing the numerical solution with the solution obtained by a standard fully-implicit scheme.

8. Mathematical formulations for two-phase flow

In this section, we briefly describe the basic concepts of two-phase flow in porous media. An extensive illustration of the phenomena involved can be found, e.g., in [110]. The basic equations are derived by mass conservation and momentum equations combined with Darcy's law for each phase. There are two major mathematical formulations for describing two-phase flow. The first one is presented in Section 8.1 and consists in a coupled system given by the combination of the mass conservation equations with generalized Darcy's equations. In this formulation, a nonlinear system of PDEs is obtained to describe the simultaneous flow of both phases. This formulation is not suitable for the streamline method and, therefore in Section 8.2, the equivalent fractional flow formulation is derived, which consists of two weakly coupled equations. Exploiting the features of the second formulation, we employ an operator splitting strategy to reformulate the transport problem along streamlines,

as we describe in Section 8.3.

8.1. Fully coupled formulation

In the case of two-phase flow simulations, we have a *wetting* and a *nonwetting phase*, denoted by with the index “w” and “n”, respectively. For their general definition, we refer the reader to [13]. For the rest of the work, we assume that water is the wetting phase with respect to oil.

The mathematical model that governs the flow of a two-phase system for incompressible fluids and porous medium is given by an advection type of equation

$$\phi \frac{\partial S_\alpha}{\partial t} + \nabla \cdot \mathbf{v}_\alpha = q_\alpha, \quad \alpha \in \{\text{w}, \text{n}\}, \quad (8.1)$$

where S_α denotes the saturation of the medium by the phase α , q_α is a source/sink term for the corresponding phase, ϕ the porosity of the medium, and \mathbf{v}_α is the velocity field associated to the phase α .

The velocity \mathbf{v}_α is usually expressed in terms of Darcy’s law [69], which is a constitutive law that describes the flow of a fluid in a porous medium. This law was originally obtained for slow laminar flow of a single phase in porous medium. A more general version for the *Darcy velocity* \mathbf{v} can be obtained, if we account for gravity effects

$$\mathbf{v} := -\frac{\mathbf{K}}{\mu} (\nabla u - \rho \mathbf{g}), \quad (8.2)$$

where \mathbf{K} is a tensor satisfying the assumptions from Section 2.2 and represents the intrinsic permeability of the medium. The function u denotes the pressure of the fluid, ρ is the density, μ the dynamic viscosity and \mathbf{g} is the gravity vector defined as $-\mathbf{g}e_d$, with g the scalar gravity and \mathbf{e}_d the d -th unit vector in \mathbb{R}^d . Darcy’s law (8.2) holds as long as the Reynolds number (3.3) is small enough. For all the simulations conducted in the following, this assumption is satisfied, since high-rate pumping or recharging wells are not considered [26, Section 4.2.6].

Darcy’s law (8.2) has been stated for single-phase flow, while the extension to multiphase flow was first proposed in [163, 164] and is based on the introduction of the relative permeability $k_{r\alpha}$. Then, for each phase $\alpha \in \{\text{w}, \text{n}\}$, the generalized Darcy’s equation reads

$$\mathbf{v}_\alpha := -\frac{k_{r\alpha}}{\mu_\alpha} \mathbf{K} (\nabla u_\alpha - \rho_\alpha \mathbf{g}), \quad (8.3)$$

where μ_α and u_α are the dynamic viscosity and the pressure of phase α respectively. The relative permeability is a function of the saturation, because two fluids filling the same pore volume tend to mutually disturb their movements. In this work, we select only two approaches to describe the relation between the relative permeability and the saturation S_w of the wetting phase. The first possibility is given by the Brooks-Corey function [43], for which we consider the following simplified version

$$k_{rw}(S_w) := S_w^{\frac{2+3\lambda}{\lambda}}, \quad k_{rn}(S_w) := (1 - S_w)^2 \cdot \left(1 - S_w^{\frac{2\lambda}{\lambda}}\right), \quad (8.4)$$

where λ is a parameter that describes the pore size distribution. The second approach is given by a quadratic relation

$$k_{rw}(S_w) := S_w^2, \quad k_{rn}(S_w) := (1 - S_w)^2. \quad (8.5)$$

Darcy's law represents the conservation of momentum, which has to be combined with the equations for mass balance (8.1). This leads to the general form of the two-phase flow model

$$\phi \frac{\partial S_\alpha}{\partial t} + \nabla \cdot (\lambda_\alpha \mathbf{K} (\nabla u_\alpha - \rho_\alpha \mathbf{g})) - q_\alpha = 0, \quad \alpha \in \{\text{w}, \text{n}\}, \quad (8.6)$$

where the ratio $\lambda_\alpha = k_{r\alpha}/\mu_\alpha$ is called *mobility* of phase α . There are four unknowns in the system (8.6), namely the two pressures u_w and u_n and the saturations S_w and S_n . Therefore, the two-phase system (8.6) has to be closed by two supplementary relations. The first one is the result of the assumption that all fluid phases fill the pore space entirely, which means that the sum of both phase saturations must be equal to one, i.e.,

$$S_w + S_n = 1. \quad (8.7)$$

The second relation defines the *capillary pressure*, which is the difference in pressure between two immiscible fluids across a curved interface at equilibrium [216], i.e.,

$$p_c := u_n - u_w. \quad (8.8)$$

The most common parametrizations for capillary pressure as a function of the wetting-phase saturation are the functions of van Genuchten [217] and Brooks-Corey [44]. In the setting considered for this work, capillary effects are neglected, i.e., we set $p_c = 0$. Combining equations (8.6)-(8.8), different fully-coupled formulations for two-phase flow can be obtained, depending on the choice of the two primary unknowns. In Section 9, we employ a pressure-saturation formulation, where we chose as primary variables the pressure u_w and the saturation S_w of the wetting-phase. Thus, the fully-coupled problem reads

$$\begin{cases} \phi \frac{\partial S_w}{\partial t} - \nabla \cdot (\lambda_w \mathbf{K} (\nabla u_w - \rho_w \mathbf{g})) - q_w = 0, \\ -\phi \frac{\partial S_w}{\partial t} - \nabla \cdot (\lambda_n \mathbf{K} (\nabla u_w - \rho_n \mathbf{g})) - q_n = 0. \end{cases} \quad (8.9)$$

The equations in the two-phase system (8.9) are coupled, parabolic and in general non-linear, due to the dependency of the mobilities λ_w and λ_n on the saturation. Thus, the two equations should be solved simultaneously, typically combining an implicit time stepping with suitable space discretizations and employing a Newton method for solving the resulting non-linear algebraic system. In Section 9, the solution of (8.9) is obtained by means of a fully-implicit finite volume method based on the two-point flux approximation (FI-TPFA), see, e.g., [90] for a description of the method. The numerical solution obtained solving (8.9) is referred in Section 9.6 to as *reference*

solution and is used to validate our discretization method, which is presented in the next section. In fact, the FI-TPFA method is often used for solving flow problems in porous media, see, e.g., [71, 127], and the references therein. Indeed, the stability of the FI-TPFA method has been demonstrated in several studies, see, e.g., [87, 162]. Furthermore, in this work, we mainly consider test cases where the \mathbf{K} -orthogonality property is fulfilled and therefore accuracy and convergence of the TPFA scheme is assured, see Section 2.2.3. Therefore, a fully-implicit finite volume method based on a multi-point flux approximation [4, 75, 195, 224] is actually beyond the scope of this chapter. Other solution strategies may be employed to compute a reference solution for our method, such as methods based on a DG spatial discretization and a diagonally implicit Runge-Kutta scheme for the time discretization [17]. However, for this method, the numerical solution may exhibit non-physical oscillations, if slope limiters or upwinding are not employed [143, 144]. Moreover, the solution of the fully-coupled system can be expensive, in particular for three-dimensional problems, and may require high performance algorithms [17, 152, 167].

8.2. Fractional flow formulation

The streamline method cannot directly be applied to the fully-implicit scheme (8.9), but instead we need to reformulate the system in the equivalent fractional flow formulation [110], which turns out to be suitable for the streamline method. In the framework of two-phase flow, the derivation of the fractional flow formulation is quite straightforward, but an extension to, e.g., three-phase flow, is not trivial [54, 122]. The fractional flow formulation for two-phase flow is derived combining the two mass balance equations (8.1) from the fully coupled formulation. The result still consists of two coupled equations, but a new solution strategy based on operator splitting can be used for solving the system, as we see in Section 8.3.

Pressure equation

Adding equation (8.1) for both phases together and using the closure relation (8.7), one obtains

$$\nabla \cdot \sum_{\alpha} \mathbf{v}_{\alpha} = q_w + q_n.$$

For the fractional flow formulation, two new variables are introduced, namely the *total velocity*

$$\mathbf{v}_t := \sum_{\alpha} \mathbf{v}_{\alpha}$$

and the *global pressure* u_{glob} , which is defined such that a relation similar to Darcy's law can be established, that is

$$\mathbf{v}_t = -\lambda_t \mathbf{K} \left(\nabla u_{\text{glob}} - \mathbf{G} \right), \quad (8.10)$$

where $\lambda_t = \sum_{\alpha} \lambda_{\alpha}$ is the *total mobility*, $f_{\alpha} = \lambda_{\alpha} / \lambda_t$ is the *fractional flow function* for each phase α and $\mathbf{G} = \sum_{\alpha} f_{\alpha} \rho_{\alpha} \mathbf{g}$ denotes the gravity term.

These new variables are “artificial” in the sense that they are only defined for this formulation without representing a measurable physical quantity. However, for the simplified case under analysis, where capillary effects are neglected, the global pressure coincides with the phase pressures, i.e., $u_{\text{glob}} = u_{\text{w}} = u_{\text{n}}$. All in all, the total set of equations defining the *pressure equation* reads

$$\begin{cases} \nabla \cdot \mathbf{v}_t = q_w + q_n, \\ \mathbf{v}_t = -\lambda_t \mathbf{K} \left(\nabla u_{\text{glob}} - \mathbf{G} \right), \\ u_{\text{glob}} = u_w. \end{cases} \quad (8.11)$$

Saturation equation

Having the pressure equation at hand, the mass balance equation can be reformulated in terms of either the wetting-phase saturation S_w or the non-wetting phase saturation S_n by rearranging Darcy’s law and using the definition of the total velocity. Here, only the equation for S_w as primary variable is derived. Thus, the Darcy velocity (8.3) for the non-wetting phase can be rewritten as

$$\mathbf{v}_n = \frac{\lambda_n}{\lambda_w} \mathbf{v}_w - (\rho_w - \rho_n) \lambda_n \mathbf{K} \mathbf{g}. \quad (8.12)$$

Combining (8.12) with the definition of the fractional flow function and of the total velocity, we obtain

$$\mathbf{v}_w = f_w \mathbf{v}_t + (\rho_w - \rho_n) \lambda_n f_w \mathbf{K} \mathbf{g}. \quad (8.13)$$

We denote the product $\lambda_n f_w$ by

$$\bar{\lambda}(S_w) := \frac{\lambda_w \lambda_n}{\lambda_w + \lambda_n}.$$

By substituting the new form of \mathbf{v}_w from (8.13) into the general balance equation (8.1) for the wetting phase, the saturation equation involving the total velocity reads

$$\phi \frac{\partial S_w}{\partial t} + \underbrace{\nabla \cdot (f_w \mathbf{v}_t)}_{\text{advection}} + \underbrace{\nabla \cdot (\bar{\lambda}(\rho_w - \rho_n) \mathbf{K} \mathbf{g})}_{\text{gravity}} - q_w = 0, \quad (8.14)$$

and consists of an advective and a gravitational part. In the following, we refer to (8.14) as the *saturation equation*. Confronting this equation with (8.9), we notice that such clear distinction between advection and gravitation is not possible for the fully-implicit formulation. Combining equations (8.11) and (8.14) yields the following system for the fractional flow formulation

$$\begin{cases} \nabla \cdot \mathbf{v}_t = q_w + q_n, \\ \mathbf{v}_t = -\lambda_t \mathbf{K} \left(\nabla u_{\text{glob}} - \mathbf{G} \right), \\ \phi \frac{\partial S_w}{\partial t} + \nabla \cdot (f_w \mathbf{v}_t) + \nabla \cdot (\bar{\lambda}(\rho_w - \rho_n) \mathbf{K} \mathbf{g}) - q_w = 0. \end{cases} \quad (8.15)$$

This system is still weakly coupled, because of the dependency of the relative permeabilities on the saturation in the first equation of the system, but allows us to employ other solution strategies instead of fully-implicit schemes. In fact, problem (8.15) is usually resolved by means of the so-called *IMPES method* (IMplicit Pressure, EXplicit Saturation), first proposed in [203, 210] and nowadays still of interest, see, e.g., [94, 130, 175, 189].

The IMPES strategy consists in solving the equations in a decoupled fashion, where the pressure equation is solved first and then the saturation equation is solved explicitly using the velocity field derived from the pressure equation. The new values of the saturation can now be inserted into the pressure equation for the computation of the solution at the new time step. The clear advantage of this strategy consists in the fact that we can treat the pressure equation as an elliptic PDE and the non-linearity in the saturation equation can be avoided, reducing the computational costs [175]. In particular, the IMPES strategy is very efficient if the pressure and transport equations are weakly coupled, which is satisfied in our setting since capillary effects are neglected [142]. Moreover, different numerical schemes can be chosen independently for solving the pressure and saturation equations. As a drawback, the method may still lead to instabilities, if the timestep for solving the saturation equation is too large, but in the following we present a method that allows us to overcome this disadvantage.

First, we briefly discuss the most common numerical methods used for solving the pressure equation (8.11), while a discussion regarding the solution of the saturation equation (8.14) is postponed to Section 8.3. If one wants to simulate a transport, then it is of great importance that the velocity field resulting from (8.11) is locally conservative. This requirement is clearly fulfilled by finite volume methods [1, 3, 5, 49, 76, 137]. Otherwise, one can employ mixed FEM [8, 40, 121, 161, 221] or mimetic finite differences [30, 41, 123, 202]. Also, it is possible to use discretization methods with non-conservative standard velocity fields and employ afterwards a fast post-processing of the solution to reconstruct a locally conservative velocity field. This procedure has been investigated, e.g., for DG methods in [21]. The main advantages of a DG approximation consist in its ability to handle fully and highly discontinuous permeability tensors and guarantees high-order accuracy, depending on the regularity of the solution, see Theorem 2.2 or [12, 16, 80, 172, 191]. Motivated by these features, the pressure equation is solved by a DG method, as we present in Section 9.1.

8.3. Operator splitting methods

We briefly review the operator splitting (OS) method we used combined with the IMPES strategy from above for solving (8.15). For simplicity, let the time interval $I = [0, T]$ be uniformly partitioned into subintervals $I_n = (t_{n-1}, t_n]$ of constant length $\Delta t = t_n - t_{n-1}$ and let us denote by $\Omega \subset \mathbb{R}^d$ the porous medium, where the problem is posed. Hereinafter, S_w^n denotes the wetting-phase saturation at time level n and $S_w^0 = \mathcal{P}S_{w0}$ the L^2 -projection of the initial data S_{w0} . First, we calculate the global pressure u_{glob}^{n+1} at the time t_{n+1} solving (8.11) using the saturation at the previous

time step, that is, for each time step the following equation in u_{glob}^{n+1} has to be solved:

$$-\nabla \cdot (\lambda_t(S_w^n) \mathbf{K} (\nabla u_{\text{glob}}^{n+1} - \mathbf{G})) = q_w + q_n, \quad \text{in } \Omega. \quad (8.16)$$

The total velocity field \mathbf{v}_t^{n+1} at time t^{n+1} is established from the global pressure using (8.10). Finally, the saturation equation (8.14) can be solved using the just-computed total velocity. The OS strategy consists now in decomposing the spatial differential operators in (8.14) into an advective part $\mathcal{A}_h(\Delta t)$ and a gravitational part $\mathcal{G}_h(\Delta t)$. A detailed description of the OS idea can be found, e.g., in [113]. The OS solution procedure for one splitting step $[t^n, t^{n+1}]$ is now defined as

$$\phi \frac{\partial S_w}{\partial t} + \nabla \cdot (f_w \mathbf{v}_t) = 0, \quad S_w^n \xrightarrow{\mathcal{A}_h(\Delta t)} \widehat{S}_w^n, \quad (8.17a)$$

$$\phi \frac{\partial S_w}{\partial t} + \nabla \cdot (\widehat{f}_w \mathbf{K} \mathbf{g}) = 0, \quad \widehat{S}_w^n \xrightarrow{\mathcal{G}_h(\Delta t)} S_w^{n+1}, \quad (8.17b)$$

with $\widehat{f}_w = \lambda_n(\widehat{S}_w^n) f_w(\widehat{S}_w^n) (\rho_w - \rho_n)$. \mathcal{A}_h and \mathcal{G}_h represent the discrete solution operators of the advective and the gravitational step, and \widehat{S}_w^n is the intermediate saturation value between two calculation steps. As already mentioned in Section 8.2, equation (8.16) is solved by means of a DG method, while we employ different schemes for solving equations (8.17a) and (8.17b). For simplicity, the gravitational step (8.17b) is solved using the one-dimensional explicit finite volume method along gravity lines from [23, Section 6.4.1] and [128]. In fact, the numerical solution of (8.17b) with this method affects the overall computational costs only in a minimal way, having to deal with just a reduced number of gravity lines. Therefore, a sufficiently small internal time step is used for solving (8.17b) explicitly, as proposed in [23].

For solving the advective step (8.17a), there is a multitude of possibilities: standard upwind finite volume approaches [86, 149], higher-order DG methods with slope limiters [63, 64, 98, 120], modified method of characteristics [55, 70, 74, 83], the Eulerian-Lagrangian localized adjoint method [84, 85, 112, 193, 220] and the streamline method [58, 97, 170, 213, 214]. In this work, the latter is employed. The basic idea of the streamlines is to reformulate the d -dimensional hyperbolic equation (8.17a) into a set of one-dimensional hyperbolic equations along streamlines which may dynamically change at each time step. We opted for the streamline approach for the following reasons:

- It is computationally efficient [7, 174, 214], in the sense that the one-dimensional transport equations along streamlines are independent of each other and can efficiently be solved in parallel. Furthermore, solving many one-dimensional equations is still cheaper than solving the full-dimensional problem (8.17a) on the original grid;
- The numerical diffusion is minimized [7, 28, 213], as well as are the grid orientation effects [22, 62, 177].

In Section 9.4 we describe the fundamental steps necessary to reformulate the advective equation (8.17a) into a system of one-dimensional hyperbolic equations along streamlines. Then, we discuss how to solve the advective step along each streamline by means of the front tracking method [114, 115, 148, 169]. The front tracking method has been used in combination with the streamline method in several works, e.g., [50, 135, 169], because it has been shown to perform very well for solving one-dimensional hyperbolic equations. In fact, the front tracking method is unconditionally stable, super fast and the discontinuities in the initial condition S_w^n are resolved naturally [114]. In this work, we decide to combine the streamline method with the front tracking because the resulting strategy is computationally efficient, unconditionally stable, reduces the numerical diffusion and is able to accurately resolve sharp fronts in advection-dominated two-phase flows.

The solution method we employ in this work can still be quite expensive, mainly because of the computational costs of the DG approximation of the pressure equation. In order to increase efficiency for large-scale applications, a domain decomposition on parallel architectures is applied exploiting the parallelisation possibilities offered by the DUNE framework [18], in which the entire method described in this chapter has been developed. Our streamline algorithm is therefore formulated for decomposed domains and requires a dynamic communication strategy between processors, where each processor can only access local memory, according to the requirements of the DUNE implementation. A streamline tracer algorithm combined with a DG approximation of the pressure equation for two-phase flow in porous media is therefore developed. Furthermore, to the best of our knowledge, an extension of streamline computation on decomposed domains has not been considered yet. The major difficulty for the streamline tracing in this setting consists in the fact that each processor has its own set of streamlines to work with, but it has no direct access to the rest of the domain and the entire velocity field. Therefore, the complete streamline paths cannot be calculated using standard strategies, as in [32, 97], where distributed- or shared-memory approaches are employed.

Let us briefly comment the other assumptions we made in this chapter. First, we assume for simplicity that both phases are incompressible, that is, the total velocity field is fixed during a global time step [23]. To this end, streamline methods can be extended to account for compressibility effects [27, 58, 169, 225]. In particular, in [58] the total velocity field is also fixed during a global time step, but the divergence of the velocity field is added as source or sink term to the one-dimensional transport equation along each streamline, which requires an extension of the front tracking method to compressible two-phase flow simulation, as proposed in [169]. In this way, the changes in the fluid volume, caused by pressure changes, are captured. In [27], a compressible formulation for streamline simulation is presented, where the cumulative volume is used, instead of time of flight. In [225], the author interpreted each streamline as a streamtube, in which each streamline has an associated volume. As mass and energy are transported along the streamlines, the fluid shrinks or expands because of temperature changes, which causes the volumetric flux to increase or decrease. The volume discrepancy is then modelled using a dimensionless velocity

approach similar to the one suggested by [156].

Furthermore, as already discussed in Section 8.1, we mainly consider test cases where the so-called \mathbf{K} -orthogonality property is fulfilled in order to guarantee the accuracy and convergence of the FI-TPFA scheme. The extension of streamline methods to unstructured grids has been proposed in several works, see for example [129, 159, 160, 166, 176, 186]. In [109, 129, 186], the authors employ Piola transformations to extend Pollock's method to distorted quadrilaterals or hexahedra. In [109], the authors also address streamline tracing on distorted hexahedra in a finite volume framework and their method relies on velocity reconstruction at cell corners combined with interpolation techniques within each cell. In [159], the authors employ a different approach, which uses a mixed finite element method to calculate the velocity field. In [176], unstructured grids are considered, without having any restrictions on the number of faces for each control volume.

Regarding the absence of capillary effects in our model, in several publications [28, 31, 50, 104, 132], capillary forces have been incorporated into a streamline framework for two-phase flow using operator splitting techniques. In these works, the advective step is still solved along streamlines, but capillary effects are incorporated using conventional discretization schemes such as finite volume [50], finite difference [28, 31, 104], or Petrov-Galerkin finite element methods [132]. Therefore, including capillary forces in a streamline-based strategy may lead to a higher computational effort. In this work, we are interested in a fast solver for advection dominated flow in porous media and therefore capillary effects are neglected. On one hand, their inclusion may be relatively easy, if one exploits the parallel features offered by our streamline solver, but, on the other hand, one would still have to handle the drawbacks of the IMPES strategy caused by the explicit treatment of the capillary effects [142].

9. Streamline method for sharp fronts in complex two-phase flow

Please note that the considerations presented in this section are partially taken from a publication by the author [218]:

E. Vidotto, R. Helmig, M. Schneider and B. Wohlmuth

Streamline method for resolving sharp fronts for complex two-phase flow in porous media

Computational Geosciences, Vol. 22(6), pp. 1487-1502, 2018.

In this section we describe the methods used for solving (8.15) by means of the operator splitting technique outlined in Section 8.3. This section is structured as follows: in 9.1, we review the DG approximation of the pressure equation (8.11) and in 9.2 some considerations on the velocity field are made. In Section 9.3, the one-dimensional front tracking method is described and in 9.4 it is combined with the

streamline method for solving the advection equation (8.17a) in two and three space dimensions. In Section 9.5, the streamline tracing strategy on decomposed domains is presented and discussed. Finally, in Section 9.6, several numerical experiments are proposed to validate our method.

9.1. Solution of the pressure equation

Having the general notation of the SIPG approximation of an elliptic boundary value problem at hand as introduced in Section 2.2.2, we focus in this section on the definitions of the penalty parameter σ_e and of the weights w_e^+ and w_e^- .

The pressure equation (8.11) is completed by appropriate boundary conditions and reads

$$\begin{cases} \nabla \cdot \left(-\lambda_t \mathbf{K} (\nabla u_{\text{glob}} - \mathbf{G}) \right) = q_w + q_n, & \text{in } \Omega, \\ u_{\text{glob}} = g_D, & \text{on } \Gamma_D, \\ \mathbf{v}_t \cdot \mathbf{n} = g_N, & \text{on } \Gamma_N. \end{cases} \quad (9.1)$$

To calculate the average (2.10) of a function v across the interface e , we consider in this section a specific permeability-dependent choice for the weights as in [16, 17, 152]. Namely, for all interior faces $e \in \Gamma_h$, we define the weights in (2.10) as

$$w_e^+ := \frac{\delta_e^-}{\delta_e^+ + \delta_e^-}, \quad \text{and} \quad w_e^- := \frac{\delta_e^+}{\delta_e^+ + \delta_e^-},$$

with

$$\delta_e^\pm := \mathbf{n}_e^\top \cdot \lambda_t (S^\pm) \mathbf{K}^\pm \cdot \mathbf{n}_e,$$

where $S^\pm := S(E_e^\pm)$ and $\mathbf{K}^\pm := \mathbf{K}(E_e^\pm)$ are the saturations and the permeability of the elements E_e^\pm , respectively. We can now define the SWIPG discretization for the pressure equation (9.1), which is a modification of (2.11) that includes gravity [172]. The DG approximation space W_h^k is given by (2.12) and the discrete solution $u_h \in W_h^k$ satisfies the variational equation

$$a(u_h, v_h) = \ell(v_h) \quad \forall v_h \in W_h^k,$$

where the bilinear and linear forms now read

$$\begin{aligned} a(u, v) &:= \sum_{T \in \mathcal{T}_h} \int_T \lambda_t \mathbf{K} \nabla u \cdot \nabla v - \sum_{e \in \Gamma_h \cup \Gamma_D} \int_e \{ \lambda_t \mathbf{K} \nabla u \cdot \mathbf{n}_e \}_{e,w} [v]_e \\ &\quad - \sum_{e \in \Gamma_h \cup \Gamma_D} \int_e \{ \lambda_t \mathbf{K} \nabla v \cdot \mathbf{n}_e \}_{e,w} [u]_e + \sum_{e \in \Gamma_h \cup \Gamma_D} \sigma_e \int_e [u]_e [v]_e, \\ \ell(v) &:= \sum_{T \in \mathcal{T}_h} \int_T qv + \lambda_t \mathbf{K} \mathbf{G} \nabla v - \sum_{e \in \Gamma_N} \int_e v g_N \\ &\quad + \sum_{e \in \Gamma_D} \int_e (\sigma_e v - \lambda_t \mathbf{K} \nabla v \cdot \mathbf{n}_e) g_D - \sum_{e \in \Gamma_D \cup \Gamma_h} \int_e \{ \lambda_t \mathbf{K} \mathbf{G} \mathbf{n}_e \}_{e,w} [v]_e, \end{aligned}$$

where σ_e is the penalty parameter defined as in [16, 17, 152], namely

$$\sigma_e := 2\gamma \frac{\delta_e^+ \cdot \delta_e^-}{\delta_e^+ + \delta_e^-} k(k+d-1) \frac{|e|}{\min(|E_e^+|, |E_e^-|)}, \quad \forall e \in \Gamma_h, \quad (9.2)$$

while for the boundary interfaces, we set

$$\sigma_e = \gamma \delta_e k(k+d-1) \frac{|e|}{|E_e^-|}, \quad \forall e \in \Gamma_D.$$

The factor γ in the penalty term (9.2) is constant for all faces in our simulations and set to one for the rest of the section.

This method results in a sparse, large, symmetric and positive definite algebraic system of equations for the pressure. These large-scale linear systems, in particular in three dimensions, can be efficiently solved using the parallelisation possibilities offered by the DUNE framework [18]. Here, we use a conjugate gradient solver combined with an AMG preconditioner, for which we refer to [20] for more details.

9.2. $H(\text{div})$ -projection of the DG-velocity

Once the numerical solution u_h of (9.1) has been computed, the corresponding velocity $\mathbf{v}_{t,h}$ can be immediately calculated by

$$\mathbf{v}_{t,h} := -\lambda_t \mathbf{K} (\nabla u_h - \mathbf{G}).$$

The velocity field $\mathbf{v}_{t,h}$ obtained is not conservative, due to its discontinuities in the normal components of the velocities across element boundaries, but a conservative velocity field is of foremost importance for streamline tracing. The disadvantage of having a non-conservative velocity field is clear: having a discontinuity of the velocity in the normal component at an interface means that the flux exiting one element is not the same that enters the neighbour element. Since a streamline \mathbf{s} is defined as a line which is everywhere instantaneously tangent to the velocity vector, it is clear that it cannot be properly traced, if the velocity field is locally non-conservative. Thus, following [21], a post-processing is applied to obtain a conservative velocity field, where a projection onto the BDM-space of first order is adopted. For quadrilateral and hexahedral elements, the corresponding definition of the BDM-space can be found in [39] and [40], respectively. This projection is an element-wise post-processing and therefore computationally inexpensive.

Before presenting the streamline method for the advection equation (8.17a), we need to make a further post-processing of the velocity field $\mathbf{v}_{t,h}^{\text{BDM}}$. In fact, in Section 9.4, streamlines are traced along the velocity field using the classical *Pollock method* [184]. However, the original version of the method is defined for orthogonal grids and it assumes that each principal velocity component varies linearly within a cell. The application of this method to the reconstructed velocity field $\mathbf{v}_{t,h}^{\text{BDM}}$ is not straightforward, since this velocity does not vary linearly within an element.

Therefore, we further project this velocity onto the RT_0 -space and obtain a new velocity $\bar{\mathbf{v}}_{t,h}$, which is constant along each interface e .

The advantages of choosing this approximated velocity field are given in terms of *time-of-flight* (TOF) and reduced computational costs. The TOF τ describes the time needed by a particle to travel a distance along a streamline based on the velocity field $\bar{\mathbf{v}}_{t,h}$, i.e.,

$$\tau(s) := \int_0^s \frac{\phi(\mathbf{x})}{|\bar{\mathbf{v}}_{t,h}|} d\mathbf{x}, \quad (9.3)$$

where ϕ is the porosity of the medium. In [159], the authors investigated numerically the accuracy of the RT_0 - and BDM-velocities in terms of TOF, and shown that the BDM-projection is more accurate than the RT_0 -projection. Our further projection of the BDM-velocity onto the RT_0 -space is necessary to fulfil the requirements of the Pollock method, where the velocity is assumed to vary only linearly within an element. Employing the Pollock method for tracing streamline results in an analytical expression for particle path lines within each cell and is computationally cheap. On the other hand, the two strategies described in [159] for tracing streamlines require computationally expensive algorithms. The first one is based on a stream function approach, which requires the solution of an algebraic equation and for which an extension to three-dimensional problems is not provided. The second one, relies on an explicit Runge-Kutta scheme as numerical integration method.

The better accuracy of our projection with respect to the simple RT_0 -projection is supported by the following numerical experiment conducted on the Test Case 5 proposed in [111].

Example 9.1. *On the unit square $\Omega = (0, 1)^2$, let us consider the following diffusion problem*

$$\begin{cases} -\nabla \cdot (\mathbf{K} \nabla u) = f, & \text{in } \Omega, \\ u = g_D, & \text{on } \partial\Omega, \end{cases}$$

where the permeability \mathbf{K} is given by the following heterogeneous and anisotropic tensor

$$\mathbf{K}(x, y) := \frac{1}{x^2 + y^2} \cdot \begin{pmatrix} 10^{-3}x^2 + y^2 & 0.999xy \\ 0.999xy & x^2 + 10^{-3}y^2 \end{pmatrix}.$$

The exact solution is given as

$$u(x, y) = \sin(\pi x) \sin(\pi y).$$

The boundary condition g_D and the right-hand side f are chosen accordingly. The numerical solution u_h is obtained by means of the SWIPG-scheme presented in Section 9.1 for $k = 1$ and the discrete velocity is defined as $\mathbf{v}_h := -\mathbf{K} \nabla u_h$. This velocity is then projected onto different spaces:

- $\mathbf{v}_h^{RT_0}$ denotes the projection of \mathbf{v}_h onto the RT_0 -space;
- \mathbf{v}_h^{BDM} denotes the projection of \mathbf{v}_h onto the BDM-space;

- $\bar{\mathbf{v}}_h$ denotes the projection of \mathbf{v}_h^{BDM} onto the RT_0 -space.

The global L^2 -error of each projected velocity is computed with respect to the mesh refinement and reported in Figure 9.1. We can notice that the global error for $\bar{\mathbf{v}}_h$ is smaller than the error of the sole RT_0 -projection $\mathbf{v}_h^{RT_0}$, which leads to a reduced error in terms of time-of-flight. All in all, first order of convergence of the global error for the approximated velocity can be observed.

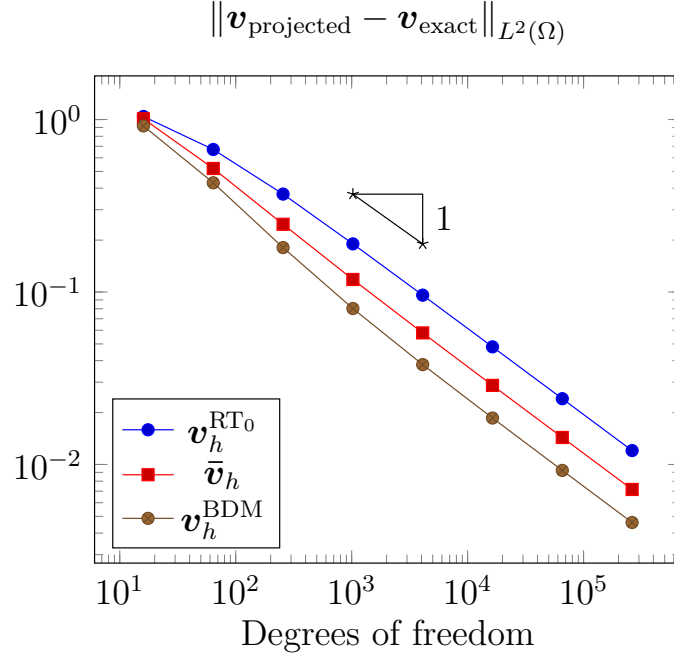


Figure 9.1.: Numerical error of the discrete velocity projected onto different spaces.

9.3. Front tracking method

Before presenting the projection of the advective step (8.17a) along streamlines, we first briefly expose the front tracking method as it has been proposed in [114, 115]. The application of the streamline method to (8.17a) yields the following type of non-linear scalar conservation problem in one space dimension

$$\begin{cases} u_t + f(u)_x = 0, & \text{in } I \times J, \\ u(x, 0) = u_0(x), & \text{in } J, \end{cases} \quad (9.4)$$

where $I, J \subset \mathbb{R}$ denote the time and space intervals, respectively, $f(u)$ represents a non-linear flux function and $u_0 \in \mathcal{C}(J)$ is an arbitrary initial condition.

The main idea of the front tracking method consists in solving rather a perturbed problem, instead of directly (9.4). To this end, the flux function f is first replaced

by a piecewise linear approximation \tilde{f} and the initial data by a piecewise constant approximation \tilde{u}_0 . This yields the perturbed problem

$$\begin{cases} u_t + \tilde{f}(u)_x = 0, \\ u(x, 0) = \tilde{u}_0(x). \end{cases} \quad (9.5)$$

In particular, the derivative \tilde{f}' is a step function taking a finite number of values and the discontinuity points of \tilde{f}' are hereinafter referred to as *breakpoints*. All in all, this problem gives rise to a series of Riemann problems, which are defined in the following.

The Riemann solver

In general, after the replacement of the initial condition with a piecewise constant function, the initial solution \tilde{u}_0 in (9.5) may consist of several discontinuities, each one of them defines a Riemann problem. Therefore, the main task of the front tracking algorithm consists in solving Riemann problems of the form

$$u_t + f(u)_x = 0, \quad u(x, 0) := \begin{cases} u_\ell & x \leq x_0, \\ u_r & x > x_0, \end{cases} \quad (9.6)$$

where x_0 is the point where the discontinuity occurs and u_ℓ and u_r are the values of the initial condition on the left and right side of the discontinuity, respectively. The solution of such Riemann problem requires us to find the correct envelope of \tilde{f} to calculate the travelling speed of each discontinuity, which may be either a shock or a rarefaction wave. If $u_\ell < u_r$, we define the *lower convex envelope* of f in the interval $[u_\ell, u_r]$ as

$$f_{\frown}(u) := \sup \left\{ g(u) : g \leq f \text{ and } g \text{ convex on } [u_\ell, u_r] \right\}.$$

If $u_\ell > u_r$, we define the *upper convex envelope* of f in the interval $[u_r, u_\ell]$ as

$$f_{\smile}(u) := \sup \left\{ g(u) : g \geq f \text{ and } g \text{ concave on } [u_r, u_\ell] \right\}.$$

Then, the following theorem holds [115, Cor. 2.4].

Theorem 9.1. *Assume that \tilde{f} is a continuous piecewise linear function $f : [-K, K] \rightarrow \mathbb{R}$ for some constant K . Denote the breakpoints of f by $-K = u_0 < u_1 < u_2 < \dots < u_{n-1} < u_n = K$. Then the Riemann problem (9.6) has a piecewise constant (in $z = x/t$) solution. If $u_\ell < u_r$, let $u_\ell = v_1 < \dots < v_m = u_r$ denote the breakpoints of f_{\frown} and, if $u_\ell > u_r$, let $u_r = v_m < \dots < v_1 = u_\ell$ denote the breakpoints of f_{\smile} . Then the weak solution of the Riemann problem is given by*

$$u(x, t) = \begin{cases} v_1 & \text{for } x \leq s_1 t, \\ v_2 & \text{for } s_1 t \leq x \leq s_2 t, \\ \vdots & \\ v_i & \text{for } s_{i-1} t \leq x \leq s_i t, \\ \vdots & \\ v_m & \text{for } s_{m-1} t \leq x, \end{cases}$$

where the speeds s_i are computed from the derivative of the envelope, i.e., as wave speed, the Rankine-Hugoniot wave speed is used, namely

$$s_i := \frac{f(v_{i+1}) - f(v_i)}{v_{i+1} - v_i}.$$

To clarify the behaviour of the solution a Riemann problem, we present the following example.

Example 9.2. Let us consider a simple Riemann problem, where the initial condition in (9.4) is given by

$$u(x, 0) := \begin{cases} u_\ell, & \text{for } x \leq x_0, \\ u_r, & \text{for } x > x_0, \end{cases} \quad (9.7)$$

where x_0 represents the discontinuity point. When the initial left state of a Riemann problem is higher than the right state, i.e., $u_\ell > u_r$, an upper concave envelope \tilde{f}_c of the approximate flux function \tilde{f} is determined restricted to the interval $[u_r, u_\ell]$. Otherwise, a lower convex envelope is constructed for $u_\ell < u_r$. In Figure 9.2, the solutions to two simple Riemann problems are depicted, where the respective initial functions, numerical and exact solutions are reported. The discontinuity is set at $x = 1$ and the solution is computed after $T = 1$ [s]. The flux function has been chosen as a quadratic law

$$f(S) := \frac{S^2}{S^2 + (1 - S)^2} \quad (9.8)$$

and approximated by 500 breakpoints. We can notice the perfect agreement of the numerical solution with the analytical solution. Furthermore, minimal numerical diffusion can be observed, where standard methods, as upwind finite difference, though stable, suffer from large numerical diffusion, if the time step is not chosen accordingly.

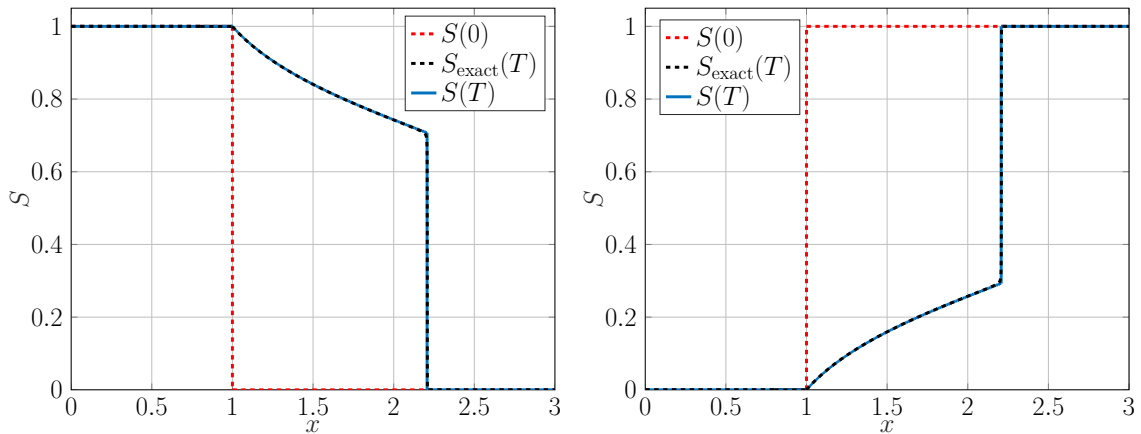


Figure 9.2.: On the left, shock, on the right, rarefaction wave. The initial condition is plotted in red.

The front tracking algorithm

The front tracking algorithm now gives a strategy to solve the initial series of Riemann problems provided by the initial function. The solution of each Riemann problem have finite speed of propagation and, therefore, they are independent of each other, until waves from neighbouring solutions collide. Then, the front tracking method resolves the collision and allows the solution to further propagate. In [115, Lemma 2.6], the authors proved that an approximate solution of the original problem(9.4) can be obtained by solving (9.5) within a finite number of steps in the algorithm. Furthermore, as \tilde{f} and \tilde{u}_0 approach the original functions f and u_0 , respectively, the solution of the perturbed problem (9.5) converges to the solution u of (9.4), see [115, Theorem 2.13].

Example 9.3. *For the sake of completeness, we show a small application of the front tracking method. We reprise the problem setting from the previous Example 9.2, but the initial condition now contains multiple discontinuities*

$$u_0(x) := \begin{cases} 1, & \text{for } x \leq 1, \\ 0.2, & \text{for } 1 < x \leq 2, \\ 0.5, & \text{for } 2 < x \leq 3, \\ 0, & \text{for } x > 3. \end{cases}$$

In Figure 9.3, the solution is shown after different times. As the time advances, we can observe how the collision of two fronts with different velocities generates a single propagation front.

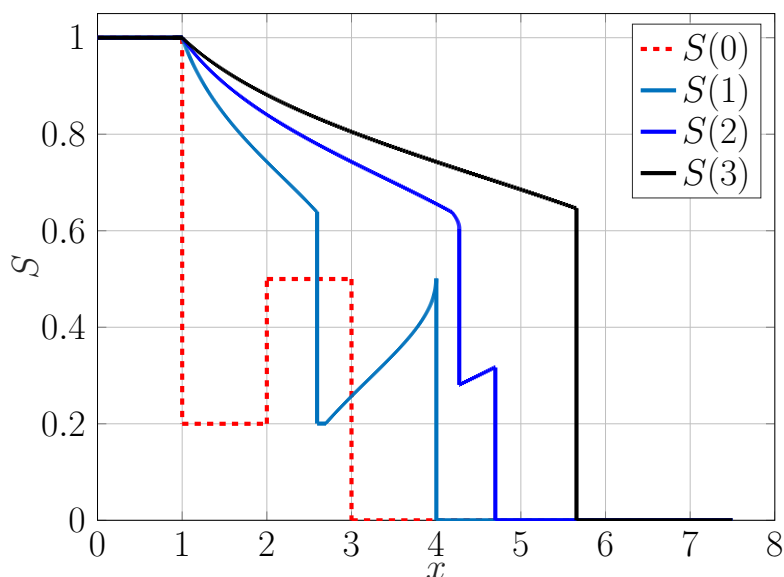


Figure 9.3.: Result of front tracking at different times for Example 9.3.

9.4. Improved streamline method for higher dimensions

In the following, we present the streamline method we use to solve equation (8.17a). The idea consists in reformulating the advective step (8.17a) along a streamline and then solving the set of one-dimensional hyperbolic equations along them with the front tracking method described previously in Section 9.3.

Having the definition (9.3) of TOF, the streamline \mathbf{s} can be defined as a vector function of τ , namely

$$\frac{d\mathbf{s}}{d\tau} = \frac{\bar{\mathbf{v}}_h}{\phi}.$$

Taking the measure $s = |\mathbf{s}|$ of the arc length along the streamline \mathbf{s} , the directional derivative along $\bar{\mathbf{v}}_h$ can be reformulated in terms of TOF, i.e., we have

$$\bar{\mathbf{v}}_h \cdot \nabla = |\bar{\mathbf{v}}_h| \frac{\partial}{\partial s} = \phi \frac{\partial}{\partial \tau}.$$

This operator identity allows us to transform the higher dimensional saturation equation (8.17a) into the streamline formulation, which contains a set of one-dimensional equations along streamlines

$$\frac{\partial S_w}{\partial t} + \frac{\partial f_w}{\partial \tau} = 0. \quad (9.9)$$

For a more extensive description of the streamline method, we refer to, e.g., [213].

The streamline tracer

As already mentioned, streamlines are traced along the velocity field $\bar{\mathbf{v}}_h$ using the standard *Pollock method* [184]. This method is provided for orthogonal grids and it assumes that each principal velocity component varies linearly within a cell. The advantage of using the Pollock method is that it provides flux conservative streamlines and that it is formulated in terms of the time of flight τ . We briefly review the Pollock method for the two-dimensional case. For three-dimensional problems, the extension is straightforward.

Let us consider the situation depicted in Figure 9.4, where the velocity field has positive components for each point of the element under consideration. All other cases, where at least one velocity component is negative, are treated in Remark 9.1 and Remark 9.2.

The scope of the method consists in finding the exit point $(x_{\text{exit}}, y_{\text{exit}})$ and the exit time Δt^* of a particle entering the element in (x_p, y_p) from the left edge. In the first step of Pollock's method, the velocity field within an element is linearly interpolated from the velocities at the element edges as

$$\begin{aligned} v_x(x) &:= v(x_0) + A_x(x - x_0), \\ v_y(y) &:= v(y_0) + A_y(y - y_0), \end{aligned} \quad (9.10)$$

where the velocity gradients A_x and A_y are easily given by linear interpolation

$$A_x := \frac{v(x_1) - v(x_0)}{x_1 - x_0} \quad \text{and} \quad A_y := \frac{v(y_1) - v(y_0)}{y_1 - y_0}.$$

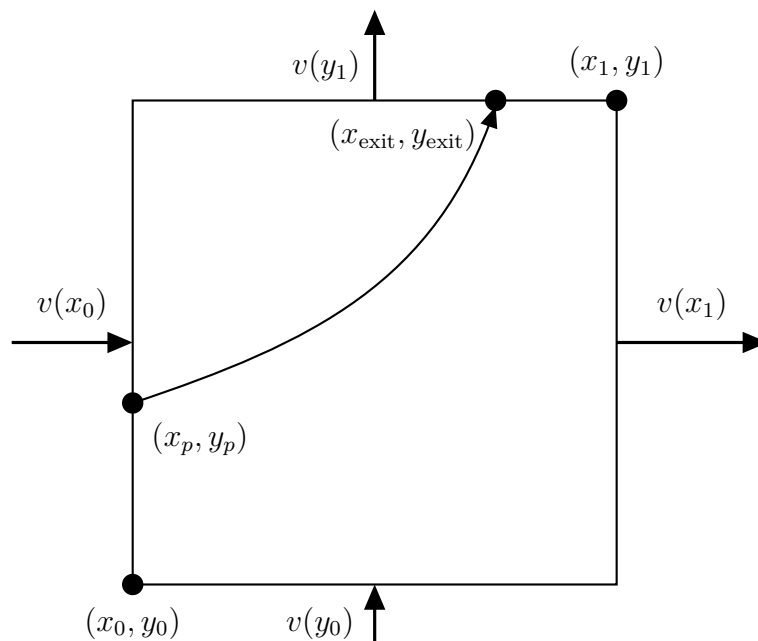


Figure 9.4.: Streamline in a two-dimension grid-block, after [184].

Given the velocity $(v(x_p), v(y_p))$ of the particle at the entry point, the method requires the computation of the time needed for the particle to reach the exit coordinates, i.e., the edge given by the coordinate (x_2, \cdot) and the edge (\cdot, y_2) . Using equations (9.10), one obtains for $A_x, A_y \neq 0$

$$\Delta t_x = \frac{1}{A_x} \ln \left(\frac{v(x_2)}{v(x_p)} \right) \quad \text{and} \quad \Delta t_y = \frac{1}{A_y} \ln \left(\frac{v(y_2)}{v(y_p)} \right).$$

The exit time at which the particle crosses one of the opposite edges is given by

$$\Delta t^* := \min(\Delta t_x, \Delta t_y).$$

Once the exit time is provided, the exit point can easily be computed as

$$\begin{aligned} x_{\text{exit}} &:= x_1 + \frac{1}{A_x} \left(v(x_p) \cdot e^{A_x \cdot \Delta t^*} - v(x_1) \right), \\ y_{\text{exit}} &:= y_1 + \frac{1}{A_y} \left(v(y_p) \cdot e^{A_y \cdot \Delta t^*} - v(y_1) \right). \end{aligned}$$

Remark 9.1 (Negative velocities.). *In Figure 9.4, the velocities are positive in each direction. Let us assume that the velocities are both negative along the x -direction. This situation can easily be rewritten in a way, such that the method described above can be applied. In fact, it is sufficient to define a mirrored point $x_p^* = x_0 + x_1 - x_p$ and invert the velocities $v^*(x_0) = -v(x_1)$ and $v^*(x_1) = -v(x_0)$ to obtain the same situation from above. After the exit time has been computed, the exit point has to be recalculated accordingly.*

Remark 9.2 (Source and sink elements.). *When implementing Pollock’s method, other cases have to be considered separately, e.g., the case where both inflow and outflow velocity in one direction have opposite sign, causing the cell to represent a source or sink for that direction. Let us assume that the element represents a source in the x -direction, i.e., $v(x_0) < 0$ and $v(x_1) > 0$. Furthermore, if the start point is inside the element, i.e., $x_0 < x_p < x_1$, we have to search in which direction the particle may exit the element. If the velocity $v(x_p)$ is positive, then we can move the left edge of the element to the coordinate (x_p, \cdot) and apply the Pollock method as in the reference case. Otherwise, if $v(x_p)$ is negative, we have to move the right edge to the coordinate (x_p, \cdot) and apply the procedure described in Remark 9.1.*

If the element is a sink in the x -direction, i.e., $v(x_0) > 0$ and $v(x_1) < 0$, the particle can not exit from the left or right edge. In order to apply the Pollock method, we need to find the point $\tilde{x} \in (x_0, x_1)$ where the x -component of the velocity is equal to zero. Then, depending of the sign of the velocity $v(x_p)$, the point (\tilde{x}, \cdot) become the new coordinate of the left edge (if $v(x_p) < 0$) or of the right edge (if $v(x_p) > 0$) and the Pollock method can be applied as described above.

Front tracking method applied along streamlines

In order to be able to apply the front tracking method on (9.9), we trace the streamlines backwards and forwards for each element, starting from its center, for a time Δt in both directions. At the end, the full-dimensional transport equation is transformed into a set of one-dimensional equations along the streamlines in terms of time-of-flight. The one-dimensional front tracking can then be naturally applied along each streamline. However, the process of mapping back the results of the front tracking from the streamline grid to the cartesian one introduces some mass balance error.

With respect to previous works, e.g., [31, 50, 135, 169], where the streamlines have been computed only backwards, we traced here the streamlines in both directions. This simple strategy allows us to improve the mass conservation of the streamline method, while other authors resorted, e.g., to particular post-processing techniques coupled with a suitable time-step [50]. Since it may not be feasible to reduce the time-step in large three-dimensional reservoir simulations, the usage of backwards and forwards streamline is employed and its advantages are reported in the paper [218] by the author.

The problem of mass balance errors due to mappings is typical to streamlines method and other techniques can be used to reduce it. For example, the errors can be tackled using higher order mapping algorithms [157] or increasing the number of streamlines. In [135], in a pure injection-extraction situation, the time-of-flight values are scaled to locally stretch or shrink the streamline grids in order to impose mass-conservation, knowing that each streamlines starts from an injector and ends in a producer. In this work, we focus on predicting accurately the front of the flow, whose simulation is not strongly influenced by a small mass loss, as the authors in [156] reported: “*despite the lack of exact mass conservation, studies have shown*

that streamline methods can predict the global sweep of water floods in heterogeneous reservoirs effectively [15, 214]". Therefore, following [37, 47], we simply employ a weighted averaging approach for the mapping from the streamline grids to the cartesian one, where each piecewise constant portion of the result obtained by the front tracking is scaled by its length.

To validate the streamline method combined with the front tracking, we present a brief convergence test with respect to h -refinement in a two-dimensional setting where the exact solution is known.

Example 9.4 (Validation test). *The computational domain is given by $\Omega = (0, 1)^2$ and is initially discretized by 4×4 elements. The relative permeabilities are given by the quadratic laws (8.5) and the viscosity are chosen as $\mu_w = \mu_n = 10^{-3}$ [Pa · s]. The absolute permeability of the medium is given by $\mathbf{K} = k\mathbf{I}$ [m²] with $k = 10^{-10}$ and the porosity by $\phi = 0.2$. On the left boundary, we set a Dirichlet condition with $g_D = 2 \cdot 10^5$ [Pa], while on the right boundary, we provide a flux given by $g_N = 0.0015/1460$ [m/s]. Initially, the domain is filled by the non-wetting phase. In this setting, the flow occurs from left to right and is independent of the y -coordinate. Therefore, we express the solution only with respect to the x -coordinate. Furthermore, in order to reduce the diffusion effects caused by the mapping from the streamline grid to the cartesian one, a single time step has been employed. The position of the shock at time t is given by*

$$x_{\text{shock}} = g_N \cdot t \cdot \frac{(1 + \sqrt{2})}{2\phi}.$$

Furthermore, the velocity in the x -direction at the point x and time t is given by

$$v(x, t) = \frac{\phi}{g_N} \cdot \frac{x}{t}.$$

Finally, the exact solution is given by:

$$S_w(x, t) = \begin{cases} \frac{v(x, t) + \sqrt{-v(x, t) (1 + v(x, t) - \sqrt{1 + 4v(x, t)})}}{2v(x, t)} & \text{if } x < x_{\text{shock}}, \\ 0 & \text{if } x > x_{\text{shock}}. \end{cases}$$

The pressure and the velocity have been computed with the strategy described in Section 9.1 and are resolved exactly by linear discontinuous elements. The numerical solution $S_{w,h}$ has been computed using the streamline method combined with the front tracking. For the error in the saturation, we employ the standard L^2 -norm on Ω , which has been reported in Figure 9.5 with respect to the meshsize h . A linear convergence to the exact solution can be observed. A theoretical justification for this behaviour can be found, e.g., in [113, Chapter 5], even though no direct convergence assertion is made for the streamline method combined with an operator splitting technique. Furthermore, in [113, Section 6.1.3], the method employed in this work

is adopted, but no convergence study is provided. As explained in [113, Example 6.5], the mapping of saturations from streamlines to the original grid and vice versa significantly smears the solution. In particular, if more solution steps are computed, the numerical diffusion accumulated by the mapping can become the dominant part of the numerical error [47, Remark 4.3.1] and [113, Chapter 5.1].

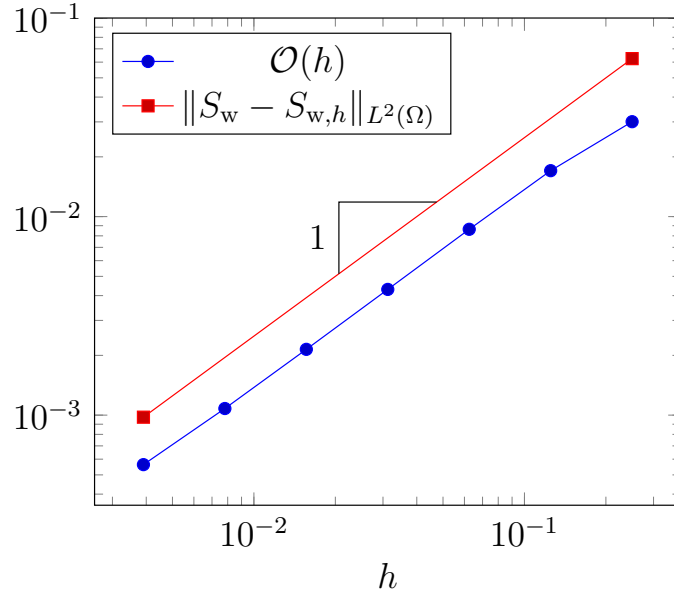


Figure 9.5.: L^2 -error of the numerical solution obtained with the streamline method with respect to h -refinement.

9.5. Streamline method on decomposed domains

As discussed in Section 9.1, the pressure field can be computed exploiting the parallel features offered by DUNE. The strategy we employed relies on a overlapping domain decomposition approach. Therefore, the module for streamline computations has to be parallelised accordingly, in the sense that at interior interfaces the streamline tracer has to include a dynamic communication strategy. A typical situation is depicted in Figure 9.6, where the computational domain is decomposed into two overlapping subdomains.

For each element, streamlines are launched from its center and are distributed among different processors. Each processor starts the computation of its own local set of streamlines independently. If a streamline reaches the boundary of the processor where it started, its computation is stopped. Once each processor is done with its own set of streamlines, a communication between processors is required to continue the streamlines that have been interrupted at the processor boundary. In the following, we present the algorithm employed to track the streamline between different processors.

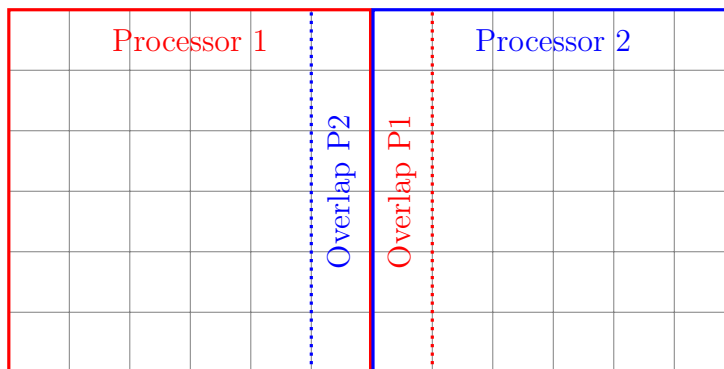


Figure 9.6.: Overlapping domain decomposition using two processors.

The communication is achieved using *Message Passing Interface* (MPI). Considering the situation presented in Figure 9.6, each processor contains a subdomain, which overlaps with the other processor. Between an overlap element in one processor and the corresponding interior element in the other processor, data can be communicated using the DUNE class

```
Dune::CommDataHandleIF<DataHandleImp, DataTypeImp>
```

To be determined are the elements crossed by the streamline, the corresponding crossing times and, eventually, the different saturation values. Let the velocity field $\bar{\mathbf{v}}_{t,h}$ be given. In Algorithm 1, a simplified version of the algorithm is presented, where the procedure for tracking the streamlines over a time Δt is provided for the case depicted in Figure 9.7. The extension to more processors follows the same strategy. Furthermore, we point out that the presented algorithm is independent of the dimension d of the problem.

Remark 9.3. Several number of cases have to be carefully treated when implementing the parallel routines. For example, it may happen that an interior element lives in the overlapping zone of multiple processors, e.g., when the unity square is subdivided

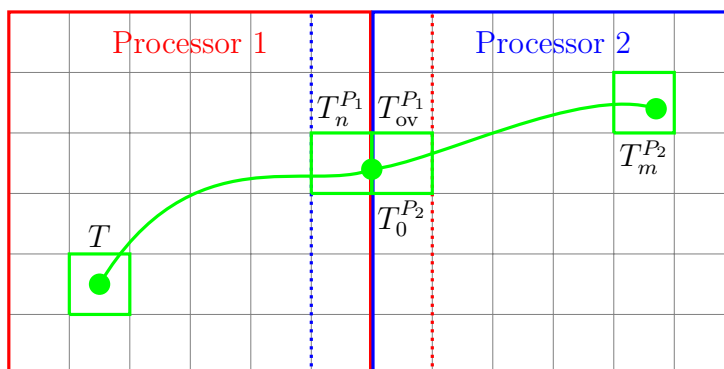


Figure 9.7.: Streamline crossing the processor border.

```

Data:  $\Delta t, \bar{v}_{t,h}$ 
Result: Streamline of length  $\Delta t$  in terms of time of flight;
           Elements crossed;
           Values of saturation along the streamline.
for Each interior element  $T$  on each processor do
  | • Compute the streamline from the center of  $T$  until time  $\Delta t$  or boundary
  |  $\partial\Omega$  is reached;
  | • if Streamline reaches an overlap element  $T_{ov}^{P_1}$  then
  | | • Interrupt the streamline;
  | | • Save current informations in  $T_{ov}^{P_1}$ ;
  | end
end
  | • Communicate interrupted streamlines from every overlap element  $T_{ov}^{P_1}$  to the
  | corresponding interior element  $T_1^{P_2}$ ;
for Each interrupted streamline starting from an element  $T_1^{P_2}$  do
  | • Continue the streamline on processor  $P_2$  until time  $\Delta t$  or boundary  $\partial\Omega$ 
  | is reached;
  | • Save informations in  $T_1^{P_2}$ ;
end
  | • Communicate informations back from  $T_1^{P_2}$  to  $T_{ov}^{P_1}$ ;
for Each interrupted streamline started in  $P_1$  do
  | • Return informations from  $T_{ov}^{P_1}$  to the original element  $T$ .
end

```

Algorithm 1: Pseudo-code for parallel computation of streamlines on decomposed domains

onto four processor, then the element with center in $\left(\frac{1}{2} - \frac{dx}{2}, \frac{1}{2} - \frac{dy}{2}\right)$ is an interior element only for one processor, and overlap for the other three. For this reason, a track with the number of the original processor has to be kept, in order to return the informations of the streamline to the correct element.

If the domain decomposition approach has been used, the front tracking routine needs to be adapted as well. Due to the independence of each streamline to the others, every processor can solve its own set of scalar one-dimensional hyperbolic problems. The communication between processors occurs when the results of the front tracking have to be distributed between all elements met by the streamline, where some of them may be living in another processor. A similar strategy as the one described in Algorithm 1 can be used in this context to communicate the results of the front tracking method to the other processors.

9.6. Numerical experiments

In this section, we validate our method on two- and three-dimensional problems. To this end, we need to introduce a new parameter. Firstly, we assume that the wetting phase is injected from a part Ω_I of the domain $\bar{\Omega}$, and extracted from another part Ω_E . We assume that Ω_I is initially filled by the wetting phase, i.e., $S_w(x) = 1$ for every $x \in \Omega_I$. For every $x \in \Omega_E$, we assume $S_w(x) = 0$. For the discretization of problem (8.15), we introduce a uniform partition of the time-interval $[0, T]$ into subintervals of length Δt , where $m\Delta t = T$. We define the *detection time* as the quantity $T_d = k\Delta t$, where $k \in \{1, \dots, m\}$, such that there is at least a $x \in \Omega_E$ with $S_w(x) > 0$ and for each $\tilde{k} < k$ the wetting phase has still not reached the extractor, i.e., $S_w(x) = 0$ for every $x \in \Omega_E$ at time $\tilde{k}\Delta t$. The actual arrival time of the wetting phase to Ω_E lies therefore in the interval $(T_d - \Delta t, T_d]$.

For all examples, \mathbb{Q}^1 -elements have been chosen for solving the pressure equation (8.11), i.e., $k = 1$ in (2.12), and the parameter γ in (9.2) is set to be constant and equal to one. Furthermore, the FI-TPFA method is used to compute a reference solution. For other numerical tests, we refer to the original article [218].

9.6.1. Two-dimensional heterogeneous problem

In this example, we test our method on the layer 16 (top formation) of the SPE10 benchmark study [59]. The permeability and porosity fields are shown in Figure 9.8

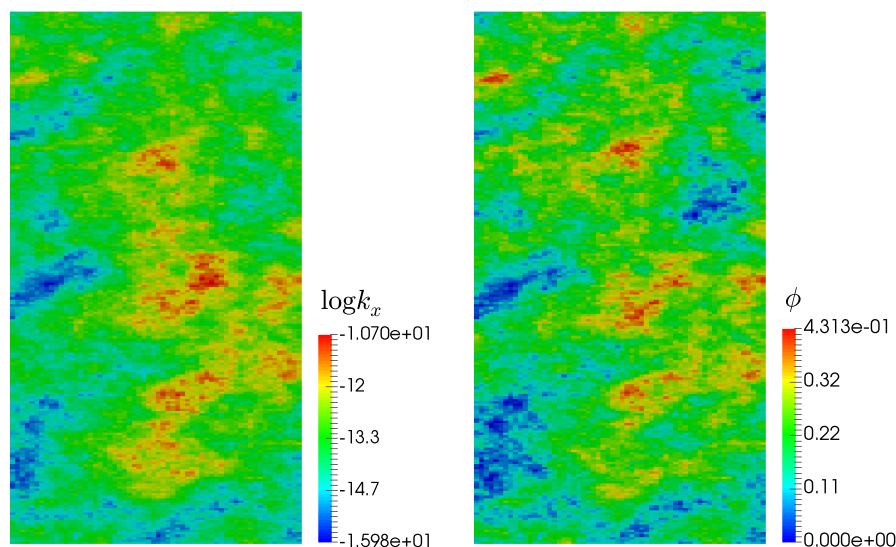


Figure 9.8.: In the left picture, the first component of the permeability field is depicted (the medium is isotropic). In the right picture, the porosity field is shown.

in the left and right pictures, respectively. Both fields show high parameter contrasts. The relative permeabilities are calculated using the quadratic law (8.5) and the fluid viscosities are $\mu_w = 10^{-3}$ [Pa · s] and $\mu_n = 5 \cdot 10^{-3}$ [Pa · s]. The domain is initially saturated by the non-wetting phase (oil), and the wetting phase (water) infiltrates the domain from the lower boundary, i.e., $S_w = 1$ for $y = 0$. The left and right boundaries are closed and a pressure difference of $2 \cdot 10^7$ [Pa] between the lower and upper boundary is applied. The domain is initially discretized by a grid of 60×220 cells of sizes $dx = 6.096$ [m] and $dy = 3.048$ [m]. Gravity is neglected. A time step of $\Delta t = 10^7$ [s] is used for the simulations.

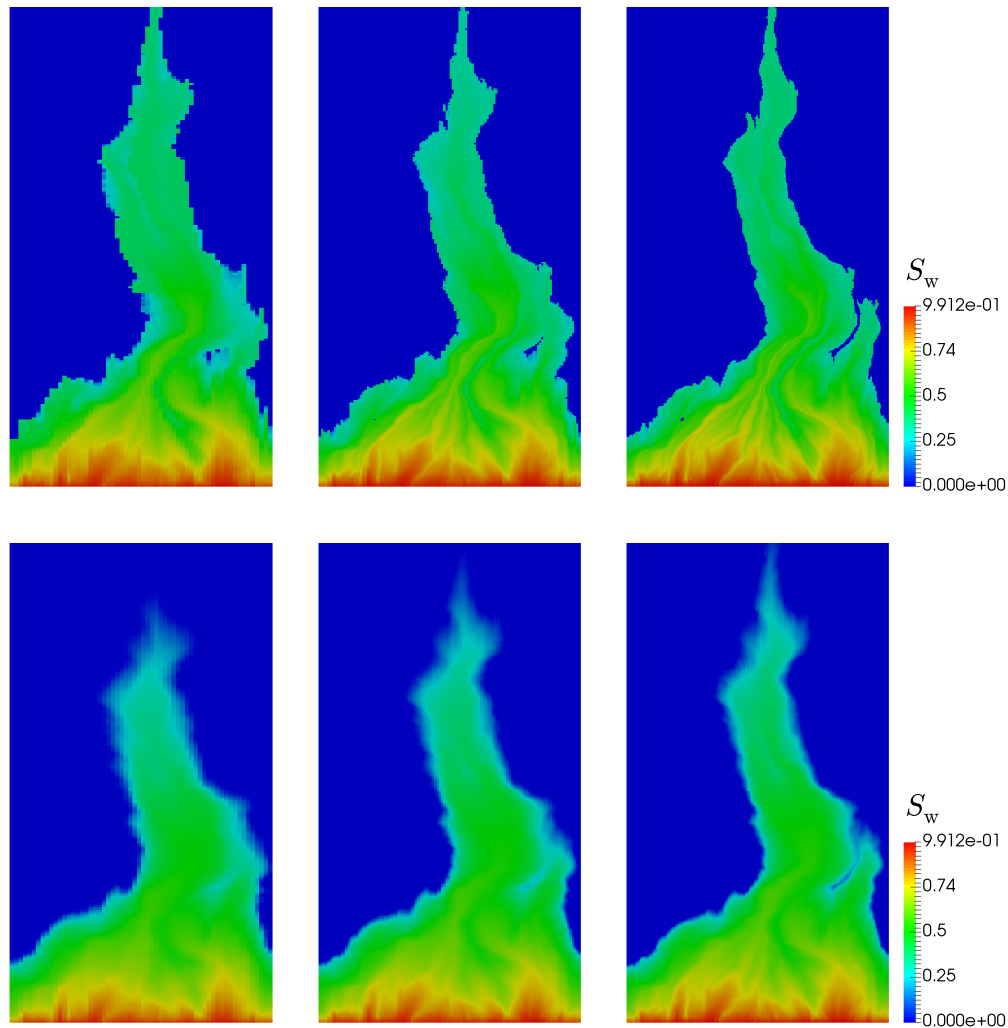


Figure 9.9.: At the top, the solutions after $1.3 \cdot 10^8$ [s] computed with our method on different meshes, from the coarsest (left picture) to the finest (right picture). At the bottom, the reference solutions computed with the FI-TPFA method on the corresponding meshes.

The results are shown in Figure 9.9, where the saturation S_w is shown at time $1.3 \cdot 10^8$ [s]. The three solutions at the top have been computed with the method described in this thesis, while the three at the bottom by means of the FI-TPFA method. The latter are referred to as reference solutions for this example. Moreover, the solutions in the left column have been computed on the initial mesh, while the mesh in the middle column has been uniformly refined and contains 120×440 elements. In the right column, a further uniform refinement has been considered, yielding a mesh that contains 240×880 elements. In Figure 9.9, on one hand, we observe that all solutions possess the same behaviour in terms of front propagation and direction of flow. On the other hand, our method yield the same detection time of $1.3 \cdot 10^8$ [s] for the water at the upper boundary independently of the mesh refinement, while a slower front propagation can be noticed for the first two FI-TPFA solutions. The detection time for the first two reference solutions is $1.4 \cdot 10^8$ [s]. These differences are due to numerical diffusion, which cause a slower front propagation. In Figure 9.10, contour plots for $S_w = 10^{-5}$ at end time are presented for each method. Here, we can observe a reduced numerical diffusion of our method in comparison to the FI-TPFA method.

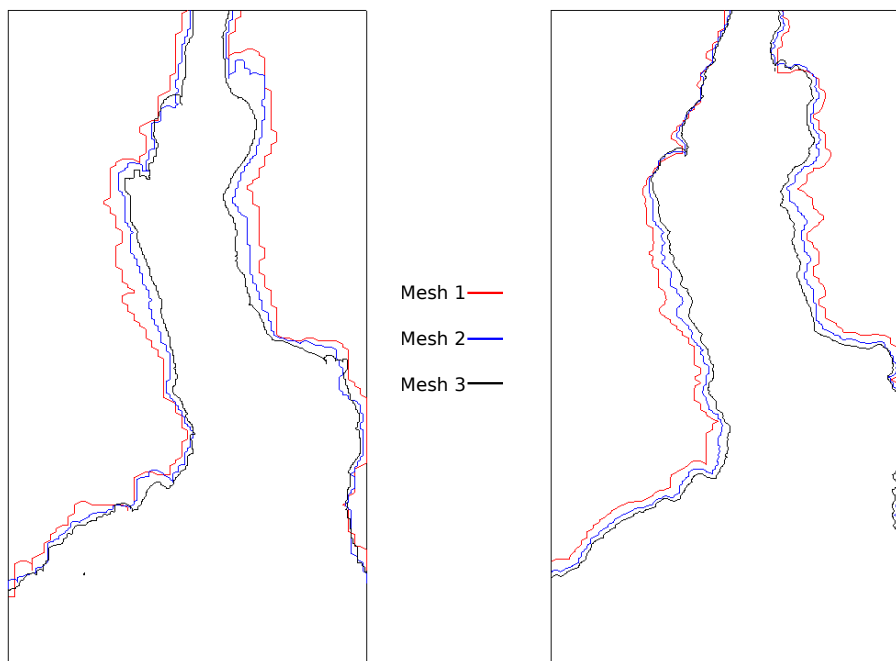


Figure 9.10.: Contour plots for $S_w = 10^{-5}$ for the solutions at the end time $1.5 \cdot 10^8$ [s] obtained with the method developed in this paper (on the left) and for the FI-TPFA solutions (on the right). In the legend, the corresponding mesh is provided.

9.6.2. Anisotropic permeability

When incorporating realistic geological models, the numerical method has to be able to handle full-tensor permeabilities. This is investigated in the following example, which has been presented in [168]. Let $\mathbf{R}(\theta)$ denote the rotation matrix of angle θ . Thus, the permeability is defined as

$$\mathbf{K} := 10^{-13} \cdot \mathbf{R}(-\theta) \begin{pmatrix} 1000 & 0 \\ 0 & 10 \end{pmatrix} \mathbf{R}(\theta) \text{ [m}^2\text{]},$$

where the angle θ is equal to 45° in the regions containing the wells, and alternates between 0° and 90° elsewhere. The tensor is depicted in Figure 7 in [218].

The problem domain is given as $\Omega = (0, 100)^2$. The penalty parameter in (9.2) is $\gamma = 10$. The viscosities are again $\mu_w = 10^{-3}$ [Pa · s] and $\mu_n = 5.7 \cdot 10^{-4}$ [Pa · s]. The flow is driven by the injection well q^I , located at the origin $(0, 0)$, and the production well q^P , located at the upper-right corner $(100, 100)$. The injection and production rates are given by $q^I = q^P = 0.1$ [m²/s] and no flow boundary condition is imposed. Gravity is neglected. The porosity is chosen constant on the entire domain and set to $\phi = 0.2$. The relative permeabilities are chosen accordingly to (8.4) with $\lambda = 2$. The transport is simulated for $2.8 \cdot 10^3$ seconds. The solution at the end time is depicted in Figure 9.11, where the domain has been discretized by 200×200 elements (middle) and by 400×400 elements (right). We notice that the anisotropy is well captured and that the amount of numerical diffusion is negligible. Furthermore, the front propagation of the wetting phase is the same for both simulations.

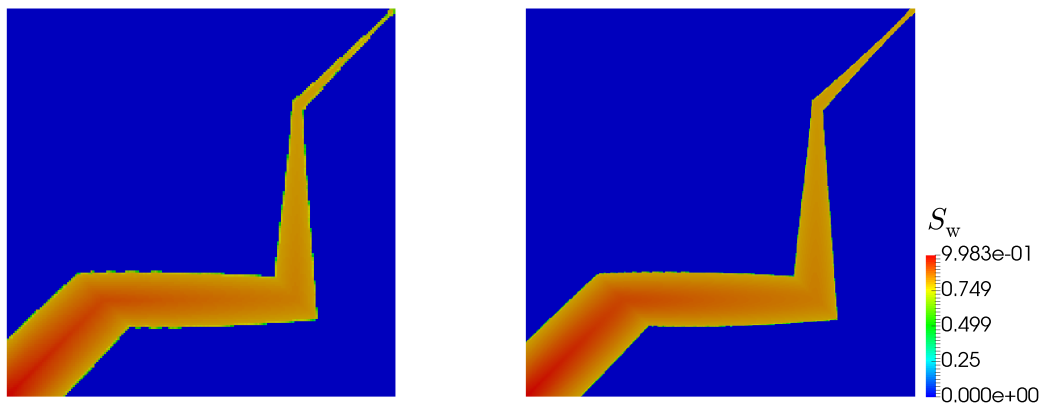


Figure 9.11.: On the left, the numerical solution on the coarse mesh is shown at end time, while on the right picture, the solution has been computed on a uniformly refined mesh.

9.6.3. Segregation test

In this example, we apply the operator splitting technique for solving a pure-gravity driven problem. The computational domain is defined as $\Omega = (0, 10) \times (0, 20) \subset \mathbb{R}^2$. Initially, water sits on the top of the domain, i.e., $S_w = 1$ if $y > 15$ [m]. Elsewhere, the domain is filled with oil. The viscosities are set to $\mu_w = 10^{-3}$ [Pa · s] and $\mu_n = 5.4 \cdot 10^{-4}$ [Pa · s]. The densities are $\rho_w = 1000$ [kg/m³] and $\rho_n = 890$ [kg/m³], while the permeability is homogeneous and isotropic with $\mathbf{K} = k\mathbf{I}$ [m²] and $k = 10^{-10}$. The porosity is chosen constant, namely $\phi = 0.2$. On the upper and lower boundaries of the domain, we set $g_D = 0$ [Pa] while no-flow conditions are posed on the left and right boundaries. This setting yields a problem, where the total velocity is zero at each time step. The simulation runs for $T = 10^5$ [s] seconds and the time-step has been chosen as $\Delta t = 10^3$ [s] seconds. The results after one time step and at the end time are shown in Figure 9.12. The swap between phases can be observed.

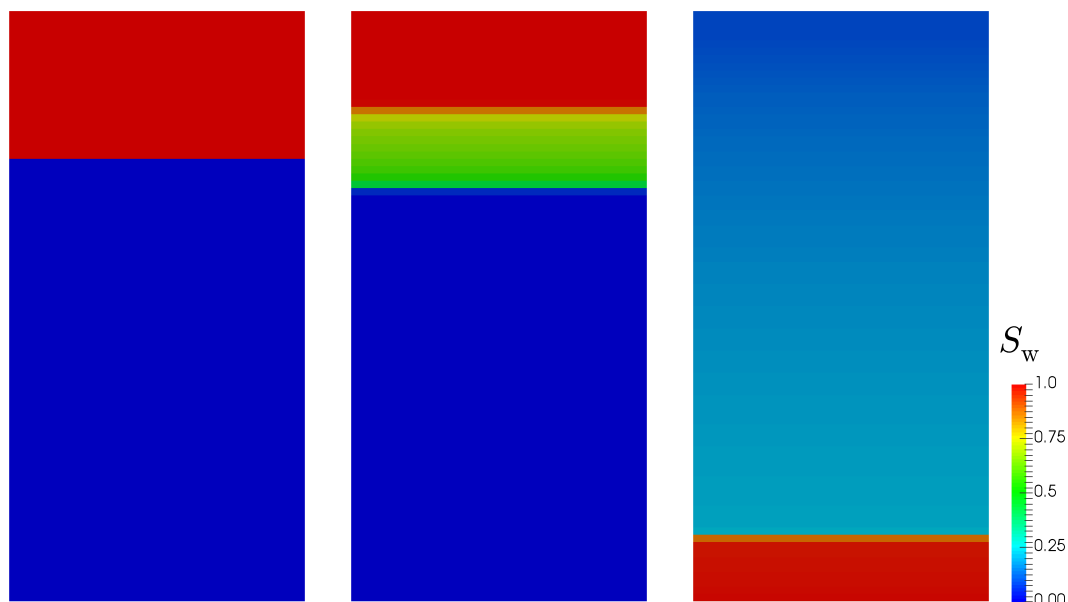


Figure 9.12.: Gravity driven test. On the left, the initial solution is depicted. In the middle, the solution is shown after Δt seconds and, on the right, at the end time

9.6.4. Application to the three-dimensional SPE10 Benchmark

In the previous numerical tests, we tested the method described in this thesis for two-dimensional problems, where it was demonstrated that fronts are well captured by our method with less numerical diffusion compared to the standard FI-TPFA method. In addition, it was shown that the scheme is also consistent for full anisotropic tensors. In the following example, we apply our method on a well-established three-dimensional problem with realistic geological data. The setting of this example is taken from the second problem of the SPE10 Benchmark [59]. The domain Ω is discretized by $60 \times 220 \times 85$ cells and has a size of $L_x \times L_y \times L_z = 365.76 \times 670.56 \times 51.816$ [m]. This yields the discretization sizes $dx = 6.096$ [m], $dy = 3.048$ [m] and $dz = 0.6096$ [m]. The permeability and porosity fields are depicted in Figure 9.13. The model consists of two different geological formations: a shallow-marine Tarbert formation in the top 35 layers and a fluvial Upper-Ness formation in the bottom 50 layers. In the upper formation, the permeability is relatively smooth, while the bottom formation possesses a more heterogeneous structure, including channels. In both formations, the permeabilities are characterized by large variations of 8-12 orders of magnitude.

We are interested in validating our method in terms of front propagation, and therefore we consider a simplified version of the original SPE10 Benchmark problem. Here, we simulate a flow driven by a pressure gradient, i.e., we impose Dirichlet boundary condition on the following sets

$$\Gamma_{D,\text{inj}} := \{(x, y, z) \in \partial\Omega : x < dx, y < dy\},$$

$$\Gamma_{D,\text{ext}} := \{(x, y, z) \in \partial\Omega : x > L_x - dx, y > L_y - dy\}.$$

On $\Gamma_{D,\text{inj}}$, we set $g_D = 6.8948 \cdot 10^7$ [Pa], while on $\Gamma_{D,\text{ext}}$, we impose $g_D = 2.7579 \cdot 10^7$ [Pa]. On the rest of the boundary $\partial\Omega \setminus (\Gamma_{D,\text{inj}} \cup \Gamma_{D,\text{ext}})$, no-flow condition is provided. Furthermore, we assume that the wetting phase (water) infiltrates from $\Gamma_{D,\text{inj}}$, i.e., $S_w = 1$.

Viscosity for the wetting phase is $\mu_w = 3 \cdot 10^{-4}$ [Pa · s], and for the non-wetting phase (oil) is $\mu_n = 3 \cdot 10^{-3}$ [Pa · s]. The relative permeabilities are chosen accordingly to the quadratic law (8.5). Initially, the domain is filled by the non-wetting phase. We choose a uniform time step of 10 days and the simulation runs until the water reaches the boundary $\Gamma_{D,\text{ext}}$. Gravity is neglected.

The original mesh consists of 1,220,000 elements making it hard to solve sequentially the linear system obtained with the SWIPG method. Therefore, the solution has been computed on 35 processors, yielding a total number of 1,326,960 elements, which includes the overlapping elements. For visualization purposes the z -axis is scaled by a factor five in all figures showing the three-dimensional model domain. We obtained a detection time of 240 days for the water front. The wetting phase saturation at this time is shown in Figure 9.14, on the bottom. On the top of Figure 9.14, the pressure field after the first time step is provided. As reference, a numerical solution is computed using the FI-TPFA method. The reference solution yields a detection time of 250 days, which is in good agreement with the result obtained with our

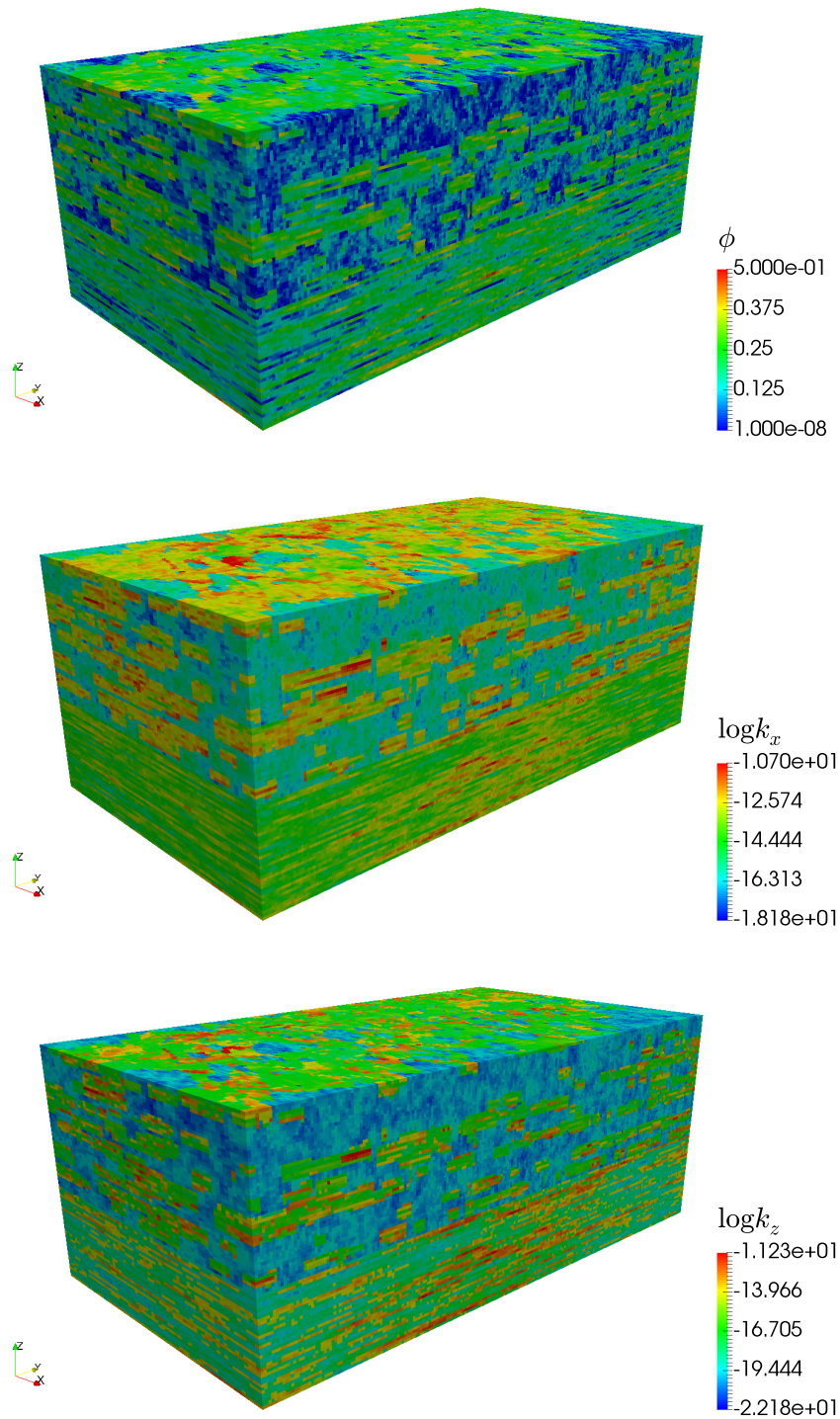


Figure 9.13.: On the top, the porosity is shown, while in the middle and on the bottom, the permeabilities in x and z direction are depicted, where the z -axis points in the depth direction. Permeabilities are isotropic in the x and y direction, i.e. $k_x = k_y$ (z -direction scaled by a factor of 5).

method (deviation of Δt). As in the two-dimensional heterogeneous problem from Section 9.6.1, the difference in the front propagation is caused by a higher numerical diffusion of the FI-TPFA method.

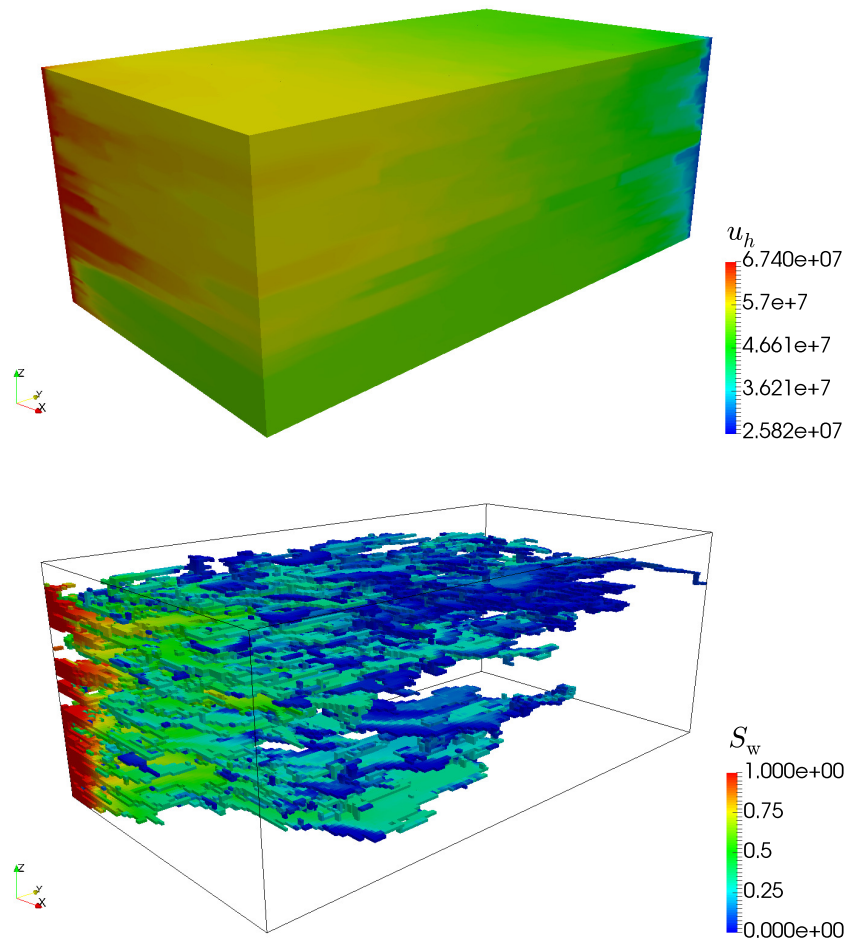


Figure 9.14.: On the top, the numerical solution of the pressure field for the SPE10 Benchmark is shown. On the bottom, saturation for the wetting phase is depicted over a threshold of 0.001 after 240 days (z -direction scaled by a factor of 5).

Conclusion and outlook

In this thesis we presented multiscale methods for solving complex flow and transport processes in porous media. In the first part of this work, we considered a mathematical model to describe blood flow in vascularized tissue. To simplify the analysis, we restricted the simulations to the microcirculation, where the assumption of stationary flow is acceptable. An accurate simulation of the flow is of foremost importance, if one wants to reproduce the transport of a substance from the circulatory system into the tissue or vice versa. Due to the huge amount of small vessels and capillaries contained even in a small portion of tissue, a well-established model reduction approach has been employed to reduce the three-dimensional microvascular system to a one-dimensional network. Considering the tissue as a porous medium, we described the interactions between capillaries and the surrounding tissue by means of Dirac measures concentrated on lower dimensional manifolds. The first possibility we considered consisted in concentrating the source term on the one-dimensional network itself, yielding coupled problems with heterogeneous dimensionality that have been employed for many years by now. The main drawback of this coupling strategy consists in having to deal with a singular right-hand sides concentrated on a manifold with codimension two. In this situation, the standard FEM fails to converge with optimal order, if graded mesh are not used in the vicinity of the singularity. In the case of a three-dimensional domain with source term concentrated on a C^2 -curve and where the coupling is neglected, we have shown that FEM converges optimal up to a log-term in a local norm, where the error is calculated away from the singularity. Thus, we were able to show that the Dirac measure does not pollute the numerical solution in the entire domain, but only in a neighbourhood of the singularity. In order to increase the regularity of the solution, we developed a new coupling approach, where the Dirac measure is concentrated on the lateral surface of the capillary, giving rise to source terms concentrated on manifolds of codimension one. Clearly, this strategy reflects the fact that the exchanges between the capillaries and the tissue actually occur across the boundary of the vessel. In a two-dimensional setting, we showed that this new approach ensures a higher regularity of the solution and higher order of convergence for a FEM approximation on uniform meshes. Furthermore, optimal order of convergence for the FEM were shown, if δ -resolving or graded meshes were employed. We investigated also the modeling error that arises when employing this coupling strategy and we were able to show both theoretically and by means of a numerical experiment a quasi-linear dependency of the modeling error with respect to the radius of the inclusion. Finally, this new coupling strategy has been employed to simulate the flow in a relatively small portion of a rat's brain. The geometry at our disposal consisted of

more than 15000 vessels. To reduce the computational costs and locally preserve mass, the numerical solution of the 3D-1D coupled problem was obtained by means of a finite volume discretization in both the porous medium and the network. However, if one plans to simulate larger portions of an organ, the 3D-1D coupled model revealed to be quite unfeasible because the data needed by the model are required at the microscale. Thus, we developed a new hybrid 3D-3D-1D approach, where the fine-structure of the capillaries has been considered as a three-dimensional porous medium. In this approach, the flow in the larger vessels has still been modeled by the same one-dimensional equations as in the 3D-1D coupled problem. On the other hand, the flow in both the tissue and the homogenized capillaries is governed by Darcy's law. New coupling strategies between the three continua were discussed. The results obtained with the new hybrid method have been compared with those obtained with the 3D-1D coupled model in terms of mass fluxes and averaged pressures.

In the second part of this thesis, an improved streamline method has been considered to simulate advection-dominated flows of two-phase systems of incompressible fluids in highly heterogeneous and anisotropic porous media, where capillary effects have been neglected. To the best of our knowledge, the streamline method has been combined for the first time with a DG approximation of the pressure equation for the computation of the velocity field in the context of an IMPES method for large three-dimensional applications. The scope of this method was to develop a fast and accurate strategy to simulate the displacement of an injected fluid in a reservoir and to predict the time of transport of such substance. To this end, an accurate approximation of the velocity field was a fundamental feature, which was guaranteed by the DG method. Due to the high computational costs of the DG approximation, the implementation of the streamline method has been developed to work on parallel architectures so that domain decomposition techniques could be used. To validate our method in terms of front displacement, the numerical solution obtained by means of a fully-implicit finite volume method based on a two-point flux approximation has been used as reference solution. By means of several two- and three-dimensional experiments, the reliability of our method has been shown for approximating sharp fronts, even if coarse meshes and large time steps are used.

The results presented in this thesis open a wide range of possible extensions. Due to the difficulties introduced by considering singular right-hand sides, we considered in this thesis only elliptic problems and the analysis of time-dependent problems with rough right-hand sides extending the results of Section 4 will be subject of future research. Furthermore, while the analysis of 3D-1D coupled problems with the source term modeled by a δ -Dirac on the line has been proposed in [66, Section 4], an extension to our new coupling strategy can be investigated. Moreover, our new hybrid model opens several directions of future works. In particular, it would be of interest to investigate the performance and the results obtained by our new model, if an entire organ is considered. In particular, we expect a reduced influence of the boundary conditions and a speed-up in the computation of the solution, when compared with the 3D-1D coupled model. However, some of the limitations of our hybrid model need first to be improved. More precisely, we employed in this

thesis the solution of the 3D-1D coupled model to tune a parameter in the hybrid model in order to optimize certain fluxes and this strategy needs to be automated. A better estimation of the involved simulation parameters may render the model more independent. We also point out that the hybrid model we presented allows us to compute only net fluxes. On the other hand, a clear advantage of the hybrid model is the fact that only data on a meso-scale are required to parametrize the model, whereas micro-scale data are necessary for 3D-1D coupled models, where a precise description of each vessel is required. Moreover, we point out that the multiscale methods presented in this work have been considered in a quite abstract setting. In fact, in Sections 4 and 5, the focus was posed on the analysis of the singularity of the solution and its FEM discretization. However, it has been shown that such coupling strategies are of interest in realistic applications, see, e.g., [52, 165]. In fact, obtaining a good approximation of the pressure and velocity fields is of foremost importance, when combined with mass transport problems for drug delivery through the microcirculation, where the velocity field is adopted to model advection. The extension of the works presented in this thesis to transport problems and the validation of the results by comparison with realistic data will be subject of future works.

To this end, an interesting research field is given by the development of models to simulate of waste removal in the brain, which may help to understand the impact of diseases such as Alzheimer's. A combination with the streamline approach developed in this thesis may be worth investigations. Related to this point, the streamline method should first be efficiently extended to incorporate capillary effects, which may be relatively easy to include introducing a further operator splitting step as in [47]. Then, the computational complexity can be contained exploiting the parallel features offered by our implementation of the streamline method. However, the major drawback of the streamline approach consists in the lack of mass-conservation and a way to improve the mass-balance in a general setting is still an open issue.

List of Figures

2.1.	Scheme of the two-point flux approximation $\overline{F}_{T,e}$ for the TPFA method.	23
II.1.	The image depicts synchrotron radiation based X-ray tomographic microscopy data of rat somatosensory cortex. Details of the data acquisition methodology can be found in [183]. The representation of the microscopy data in the vascular graph model is shown. The tortuous vessel parts between bifurcation or end points are replaced by straight connections, i.e., cylinders with a radius corresponding to the mean radius R of the vessel [190].	26
II.2.	The figure shows the generation of a vascular graph model for an arteriole. On the left, the arteriole is fully resolved and approximated by cylinders. In the middle, the centerlines are depicted and on the right, the vascular graph model for the arteriole is extracted. The arteriole is taken from Figure II.1.	27
3.1.	Ratio $\eta_r = \mu_{bl}/\mu_p$ after the <i>in vivo</i> viscosity (3.2) with respect to the diameter D of the vessel. The values for ν_r are plotted for different hematocrit levels.	31
3.2.	Schematic representation of the different coupling concepts: in the left figure, the exchange between the one-dimensional network and the porous medium is concentrated on the point s . On the right picture, the exchange between the two systems occurs at the surface of the circle centered in s	37
3.3.	Simplified two-dimensional situation obtained from a particular three-dimensional setting. On the top right figure, the coupling strategy (S1) is employed and therefore the source terms are concentrated on zero-dimensional manifolds. On the bottom right figure, the new coupling strategy (S2) is used and the exchanges occur across circular inclusions.	39
4.1.	The figure shows a contour plot for $u_{2,\text{fine}} = 0.1$ together with three different slices at $z = 0.2, 0.5, 0.8$	46
5.1.	Adapted meshes for a circular interface ∂B : δ -resolving mesh with $\delta = \mathcal{O}(h^2)$ (top), graded mesh (bottom).	61
5.2.	The numerical modeling error is calculated for different values of the mesh characteristic size ($h = 2^{-i}$ for $i = 3, \dots, 8$) and for different radii of the ball B_1 (each line shown with different colors). For each radius the modeling error values are interpolated using splines. We observe that as the mesh size h tends to zero, the error converges to a fixed value, which is the actual modeling error.	64

5.3.	Three different types of meshes are used for the first convergence test (single point source term). left: Uniform mesh (521 elements), middle: δ -resolving mesh, $\delta = \mathcal{O}(h^2)$ (1368 elements), right: Graded mesh (870 elements).	65
5.4.	Three-dimensional graph of the numerical solution $u_{h,2}$ based on the parameters in Table 5.4.	68
6.1.	Schematic representation of the average computation for the segment Λ_i . Around the quadrature points \mathbf{x}_1 , \mathbf{x}_2 and \mathbf{x}_3 , the corresponding circles with radius R_i are drawn, together with the quadrature points \mathbf{p}_t along them. No alignment of the segments with the three-dimensional mesh is required.	72
6.2.	Slice in the x -direction of the numerical solution of problem (6.7) on the finest mesh. The tube corresponding to the line Λ is depicted with a smaller radius that 0.15 for graphical reasons, so that the plateau of the solution u_H^t corresponding to each height z can easily be recognized.	75
6.3.	Discrete network structure Γ from [199] used for the simulations in this section.	77
6.4.	Numerical solution of problem (6.8). On the left, a slice in the z -axis of the numerical solution is depicted. The solution in the tissue appears to behave in accordance to the solution in the network.	78
6.5.	Plasma fluid paths from high-pressure capillaries to low-pressure capillaries through the interstitial space for the 3D-1D coupled problem (6.8).	79
7.1.	On the top, the microvascular network from Figure II.1 is reported. A subdivision based on the vessel radius can be seen at the bottom of the figure. The network at the bottom left consists of the network Λ_C of capillaries contained in the microvascular network, whose radius is smaller than a given threshold R_T , here 7 [μm]. The motivation for such threshold is postponed to Section 7.3.1. At the bottom right, the set Λ_L of arterioles and venules is reported.	81
7.2.	Subdivision of the capillary bed Λ_C into eight REV _s	83
7.3.	Homogenization of a capillary network contained in a REV _{j} . On the facets $F_{\text{in},x}^{(j)}$ and $F_{\text{out},x}^{(j)}$ whose normals are aligned with the x -axis, we apply pressures $u_{\text{in},x}$ and $u_{\text{out},x}$, while on the other facets a no-flow condition is imposed. Having the value of the numerical flux between $F_{\text{in},x}^{(j)}$ and $F_{\text{out},x}^{(j)}$ at hand, the permeability component $k_x^{(j)}$ can be estimated.	85
7.4.	The figure shows a two-dimensional layout parallel to the xy -plane of an REV _{j} that is located at an edge of the domain Ω . At the top of the figure, the discrete capillary network contained in the REV _{j} is shown, while in the bottom part of the figure, the homogenized system with the tensor $\mathbf{K}_{\text{up}}^{(j)}$ and the averaged boundary pressures $g_D^{(j2)}$ and $g_D^{(j3)}$ can be seen.	87

7.5.	Representation of the numerical fluxes through the surface of the control volume CV_i with center in \mathbf{x}_i	90
7.6.	Sparsity pattern of the discretization matrix of the hybrid model.	92
7.7.	On the left, the blood velocity for each vessel in the system Λ , where each segment is subject to a 1 [Pa] pressure difference. Setting the threshold to $R_T = 7$ [μm] yields 14918 vessels in the set Λ_C with average velocity of 0.00714 [mm/s], and 337 vessels in the set Λ_L with average velocity of 0.41533 [mm/s]. On the right, the system Λ_L is depicted in red for the threshold $R_T = 7$ [μm] and in green for the threshold $R_T = 18$ [μm].	93
7.8.	On the left, the upscaled permeability is computed in the case where a single control volume is positioned in the center of the domain Ω . The dimensions of the control volume are enlarged by approximately $4 \times 4 \times 8$ [μm] in each step until the control volume fills the entire domain Ω . The length of the control volume in the plot has to be doubled to obtain the actual size of the control volume in the z -direction. After an oscillating transition zone, each permeability stabilizes around a fixed value. On the right, the blood volume fraction of the corresponding control volume is reported.	94
7.9.	Histograms of the radii distributions of the capillaries contained in each control volume (CV), which are given as in Figure 7.10. The numeration is given according to Table 7.3. For each CV, the mean value $\text{avg}(\mathbf{R})$ of the radii and the standard deviation $\text{std}(\mathbf{R})$ are provided. In the last histogram, the radii distribution of the capillaries contained in the REV with the same center as the domain Ω and same dimensions as the other control volumes is reported.	95
7.10.	Permeability tensors \mathbf{K}_{up} in the case of $2 \times 2 \times 2$ REVs. The heterogeneous distribution of the capillaries from Figure 7.1 is therefore incorporated, in the sense that in the lower part of the domain, the flow occurs mainly in the xy -plane, while on the top in the z -direction.	96
7.11.	Graphs of the objective functions f_1 and f_2 . For f_1 , the minimum is reached at $\alpha = 0.46$, while, for f_2 it can be seen at a first glance that the minimum is attained at $\alpha = 0.4$	99
7.12.	Behaviour of the mass fluxes for the hybrid approach with respect to the number of degrees of freedom. At the top, the fluxes at the boundaries of the capillaries and of the large vessels are reported. At the bottom, the total net flux from the capillary bed into the tissue for the hybrid approach is presented.	101
9.1.	Numerical error of the discrete velocity projected onto different spaces.	118
9.2.	On the left, shock, on the right, rarefaction wave. The initial condition is plotted in red.	120
9.3.	Result of front tracking at different times for Example 9.3.	121
9.4.	Streamline in a two-dimension grid-block, after [184].	123

9.5.	L^2 -error of the numerical solution obtained with the streamline method with respect to h -refinement.	126
9.6.	Overlapping domain decomposition using two processors.	127
9.7.	Streamline crossing the processor border.	127
9.8.	In the left picture, the first component of the permeability field is depicted (the medium is isotropic). In the right picture, the porosity field is shown.	129
9.9.	At the top, the solutions after $1.3 \cdot 10^8$ [s] computed with our method on different meshes, from the coarsest (left picture) to the finest (right picture). At the bottom, the reference solutions computed with the FI-TPFA method on the corresponding meshes.	130
9.10.	Contour plots for $S_w = 10^{-5}$ for the solutions at the end time $1.5 \cdot 10^8$ [s] obtained with the method developed in this paper (on the left) and for the FI-TPFA solutions (on the right). In the legend, the corresponding mesh is provided.	131
9.11.	On the left, the numerical solution on the coarse mesh is shown at end time, while on the right picture, the solution has been computed on a uniformly refined mesh.	132
9.12.	Gravity driven test. On the left, the initial solution is depicted. In the middle, the solution is shown after Δt seconds and, on the right, at the end time	133
9.13.	On the top, the porosity is shown, while in the middle and on the bottom, the permeabilities in x and z direction are depicted, where the z -axis points in the depth direction. Permeabilities are isotropic in the x and y direction, i.e. $k_x = k_y$ (z -direction scaled by a factor of 5).	135
9.14.	On the top, the numerical solution of the pressure field for the SPE10 Benchmark is shown. On the bottom, saturation for the wetting phase is depicted over a threshold of 0.001 after 240 days (z -direction scaled by a factor of 5).	136

List of Tables

2.1.	Numerical L^2 -convergence rates for the FEM solution of problem (2.9) with singular right hand side and trial functions of order one and two.	20
4.1.	L^2 -error on $\Omega \setminus Z_R$ for $\Lambda = \Lambda_1$.	47
4.2.	Discrete L^2 -error on $\Omega \setminus Z_R$ for $\Lambda = \Lambda_2$.	47
5.1.	The numerical modelling error is shown for different radii and $L_{p,1} = U = 1$. The numerical convergence rate is reported in the last column.	64
5.2.	L^2 -norms of $e_{h,1}$ and convergence rates for three different meshes (uniform, δ -resolving, graded). In the last line of the table the theoretical convergence rates are listed.	66
5.3.	H^1 -norms of $e_{h,1}$ and convergence rates for three different meshes (uniform, δ -resolving, graded). In the last line of the table the theoretical convergence rates are listed.	66
5.4.	Parameter set used for problem (5.3) with $N = 5$ source terms.	67
5.5.	L^2 - and H^1 -norms and of $e_{h,2}$. The theoretical convergence rates are listed in the last line of the table.	69
6.1.	L^2 -norm of the errors e_h^v and e_H^t for the 3D-1D coupled problem (6.7).	76
6.2.	Positions and corresponding pressure values for the boundary nodes in the network from [199].	78
6.3.	Discrete L^2 -norm of the errors in the network and in the tissue for the 3D-1D coupled problem (6.8).	79
7.1.	Values of the parameters used for the numerical experiments.	92
7.2.	Mass fluxes at the boundaries and interfaces of the vascular system. All the fluxes that are presented in this table are reported in $\mu\text{g/s}$. For the hybrid method, the fluxes are obtained for two different α according to the minima of the objective functions f_1 and f_2 .	100
7.3.	Averaged REV-pressures in the capillaries and in the tissue.	102
7.4.	Averaged relative errors of the REV-pressures in the capillaries and in the tissue with respect to the degrees of freedom (dofs).	102

Bibliography

- [1] I. AAVATSMARK, *An introduction to multipoint flux approximations for quadrilateral grids*, Computational Geosciences, 6 (2002), pp. 405–432. 111
- [2] —, *Interpretation of a two-point flux stencil for skew parallelogram grids*, Computational geosciences, 11 (2007), pp. 199–206. 23
- [3] —, *Comparison of monotonicity for some multipoint flux approximation methods*, in Finite Volumes for Complex Applications, vol. 5, Citeseer, 2008, pp. 19–34. 111
- [4] I. AAVATSMARK, T. BARKVE, Ø. BØE, AND T. MANNSETH, *Discretization on non-orthogonal, quadrilateral grids for inhomogeneous, anisotropic media*, Journal of Computational Physics, 127 (1996), pp. 2–14. 109
- [5] I. AAVATSMARK, G. EIGESTAD, B. MALLISON, AND J. NORDBOTTEN, *A compact multipoint flux approximation method with improved robustness*, Numerical Methods for Partial Differential Equations: An International Journal, 24 (2008), pp. 1329–1360. 111
- [6] R. A. ADAMS AND J. J. FOURNIER, *Sobolev spaces*, vol. 140, Academic press, 2003. 15, 16, 44
- [7] M. AHMADPOUR, M. SIAVASHI, AND M. MOGHIMI, *Numerical simulation of two-phase mass transport in three-dimensional naturally fractured reservoirs using discrete streamlines*, Numerical Heat Transfer, Part A: Applications, 73 (2018), pp. 482–500. 112
- [8] M. B. ALLEN, R. E. EWING, AND P. LU, *Well-conditioned iterative schemes for mixed finite-element models of porous-media flows*, SIAM Journal on Scientific and Statistical Computing, 13 (1992), pp. 794–814. 111
- [9] F. ANDREU, J. MAZÓN, AND J. ROSSI, *The best constant for the Sobolev trace embedding from $W^{1,1}(\Omega)$ into $L^1(\partial\Omega)$* , Nonlinear Analysis: Theory, Methods & Applications, 59 (2004), pp. 1125–1145. 49
- [10] T. APEL, O. BENEDIX, D. SIRCH, AND B. VEXLER, *A priori mesh grading for an elliptic problem with Dirac right-hand side*, SIAM Journal on Numerical Analysis, 49 (2011), pp. 992–1005. 19, 37, 60

- [11] D. N. ARNOLD AND F. BREZZI, *Mixed and nonconforming finite element methods: implementation, postprocessing and error estimates*, ESAIM: Mathematical Modelling and Numerical Analysis, 19 (1985), pp. 7–32. 106
- [12] D. N. ARNOLD, F. BREZZI, B. COCKBURN, AND L. D. MARINI, *Unified analysis of discontinuous Galerkin methods for elliptic problems*, SIAM Journal on Numerical Analysis, 39 (2002), pp. 1749–1779. 111
- [13] P. W. ATKINS AND J. DE PAULA, *Physikalische Chemie*, John Wiley & Sons, 2013. 107
- [14] C. BACUTA, J. BRAMBLE, AND J. XU, *Regularity estimates for elliptic boundary value problems in Besov spaces*, Mathematics of Computation, 72 (2003), pp. 1577–1595. 60
- [15] R. BAKER, F. KUPPE, S. CHUGH, R. BORA, S. STOJANOVIC, R. BATYCKY, ET AL., *Full-field modeling using streamline-based simulation: 4 case studies*, in SPE Reservoir Simulation Symposium, Society of Petroleum Engineers, 2001. 125
- [16] P. BASTIAN, *Benchmark 3D: Symmetric weighted interior penalty discontinuous Galerkin scheme*, in Finite Volumes for Complex Applications VI Problems & Perspectives, Springer, 2011, pp. 949–959. 111, 115, 116
- [17] —, *A fully-coupled discontinuous Galerkin method for two-phase flow in porous media with discontinuous capillary pressure*, Computational Geosciences, 18 (2014), pp. 779–796. 106, 109, 115, 116
- [18] P. BASTIAN, M. BLATT, A. DEDNER, C. ENGWER, R. KLÖFKORN, R. KORNHUBER, M. OHLBERGER, AND O. SANDER, *A generic grid interface for parallel and adaptive scientific computing. Part II: Implementation and tests in DUNE*, Computing, 82 (2008), pp. 121–138. 46, 73, 113, 116
- [19] P. BASTIAN, M. BLATT, A. DEDNER, C. ENGWER, R. KLÖFKORN, M. OHLBERGER, AND O. SANDER, *A generic grid interface for parallel and adaptive scientific computing. Part I: Abstract framework*, Computing, 82 (2008), pp. 103–119. 73
- [20] P. BASTIAN, M. BLATT, AND R. SCHEICHL, *Algebraic multigrid for discontinuous Galerkin discretizations of heterogeneous elliptic problems*, Numerical Linear Algebra with Applications, 19 (2012), pp. 367–388. 116
- [21] P. BASTIAN AND B. RIVIÈRE, *Superconvergence and $H(\text{div})$ projection for discontinuous Galerkin methods*, International Journal for Numerical Methods in Fluids, 42 (2003), pp. 1043–1057. 111, 116

- [22] R. BATYCKY, M. J. BLUNT, M. R. THIELE, ET AL., *A 3D field-scale streamline-based reservoir simulator*, SPE Reservoir Engineering, 12 (1997), pp. 246–254. 112
- [23] R. P. BATYCKY, *A three-dimensional two-phase field scale streamline simulator*, PhD thesis, Stanford University, 1997. 112, 113
- [24] Y. BAYAZITOGLU, S. KHERADMAND, AND T. K. TULLIUS, *An overview of nanoparticle assisted laser therapy*, International Journal of Heat and Mass Transfer, 67 (2013), pp. 469–486. 11
- [25] J. BEAR, *Dynamics of fluids in porous media*, Courier Corporation, 2013. 83, 88
- [26] ———, *Modeling Phenomena of Flow and Transport in Porous Media*, vol. 31, Springer, 2018. 107
- [27] V. T. BERALDO, M. J. BLUNT, D. J. SCHIOZER, ET AL., *Compressible streamline-based simulation with changes in oil composition*, SPE reservoir evaluation & engineering, 12 (2009), pp. 963–973. 113
- [28] R. BERENBLYUM, *Streamline simulation with capillary effects applied to petroleum engineering problems*, PhD thesis, Technical University of Denmark, 2004. 112, 114
- [29] J. BERGH AND J. LÖFSTRÖM, *Interpolation Spaces: An Introduction*, vol. 223, Springer Science & Business Media, 2012. 16
- [30] M. BERNDT, K. LIPNIKOV, M. SHASHKOV, M. F. WHEELER, AND I. YOTOV, *Superconvergence of the velocity in mimetic finite difference methods on quadrilaterals*, SIAM Journal on Numerical Analysis, 43 (2005), pp. 1728–1749. 111
- [31] I. BERRE, H. K. DAHLE, K. H. KARLSEN, AND H. F. NORDHAUG, *A streamline front tracking method for two-and three-phase flow including capillary forces*, Contemporary Mathematics, 295 (2002), pp. 49–62. 114, 124
- [32] P. BHAMBRI AND K. MOHANTY, *Compositional streamline simulation: a parallel implementation*, Transport in porous media, 90 (2011), pp. 741–761. 113
- [33] M. BLATT AND P. BASTIAN, *The Iterative Solver Template Library*, in International Workshop on Applied Parallel Computing, Springer, 2006, pp. 666–675. 91
- [34] ———, *On the generic parallelisation of iterative solvers for the finite element method*, International Journal of Computational Science and Engineering, 4 (2008), pp. 56–69. 91

- [35] M. BLATT, A. BURCHARDT, A. DEDNER, C. ENGWER, J. FAHLKE, B. FLEMISCH, C. GERSBACHER, C. GRÄSER, F. GRUBER, C. GRÜNINGER, ET AL., *The distributed and unified numerics environment, version 2.4*, Archive of Numerical Software, 4 (2016), pp. 13–29. 86
- [36] D. BRAESS, *Finite elements: Theory, fast solvers, and applications in solid mechanics*, Cambridge University Press, 2007. 15, 18
- [37] F. BRATVEDT, T. GIMSE, AND C. TEGNANDER, *Streamline computations for porous media flow including gravity*, Transport in Porous Media, 25 (1996), pp. 63–78. 125
- [38] S. BRENNER AND R. SCOTT, *The mathematical theory of finite element methods*, vol. 15, Springer Science & Business Media, 2007. 15, 18, 19, 56, 59
- [39] F. BREZZI, J. DOUGLAS, AND L. D. MARINI, *Two families of mixed finite elements for second order elliptic problems*, Numerische Mathematik, 47 (1985), pp. 217–235. 116
- [40] F. BREZZI AND M. FORTIN, *Mixed and hybrid finite element methods*, vol. 15, Springer Science & Business Media, 2012. 111, 116
- [41] F. BREZZI, K. LIPNIKOV, AND M. SHASHKOV, *Convergence of the mimetic finite difference method for diffusion problems on polyhedral meshes*, SIAM Journal on Numerical Analysis, 43 (2005), pp. 1872–1896. 111
- [42] F. BREZZI, K. LIPNIKOV, AND V. SIMONCINI, *A family of mimetic finite difference methods on polygonal and polyhedral meshes*, Mathematical Models and Methods in Applied Sciences, 15 (2005), pp. 1533–1551. 106
- [43] R. H. BROOKS AND A. T. COREY, *Hydraulic properties of porous media*, vol. 3 of Hydrology papers, Fort Collins, Colo., 1964. 107
- [44] R. H. BROOKS AND A. T. COREY, *Hydraulic properties of porous media and their relation to drainage design*, Trans. ASAE, 7 (1964), pp. 26–28. 108
- [45] Z. CAI, *On the finite volume element method*, Numerische Mathematik, 58 (1990), pp. 713–735. 23
- [46] S. ČANIĆ AND E. H. KIM, *Mathematical analysis of the quasilinear effects in a hyperbolic model blood flow through compliant axi-symmetric vessels*, Mathematical Methods in the Applied Sciences, 26 (2003), pp. 1161–1186. 27
- [47] Y. CAO, *Robust numerical algorithms based on corrected operator splitting for two-phase flow in porous media*, PhD thesis, Universität Stuttgart, 2010. 125, 126, 139

- [48] Y. CAO, B. EIKEMO, AND R. HELMIG, *Fractional flow formulation for two-phase flow in porous Media*, GRK 1398/1, 2007. 12, 105
- [49] Y. CAO, R. HELMIG, AND B. WOHLMUTH, *The influence of the boundary discretization on the multipoint flux approximation L-method*, Finite Volumes for Complex Applications V, ISTE, London, (2008), pp. 257–263. 111
- [50] Y. CAO, R. HELMIG, AND B. WOHLMUTH, *A two-scale operator-splitting method for two-phase flow in porous media*, Advances in Water Resources, 34 (2011), pp. 1581–1596. 113, 114, 124
- [51] E. CASAS, *L^2 estimates for the finite element method for the Dirichlet problem with singular data*, Numerische Mathematik, 47 (1985), pp. 627–632. 20, 41
- [52] L. CATTANEO AND P. ZUNINO, *A computational model of drug delivery through microcirculation to compare different tumor treatments*, International journal for numerical methods in biomedical engineering, 30 (2014), pp. 1347–1371. 12, 25, 28, 139
- [53] L. CATTANEO AND P. ZUNINO, *Numerical investigation of convergence rates for the FEM approximation of 3D-1D coupled problems*, in Numerical Mathematics and Advanced Applications-ENUMATH 2013, Springer, 2015, pp. 727–734. 41
- [54] Z. CHEN AND R. E. EWING, *Numerical methods for three models of compositional flow in porous media*, IMACS Series in Computational and Applied Mathematics J. Wang, et al. eds, 4 (1998), pp. 85–90. 109
- [55] Z. CHEN, R. E. EWING, Q. JIANG, AND A. M. SPAGNUOLO, *Degenerate two-phase incompressible flow V. Characteristic finite element methods*, Journal of Numerical Mathematics, 10 (2002), pp. 87–107. 112
- [56] Z. CHEN, G. HUAN, AND Y. MA, *Computational methods for multiphase flows in porous media*, SIAM, 2006. 105
- [57] Z. CHEN AND X. YUE, *Numerical homogenization of well singularities in the flow transport through heterogeneous porous media*, Multiscale Modeling & Simulation, 1 (2003), pp. 260–303. 39
- [58] H. CHENG, I. OSAKO, A. DATTA-GUPTA, M. J. KING, ET AL., *A rigorous compressible streamline formulation for two and three-phase black-oil simulation*, SPE Journal, 11 (2006), pp. 407–417. 112, 113
- [59] M. CHRISTIE, M. BLUNT, ET AL., *Tenth SPE comparative solution project: A comparison of upscaling techniques*, in SPE Reservoir Simulation Symposium, Society of Petroleum Engineers, 2001. 129, 134

- [60] P. G. CIARLET, *Basic error estimates for elliptic problems*, Handbook of Numerical Analysis, 2 (1991), pp. 17–351. 45
- [61] —, *The finite element method for elliptic problems*, SIAM, 2002. 17
- [62] O. A. CIRPKA, E. O. FRIND, AND R. HELMIG, *Streamline-oriented grid generation for transport modelling in two-dimensional domains including wells*, Advances in Water Resources, 22 (1999), pp. 697–710. 112
- [63] B. COCKBURN, S.-Y. LIN, AND C.-W. SHU, *TVB Runge-Kutta local projection discontinuous Galerkin finite element method for conservation laws III. One-dimensional systems*, Journal of Computational Physics, 84 (1989), pp. 90–113. 112
- [64] B. COCKBURN AND C.-W. SHU, *TVB Runge-Kutta local projection discontinuous Galerkin finite element method for conservation laws. II. General Framework*, Mathematics of computation, 52 (1989), pp. 411–435. 112
- [65] C. D'ANGELO, *Multi scale modelling of metabolism and transport phenomena in living tissues*, PhD thesis, École Polytechnique Fédérale de Lausanne, 2007. 12, 28, 35, 36, 37, 70, 73
- [66] C. D'ANGELO, *Finite element approximation of elliptic problems with Dirac measure terms in weighted spaces: Applications to one- and three-dimensional coupled problems*, SIAM Journal on Numerical Analysis, 50 (2012), pp. 194–215. 28, 37, 60, 77, 138
- [67] C. D'ANGELO AND A. QUARTERONI, *On the coupling of 1D and 3D diffusion-reaction equations: Application to tissue perfusion problems*, Mathematical Models and Methods in Applied Sciences, 18 (2008), pp. 1481–1504. 13, 37
- [68] M. Y. DARCIS, *Coupling models of different complexity for the simulation of CO₂ storage in deep saline aquifers*, PhD thesis, Universität Stuttgart, 2013. 105
- [69] H. DARCY, *Les Fontaines publiques de la ville de Dijon. Exposition et application des principes à suivre et des formules à employer dans les questions de distribution d'eau, etc*, Victor Dalmont, 1856. 107
- [70] C. DAWSON, T. RUSSELL, AND M. WHEELER, *Some improved error estimates for the modified method of characteristics*, SIAM Journal on Numerical Analysis, 26 (1989), pp. 1487–1512. 112
- [71] C. N. DAWSON, H. KLÍE, M. F. WHEELER, AND C. S. WOODWARD, *A parallel, implicit, cell-centered method for two-phase flow with a preconditioned Newton-Krylov solver*, Computational Geosciences, 1 (1997), pp. 215–249. 109

- [72] D. A. DI PIETRO AND A. ERN, *Analysis of a discontinuous Galerkin method for heterogeneous diffusion problems with low-regularity solutions*, Numerical Methods for Partial Differential Equations, 28 (2012), pp. 1161–1177. 21
- [73] P. A. M. DIRAC, *The principles of quantum mechanics*, no. 27, Oxford university press, 1981. 19
- [74] J. DOUGLAS JR, C.-S. HUANG, AND F. PEREIRA, *The modified method of characteristics with adjusted advection*, Numerische Mathematik, 83 (1999), pp. 353–369. 112
- [75] M. G. EDWARDS AND C. F. ROGERS, *Finite volume discretization with imposed flux continuity for the general tensor pressure equation*, Computational geosciences, 2 (1998), pp. 259–290. 109
- [76] G. EIGESTAD AND R. KLAUSEN, *On the convergence of the multi-point flux approximation O-method: Numerical experiments for discontinuous permeability*, Numerical Methods for Partial Differential Equations: An International Journal, 21 (2005), pp. 1079–1098. 111
- [77] W. EL-BOURI AND S. PAYNE, *Investigating the effects of a penetrating vessel occlusion with a multi-scale microvasculature model of the human cerebral cortex*, NeuroImage, 172 (2018), pp. 94–106. 80, 93
- [78] W. K. EL-BOURI AND S. J. PAYNE, *Multi-scale homogenization of blood flow in 3-dimensional human cerebral microvascular networks*, Journal of Theoretical Biology, 380 (2015), pp. 40–47. 28, 84
- [79] A. ENGLERT, U. HASHAGEN, U. JAEKEL, O. NITZSCHE, H. SCHWARZE, AND H. VEREECKEN, *Transport von gelösten Stoffen im Grundwasser: Untersuchungen am Testfeld Krauthausen*, Grundwasser, 5 (2000), pp. 115–124. 105
- [80] Y. EPSHTEYN AND B. RIVIERE, *Convergence of high order methods for miscible displacement*, International Journal of Numerical Analysis and Modeling, 5 (2008), pp. 47–63. 111
- [81] K. ERBERTSEDER, J. REICHOLD, B. FLEMISCH, P. JENNY, AND R. HELMIG, *A coupled discrete/continuum model for describing cancer-therapeutic transport in the lung*, PLoS ONE, 7 (2012), p. e31966. 80, 90
- [82] L. EVANS, *Partial differential equations*, vol. 19, American Mathematical Society, 1998. 15, 16, 67
- [83] R. E. EWING, T. F. RUSSELL, AND M. F. WHEELER, *Convergence analysis of an approximation of miscible displacement in porous media by mixed finite elements and a modified method of characteristics*, Computer Methods in Applied Mechanics and Engineering, 47 (1984), pp. 73–92. 112

- [84] R. E. EWING AND H. WANG, *Eulerian-Lagrangian localized adjoint methods for variable-coefficient advective-diffusive-reactive equations in groundwater contaminant transport*, in *Advances in Optimization and Numerical Analysis*, Springer, 1994, pp. 185–205. 112
- [85] —, *An optimal-order estimate for Eulerian-Lagrangian localized adjoint methods for variable-coefficient advection-reaction problems*, *SIAM Journal on Numerical Analysis*, 33 (1996), pp. 318–348. 112
- [86] R. EYMARD, T. GALLOUËT, AND R. HERBIN, *Finite volume methods*, *Handbook of Numerical Analysis*, 7 (2000), pp. 713–1018. 112
- [87] R. EYMARD, R. HERBIN, AND A. MICHEL, *Mathematical study of a petroleum-engineering scheme*, *ESAIM: Mathematical Modelling and Numerical Analysis*, 37 (2003), pp. 937–972. 109
- [88] R. FAHRAEUS AND T. LINDQVIST, *The viscosity of the blood in narrow capillary tubes*, *American Journal of Physiology-Legacy Content*, 96 (1931), pp. 562–568. 30
- [89] R. FARAJZADEH, A. EFTEKHARI, H. HAJIBEYGI, S. KAHROBAEI, J. VAN DER MEER, S. VINCENT-BONNIEU, AND W. ROSSEN, *Simulation of instabilities and fingering in surfactant alternating gas (SAG) foam enhanced oil recovery*, *Journal of Natural Gas Science and Engineering*, 34 (2016), pp. 1191–1204. 105
- [90] B. FLEMISCH, J. FRITZ, R. HELMIG, J. NIESSNER, AND B. WOHLMUTH, *DUMUX: A multi-scale multi-physics toolbox for flow and transport processes in porous media*, in *ECCOMAS Thematic Conference on Multiscale Computational Methods for Solids and Fluids*, 2007, pp. 82–87. 73, 108
- [91] L. FORMAGGIA, A. FUMAGALLI, A. SCOTTI, AND P. RUFFO, *A reduced model for Darcy’s problem in networks of fractures*, *ESAIM: Mathematical Modelling and Numerical Analysis*, 48 (2014), pp. 1089–1116. 37
- [92] L. FORMAGGIA, F. NOBILE, A. QUARTERONI, AND A. VENEZIANI, *Multiscale modelling of the circulatory system: A preliminary analysis*, *Computing and visualization in science*, 2 (1999), pp. 75–83. 27
- [93] L. FORMAGGIA, A. QUARTERONI, AND A. VENEZIANI, *Cardiovascular mathematics: Modeling and simulation of the circulatory system*, vol. 1, Springer Science & Business Media, 2010. 12, 25, 27, 30, 31, 32
- [94] J. FRANC, P. HORGUE, R. GUIBERT, AND G. DEBENEST, *Benchmark of different CFL conditions for IMPES*, *Comptes Rendus Mécanique*, 344 (2016), pp. 715–724. 111

- [95] S. FREI AND T. RICHTER, *A locally modified parametric finite element method for interface problems*, SIAM Journal on Numerical Analysis, 52 (2014), pp. 2315–2334. 60
- [96] H. FRIEBOES, M. WU, J. LOWENGRUB, P. DECUZZI, AND V. CRISTINI, *A computational model for predicting nanoparticle accumulation in tumor vasculature*, PLoS ONE, 8 (2013). 25
- [97] M. G. GERRITSEN, H. LÖF, AND M. R. THIELE, *Parallel implementations of streamline simulators*, Computational Geosciences, 13 (2009), p. 135. 112, 113
- [98] R. GHOSTINE, G. KESSERWANI, R. MOSÉ, J. VAZQUEZ, AND A. GHENAIM, *An improvement of classical slope limiters for high-order discontinuous Galerkin method*, International Journal for Numerical Methods in Fluids, 59 (2009), pp. 423–442. 112
- [99] D. GILBARG AND N. TRUDINGER, *Elliptic Partial Differential Equations of Second Order*, vol. 224, Springer Science & Business Media, 2001. 42, 44, 54
- [100] B. GINZBURG AND A. KATCHALSKY, *The frictional coefficients of the flows of non-electrolytes through artificial membranes*, The Journal of General Physiology, 47 (1963), pp. 403–418. 36
- [101] V. GIRAULT, K. KUMAR, AND M. F. WHEELER, *Convergence of iterative coupling of geomechanics with flow in a fractured poroelastic medium*, Computational Geosciences, 20 (2016), pp. 997–1011. 37
- [102] I. G. GJERDE, K. KUMAR, J. M. NORDBOTTEN, AND B. WOHLMUTH, *Splitting method for elliptic equations with line sources*, <https://arxiv.org/abs/1810.12979>, (2018). 69
- [103] W. GONG, G. WANG, AND N. YAN, *Approximations of elliptic optimal control problems with controls acting on a lower dimensional manifold*, SIAM Journal on Control and Optimization, 52 (2014), pp. 2008–2035. 41, 46, 53
- [104] P. GONZÁLEZ, M. KINDELAN, AND F. J. MUSTIELES, *Modelling capillary pressure in a streamline reservoir simulator using operator splitting*, in Progress in Industrial Mathematics at ECMI 2002, Springer, 2004, pp. 291–296. 114
- [105] P. GRASSIA, *Pressure-driven growth in strongly heterogeneous systems*, European Physical Journal E, (2018). 105
- [106] S. D. GREGORIO, L. POSSENTI, S. DI GREGORIO, F. M. GEROSA, G. RAIMONDI, G. CASAGRANDE, M. L. COSTANTINO, AND P. ZUNINO, *A computational model for microcirculation including fahraeus-lindqvist effect, plasma skimming and fluid exchange with the tissue interstitium*, International Journal for Numerical Methods in Biomedical Engineering, (2018). 12, 29

- [107] E. GUNDERSEN AND H. P. LANGTANGEN, *Finite element methods for two-phase flow in heterogeneous porous media*, in Numerical Methods and Software Tools in Industrial Mathematics, Springer, 1997, pp. 213–234. 105
- [108] S. GUPTA, R. HELMIG, AND B. WOHLMUTH, *Non-isothermal, multi-phase, multi-component flows through deformable methane hydrate reservoirs*, Computational Geosciences, 19 (2015), pp. 1063–1088. 105
- [109] H. HÆGLAND, H. DAHLE, G. EIGESTAD, K.-A. LIE, AND I. AAVATSMARK, *Improved streamlines and time-of-flight for streamline simulation on irregular grids*, Advances in Water Resources, 30 (2007), pp. 1027–1045. 114
- [110] R. HELMIG, *Multiphase flow and transport processes in the subsurface: a contribution to the modeling of hydrosystems*, Springer-Verlag, 1997. 28, 33, 83, 88, 106, 109
- [111] R. HERBIN AND F. HUBERT, *Benchmark on discretization schemes for anisotropic diffusion problems on general grids*, in Finite volumes for complex applications V, Wiley, 2008, pp. 659–692. 117
- [112] I. HERRERA, R. E. EWING, M. A. CELIA, AND T. F. RUSSELL, *Eulerian-Lagrangian localized adjoint method: The theoretical framework*, Numerical Methods for Partial Differential Equations, 9 (1993), pp. 431–457. 112
- [113] H. HOLDEN, *Splitting methods for partial differential equations with rough solutions: Analysis and MATLAB programs*, European Mathematical Society, 2010. 112, 125, 126
- [114] H. HOLDEN, L. HOLDEN, AND R. HØEGH-KROHN, *A numerical method for first order nonlinear scalar conservation laws in one-dimension*, Computers & Mathematics with Applications, 15 (1988), pp. 595–602. 113, 118
- [115] H. HOLDEN AND N. H. RISEBRO, *Front tracking for hyperbolic conservation laws*, vol. 152, Springer, 2015. 113, 118, 119, 121
- [116] K. E. HOLTER, B. KEHLET, A. DEVOR, T. J. SEJNOWSKI, A. M. DALE, S. W. OMHOLT, O. P. OTTERSEN, E. A. NAGELHUS, K.-A. MARDAL, AND K. H. PETTERSEN, *Interstitial solute transport in 3D reconstructed neuropil occurs by diffusion rather than bulk flow*, Proceedings of the National Academy of Sciences, 114 (2017), pp. 9894–9899. 25
- [117] C. HORGAN, *Eigenvalue estimates and the trace theorem*, Journal of Mathematical Analysis and Applications, 69 (1979), pp. 231–242. 50
- [118] S. M. HOSSEINI-NASAB AND P. L. ZITHA, *Investigation of chemical-foam design as a novel approach toward immiscible foam flooding for enhanced oil recovery*, Energy & Fuels, 31 (2017), pp. 10525–10534. 105

- [119] H. HOTEIT, P. ACKERER, AND R. MOSÉ, *Nuclear waste disposal simulations: Coupled test cases*, Computational Geosciences, 8 (2004), pp. 99–124. 12, 105
- [120] H. HOTEIT, P. ACKERER, R. MOSÉ, J. ERHEL, AND B. PHILIPPE, *New two-dimensional slope limiters for discontinuous Galerkin methods on arbitrary meshes*, International Journal for Numerical Methods in Engineering, 61 (2004), pp. 2566–2593. 112
- [121] C.-S. HUANG, *Convergence analysis of a mass-conserving approximation of immiscible displacement in porous media by mixed finite elements and a modified method of characteristics with adjusted advection*, Computational Geosciences, 4 (2000), pp. 165–184. 111
- [122] R. U. HUBER, *Compositional multiphase flow and transport in heterogeneous porous media*, Eigenverl. d. Inst. f. Wasserbau an d. Univ. Stuttgart, 2000. 109
- [123] J. HYMAN, J. MOREL, M. SHASHKOV, AND S. STEINBERG, *Mimetic finite difference methods for diffusion equations*, Computational Geosciences, 6 (2002), pp. 333–352. 111
- [124] M. INTAGLIETTA AND B. ZWEIFACH, *Indirect method for measurement of pressure in blood capillaries*, Circulation Research, 19 (1966), pp. 199–205. 77
- [125] Y. ITURRIA-MEDINA, R. C. SOTERO, P. J. TOUSSAINT, J. M. MATEOS-PÉREZ, A. C. EVANS, M. W. WEINER, P. AISEN, R. PETERSEN, C. R. JACK, W. JAGUST, ET AL., *Early role of vascular dysregulation on late-onset Alzheimer’s disease based on multifactorial data-driven analysis*, Nature Communications, 7 (2016), p. 11934. 25
- [126] J. JAFFRÉ AND J. ROBERTS, *Modeling flow in porous media with fractures: Discrete fracture models with matrix-fracture exchange*, Numerical Analysis and Applications, 5 (2012), pp. 162–167. 37
- [127] P. JENNY, S. H. LEE, AND H. A. TCHELEPI, *Adaptive fully implicit multi-scale finite-volume method for multi-phase flow and transport in heterogeneous porous media*, Journal of Computational Physics, 217 (2006), pp. 627–641. 109
- [128] K. JESSEN, F. ORR JR, ET AL., *Gravity segregation and compositional streamline simulation*, in SPE/DOE Symposium on Improved Oil Recovery, Society of Petroleum Engineers, 2004. 112
- [129] E. JIMENEZ, K. SABIR, A. DATTA-GUPTA, M. J. KING, ET AL., *Spatial error and convergence in streamline simulation*, in SPE Reservoir Simulation Symposium, Society of Petroleum Engineers, 2005. 114
- [130] G. JO AND D. Y. KWAK, *An IMPES scheme for a two-phase flow in heterogeneous porous media using a structured grid*, Computer Methods in Applied Mechanics and Engineering, 317 (2017), pp. 684–701. 111

- [131] W. JONES AND K. MENZIES, *Analysis of the cell-centred finite volume method for the diffusion equation*, Journal of Computational Physics, 165 (2000), pp. 45–68. 24
- [132] K. H. KARLSEN, K.-A. LIE, N. H. RISEBRO, J. FROYEN, ET AL., *A front tracking approach to a two-phase fluid flow model with capillary forces*, In Situ, 22 (1998), pp. 59–90. 114
- [133] A. KHALED AND K. VAFAI, *The role of porous media in modeling flow and heat transfer in biological tissues*, International Journal of Heat and Mass Transfer, 46 (2003), pp. 4989–5003. 28
- [134] M. F. KIANI AND A. G. HUDETZ, *A semi-empirical model of apparent blood viscosity as a function of vessel diameter and discharge hematocrit*, Biorheology, 28 (1991), pp. 65–73. 30
- [135] V. KIPPE, H. HÆGLAND, K.-A. LIE, ET AL., *A method to improve the mass balance in streamline methods*, in SPE Reservoir Simulation Symposium, Society of Petroleum Engineers, 2007. 113, 124
- [136] R. A. KLAUSEN AND A. F. STEPHANSEN, *Convergence of multi-point flux approximations on general grids and media*, International Journal of Numerical Analysis & Modeling, 9 (2012). 23, 24
- [137] R. A. KLAUSEN AND R. WINTHER, *Robust convergence of multi point flux approximation on rough grids*, Numerische Mathematik, 104 (2006), pp. 317–337. 111
- [138] T. KÖPPL, E. VIDOTTO, AND B. WOHLMUTH, *A local error estimate for the Poisson equation with a line source term*, in Numerical Mathematics and Advanced Applications ENUMATH 2015, Springer, 2016, pp. 421–429. 7, 28, 37, 40, 42, 46
- [139] T. KÖPPL, E. VIDOTTO, B. WOHLMUTH, AND P. ZUNINO, *Mathematical modeling, analysis and numerical approximation of second-order elliptic problems with inclusions*, Mathematical Models and Methods in Applied Sciences, 28 (2018), pp. 953–978. 7, 28, 35, 36, 47, 70
- [140] T. KÖPPL AND B. WOHLMUTH, *Optimal a priori error estimates for an elliptic problem with Dirac right-hand side*, SIAM Journal on Numerical Analysis, 52 (2014), pp. 1753–1769. 37, 44, 45, 60
- [141] T. T. KÖPPL, *Multi-scale modeling of flow and transport processes in arterial networks and tissue*, PhD thesis, Universität München, 2015. 28, 34, 35
- [142] J. KOU AND S. SUN, *A new treatment of capillarity to improve the stability of IMPES two-phase flow formulation*, Computers & Fluids, 39 (2010), pp. 1923–1931. 111, 114

- [143] —, *Convergence of discontinuous galerkin methods for incompressible two-phase flow in heterogeneous media*, SIAM Journal on Numerical Analysis, 51 (2013), pp. 3280–3306. 109
- [144] —, *Upwind discontinuous Galerkin methods with mass conservation of both phases for incompressible two-phase flow in porous media*, Numerical Methods for Partial Differential Equations, 30 (2014), pp. 1674–1699. 109
- [145] M. KUČHTA, M. NORDAAS, J. VERSCHAEVE, M. MORTENSEN, AND K. MARDAL, *Preconditioners for saddle point systems with trace constraints coupling 2D and 1D domains*, SIAM Journal on Scientific Computing, 38 (2016), pp. B962–B987. 37
- [146] C. S. KUMAR AND F. MOHAMMAD, *Magnetic nanomaterials for hyperthermia-based therapy and controlled drug delivery*, Advanced Drug Delivery Reviews, 63 (2011), pp. 789–808. 11
- [147] J. KUTTLER AND V. SIGILLITO, *An inequality for a stekloff eigenvalue by the method of defect*, Proceedings of the American Mathematical Society, 20 (1969), pp. 357–360. 50
- [148] J. LANGSETH, *On an implementation of a front tracking method for hyperbolic conservation laws*, Advances in Engineering Software, 26 (1996), pp. 45–63. 113
- [149] R. J. LEVEQUE, *Finite volume methods for hyperbolic problems*, vol. 31, Cambridge University Press, 2002. 15, 23, 112
- [150] J. R. LEVICK AND C. C. MICHEL, *Microvascular fluid exchange and the revised starling principle*, Cardiovascular research, 87 (2010), pp. 198–210. 36
- [151] J. LI, J. MELENK, B. WOHLMUTH, AND J. ZOU, *Optimal a priori estimates for higher order finite elements for elliptic interface problems*, Applied Numerical Mathematics, 60 (2010), pp. 19–37. 60, 62
- [152] J. LI AND B. RIVIERE, *High order discontinuous Galerkin method for simulating miscible flooding in porous media*, Computational Geosciences, 19 (2015), p. 1251. 109, 115, 116
- [153] J. LIONS AND E. MAGENES, *Non-Homogeneous Boundary Value Problems Vol. I*, Springer-Verlag, New York, 1972. 53
- [154] A. LOGG, *Efficient representation of computational meshes*, International Journal of Computational Science and Engineering, 4 (2009), pp. 283–295. 73
- [155] S. MAHJOOB AND K. VAFAI, *Analytical characterization of heat transport through biological media incorporating hyperthermia treatment*, International Journal of Heat and Mass Transfer, 52 (2009), pp. 1608–1618. 25

- [156] B. T. MALLISON, *Streamline-based simulation of two-phase, multicomponent flow in porous media*, PhD thesis, Stanford University, 2004. 113, 124
- [157] B. T. MALLISON, M. G. GERRITSEN, S. F. MATRINGE, ET AL., *Improved mappings for streamline-based simulation*, SPE Journal, 11 (2006), pp. 294–302. 124
- [158] V. MARTIN, J. JAFFRÉ, AND J. ROBERTS, *Modeling fractures and barriers as interfaces for flow in porous media*, SIAM Journal on Scientific Computing, 26 (2005), pp. 1667–1691. 37
- [159] S. F. MATRINGE, R. JUANES, AND H. A. TCHELEPI, *Robust streamline tracing for the simulation of porous media flow on general triangular and quadrilateral grids*, Journal of Computational Physics, 219 (2006), pp. 992–1012. 114, 117
- [160] S. F. MATRINGE, R. JUANES, H. A. TCHELEPI, ET AL., *Tracing streamlines on unstructured grids from finite volume discretizations*, in SPE Annual Technical Conference and Exhibition, Society of Petroleum Engineers, 2006. 114
- [161] A. MAZZIA AND M. PUTTI, *Three-dimensional mixed finite element-finite volume approach for the solution of density-dependent flow in porous media*, Journal of Computational and Applied Mathematics, 185 (2006), pp. 347–359. 111
- [162] A. MICHEL, *A finite volume scheme for two-phase immiscible flow in porous media*, SIAM Journal on Numerical Analysis, 41 (2003), pp. 1301–1317. 109
- [163] M. MUSKAT AND M. W. MERES, *The flow of heterogeneous fluids through porous media*, Physics, 7 (1936), pp. 346–363. 107
- [164] M. MUSKAT, R. WYCKOFF, H. BOTSET, M. MERES, ET AL., *Flow of gas-liquid mixtures through sands*, Transactions of the AIME, 123 (1937), pp. 69–96. 107
- [165] M. NABIL AND P. ZUNINO, *A computational study of cancer hyperthermia based on vascular magnetic nanoconstructs*, Royal Society Open Science, 3 (2016), pp. 1–15. 12, 25, 28, 139
- [166] R. L. NAFF, T. F. RUSSELL, AND J. D. WILSON, *Shape functions for velocity interpolation in general hexahedral cells*, Computational Geosciences, 6 (2002), pp. 285–314. 114
- [167] J. R. NATVIG AND K.-A. LIE, *Fast computation of multiphase flow in porous media by implicit discontinuous Galerkin schemes with optimal ordering of elements*, Journal of Computational Physics, 227 (2008), pp. 10108–10124. 109

- [168] K. NIKITIN, K. TEREKHOV, AND Y. VASSILEVSKI, *A monotone nonlinear finite volume method for diffusion equations and multiphase flows*, Computational Geosciences, 18 (2014), pp. 311–324. 132
- [169] H. M. NILSEN, K.-A. LIE, ET AL., *Front tracking methods for use in streamline simulation of compressible flow*, in SPE Reservoir Simulation Symposium, Society of Petroleum Engineers, 2009. 113, 124
- [170] H. M. NILSEN AND J. R. NATVIG, *Improved gravity splitting for streamline and reordering methods*, in ECMOR XII-12th European Conference on the Mathematics of Oil Recovery, 2010. 112
- [171] D. NOTARO, L. CATTANEO, L. FORMAGGIA, A. SCOTTI, AND P. ZUNINO, *A mixed finite element method for modeling the fluid exchange between micro-circulation and tissue interstitium*, Springer International Publishing, 2016, pp. 3–25. 33
- [172] J. T. ODEN, I. BABUŠKA, AND C. E. BAUMANN, *A discontinuous hp finite element method for diffusion problems*, Journal of Computational Physics, 146 (1998), pp. 491–519. 111, 115
- [173] M. S. OLUFSEN AND A. NADIM, *On deriving lumped models for blood flow and pressure in the systemic arteries*, in Computational Fluid and Solid Mechanics 2003, Elsevier, 2003, pp. 1786–1789. 27
- [174] I. OSAKO, M. KUMAR, V. T. HOANG, G. K. BALASUBRAMANIAN, ET AL., *Evaluation of streamline simulation: Application to heavy oil waterflood*, in Latin American and Caribbean Petroleum Engineering Conference, Society of Petroleum Engineers, 2009. 105, 112
- [175] T. B. PACHECO, A. F. C. DA SILVA, AND C. R. MALISKA, *Comparison of IMPES, sequential, and fully implicit formulations with element-based finite volume method*, Revista Interdisciplinar de Pesquisa em Engenharia-RIPE, 2 (2016), pp. 194–205. 106, 111
- [176] S. PAINTER, C. GABLE, AND S. KELKAR, *Pathline tracing on fully unstructured control-volume grids*, Computational Geosciences, 16 (2012), pp. 1125–1134. 114
- [177] S. PEDDIBHOTLA, A. DATTA-GUPTA, G. XUE, ET AL., *Multiphase streamline modeling in three dimensions: Further generalizations and a field application*, in SPE Reservoir Simulation Symposium, Society of Petroleum Engineers, 1997. 112
- [178] R. PENTA, D. AMBROSI, AND A. QUARTERONI, *Multiscale homogenization for fluid and drug transport in vascularized malignant tissues*, Mathematical Models and Methods in Applied Sciences, 25 (2015), pp. 79–108. 28

- [179] K. PERKTOLD, M. PROSI, AND A. LEUPRECHT, *Computer simulation of arterial flow and related transport phenomena*, in Computer Methods in Biomechanics and Biomedical Engineering, University of Wales College of Medicine, 2002. 27, 29
- [180] D. PETRUZZELLI AND F. G. HELFFERICH, *Migration and fate of pollutants in soils and subsoils*, vol. 32, Springer Science & Business Media, 2013. 105
- [181] A. A. PETRYK, A. J. GIUSTINI, R. E. GOTTESMAN, P. A. KAUFMAN, AND P. J. HOOPES, *Magnetic nanoparticle hyperthermia enhancement of cisplatin chemotherapy cancer treatment*, International Journal of Hyperthermia, 29 (2013), pp. 845–851. 11, 25
- [182] M. PEYROUNETTE, Y. DAVIT, M. QUINTARD, AND S. LORTHOIS, *Multiscale modelling of blood flow in cerebral microcirculation: Details at capillary scale control accuracy at the level of the cortex*, PLoS ONE, 13 (2018), p. e0189474. 80, 90
- [183] F. PLOURABOUÉ, P. CLOETENS, C. FONTA, A. STEYER, F. LAUWERS, AND J.-P. MARC-VERGNES, *X-ray high-resolution vascular network imaging*, Journal of Microscopy, 215 (2004), pp. 139–148. 26, 141
- [184] D. W. POLLOCK, *Semianalytical computation of path lines for finite-difference models*, Ground Water, 26 (1988), pp. 743–750. 116, 122, 123, 143
- [185] L. POSSENTI, G. CASAGRANDE, S. DI GREGORIO, P. ZUNINO, AND M. L. COSTANTINO, *Numerical simulations of the microvascular fluid balance with a non-linear model of the lymphatic system*, Microvascular Research, (2018). 28
- [186] M. PREVOST, M. G. EDWARDS, M. J. BLUNT, ET AL., *Streamline tracing on curvilinear structured and unstructured grids*, in SPE Reservoir Simulation Symposium, Society of Petroleum Engineers, 2001. 114
- [187] A. PRIES, T. SECOMB, AND P. GAEHTGENS, *Biophysical aspects of blood flow in the microvasculature*, Cardiovascular Research, 32 (1996), pp. 654–667. 30
- [188] A. QUARTERONI AND L. FORMAGGIA, *Mathematical modelling and numerical simulation of the cardiovascular system*, Handbook of Numerical Analysis, 12 (2004), pp. 3–127. 27
- [189] C. REDONDO, G. RUBIO, AND E. VALERO, *On the efficiency of the IMPES method for two phase flow problems in porous media*, Journal of Petroleum Science and Engineering, 164 (2018), pp. 427–436. 111
- [190] J. REICHOLD, M. STAMPANONI, A. L. KELLER, A. BUCK, P. JENNY, AND B. WEBER, *Vascular graph model to simulate the cerebral blood flow in realistic*

- vascular networks*, Journal of Cerebral Blood Flow & Metabolism, 29 (2009), pp. 1429–1443. 25, 26, 32, 34, 84, 90, 141
- [191] B. RIVIERE, *Discontinuous Galerkin methods for solving elliptic and parabolic equations: Theory and implementation*, Society for Industrial and Applied Mathematics, 2008. 15, 17, 21, 22, 111
- [192] T. ROOSE AND M. SWARTZ, *Multiscale modeling of lymphatic drainage from tissues using homogenization theory*, Journal of Biomechanics, 45 (2012), pp. 107–115. 28
- [193] T. RUSSELL, *Eulerian-Lagrangian localized adjoint methods for advection-dominated problems*, Numerical Analysis, 228 (1989), pp. 206–228. 112
- [194] S. SAUTER AND R. WARNKE, *Extension operators and approximation on domains containing small geometric details*, East West Journal of Numerical Mathematics, 7 (1999), pp. 61–77. 54, 55
- [195] M. SCHNEIDER, B. FLEMISCH, AND R. HELMIG, *Monotone nonlinear finite-volume method for nonisothermal two-phase two-component flow in porous media*, International Journal for Numerical Methods in Fluids, 84 (2017), pp. 352–381. 105, 106, 109
- [196] N. SCHWENCK, B. FLEMISCH, R. HELMIG, AND B. WOHLMUTH, *Dimensionally reduced flow models in fractured porous media: crossings and boundaries*, Computational Geosciences, 19 (2015), pp. 1219–1230. 37
- [197] L. SCOTT AND S. ZHANG, *Finite element interpolation of nonsmooth functions satisfying boundary conditions*, Mathematics of Computation, 54 (1990), pp. 483–493. 43, 44, 59, 62
- [198] R. SCOTT, *Finite element convergence for singular data*, Numerische Mathematik, 21 (1973), pp. 317–327. 20
- [199] T. SECOMB, R. HSU, N. B. BEAMER, AND B. M. COULL, *Theoretical simulation of oxygen transport to brain by networks of microvessels: effects of oxygen supply and demand on tissue hypoxia*, Microcirculation, 7 (2000), pp. 237–247. 76, 77, 78, 142, 145
- [200] M. SEFIDGAR, M. SOLTANI, K. RAAHEMIFAR, M. SADEGHI, H. BAZMARA, M. BAZARGAN, AND M. M. NAEENIAN, *Numerical modeling of drug delivery in a dynamic solid tumor microvasculature*, Microvascular Research, 99 (2015), pp. 43–56. 25
- [201] S. E. SERRANO, *Propagation of nonlinear reactive contaminants in porous media*, Water Resources Research, 39 (2003). 105

- [202] M. SHASHKOV, *Conservative finite-difference methods on general grids*, CRC Press, 2018. 111
- [203] J. SHELDON, W. CARDWELL JR, ET AL., *One-dimensional, incompressible, noncapillary, two-phase fluid flow in a porous medium*, Society of Petroleum Engineers, (1959). 111
- [204] R. SHIPLEY AND S. CHAPMAN, *Multiscale modelling of fluid and drug transport in vascular tumours*, *Bulletin of Mathematical Biology*, 72 (2010), pp. 1464–1491. 28
- [205] R. SHIPLEY, A. SMITH, P. SWEENEY, A. PRIES, AND T. SECOMB, *A hybrid discrete-continuum approach for modelling microcirculatory blood flow.*, *Mathematical medicine and biology: a journal of the IMA*, (2019). 103
- [206] M. SOLTANI AND P. CHEN, *Numerical modeling of interstitial fluid flow coupled with blood flow through a remodeled solid tumor microvascular network*, *PLoS ONE*, 8 (2013), p. e67025. 25
- [207] S. A. STACKER AND M. G. ACHEN, *Emerging roles for VEGF-D in human disease*, *Biomolecules*, 8 (2018), p. 1. 25
- [208] E. H. STARLING, *On the absorption of fluids from the connective tissue spaces*, *The Journal of Physiology*, 19 (1896), pp. 312–326. 36
- [209] O. STEINBACH, *Numerical approximation methods for elliptic boundary value problems: finite and boundary elements*, Springer Science & Business Media, 2007. 53
- [210] H. STONE, A. GARDER JR, ET AL., *Analysis of gas-cap or dissolved-gas drive reservoirs*, *Society of Petroleum Engineers Journal*, 1 (1961), pp. 92–104. 111
- [211] P. J. STUYFZAND, *Simple models for reactive transport of pollutants and main constituents during artificial recharge and bank filtration*, in *Artificial Recharge of Groundwater*, Proceedings of the Third International Symposium on Artificial Recharge of Groundwater, TISAR, vol. 98, 1998. 105
- [212] L. TARTAR, *An introduction to Sobolev spaces and interpolation spaces*, vol. 3, Springer Science & Business Media, 2007. 16
- [213] M. R. THIELE, *Streamline simulation*, in *In Proceedings of the Sixth International Forum on Reservoir Simulation*, Citeseer, 2001. 14, 112, 122
- [214] M. R. THIELE, R. BATYCKY, ET AL., *Water injection optimization using a streamline-based workflow*, in *SPE Annual Technical Conference and Exhibition*, Society of Petroleum Engineers, 2003. 112, 125

- [215] V. THOMÉE, *Galerkin finite element methods for parabolic problems*, vol. Second Edition, Springer, 2006. 49
- [216] D. TIAB AND E. C. DONALDSON, *Petrophysics: Theory and practice of measuring reservoir rock and fluid transport properties*, Gulf Professional Publishing, 2015. 108
- [217] M. T. VAN GENUCHTEN, *A closed-form equation for predicting the hydraulic conductivity of unsaturated soils 1*, Soil Science Society of America Journal, 44 (1980), pp. 892–898. 108
- [218] E. VIDOTTO, R. HELMIG, M. SCHNEIDER, AND B. WOHLMUTH, *Streamline method for resolving sharp fronts for complex two-phase flow in porous media*, Computational Geosciences, 22 (2018), pp. 1487–1502. 7, 114, 124, 129, 132
- [219] E. VIDOTTO, T. KOCH, T. KÖPPL, R. HELMIG, AND B. WOHLMUTH, *Hybrid models for simulating blood flow in microvascular networks*, <https://arxiv.org/abs/1811.10373>, (2018). 7, 80
- [220] H. WANG, D. LIANG, R. EWING, S. LYONS, AND G. QIN, *An ELLAM approximation for highly compressible multicomponent flows in porous media*, Computational Geosciences, 6 (2002), pp. 227–251. 112
- [221] H. WANG, D. LIANG, R. E. EWING, S. L. LYONS, AND G. QIN, *An approximation to miscible fluid flows in porous media with point sources and sinks by an Eulerian-Lagrangian localized adjoint method and mixed finite element methods*, SIAM Journal on Scientific Computing, 22 (2000), pp. 561–581. 111
- [222] F. M. WATERMAN, L. TUPCHONG, R. E. NERLINGER, AND J. MATTHEWS, *Blood flow in human tumors during local hyperthermia*, International Journal of Radiation Oncology* Biology* Physics, 20 (1991), pp. 1255–1262. 25
- [223] S. WHITAKER, *Flow in porous media I: A theoretical derivation of Darcy’s law*, Transport in Porous Media, 1 (1986), pp. 3–25. 29
- [224] M. WOLFF, Y. CAO, B. FLEMISCH, R. HELMIG, AND B. WOHLMUTH, *Multi-point flux approximation L-method in 3D: numerical convergence and application to two-phase flow through porous media*, Radon Ser. Comput. Appl. Math., De Gruyter, 12 (2013), pp. 39–80. 109
- [225] Z. ZHU, *Efficient simulation of thermal enhanced oil recovery processes*, PhD thesis, Stanford University, 2011. 105, 113
- [226] P. ZUNINO, *Discontinuous Galerkin methods based on weighted interior penalties for second order PDEs with non-smooth coefficients*, Journal of Scientific Computing, 38 (2009), pp. 99–126. 21